

The Effect of Free Stream Disturbances and Control Surface  
Deflections on the Performance of the Wortmann Airfoil at Low  
Reynolds Numbers ,

by

V. Sumantran,,

Dissertation submitted to the Faculty of the  
Virginia Polytechnic Institute and State University  
in partial fulfillment of the requirements for the degree of  
Doctor of Philosophy  
in  
Aerospace Engineering

APPROVED:

 ~~Prof. J.F. Marchman III,~~  
Chairman

~~Prof. J.A. Schetz~~

~~Prof. B. Grossman~~

~~Prof. F.H. Lutze~~

~~Prof. W.L. Neu~~

October, 1985.

Blacksburg, Virginia

McR  
98/82/4  
4/28/86

The Effect of Free Stream Disturbances and Control Surface  
Deflections on the Performance of the Wortmann Airfoil at Low  
Reynolds Numbers

by

V. Sumantran

Prof. J.F. Marchman III, Chairman

Aerospace Engineering

(ABSTRACT)

A wing with a Wortmann FX-63-137-ESM airfoil section has been used to study some unique problems encountered in wing aerodynamics in the range of Reynolds numbers between 50,000 and 500,000. The wind-tunnel testing conducted in the 6'x 6' Stability tunnel included strain-gauge data, pressure data and flow-visualization studies. The laminar separation bubble which frequently occurs on the upper surface of the wing is found to dominate its performance and gives rise to a hysteresis loop for lift and drag. Changes in airfoil performance due to positive flap or control surface deflections resemble changes witnessed at higher Reynolds numbers. Negative deflections are seen to considerably change the stall behavior and the flow over the airfoil. This is due to the considerably greater effect on the separation bubble for negative flap deflections.

The structure and mechanism of the laminar separation bubble can also be altered by the introduction of selected

acoustic disturbances and increased free-stream turbulence. The wind-tunnel test-section environment is, therefore, capable of considerably altering wing performance in this regime.

To my father and my mother.

## ACKNOWLEDGEMENTS

First, I would like to express my gratitude to Dr. J.F. Marchman, III. Throughout my involvement in this project, I have received from him all the encouragement and counsel I could have asked for. His supervision afforded me an ideal mix of independence and guidance from which, I believe, I have learnt a great deal.

I would like to extend a special word of thanks to Dr. B. Grossman who devoted some of his time to guide me through some related computational efforts.

In addition, I would like to thank Dr. Schetz, Dr. Lutze and Dr. Neu for agreeing to be on my advisory committee and for their suggestions in the preparation of this dissertation.

Thanks are also due to Mr. Z. Sun for his comments while preparing the dissertation. Mr. G.C. Bandy assisted me in setting up and running the wind tunnel and I would like to record my appreciation for his efforts.

This research was sponsored by the Office of Naval Research and I thank them for their support.

## LIST OF SYMBOLS

AR	.....	Wing aspect ratio
$A_0$	.....	Fourier coefficient
$C_D$	.....	Drag coefficient
$C_L$	.....	Lift coefficient
$C_p$	.....	Pressure coefficient
$C_M$	.....	Pitching moment coefficient
F	.....	Complex potential
k	.....	Roughness dimension
L	.....	Length of the laminar portion of the shear layer
p	.....	Airfoil surface pressure
Re	.....	Reynolds number
Tu	.....	Free stream turbulence intensity
U	.....	Free stream velocity
W	.....	Aircraft weight
w	.....	Normal velocity component
x	.....	Streamwise coordinate
$x_f$	.....	Streamwise location of the flap hinge
z	.....	Airfoil camber

## GREEK SYMBOLS

$\alpha$	.....	Wing angle of attack
$\Gamma$	.....	Circulation strength
$\delta$	.....	Thickness of the boundary layer
$\delta^*$	.....	Displacement thickness of the boundary layer
$\eta_f$	.....	Flap deflection angle
$\lambda$	.....	Pohlhausen pressure gradient parameter
$\mu$	.....	Coefficient of viscosity
$\sigma$	.....	Pressure recovery factor

# TABLE OF CONTENTS

Chapter 1. Introduction . . . . .	1
Chapter 2. Theory of low Reynolds number flows. . . . .	7
2.1: Introduction . . . . .	7
2.2: The Separation Bubble. . . . .	10
2.3 : Trailing-Edge Stall. . . . .	21
2.4 : Leading-Edge Stall. . . . .	22
2.5 : Thin Airfoil Stall. . . . .	24
2.6 : Stall Hysteresis. . . . .	26
Chapter 3. Experiment - Set-up and Operation. . . . .	28
3.1: Wind-tunnel . . . . .	28
3.2: Data Acquisition - Components. . . . .	30
3.3: Data Acquisition - Procedure. . . . .	35
3.4 : Flow Visualization Techniques. . . . .	37
3.5 : Wing Models. . . . .	39
Chapter 4. Basic Experimental Results. . . . .	44
Chapter 5. Effect of Free-stream Disturbances. . . . .	54
5.1 : Effect of Increased Free Stream Turbulence. . . . .	59
5.2 : Effect of Increased Acoustic Disturbance. . . . .	65

Chapter 6. Effect of Control Surface Deflections. . . . .	74
Chapter 7. Conclusions and Recommendations. . . . .	88
Appendix I. Coordinates of the Wortmann Airfoil. . . . .	99
Appendix II. Coordinates of the Pressure Taps. . . . .	101
Appendix III Thin Airfoil Theory - Bent Flat Plate. . . . .	103
List of References. . . . .	114
Vita . . . . .	233

## LIST OF FIGURES

FIG.	TITLE	PAGE
1.1	Typical Re. range for various applications.....	124
2.1	Typical airfoil surface pressure distribution...	125
2.2	Schematic of a typical separation bubble .....	126
2.3	Airfoil surface pressure with bubble .....	127
2.4	Boundary layer profiles with bubble .....	128
2.5	Stall patterns for N60 airfoil .....	129
2.6	Correlation of Re. and stall type .....	130
2.7	History of events during stall .....	131
2.8	A typical stall hysteresis loop .....	132
3.1	Schematic of the Stability Wind Tunnel .....	133
3.2	Arrangement of turbulence strips .....	134
3.3	Remote actuation of the angle of attack .....	135
3.4	Shrouded strut and wing in the test section ....	136
3.5	Acoustic disturbance setup .....	137
3.6	Force data acquisition setup .....	138
3.7	Flow chart for force data acquisition program ..	139
3.8	Pressure data acquisition setup .....	140
3.9	Flow chart for pressure data acquisition .....	141
3.10	Contour of FX-63-137-ESM airfoil .....	142
3.11	Modular plain metal wing .....	143

FIG	TITLE	PAGE
3.12	Modular wing with flap and control surfaces . . . .	144
3.13	Construction of flaps and control surfaces . . . . .	145
3.14	Turbulence spectrum at U=15 m/s . . . . .	146
4.1	Flat plate lift data . . . . .	147
4.2	Two configurations of the top shroud . . . . .	148
4.3	Lift data for the two shrouds . . . . .	149
4.4	Drag data - comparison with momentum deficit . . .	150
4.5	Lift data - comparison with pressure integration	151
4.6	Effective aspect ratios for the wings . . . . .	152
4.7	Typical stall patterns for FX-63-137-ESM . . . . .	153
4.8	Pressure distribution history at stall - 150K ..	154
4.9	Pressure distribution history at stall - 200K ..	155
4.10	Stall hysteresis for AR=8 and Re.=200K . . . . .	156
4.11	Pressure distributions for hysteresis loop . . . . .	157
4.12	Drag data for stall hysteresis - AR=8 Re.=200K .	158
4.13	Flow visualization & pressure data - 0 deg. . . . .	159
4.14	Flow visualization & pressure data - 10 deg. . . .	160
4.15	Oil drop flow visualization . . . . .	161
4.16	Aspect ratio effects for Re.=200K . . . . .	162
5.1	Idealized sketch of flat plate transition . . . . .	163
5.2	Effect of free stream turbulence on transition .	164

FIG	TITLE	PAGE
5.3	Turbulence effect-lift data Re.=200K .....	165
5.4	Turbulence effect-pressure data Re.=200K 12 deg.	166
5.5	Turbulence effect-pressure data Re.=200K 14 deg.	167
5.6	Turbulence effect-drag data Re.=200K .....	168
5.7	Turbulence effect-L/D ratio Re.=200K .....	169
5.8	Turbulence effect-lift data Re.=100K .....	170
5.9	Turbulence effect-pressure data Re.=100K 10 deg.	171
5.10	Turbulence effect-pressure data Re.=100K 14 deg.	172
5.11	Turbulence effect-lift data Re.=150K .....	173
5.12	Turbulence effect-pressure data Re.=150K 10 deg.	174
5.13	Turbulence effect-pressure data Re.=150K 14 deg.	175
5.14	Effect of acoustics on NACA 2412 pressure data .	176
5.15	Variation of lift with excitation level .....	177
5.16	Variation of lift with excitation frequency ....	178
5.17	Variation of speaker output with frequency .....	179
5.18	Acoustic effect-lift data Re.=200K .....	180
5.19	Acoustic effect-pressure data Re.=200K 14 deg ..	181
5.20	Spectrum of dominant frquencies for 5600 Hz. ...	182
5.21	Acoustic effect-lift data Re.=150K .....	183
5.22	Acoustic effect-pressure data Re.=150K 11 deg...	184
5.23	Spectrum of dominant frequencies for 580 Hz.....	185
5.24	Acoustic effect-stall behavior Re.=70K .....	186

FIG	TITLE	PAGE
5.25	Spectrum of dominant frequencies for 1200 Hz. . .	187
5.26	Acoustic partial/full effect-pressure data . . . . .	188
6.1	Principal types of trailing edge flaps . . . . .	189
6.2	Representation of plain flap - bent flat plate .	190
6.3	Zero lift angle variation with flap deflection .	191
6.4	Pitching moment variation with flap deflection .	192
6.5	Flap deflection - Clark-Y performance . . . . .	193
6.6	Lift increment for flap deflection - theory . . . .	194
6.7	Lift curve slope change for flap deflection . . . .	195
6.8	Zero lift angle change with flap deflection . . . .	196
6.9	Effect of hinge gap - lift data $Re.=200K$ . . . . .	197
6.10	Effect of hinge gap - drag data $Re.=200K$ . . . . .	198
6.11	Lift data for plain and flap wing $Re.=200K$ . . . . .	199
6.12	Drag data for plain and flap wing $Re.=200K$ . . . . .	200
6.13	Lift data for plain and flap wing $Re.=300K$ . . . . .	201
6.14	Flap deflection effect - lift data $Re.=200K$ . . . .	202
6.15	Post stall pressure distribution 18,30 deg. . . . .	203
6.16	Flap deflection effect - drag data $Re.=200K$ . . . .	204
6.17	Pressure distribution history at stall $Re.=200K$ .	205
6.18	+/- flap deflection effect - lift data $Re.=200K$ .	206
6.19	+/- flap deflection pressure data $Re.=200K$ . . . . .	207
6.20	+/- flap deflection pressure data $Re.=200K$ . . . . .	208

FIG	TITLE	PAGE
6.21	+/- flap deflection effect - lift data Re.=200K.	209
6.22	+/- flap deflection effect - drag data Re.=200K.	210
6.23	+/- flap deflection effect - pitching moment ...	211
6.24	Flap deflection effect - lift data Re.=100K ....	212
6.25	+/- flap deflection effect - lift data Re.=100K.	213
6.26	Pressure distribution history at stall Re.=100K.	214
6.27	Reynolds number effect - lift data @ 0 deg.....	215
6.28	Reynolds number effect - lift data @ 33 deg.....	216
6.29	Reynolds number effect - lift data @ 15 deg.....	217
6.30	Symmetric C-S deflection - lift data Re.=200K...	218
6.31	Symmetric C-S deflection - drag data Re.=200K...	219
6.32	AR=4 and AR+9 lift data @ 15 deg. Re.=200K.....	220
6.33	Reynolds number effect with symmetric C-S def...	221
6.34	Comparison of max. lift coefficient .....	222
6.35	Comparison of zero lift angle .....	223
6.36	Comparison of L/D @ max. lift .....	224
6.37	Rolling moment data for Re.=100K @ 30 deg.....	225
6.38	Lift data for asymmetric C-S deflections 30 deg.	226
6.39	Rolling moment data for Re.=200K @ 15 deg.....	227
6.40	Lift data for asymmetric C-S deflections 15 deg.	228
6.41	Variation of rolling moment with flap deflection	229
6.42	Variation of Yaw moment with flap deflection ...	230

FIG	TITLE	PAGE
A3.1	Vortex distribution for thin airfoil theory . . . .	231
A3.2	Representation of the bent flat plate for theory	232

## LIST OF TABLES

TABLE	TITLE	PAGE
3.1	Table of free stream turbulence intensity .....	121
3.2	Assignment of hard wired channels .....	122
6.1	Data for flap performance comparison .....	123

## CHAPTER 1. INTRODUCTION

In recent years, there has been an awakening of interest in the field of low Reynolds number wing aerodynamics for many reasons. The Reynolds number represents the ratio of inertial forces to viscous forces in the flow. In conventional wing and aircraft aerodynamics, the characteristic length used to evaluate the Reynolds number is the wing chord and any flow situation where the Reynolds number falls below 500,000 is said to fall in the low Reynolds number flow regime.

Based on the definition of Reynolds number, for an aircraft in level flight, it can be shown that

$$Re = \sqrt{\frac{2W}{C_L} \frac{L}{AR} \frac{\rho}{\mu^2}} \quad (1.1)$$

where  $\mu$  is the viscosity of air,  $W$  the weight of the vehicle and  $AR$ , the aspect ratio of the wing. Low Reynolds number flow situations can therefore occur for flight at high altitude, low velocity or involving small reference lengths.

The desire of the United States Navy to design Remotely-Piloted Vehicles (RPVs) capable of cruise at ship speed at very low altitudes has motivated considerable research in this area. These RPVs are comparable to highly efficient model airplanes and are intended for use as target vehicles,

decoys and surveillance aircraft. Another important application concerns High-Altitude Aircraft Platforms (HAAPs) which may be used for environmental and weather research. Other areas of application include sailplanes, ultra-light aircraft, wind-turbines and inboard sections of helicopter rotor blades. In this study, in view of the applications of interest, the range from 50,000 to 500,000 is addressed.

Examining Fig.(1.1), one can see the operational environment of these vehicles in relation to others. Indeed, low Reynolds number wing aerodynamics has received significant contributions from the fields of sailplane and model-aircraft aerodynamics.

Well-known airfoil sections used successfully at higher Reynolds number possess many inherent deficiencies for use at Reynolds number less than 500,000. Furthermore, Lissaman (1) has noted a typical critical Reynolds number of about 70,000, below which the section fails to behave like an airfoil, causing an even greater deterioration in performance. These decreases in performance are mainly due to relatively large viscous effects leading to premature flow separation.

Certain flow phenomena are peculiar in this Reynolds number regime. One of these is the 'separation bubble', where a local region of separated flow occurs over the airfoil surface. The laminar boundary-layer separates from the airfoil surface and the flow reattaches further down-

stream as a turbulent boundary layer. The effect of this bubble on the flow over the upper surface can be localized or extend over the entire upper surface depending on the conditions. However, a consequence of the occurrence of the bubble is the phenomenon of 'stall hysteresis'.

Stall hysteresis is the phenomenon whereby, subsequent to stall, a reduction the airfoil angle of attack does not restore the value of lift immediately. A substantial reduction in the incidence is necessary to achieve restoration of the flow. This behavior can pose critical problems for RPVs operating at an altitude of about 50 feet. Should stall occur upon encountering a gust, the recover should be immediate to avoid any significant loss in altitude. The understanding of this mechanism is therefore essential.

Many design procedures exist (2,3,4) for the development of efficient airfoils for this regime. These airfoils are designed to operate with the separation bubble taken into account and achieve a maximum  $C_L$  of over 1.5. The FX-63-137 section is one such airfoil, developed by Wortmann (4) for use on sailplanes at a Reynolds number of around 500,000. This contour was subsequently smoothed by Eppler (3) whereupon the section was titled FX-63-137-ESM. This airfoil section was used in the present study.

A bulk of earlier wind tunnel testing with these airfoils was aimed at obtaining two-dimensional data. Very little data is available for the three-dimensional effects and for

finite aspect ratio wings. This can mainly be attributed to scaling and the magnitudes of the forces involved. The models need to be small enough to permit free development of the wingtip vortices without wind tunnel wall interference. At the same time, the forces generated by the model must be large enough to permit extraction of repeatable and accurate data.

Many unknowns exist with regard to low Reynolds number airfoil behavior due to the complicated nature of the boundary layer with the separation bubble. While the size and the shape of the hysteresis loop is very much a function of airfoil shape, the results can be greatly affected by the wind tunnel disturbance environment (free-stream turbulence and acoustics) as well as the model surface condition.

Unfortunately, not enough studies have been conducted in different wind tunnel facilities to satisfactorily define the role of these disturbances in the test results. It is evident, however, that a unique type of wind tunnel facility is essential where the test-section is large enough to permit testing of suitably sized models while possessing a low disturbance level free-stream and sensitive data acquisition equipment. It is also essential that remote model actuation capability be available in order to observe both halves of the hysteresis loop.

The Virginia Tech Stability Tunnel is a facility where the above conditions for low Reynolds number wind tunnel

testing are met satisfactorily. The 6'x 6' test-section has a catalogued free-stream turbulence intensity of about 0.02% and is equipped with a suitably sensitive strain-gauge strut to obtain consistent data.

Very little is known today about the effect of flap or control surface deflection on the performance of airfoils in these low Reynolds number regimes. This is particularly true for the cases where the upper surface flow is complicated by the presence of the separation bubble. The behavior of the separation bubble is closely related to the boundary layer characteristics and the pressure gradient distribution on the airfoil upper surface. A change in these factors due to flap or control surface deflection would considerably alter the separation bubble possibly eliminating the bubble altogether. In this situation, the airfoil could experience a decrease rather than an increase in performance with flap deflection. A better understanding of the effect of flap or control surface deflection on the performance of these airfoils in the low Reynolds number regime is therefore essential.

The current research program was formulated with two major objectives. First, a better understanding of the effects of increased disturbance levels on the airfoil performance was sought. Here, the emphasis was on obtaining force, moment and pressure data for the wing subjected to different levels of free-stream turbulence and acoustic disturbances. No attempt was made, at this stage, to document detailed

changes within the boundary-layer. Subsequently, the effect of control surface deflections on the airfoil performance was also to be determined. An earlier study in the same tunnel and with a practically identical set-up had examined the effect of wing aspect ratio for this flow regime (6). The present study involved :

1. Force and Moment data obtained from the strain-gauge strut.
2. Pressure distribution data using a Scanivalve selector unit.
3. Flow visualization using the evaporative naphthalene-trichloroethane technique.

## CHAPTER 2. THEORY OF LOW REYNOLDS NUMBER FLOWS.

### 2.1: INTRODUCTION

The origins of the field under study can be traced back to the considerable contributions made to airfoil research in the early 1930s. Millikan and Klein (5) are generally credited with the earliest study attempting to relate the behavior of the boundary layer on the airfoil to the stalling patterns observed. Their study recognized the ability of a turbulent boundary layer on the airfoil to remain attached longer compared to a laminar boundary layer thereby delaying stall and resulting in higher possible values of  $C_{Lmax}$ .

At about the same time, Jones (6) was involved in the study of the performance of many airfoil sections, particularly in relation to their stalling patterns. His investigations led to a classification of stalling behavior into three types, one due to flow separation at the leading edge and two types due to trailing edge flow separation. A detailed distinction between the mechanism of the latter two cases could not be made due to lack of boundary layer information - this being now recognized as caused by the 'separation bubble'.

Von Doenhoff (7) was one of the earliest investigators to study the separation bubble phenomena. The separation

bubble, commonly termed 'laminar separation bubble' in older literature, can be briefly explained in the current context as follows. The laminar boundary layer, depending on local conditions, can easily separate from the airfoil surface upon encountering a suitably adverse pressure gradient. Transition occurs in the free shear layer and the entrainment of the turbulent flow may result in reattachment to the airfoil surface as a turbulent boundary layer (Fig.((2.2)). This region, between the point of separation and the point of reattachment, is characterized by recirculatory flow, and is termed the separation bubble. In view of its importance in dictating boundary layer behavior over the airfoil and thereby, airfoil performance, a more detailed examination of the separation bubble would appear appropriate.

It is quite understandable that the phenomena of separation bubbles is not widely observed in airfoil research. The formation of these bubbles is possible only for a given range of conditions involving Reynolds number, the imposed pressure distribution, model geometry and flow conditions.

Consider briefly the process of boundary layer transition on a flat plate. A commonly used approximation for transition is given by (8):

where

$$\lambda = \frac{\delta^2}{\nu} \frac{dU}{dx}$$

the Pohlhausen pressure gradient parameter, whereby,

$$\delta_{tr}^* = \frac{2900}{U} \nu \exp(0.08\lambda) \quad (2.2)$$

For a given range of Reynolds numbers (assuming negligible change to the pressure gradient parameter) we find that increasing  $U$  results in decreasing  $\delta_{tr}^*$ . Since for the laminar boundary layer on a flat plate, we have the Blasius relation

$$\begin{aligned} Re_{\delta}^* &= 1.72 \sqrt{Re_x} \\ \delta^* &\propto \sqrt{x} \end{aligned} \quad (2.3)$$

the value of  $x_{tr}$  also decreases. Thus for higher velocities, one can see the trend in a more upstream location of transition. With this physical picture, one may examine the conditions conducive to the formation of the separation bubble. The pressure distribution around an airfoil at a given incidence due to potential flow is characterized by a decreasing upper surface pressure coefficient, followed by a location of peak suction (Fig.(2.1)) and a subsequent length of pres-

sure recovery (adverse pressure gradient). The magnitudes of these favorable and adverse pressure gradients and the location of the suction peak are governed by the profile shape. Now, in order for the separation bubble to form,

- The flow Reynolds number should be low enough so that the adverse pressure gradient, aft of the suction peak, is imposed on the laminar boundary layer causing laminar separation. In other words, the location of transition should not preclude laminar separation.
- The flow Reynolds number should be high enough so that subsequent to laminar separation, there is sufficient energy in the shear layer to permit reattachment.

While these threshold values of Reynolds number vary depending on airfoil geometry, for many low Reynolds number airfoils, the range of Reynolds number from 50,000 to 500,000 is conducive to the formation of such separation bubbles.

## 2.2: THE SEPARATION BUBBLE.

Prior to the examination of the separation bubble, a word of caution is necessary with regard to the terminology in use to characterize these bubbles. As mentioned, older literature refer to these separation bubbles as 'laminar separation

bubbles', with the understanding that the laminar boundary layer separation is followed by transition in the free shear layer and reattachment. Current literature, however, distinguishes between three types of separation bubbles, laminar, transitional or turbulent, depending on where the transition occurs. In view of this definition, the separation bubble of interest in the current research are transitional separation bubbles with transition occurring within the chordwise extent of the bubble, in the free shear layer. All references to the separation bubble in the text that follows will be understood to mean these transitional separation bubbles. It may be mentioned that Briley (9) has conducted numerical computations of 'laminar separation bubbles' with laminar reattachment caused by the removal of the adverse pressure gradient immediately after laminar separation.

Many attempts have been made in the past to relate the global conditions such as Reynolds number based on airfoil chord and the mean free-stream velocity to the parameters of the separation bubble with very limited success. In view of the direct relationship between the boundary layer behavior and the separation bubble, it would appear more appropriate to seek correlations between local boundary layer parameters and the separation bubble. This approach has achieved better, though not complete success. With an increased number of variables to be taken into consideration such as different

airfoil profiles, pressure gradients and test conditions, this attempt to achieve satisfactory correlation has been, at best, partially successful.

A schematic of the separation bubble is presented in Fig.(2.2). As stated, the bubble occurs due to a separation of the laminar boundary layer which is due to the imposed pressure gradient. Fig.(2.3) shows a typical pressure distribution plot for the FX-63-137-ESM airfoil with the presence of the separation bubble. The fluid below the shear layer, in the forward portion of the bubble is more or less static, and hence the term 'dead air' region. This shows up as a region of constant airfoil surface pressure - the pressure plateau. The location of transition in the shear layer corresponds roughly to the start of the pressure recovery region. Typically, the location of flow separation moves upstream with increasing incidence. While the nose geometry of the airfoil plays an important role in determining this behavior, in most cases, increasing the incidence is accompanied by creating a more adverse pressure gradient upstream and close to the leading edge. Gault (10) has also observed a decrease in the boundary layer displacement thickness at separation with increasing angle of attack. Here again, the behavior is in fair agreement with our basic understanding of boundary layer theory where

$$\delta_x \propto \sqrt{x}$$

and indeed Gault has observed this correlation. The importance of obtaining accurate estimates of the boundary layer parameters at separation cannot be overstated as they form a bulk of the correlation parameters used to characterize bubble length, bursting criteria, location of transition and other features of the separation bubble

At the point of separation, the free shear layer develops and the flow moves away from the airfoil surface. Different models have been proposed to calculate this separation streamline. Von Doenhoff's early model (7) predicted a tangential path for the separation streamline from the airfoil surface. Later observations by Gault (10) showed that this streamline could curve away from the tangent. Based on some of his smoke studies on such airfoils, van Ingen (14) has proposed a semi-empirical expression for the angle of the separation streamline based on the momentum thickness Reynolds number just prior to separation and an experimentally observed constant.

This initial portion of the separated shear layer (Fig.(2.2)) is crucial in determining the overall bubble characteristics. These flows are unstable and the growth of instabilities occur quickly, causing transition of the flow

further downstream in this shear layer. Stability calculations in this region are even more difficult since the mean flow can be far from parallel. Prediction of transition in this shear layer is therefore extremely complicated. Some of the early models (7) predicted a fixed Reynolds number based on the length along the shear layer from separation to transition.

$$Re_L = \frac{U_s L}{\nu} = 50,000 \quad (2.4)$$

where  $L$  is the length of the laminar portion of the shear layer. Further research has shown that this relation is of restricted applicability.

At this stage, two matters of considerable complexity need to be addressed. The actual sequence of events leading to transition requires examination. Secondly, the distinction between 'short' and 'long' bubbles should be examined.

The study of the transition process requires the examination of the propagation of the instabilities in the free shear layer. Here both the nature of the primary (T-S waves) as well as the secondary instabilities need to be studied. A detailed examination of the theory of hydrodynamic instability is beyond the scope of the current study. The reader is referred to two excellent treatises by Tani (11) and Gaster (12). Herbert (13) uses Floquet theory to analyse the

behavior of secondary instabilities, tracking their growth to predict transition. This latter procedure can also account for the characteristics of the disturbance environment.

Van Ingen (14), had used a simpler  $e^n$  method with modifications to include the free-stream turbulence effect. This procedure recognizes transition as a process and calculates two critical amplification factors corresponding to the beginning and the end of the transition region.

$$\begin{aligned}\sigma_1 &= 2.13 - 6.18^{10} \log (Tu) \\ \sigma_2 &= 5 - 6.18^{10} \log (Tu) \\ Tu^2 &= \frac{\overline{|u'|^2}}{U^2}\end{aligned}\tag{2.5}$$

Here again, it is the RMS value of the free stream turbulence alone that is used to characterize the disturbance. For values of Tu less than 0.1%, this expression has poorer correlation with available data and this was attributed to the role of the acoustic disturbances that were ignored.

Subsequent to transition, reattachment occurs due to the increasing width of the shear layer due to turbulent mixing. On the basis of his well known Series I and Series II experiments, Gaster (15) produced contour maps of constant velocity lines throughout the bubble region. These show that the laminar portion of the free shear layer is very insensitive to free stream velocity variations. However, the turbulent mixing region occurs over a greater chordal extent when the

free stream velocity is reduced. The observed increase in bubble length due to a reduction in the flow velocity is thus due to slower entrainment of the reattaching turbulent flow. The reattached boundary layer may require as much as 10 percent of the chord before developing the characteristics of a fully turbulent boundary layer. Many theories have been proposed as to when and whether reattachment will occur (14,15,16). The more promising of these are based on the pressure recovery criterion for the reattaching flow. The limiting pressure recovery allowable in this region is related to the adverse pressure gradient that a fully turbulent boundary layer can just overcome without separating.

Crabtree has defined a pressure rise coefficient as (16)

$$\sigma = 1 - \frac{U_R^2}{U_T^2} \quad (2.6)$$

where  $U_R$  is the mean velocity of the flow at reattachment and  $U_T$ , the mean flow velocity at transition. His experiments revealed that the maximum allowable pressure recovery corresponded to

$$\sigma_{cr} = 0.35 \quad (2.7)$$

Requiring a greater pressure recovery in the reattachment region would result in bursting of the bubble. This phenom-

ena can be related to the mechanism of leading edge stall, that will be studied in greater detail.

Wallis (17) has related the bubble 'bursting' with turbulent separation of the flow immediately after reattachment, this process being called 'reseparation'. In this case, the breakdown of the bubble is caused by the inability of the reattaching turbulent layer to remain attached. It is arguable that this process is evident during the mechanism of trailing edge stall. Fig.(2.4) depicts the typical change in boundary layer profiles for the FX-63-137-ESM airfoil through the separation bubble and is due to Ref.(26). The location of flow separation, the regions of reversed flow, the reattachment to the surface and the development of the fully turbulent boundary layer are all clearly visible.

'Long' and 'short' bubbles display rather different behavior and their nomenclature stems from their initially observed geometry - 'short' bubbles extending over the order of one percent of the chord and 'long' bubbles extending over several percent of the chord. More recent experience has shown that this nomenclature is confusing and that the proper criterion for distinguishing the two bubble mechanisms ought to be their influence on the pressure distribution. The 'short' bubble type is characterized by a strong suction peak with a local influence on the pressure distribution. The 'short' bubble type has been observed extending over as much as 20 percent of the chord (18). On the other hand, the

'long' bubble is associated with a collapsed suction peak with degraded airfoil performance.

While many researchers have recorded an abrupt bursting of the 'short' bubble to a 'long' bubble, there is some evidence to show that under some circumstances, this transformation can be gradual. In these cases, the demarkation between the two cases is rather arbitrary. The Series I set of experiments performed by Gaster (15) have shown this gradual expansion process merely through the reduction of the free stream velocity. This is accompanied by an increase in the chordwise extent of the constant pressure plateau and a decrease in the strength of the suction peak. These results have been confirmed by the independent experiments of Gleyzes et. al. (19), where a measurement of the boundary layer momentum thickness at 0.75 chordlengths showed a continuous change with a decrease in the free stream velocity.

Many of these mechanisms such as laminar separation, reattachment and bubble bursting have been independently studied by many researchers using semi-empirical procedures. However, the agreement between any two methods is seldom satisfactory. This is hardly surprising since these procedures rely on the available database. Further, since many of the factors influencing the flow are unknown, these results cannot be corrected to take into account the variation in these test conditions.

In recent years, many computational models have been constructed to calculate the properties of separation bubbles. Some of these are semi-empirical (20) and use experimental bubble data together with inviscid flow theory and unsteady finite difference laminar and turbulent boundary layer calculation procedures. Carter and Vatsa (21) use an inverse boundary layer finite difference analysis coupled to a local inviscid-viscous interaction technique to study these separation bubbles for two dimensional flows. This code uses a forced transition model in which the length and the onset of transition are specified a priori. Good agreement of the results is reported with available experimental data. This code has, however, yet to be tested for predicting the effect of Reynolds number and angle of attack variation for airfoil transitional separation bubbles. Briley and McDonald (22) also use a inviscid-viscous interaction model coupled however to the time dependent Navier-Stokes equations. The interaction model provides an inherent and detailed description of the location of transition and the behavior of the mean flow during and after transition. Reasonably good agreement is again reported for both qualitative and quantitative comparisons with experimental data. Nevertheless, solutions with these levels of accuracy for three dimensional flows are still unavailable.

Returning now to the performance of the airfoil, the now accepted classification of airfoil stall patterns for low

Reynolds number flows is due to McCullough and Gault (23). Based on extensive measurements made on NACA 63<sub>3</sub>-018 and NACA 63<sub>3</sub>-012 airfoil sections in the NACA 7'x10' wind tunnel, they observed :

1. Trailing-Edge Stall : due to a forward motion of the reattached turbulent boundary layer separation point from the trailing edge with increasing incidence.
2. Leading-Edge Stall : due to the abrupt 'bursting' of the shortened separation bubble causing separation of the laminar boundary layer at the leading edge without subsequent reattachment.
3. Thin-Airfoil Stall : due to laminar boundary layer separation near the leading- edge followed by progressively delayed reattachment further downstream with increasing incidence.

Fig.(2.5) shows the three stall types observed on an N60 airfoil. A detailed discussion of the three stall types follows.

### 2.3 : TRAILING-EDGE STALL.

This is the most commonly observed form of 'gentle' stall typical of most thick or moderately thick airfoils at the higher ranges of Reynolds number. Observing a typical  $C_L$  versus angle of attack plot, one sees a gradual decrease in the lift slope prior to attainment of  $C_{Lmax}$  and a smooth and continuous decrease beyond  $C_{Lmax}$ . The drag and pitching moment data also display this continuous variation.

Examining the chordwise pressure distribution histories, one observes an increase in the leading edge suction peak on the upper surface with increasing incidence. For small angles of attack, the pressure recovery aft of the suction peak is continuous. For higher angles of attack (say over 10 degrees), a flat pressure profile near the trailing edge can be observed indicating some flow separation. This is actually separation of the reattached turbulent boundary layer and this point of separation moves upstream with increasing incidence causing an increased proportion of the flat pressure profile in the aft portion of the airfoil.

Stall occurs when the point of turbulent boundary layer separation advances 'close enough' to the location of flow reattachment. Now, the reattaching turbulent flow is unable to remain attached. At this stage, the bubble mechanism breaks down causing a collapse in the suction peak. There-

after, the flow separates as a laminar boundary layer close to the leading edge without subsequent reattachment.

The start of the non-linear portion of the lift curve slope (Fig.(2.5)) coincides with the onset of turbulent separation near the trailing edge. The upstream movement of the turbulent separation with increasing angle of attack is continuous through and beyond  $C_{Lmax}$ .

#### 2.4 : LEADING-EDGE STALL.

This is a rather abrupt form of stall rarely observed at higher Reynolds number. Examining the  $C_L$  versus angle of attack plots (Fig.(2.5)), one observes a constant lift curve slope all the way up to stall. At stall, the value of  $C_L$  is discontinuous with a sudden drop in lift for higher angles of attack. This discontinuous change is also seen in the drag data at stall.

The pressure distribution plots show a continuous increase in the suction peak up to  $C_{Lmax}$ . The bubble is usually easily visible and pressure recovery at the aft portion of the airfoil is continuous up to the trailing edge. Typically, increasing the angle of attack causes the imposition of a more adverse pressure gradient close to the leading edge. This causes the laminar separation point of the bubble to move upstream ; simultaneously, the laminar portion of the shear layer is now more unstable, causing transition to occur

sooner and, effectively, there is a contraction in the total bubble length with increasing incidence. This places the location of reattachment in the region of a more adverse pressure gradient and greater airfoil surface curvature. These conditions may cause a 'bursting' of the bubble causing stall.

Pressure distribution histories, prior to stall, show the prominent suction peak and the continuous pressure recovery aft of the peak indicating no turbulent separation near the trailing edge. Calculations have also shown that the shape factor of the turbulent boundary layer is not close to the critical value required for turbulent separation. However, with a shortening of the bubble, the adverse pressure gradient close to reattachment is seen to increase. It has been suggested that this form of stall occurs due to requiring a greater pressure recovery than the maximum allowable value in the reattachment process.

Beyond stall, the suction peak collapses abruptly and the laminar boundary layer separates near the leading edge and there is no subsequent flow reattachment. Again, as in the case of trailing edge stall, there is a flat pressure profile indicative of separated flow over most of the upper surface.

## 2.5 : THIN AIRFOIL STALL.

This form of stall is observed on thin airfoils with small leading edge radii and at the lower end of the Reynolds number range. It is difficult to locate the exact point of stall from the  $C_L$  versus  $\alpha$  plots since there is little or no loss in lift at stall. The value of lift is much poorer compared to the other two cases and the maximum lift values correspond to the post stall values of lift for the cases of trailing edge or leading edge stall. Thereafter, further increases in angle of attack causes no appreciable change in the value of lift (Fig.(2.5)).

Here, the flow separates close to the leading edge due to a combination of low Reynolds number and small nose radius. Flow attachment takes place considerably aft of separation (say 30 to 40 percent chord) with the bubble now in the 'long' mode. Increasing incidence causes this point of reattachment to move aft, increasing the length of the bubble. The pressure distribution plots show poor values of the suction peak. Stall occurs when the point of reattachment reaches the trailing edge.

For airfoils displaying thin airfoil stall, the values of lift are very low due to early flow separation and a poor suction peak. Furthermore, this reduced leading edge suction also results in a relatively large value of the drag.

Having classified typical airfoil stall patterns in the low Reynolds number regime, it must be pointed out that in some cases, a combination of the behavior of two types of stall may be observed. For many airfoils, for  $Re=150,000$  to  $Re=300,000$ , the type of stall observed may be a combination of leading edge stall and trailing edge stall. Here, the lift curve slope loses linearity prior to  $C_{Lmax}$  and some turbulent separation may be observed near the trailing edge. However, stall may occur due to the 'bursting' of the bubble showing a discontinuous  $C_L$  curve at stall.

Likewise, many airfoils that undergo thin airfoil stall indicate evidence of a 'short' bubble bursting to form a 'long' bubble at low incidence this event being visible through a kink in the lift curve slope.

Another point to note is that a single airfoil, depending upon operating conditions, may experience all or some of the stall types mentioned. Gault (24) has compiled a correlation of these stall types to the flow Reynolds number and one airfoil nose geometry parameter - in this case, the upper surface ordinate at 0.0125 chordlength from the leading edge (Fig.(2.6)). For the given airfoil, merely increasing the Reynolds number can cause the stall type to change from thin airfoil stall to leading edge stall to trailing edge stall.

## 2.6 : STALL HYSTERESIS.

A major effect of the separation bubble on the overall performance of the airfoil is the so-called 'stall hysteresis' phenomena. This may be observed by fixing airfoil incidence and causing a cyclical variation in the Reynolds number (through wind tunnel velocity) or by fixing the Reynolds number and causing a cyclical (and uninterrupted) variation in the airfoil incidence.

Fig.(2.7) depicts a typical cycle of situations experienced by an airfoil undergoing stall hysteresis. At moderate to low incidence, the upper surface flow is characterized by the occurrence of the separation bubble with an attached turbulent boundary layer downstream. On increasing incidence, the bubble contracts and moves upstream and some turbulent separation near the trailing edge may be observed. Further increases in incidence causes the point of turbulent separation to move further upstream and a greater contraction in bubble length. Stall occurs due to the 'bursting' of the bubble due to excess required pressure recovery or the forward location of turbulent separation. At this stage, the flow separates near the leading edge and remains separated over the rest of the airfoil. Now, a reduction in incidence does not cause the flow to retrace the sequence of events preceding stall. The upper surface flow remains separated for a considerable range of decreasing angle of attack before

the restoration of the bubble mechanism is achieved and the values of  $C_L$  restored. Fig.(2.8) depicts this same series of events on the  $C_L$  versus  $\alpha$  plots.

In terms of the airfoil performance, this means that once the airfoil stalls, a considerable decrease in incidence is necessary before the values of  $C_L$  are restored. It is very important, therefore, to fully understand stall hysteresis. Many aircraft operating in this regime are also required to operate at low-speed, low-altitude conditions. Should the wing stall due to encountering a gust, then a quick recovery is vital to avoid significant losses in altitude.

## CHAPTER 3. EXPERIMENT - SET-UP AND OPERATION.

### 3.1: WIND-TUNNEL

The Virginia Tech Stability Wind-tunnel was used to conduct all experiments for this study. This is a single return subsonic wind-tunnel and was used with a 6'x6'x28' closed test section. The nozzle contraction ratio for this tunnel is 10 to 1. Drive to the 14' diameter propeller was provided by a 600hp DC motor which was in turn powered by a 720hp AC synchronous motor-generator set. The tunnel has the capability of providing steady flow for a velocity range from about 20 ft/s to 240 ft/s. A schematic of this tunnel is presented in Fig. (3.1).

Many features of this wind-tunnel are particularly suited to carrying out aerodynamic testing in the low Reynolds number regime. The quality of the flow has been shown to be very good with the levels of free-stream turbulence down to about 0.02% at speeds of less than 50 ft/s. This can be mainly attributed to the set of seven fine-mesh anti-turbulence screens upstream of the test section. Turning vanes are provided at each corner, with finer spacing for the last corner - this reducing any large scale vorticity introduced in turning the flow. The anti-turbulence screens are made of 0.2 mm diameter stainless steel wire with an open

area ratio of the mesh being 0.6. This compares well with an optimum damping screen mesh-size of greater than 0.57 for low turbulence experiments as obtained by Bradshaw (25). A large air-exchange chamber is present between the fan and the test section and this has proven effective in isolating the test section from the effects of fan pressure pulses and acoustics. This feature is of great importance since it has been seen that for low Reynolds number-low free-stream turbulence level conditions the acoustics and, indeed, the whole disturbance environment play a dominant role. Table (3.1) catalogues the free-stream turbulence intensities compiled by Yeates and Saric (25). All values of free-stream turbulence intensities quoted in this study were measured using this technique which has a low-frequency cut-off value of 0.1 Hz.

The large size of the test section permits testing full-span models with negligible effects due to blockage. Three-dimensional effects, such as aspect ratio, can also be studied for reasonable large models.

Fig. (3.14) gives the plot of the turbulence spectrum for this tunnel at a velocity of 15 m/s due to (26). This shows a remarkably clean flow with few inherent frequency spikes except for one peak at 60 Hz. corresponding to the supply frequency. Some signal at 15 Hz. is also picked up - this corresponding to the frequency of the motor-generator unit housed in a separate room on its own foundation.

The controls and instrumentation relating to data reduction and experiment control are located in an air-tight room surrounding the test section and accessible through an air lock. This permits easy test section accessibility for modifications and instrumentation without altering static pressure during testing. This control room also houses the instrumentation for wind-tunnel speed control.

### 3.2: DATA ACQUISITION - COMPONENTS.

(All the force data presented, unless otherwise stated, were obtained from the strain gauge strut and associated bridge amplifiers. This 6-component STI-STO3M strut has a maximum load rating of 200 lb. normal load, 100 lb. each of axial and lateral loads, 200 in.lb. each of pitching and yawing moments and 300 in.lb. of rolling moments. This unit was originally designed and built by NASA Langley and was later regauged before use at the Virginia Tech Stability Tunnel. The output of the strain gauge is 0.001 volt per 22.0 lb. Noise generated in the amplifier can cause fluctuations of 1 micro-volt resulting in an accuracy of the force data of 0.022 lb. This accuracy was found to be acceptable for most of the test cases of interest ; reading drag data for Reynolds number less than 80,000 was, however, not of satisfactory accuracy. In this case, a least squares curve was used to approximate the actual value. Since the bulk of the

experiments were conducted at a Reynolds number of 100,000 and above, this procedure was deemed acceptable.

In order to be able to obtain force data throughout the hysteresis loop, remote actuation of the model angle of attack was necessary. For this purpose, an actuator was designed to fit on top of the strut ; the details of the construction of this unit are available in Fig. (3.3). A DC drive motor and a rotational to linear motion converter was used to vary the incidence of a small hinged platform onto which the wing was mounted. An electronic inclinometer was used to read the relative orientation of the mount in the form of a DC voltage which could be calibrated to yield the model angle of attack. The drive motor could be actuated by the HP computer through an interfacing relay box which could also read the voltage read-out of the inclinometer. The whole unit was designed such that, with the wing mounted to the hinged platform, it would be positioned at the center of the test section. Model angle of attack could thus be varied and estimated with an error of less than 0.5 degrees.

The entire strut and the angle of attack control unit was shrouded to prevent contamination of the model force data with the forces on the support structure. The portion of the strut close to the wing was made as slim as possible to prevent significant alteration of the flow near the region of the mount Fig.(3.4).

A Hewlett-Packard 3052 Automatic Data Acquisition System in conjunction with a Hewlett-Packard 9836 Desktop Computer was used for the experiments. The HP 9836 computer is particularly suited for high speed data acquisition with an internal memory of up to 1 megabyte and two flexible disk drives. All the software was written using HP Basic Version 2.0 which is a powerful language for interaction with peripheral devices. A HP-IB 8 Bit parallel interface was used for communication between computer and externals.

All analog to digital voltage conversions were made using a Hewlett-Packard 3455A Digital Voltmeter which has the capability of reading both AC and DC voltages at a resolution of 0.5 microvolts and a speed of up to 24 samples per second. Switching the channels that form the input to the DVM was achieved using a Hewlett-Packard 3495A Scanner. 9 out of a total of 40 channels were hardwired to fixed inputs such as tunnel temperature, static pressure etc. (see Table 3.2)

Actuation of external devices such as the angle of attack drive motor or the Scanivalve selector was achieved with a HP 59306A Relay Box containing 6 individually controlled Potter Brumfield relays. These relays could be opened or closed by the computer by means of commands passed to the bus decoder on the HP-IB. References (28) and (29) contain more detailed information with regard to interfacing techniques and the operation of the data acquisition system.

Test section static pressure, temperature and dynamic pressure were obtained through three of the nine hardwired channels for data acquisition. A Validyne D899 electronic barometer was used to obtain the tunnel static pressure and a thermistor was used to read tunnel temperature. The thermistor was mounted on a wooden base to achieve insulation from the control room. The tunnel dynamic pressure was obtained by using a pitot-static tube located near the model and connected to Datametrix 1173 Electronic manometer which gave a reading in inches of water.

Wing chordwise pressure distributions were obtained via a computer controlled Scanivalve Model J system using a Setra Systems Model 237 pressure transducer. This system permits connecting, sequentially, one of 48 input ports to the output port. The surface pressure taps on the model were connected to the Scanivalve input ports by means of plastic tubing (#19) of 0.035 in. inner diameter. The single Scanivalve output port was connected to a Druck pressure transducer and the reading was transferred to the 9836 computer through one of the available 31 channels. Sequential switching of the scanivalve ports was achieved by using the HP 59306A Relay box and an interfacing relay unit.

The arrangement used to create the acoustic disturbance in the test section is shown in Fig.(3.5). The tone frequencies were generated using a HP Model 209A Oscillator with a range of 4 Hz. to 2 MHz. This was connected to a Realistic

Model MPA90 100W Solid State PA Amplifier and a Realistic Model 40-1251 Super-powerhorn speaker. The speaker frequency response for the range of desired test frequencies (200Hz. to 5000Hz.) was not constant. Furthermore, it was deemed necessary to detect not only the sound pressure levels of the dialled frequencies, but also the presence and levels of any off-tone frequencies caused by the acoustics of the test section chamber. For this purpose, a Sennheiser Model BT-1753 microphone (dimensions:0.31"x 0.22"x 0.05") was built into the wooden wing of AR=6. It was located flush with the wing upper surface, along the centerline and at 20 percent chord from the leading edge. The microphone was calibrated for the given frequency range and had a sensitivity of 20 mv/Pa. The microphone output was connected to a Princeton Applied Research Model 4512 FFT Real-Time Spectrum Analyser and a HP Model 120B Oscilloscope. The oscilloscope could then record the frequency spectrum of the microphone signal. A convenient feature of this spectrum analyser is the availability of a cursor which could be moved along the spectrum to any desired frequency and the sound pressure level (SPL) at that frequency could then be obtained from a digital read-out. Since only the dominant frequencies of the signal were of interest, this procedure was convenient and quick.

### 3.3: DATA ACQUISITION - PROCEDURE.

The bulk of the data acquisition involved :

1. Global force measurements using the strain gauge strut.
2. Airfoil surface pressure measurements.

There are many advantages in being able to obtain total force data as from a strain gauge strut. Firstly, compared to an integration of the pressure data, this procedure is able to account for not only the pressure forces but also the viscous forces. Secondly, high speed data acquisition for a complete range of conditions is possible.

If the force data have any drawbacks, it is that they are not able to indicate much about the actual flow behavior. Since an understanding of the various flow mechanisms is as important as estimating airfoil performance in order to fully understand low Reynolds number flows over airfoils, a complete set of pressure distribution data were also obtained. Wherever possible, flow visualization studies were conducted to back up the conclusions drawn from the pressure distribution plots. This eliminated any uncertainty in interpreting the picture of the flow from the pressure distribution over

the airfoil. The two sets of experiments were conducted independently, but using the same model and set-up.

Fig.(3.6) depicts the arrangement of the experimental set-up used for force data acquisition. The scanner is used to selectively link the digital voltmeter to the 10 transducers. These are the angle of attack, three force and three moment transducers, and the three for the test section conditions. The computer can be triggered to read the register of the DVM. In addition, the computer can, through the relay box and the drive motor, vary the model incidence. The software developed to execute the complete experiment is presented in the form of a flow chart which is self-explanatory (Fig.(3.7)). Inputs to the program are the model and instrumentation data, the calibration of the angle of attack voltage, range of incidences desired and the number of samplings per data point. Usually, 50 samples of each quantity was taken during data acquisition and averaged for each data point. A tare reading was obtained prior to each run to account for any mounting variations as well as any residual voltages present in any of the channels. Two or more runs were usually conducted for each situation to ensure repeatability of the data. For each datapoint, the computer would automatically reduce the data, create a printout and file the data on a flexible disk.

The arrangement of the data acquisition components to obtain surface pressure measurements is very similar to the

one just described for force measurements (Fig.(3.8)). One additional channel was used to link to the output port of the scanivalve unit and the relay box was now used to drive both the angle of attack drive motor as well as the scanivalve trigger. Again, a flow chart is provided to explain the sequence of events during the experiment (Fig.(3.9)). Since the force measurements were conducted independently, only the test section conditions, the angle of attack and the scanivalve output port were scanned by the scanner.

### 3.4 : FLOW VISUALIZATION TECHNIQUES.

Flow visualization studies were conducted to confirm the conclusions drawn on the basis of the pressure distribution plots. Conventional techniques used at higher Reynolds numbers such as wool-tufts were considered unacceptable due to the expected disruption of the boundary layer flow caused by the presence of the tufts themselves. The flow visualization technique was also expected to clearly indicate the separation bubble and its behavior under various conditions. For this reason, smoke flow visualization techniques were ruled out since in many flow situations, the height of the bubble could be less than 0.1 inches and could therefore not be clearly observed with smoke.

The technique used for the bulk of the flow visualization studies was the evaporative film technique where the rate of

mass transfer at the surface was used to provide insight into the behavior of the boundary layer. A solution of naphthalene in tri-chloroethane was sprayed onto the wing in the form of a super-fine mist using a professional spray-gun. At this stage, the wing appears wet and dark due to the presence of the coating. When the wind-tunnel is turned on, initial evaporation of the solvent leaves a coating of white naphthalene on the wing. Regions of separated flow or low surface velocity (the dead-air region of the separation bubble) have much poorer rates of surface evaporation and this shows up clearly in contrast to regions of attached flow. However, prolonged exposure to the free-stream can cause reverse coloration due to sublimation of naphthalene causing darker regions while slow evaporation of the solvent in regions of separated flow causes the appearance of the white naphthalene coating. This technique works very well for situations where the boundary layer flow can be easily disturbed.

A drawback of this technique is that regions of reverse flow may appear the same as a laminar boundary layer in a region of adverse pressure gradient. To resolve these questions, the above technique was complemented by oil-drop studies. Here, a suitably viscous oil (SAE 10W40 with STP oil treatment) was placed in the form of drops on the upper surface of the wing. These drops were arranged along a diagonal to prevent interference between drops. When the

free-stream is turned on, the smearing of these drops clearly shows regions of attached, separated and reverse flows. While the drops do cause interference to the surface flow, their effect was not very large and this technique worked much better than the oil-film technique.

### 3.5 : WING MODELS.

The airfoil used throughout this study was the FX-63-137-ESM section, originally developed by F.X. Wortmann for optimum performance at a Reynolds number of about 500,000. Modifications to the contour in the form of a smoother leading edge were later effected by Eppler at which stage the ESM suffix was appended to the name. Fig.(3.10) shows the contour of this section and the airfoil coordinates are presented in Appendix I.

Three different wing models were made of this contour.

1. A modular plain metal wing with AR=4,6,8,10. Pressure taps were later added to the outboard sections of this wing in the AR=8 configuration (Fig.(3.11)).
2. A modular metal wing with flap and aileron combinations with AR=4 or 9 with pressure taps provided on the starboard outer section (Fig.(3.12)).

3. A styrofoam-wood wing of  $AR=6$  with a built in microphone.

The dimensions of these models had to be chosen in the face of many constraints. Since an examination of the aspect ratio effects was a part of the overall study, a range of  $AR$  from 4 to 10 was needed. The tunnel test section being 6 feet wide, the maximum allowable span for the model was deemed to be 50 in. ; this would avoid excessive wing-tip vortex and wind-tunnel wall interaction. A wing chord of 5.0 in. was therefore chosen. While it might appear useful to choose a larger chord wing model for the case of  $AR=4$ , it must be remembered that reliable tests were required at a Reynolds number of 70,000, at which point the flow behavior was expected to be different. A larger wing chord would have dictated a lower flow velocity than was acceptable for this tunnel. Further, in view of the model construction experience, the construction of specialized models would have been very expensive and time-consuming.

The modular plain metal wing is shown in Fig.(3.11). Each section was milled as one piece out of a solid aluminium block. An alignment hole was drilled to permit stringing together the required sections to form the desired aspect ratio.

A channel (1/2 in. wide) was cut through the lower surface to route the pressure tubing from the outboard sections.

The upper and lower surface pressure taps were split between the starboard and port outboard sections to avoid congestion of the pressure tubing.

In the past, there have been many questions raised as to the validity of surface pressure measurements at low Reynolds numbers. The presence of the pressure tap itself was considered a sufficient disturbance to alter the flow phenomena. For this reason, great care was taken to ensure satisfactory smoothness near the tap locations. In addition, preliminary flow visualization studies indicated that surface imperfections tended to cause a turbulent wedge locally with a semi-angle of about 11 degrees. Therefore, the pressure taps were arranged along a diagonal on the surface, thereby preventing any upstream tap influencing one downstream. This diagonal was inclined at an angle of about 25 degrees from the streamwise direction with the tap at the leading edge located two chordlengths from the wing-tip. This spanwise location was chosen to minimize the effects due to the wing-tip as well as the strut shroud. The coordinates of the pressure taps for this wing are presented in Appendix II.

The wing surface was coated with epoxy, painted red and always finally polished with No.600 Emery paper. After each assembly of the modules to the required aspect ratio, the joints were cemented with Bondo-body filler and again sanded and polished to prevent any creases or seams. The red-color paint was chosen to highlight the chosen flow visualization

technique. End-plates were also constructed and could be added on to the models to simulate two-dimensional flow for the measurement of the pressure distribution.

The second metal modular wing with the flap-aileron combination was constructed rather differently (Fig.(3.12)). Here again, the wing was constructed out of solid aluminium blocks ; however, each section was made out of 0.65 in. aluminium ribs that were milled using a numerically controlled milling machine. Each rib was milled using 1924 steps ensuring contour error of less than 0.004 in. for the ribs. Here, two alignment holes were drilled - one to string the sections together and the other to string the wing together. Initially, each section was assembled and finished with the epoxy coating and paint. The two outboard sections and the one inboard section were then cut to construct the control surfaces which were in the form of 30 percent chord 'plain' or 'cambered' flaps (Fig.(3.13)). The wing chord was again chosen to be 5 in. for uniformity.

All pressure taps were built into the starboard section. 20 pressure taps (13 on the upper surface, 7 on the lower surface) were all that could be accommodated due to the complexity of the construction. All taps were built into the main body ; the control surface was too small to accommodate any pressure tubing. Here again, care was taken to ensure smoothness of the surface in the area around the pressure taps. The taps were again arranged along a staggered 15 de-

gree diagonal with the leading edge tap approximately 1.7 chordlengths from the wing-tip. The coordinates of the pressure taps for this wing are also presented in Appendix II.

Flap deflection was achieved by using an arrangement of punched holes in a 0.01 in. steel sheet and fixed with screws edgeways into the control-surface and the wing section. A range of positive and negative control-surface deflections could easily be achieved with minimal disruption to the flow.

The third wing of AR=6 was constructed using a styrofoam core with a steel-flat backbone and a thin plywood covering. The styrofoam was cut from blocks in the form of ribs using a template and the hot-wire technique. These ribs were then glued together with epoxy and a laminate wood sheet was glued to the surface. Balsa-wood strips were contoured to form the leading edge and the trailing edge. The steel-flat in the core provided the required bending strength. The surface of the wing was then painted and sanded to the desired finish.

This third wing was used only for the acoustic level measurements. The microphone described, was built in flush with the upper surface of the wing, along the centerline and at 20 percent chord from the leading- edge.

## CHAPTER 4. BASIC EXPERIMENTAL RESULTS.

Before proceeding with experimentation to study the effect of the disturbance environment and control surface deflection, a number of experiments were conducted to ensure accuracy and repeatability of the experimental set-up and procedures.

As mentioned previously, there are many advantages to wind tunnel testing of wings using the strut mount. For the available test section, this permits full-span testing of reasonably large models for a range of aspect ratio. One question that has been raised, however, is the creation of some angularity of the free stream flow due to the differential blockage of the upper and lower halves of the test section due to the shroud. For the 6'x6' test section equipped with a streamlined shroud with a maximum width of 5 inches, as was used, this effect was seen to be negligible. This fact was confirmed by conducting force measurements on a flat plate of  $AR=6$  mounted onto the strut in an identical fashion as the wing. The angle of attack of the flat plate was measured, just as with the wing, with respect to the center line of the tunnel test section and normal to the gravity vector. Any angularity of the flow caused by the shroud would therefore show up as a non-zero value of lift for zero incidence.

Fig.(4.1) shows a variation of the lift coefficient with angle of attack for this flat plate. Considering that the overall accuracy of the angle of attack machine and mount is less than 0.5 degrees, this plot shows no perceivable angularity of the flow.

Two different configurations were tested for the upper piece of the shroud. This piece, about 5 in. high, fitted on to the top of the shroud and was positioned just below the wing. The two pieces were used in an attempt to minimize flow disturbance near the wing while providing an effective shroud for the wing mount. Fig.(4.2) illustrates the two configurations used. Piece A was tapered from the top of the main shroud to about 1 in. below the wing. Piece B was a slimmer top-shroud with a maximum width of 1.5 in.

Fig.(4.3) shows the wing force data obtained for the two different top-shroud pieces. It is evident that there is no effective shift in the angle of attack between the two cases. The stalling angles also show very good agreement. However, in view of the marginally cleaner flow in the proximity of the wing, afforded by the slimmer shroud B, this configuration was chosen.

Another factor that needed to be checked prior to the complete range of experiments was the accuracy of estimation of drag forces, particularly at low incidence. Particularly for low Reynolds number and efficient profiles, such as the one in use, the values of drag corresponding to points close

to the point of minimum drag can be of the order of 0.5 lb. for the wing of  $AR=4$ . This required comparing the strut drag data with those obtained using other procedures. While the integrated pressure loads could be used to obtain drag force, this would not include skin-friction drag, which could form a significant constituent of the total drag under these conditions. The momentum deficit procedure was chosen using a continuously traversing probe for one spanwise location. A more detailed description of this procedure was reported in an earlier study (27).

Fig.(4.4) shows drag data obtained from these two sources. The wake survey was conducted at one spanwise location, about two chordlengths inboard of the starboard wing-tip for the plain  $AR=8$  wing. At this location, the flow is predominantly two-dimensional, as was confirmed with the flow visualization studies. The strain gauge data in Fig.(4.4) was corrected to two-dimensional data using the procedure mentioned in reference (27). Within the extent of the drag bucket, the agreement is satisfactory. For higher incidence, the occurrence of some flow separation causes significant angular momentum contributions in the wake and the agreement is not expected to be good.

It was also necessary to check the quality and consistency of the pressure distribution data as well as the effectiveness of the pressure tap arrangement. This latter check was made by examining the flow visualization pictures. Any

disturbance caused by any one of the pressure taps would show up in the form of a turbulent wedge. Extensive flow visualization studies failed to show any perceivable disturbance caused by the taps.

To compare the accuracy of the pressure tap reading as well as to check this set-up, a comparison was made of the lift calculated from the integrated pressure loads and the strain gauge lift data. Fig.(4.5) shows the case of this comparison for  $Re.=150,000$ . Very good agreement is seen in the value of the lift curve slope and the value of  $C_{Lmax}$ . More importantly, good agreement is also seen in the angular extent of the hysteresis loop with the angle of attack at stall and reattachment showing good correlation. As will be seen later in this study, the introduction of disturbances would cause a reduction in the size of the hysteresis loop, causing earlier reattachment after stall.

It must be mentioned that the end-plates were fitted to the wing model to obtain pressure data. Therefore, the strain gauge data were corrected, using the procedure of reference (27), to the two-dimensional case for the purposes of comparison. This explains the post-stall values of lift from the strain gauge data which are higher than those of the integrated pressure loads. This is due to some additional contributions to the strain gauge lift from the wing-tips after stall.

The effect of the wind tunnel walls on wings of various aspect ratios was examined in the study by Abtahi (27). The presence of the tunnel walls alters the behavior of the wing-tip vortices preventing their free formation compared to the same wing in free flight. Thus, the wing tested within the confines of the tunnel test section would behave like a wing of different aspect ratio in free flight. Indeed, in the limiting case, a full-span wing in a wind tunnel would behave much like a wing of infinite aspect ratio.

In an attempt to investigate the extent of tunnel-wall influence, an inviscid study was performed, to calculate the effective aspect ratios of the various wing models tested. This procedure uses the method of images to require zero normal velocity at the wind-tunnel walls ( the tangential velocity could be non-zero ). Fig.(4.6) shows a plot of the effective aspect ratios for various wings used. As is to be expected, the wing of  $AR=4$  had negligible effects while the wing of  $AR=8$  had an effective aspect ratio that was about 2.5% higher. However, conforming to conventional data presentation, no corrections for the presence of the tunnel walls were made to the data presented.

In view of the small chord of the model, the width of the streamlined shroud and the large tunnel test section, blockage effects were found to be negligible. All data presented in this study are uncorrected for blockage. Horizontal buoyancy corrections were likewise neglected since the

tunnel is known to have a free stream static pressure coefficient gradient of around  $-0.003$  per meter (26).

Fig.(4.7) shows a plot of the variation of lift coefficient with angle of attack. Referring to the classification of stalling types, all three stalling patterns can be observed for this wing for the range of Reynolds number of 70,000 to 300,000. For the case of  $Re.=70,000$ , the wing experiences 'thin airfoil' stall, with very poor performance as predicted by Lissaman (1). No particular stalling angle can be observed from the force data and the behavior of the wing is more like that of a flat plate. Typically, for angles of attack greater than 4 to 6 degrees, the flow over the upper surface is, for the most part, separated.

For the case of  $Re.=100,000$ , Fig(4.7) shows behavior typical of a wing undergoing 'leading edge' stall. The lift curve slope is practically constant all the way upto stall, at which point the drop in lift is significant and abrupt. Fig.(4.8) depicts the pressure distribution history for a similar stall type observed at  $Re.=150,000$ . Here, it is evident that increasing the angle of attack from 14 degrees to 16 degrees increases the amount of upper surface suction, close to the leading edge. The separation bubble is clearly visible with flow reattachment taking place at about 30 percent chord. Subsequently, pressure recovery is continuous on the aft portion of the airfoil. The flow remains attached all the way to the trailing edge. While the location of flow

reattachment shows no significant change due to the increase in incidence, the pressure gradient and the pressure recovery in the region of flow reattachment are substantially increased. A further increase in incidence from 16 degrees to 18 degrees, causes an abrupt breakdown of the whole bubble mechanism corresponding to stall and the abrupt drop in lift (Fig.(4.7)). This is also seen as an abrupt collapse in the upper surface suction and the flow now separates near the leading edge and remains separated over almost the entire upper surface. Throughout this sequence, little change can be observed in the behavior of the lower surface pressure distribution, although subsequent to stall, some loss in lower surface positive pressure coefficients can be observed.

For the case of  $Re.=300,000$ , the force data (Fig.(4.7)) shows trailing edge stall with the lift curve losing linearity prior to achievement of maximum lift. The lift variation is continuous and smooth in the region of maximum  $C_L$  beyond which the value of lift drops gradually, resulting in a 'gentle' stall.

For  $Re.=200,000$ , Fig.(4.7) shows the wing experiencing 'combined leading- edge and trailing edge' stall. Here, the region around  $C_{Lmax}$  shows a smooth variation of lift. The lift curve again loses linearity prior to  $C_{Lmax}$  as is typical of trailing edge stall. However, at stall, the value of lift is discontinuous as is seen in the case of leading edge stall. Examining the pressure distribution history in this

case (Fig.(4.9)), corresponding to the region near  $C_{Lmax}$ , the significant amount of flow separation near the trailing edge is visible as the flat region thereby causing the non-linearity in the  $C_L$  versus angle of attack curve. Increasing the incidence from 18 to 20 degrees, cause the point of flow separation to move forward from about 55 percent chord to about 30 percent chord measured from the leading edge.. This causes the point of turbulent boundary layer separation to occur close to the point of reattachment. Further increases in incidence causes stall with a collapse of upper-surface leading edge suction. The flow now separates near the leading edge without subsequent reattachment. This flow situation is similar to the case of post-stall behavior of the  $Re.=100,000$  case. This explains similar  $C_L$  variations beyond stall for these cases.

Fig.(4.10) shows the typical stall hysteresis phenomena exhibited by this airfoil. In this case, the airfoil stalls at an angle of about 20 degrees. Subsequent to stall, in order to recover the values of pre-stall lift, it is necessary to reduce the angle of attack to about 12 degrees before the restoration of the upper-surface flow and the formation of the separation bubble can occur.

Fig.(4.11) shows typical pressure distribution plots for a single angle of attack corresponding to two points on the hysteresis loop, one on the upper half of the lift hysteresis loop (hereafter referred to as the upper portion of the loop)

and one on the lower half (corresponding to separated flow). In the case of the former, the pressure distribution clearly shows the upper surface suction and the separation bubble. Some amount of trailing edge separation may occur depending on the case. However, for the case of the second point, the flow over most of the upper surface is separated as is typical of a stalled wing. Fig.(4.12) depicts the hysteresis loop observed in the drag data.

Some of the results of the flow visualization study are presented together with the corresponding pressure distribution plots (Fig.(4.13) and Fig.(4.14)) for  $Re.=200,000$ . The good agreement is seen for bubble location and the location of turbulent reattachment. The darker coloration near the trailing edge denotes the region of attached turbulent boundary layer.

That the boundary layer in this aft region is attached is confirmed not only by the pressure distribution plots that indicate continuous pressure recovery for  $x/c$  greater than 0.5 but also the oil drop flow visualization picture (Fig.(4.15)). Here again, the oil drops were arranged along a diagonal to prevent interference between drops and their disturbance to the flow. This picture also shows the stagnant drops upstream of the half-chord line indicating the dead-air region of the bubble. In some cases, the indications of reverse flow could also be observed.

The effect of aspect ratio in this regime was examined by the related study performed by Abtahi (27). A typical plot is shown in Fig.(4.16) for  $Re.=200,000$ , where the greater lift curve slope for greater aspect ratios is clearly seen. Furthermore, wings with smaller aspect ratios stall later. These are, however, trends that would also be observed at higher Reynolds numbers.

## CHAPTER 5. EFFECT OF FREE-STREAM DISTURBANCES.

It is evident, subsequent to the discussion in Chapter 2, that there is a close relationship between the separation bubble and the overall performance of the airfoil. As was seen, upstream of the separation bubble, the boundary layer is laminar while downstream of the bubble, there exists an attached turbulent boundary layer. For this reason, the separation bubble is often described as a 'natural trip mechanism'. It is well known that the initial disturbance spectrum (including free stream turbulence, ambient acoustics and surface roughness) plays a key role in the process of transition. It is therefore reasonable to expect a similar effect of the disturbance environment on the mechanism of the separation bubble.

At the outset, it must be pointed out that a complete understanding of the transition process still eludes researchers today. Lack of sufficient and cumulative studies has resulted in, to quote White (8), 'the bulk of opinion about transition swaying drastically from one misconception to another'. However, some global observations regarding the effects of transition and the factors governing transition can be made.

Consider, for example, the transition process on a smooth flat plate where the initial disturbance spectrum is

infinitesimal and random. Close to the leading edge, the flow is laminar and stable. Next, unstable two-dimensional Tollmein-Schlichting waves appear as travelling waves in the direction of the free stream as shown in Fig.(5.1) from reference (8). These waves quickly become three-dimensional resulting in unstable waves and hairpin eddies. This process is particularly accelerated in a shear layer. These three-dimensional vortices undergo stretching and breakdown causing fully three-dimensional fluctuations. At this stage, in local regions of intense fluctuations, turbulent spots appear. Fully turbulent flow results when these turbulent spots coalesce.

It is well known that a 'dirty' free stream hastens the process of transition. Indeed, the semi-empirical relation used by van Driest and Blumer for laminar profiles described by the Pohlhausen pressure gradient parameter  $\lambda$  is (30) :

$$\frac{9860}{Re_{\delta}} = 1.0 - 0.049\lambda + 3.36 Re_{\delta} Tu^2 \quad (5.1)$$

where  $\lambda = \frac{\delta^2}{\nu} \frac{dU}{dx}$

It has been observed that the free stream turbulence does not affect the initial linear amplification rates of the in-

stabilities but rather accelerates the breakdown of the amplified waves.

In their now classic study of transition on a flat plate in 1948, Schubauer and Skramstad (31) had observed the effect of acoustic disturbances. Using a 25 watt loudspeaker installed above the leading edge of a flat plate, they observed that introducing the right combination of frequency and intensity of the acoustic disturbance, they could move the process of transition by almost 1 to 2 feet upstream of its natural location. When random noise was used, the effect on the boundary layer oscillations was not so marked. The sound frequencies that produced oscillations of maximum amplitude at chosen velocities were found to be in fair agreement with the predictions of the hydrodynamic stability theory (31).

In his study on the effects of free stream turbulence on boundary layer transition, Wells (32) observed maximum transition Reynolds numbers of 5 million for a flat plate compared to 2.8 million observed by Schubauer and Skramstad (Fig.(5.2)). While these two sets of experiments show fairly good agreement for levels of free stream turbulence intensity greater than 0.2%, the difference was of the order of 80% for levels of  $Tu$  less than 0.1%. Examination of the energy spectra of the two free stream disturbance environments showed significantly different acoustic content. In the experiment of Wells, the acoustic content was less than 10% of the total energy with most frequencies below 150 Hz. The

Schubauer-Skramstad experiments, on the other hand, contained significant disturbance frequencies up to 400 Hz. with acoustic disturbances accounting for up to 90% of the total disturbance energy.

In the light of these results, it is clear that in order to fully understand the disturbance effects, it is important that the whole of the disturbance environment be fully understood and catalogued. This is most often very difficult to achieve due to complications arising out of wind tunnel test section acoustics and contributions from the propeller and ancillary equipment. Fortunately, most researchers have found a limiting value for acoustic disturbances ; below this level of acoustic intensity, hardly any changes are observed in global airfoil performance.

The third major mechanism to accelerate transition is surface roughness, either in the form of single or distributed roughness elements. Two-dimensional roughness elements of height 'k', accelerate transition to turbulence by creating locally separated profiles (when  $k/\delta^*$  exceeds 0.3). These unstable profiles accelerate the growth of the T-S waves, the secondary three-dimensional instabilities and ultimately bring about turbulence. For an isolated three-dimensional roughness element, the flow downstream is more often a wedge of continuous turbulence. Spanwise rows of such isolated roughness elements (as a sandpaper strip) were also believed to cause transition through this non T-S mech-

anism. However, Corke and Morokovin (33) have recently shown that for such roughness elements, the process of transition is achieved due to a combination of the two mechanisms. Here, irregular streamwise vorticity structures trailing from higher roughness peaks merge. Furthermore, locally separated regions downstream of the peaks and the low inertia fluid in the valleys, are more susceptible to external disturbances. This could explain the ability of the surface roughness to accelerate transition as well as to make a rough surface more 'receptive' to external disturbances than a smooth surface. It is therefore necessary to know not only the characteristics of the external disturbances but also the 'receptivity' of the surface.

The problem discussed thus far concerns the relatively 'simple' problem of flow over a flat plate. When one now moves on to the airfoil, there is even less known about the detailed flow behavior. As far as trends are concerned, calculations as well as experiments have shown that an adverse pressure gradient tends to destabilize the flow while a favorable pressure gradient tends to stabilize the flow. When the flow situation is compounded by the occurrence of a separation bubble with an unstable shear layer and a reattachment region of large pressure recovery, prediction of transition and more importantly, reattachment, becomes very difficult.

The objectives of this research study were not to obtain the detailed changes in the boundary layer behavior due to the presence of the external disturbances, but to gain better understanding of the effect of these disturbances on global airfoil performance. To this end, force measurements were made for the wings under various external disturbances (mainly acoustic and free stream turbulence). With these experiments, it was hoped to gain better understanding of wing stall and hysteresis behavior.

#### 5.1 : EFFECT OF INCREASED FREE STREAM TURBULENCE.

Prior to discussing the effects of increased free stream turbulence, it is appropriate to describe, in greater detail, the natural flow conditions in the wind tunnel. Table 3.1 lists the measured levels of free stream turbulence intensity due to Yeates and Saric (25). A bulk of the experiments were carried out for free stream velocities between 25 ft/s to 90 ft/s (7.6 m/s to 27.3 m/s) for which range, the free stream turbulence intensity, under natural flow conditions, was between 0.018% to about 0.03%. Fig.(3.14) depicts the turbulence spectrum for this wind tunnel at a velocity of 15 m/s.

The special low-turbulence features of the flow have already been pointed out in chapter 3. Likewise, the method of increasing the level of turbulence and the data acquisi-

tion procedures were also discussed. Here, some of the results of the experiments will be presented.

Fig.(4.10) shows a typical stall hysteresis loop at a Reynolds number of 200,000 and under natural conditions. Subsequent to stall, there is a large drop in lift. Reducing the angle of attack does not immediately restore the pre-stall values of lift. A considerable reduction in incidence is necessary to achieve this. Fig.(4.11) shows the pressure data for this case. For case A, corresponding to point A of Fig.(4.10), on the upper part of the hysteresis loop, the flow is seen to be attached over most of the upper surface. The separation bubble, aft of the leading edge suction peak, is seen between about 15 percent chord and 35 percent chord. Some evidence of trailing edge separation close to the trailing edge may be seen.

Case B of Fig.(4.11) represents the situation after stall, corresponding to point B of Fig.(4.10) Here, for the same angle of attack as A, the flow remains separated over most of the upper surface. Some reduction in the values of lower surface positive pressure coefficient is also seen, due probably to the reduction in overall circulation over the wing.

Fig.(5.3) depicts the stall hysteresis loop under natural flow conditions as well as with increased free stream turbulence. In this case, the baseline level of free stream turbulence was increased from about 0.02% to about 0.2% using

the procedure described in chapter 3. The main effect of this increase is seen to be a reduction in the size of the hysteresis loop. Both cases have very similar stall behavior. It is in fact true that prior to stall, there is no effect due to increased turbulence. The stall angle of attack remains the same although post-stall values of lift appear to be higher for the case with higher levels of free stream turbulence. This is attributed to a slightly delayed point of separation and greater upper surface suction near the leading edge. The closure of the hysteresis loop, as has been seen, coincides with the restoration of the bubble mechanism on the upper surface and attached flow. It can be seen that the increased turbulence had led to an earlier re-attachment when the angle of attack is reduced after stall.

Fig.(5.4) depicts the pressure distribution for this case. Points A and B correspond to the baseline turbulence level data for points on the upper and lower portions of the hysteresis loop respectively. Point C corresponds to the abbreviated hysteresis loop due to increased turbulence at an angle of attack of 12 degrees (Fig.5.3)). The force data shows that for this point, the increased turbulence has already caused closure of the loop. This is also seen in Fig.(5.4) where the cases A and C are almost identical. In effect, the increased turbulence from about 0.02% to 0.2% has caused the flow to change from situation B to situation C

which is seen to be a restoration of the flow to its original pre-stall state, as depicted by point A.

Examining the behavior within the hysteresis loop, for  $\alpha=14$  degrees, one finds increased values of post-stall lift for  $Tu=0.20\%$ , shown by point F in Fig.(5.3). Fig.(5.5) depicts the pressure distribution for these cases. Here, D and E correspond to the case of pre- and post-stall values for  $Tu=0.02\%$  and F the case for post-stall value for  $Tu=0.2\%$ . Comparing F to E, one finds the changes caused by the increased disturbance. Here, the increased disturbance has caused attached flow over the aft portion of the wing. This is indicated by a continuous pressure recovery, all the way to the trailing edge. The suction on the upper surface is poorer for F than for D, although it is still larger than that for case E. It appears that the first effect of increased turbulence is to promote earlier reattachment. However, the development of leading edge suction progresses more slowly, although it is still stronger than the case of fully separated flow. It is this improved leading edge suction for F compared to E that explains the increased value of lift post-stall.

Behavior of the airfoil outside of the hysteresis loop does not appear to be affected by the increased turbulence. The lift curve slope and the values of zero-lift angle remain unaltered.

Fig.(5.6) displays the drag data for the same case. Here again, no major changes are evident apart from a reduction in the size of the hysteresis loop. The fact that the airfoil performance does not incur a drag penalty due to the increased turbulence while decreasing the size of the hysteresis loop, leads to interesting conclusions. In view of the negligible change in drag, the skin-friction drag increase does not seem to be an important constituent of the total drag. In addition, the greater resistance of the flow to separation or rather, the increased tendency of the separated flow to reattach for higher levels of turbulence, may be considered beneficial to overall wing performance. This is also seen in the plot of the lift/drag (L/D) ratio shown in Fig.(5.7), especially for the higher angles of attack. For low angles of attack (-3 to +3 degrees), there is however, a penalty incurred due to the increased turbulence.

When the Reynolds number of the flow is decreased to 100,000 (Fig.(5.8)), the effect of the same increase in turbulence is an even more dramatic reduction in the size of the hysteresis loop. It appears possible that the phenomena of stall hysteresis may not be observed under certain combinations of low Reynolds number and high free stream turbulence. One must be cautioned again that the free stream turbulence intensity alone is inadequate to characterize the flow and to make any predictions about the flow phenomena. It is only

intended, at this stage, to qualitatively study the effect of the increased disturbances.

Fig.(5.8) in conjunction with Fig.(5.9) and Fig.(5.10) may be used to study the flow under these conditions. Once again, the increased disturbances appear capable of restoring the upper surface flow (B to C) outside of the reduced hysteresis loop. Inside, the increased disturbance is once again observed to be capable of achieving reattached flow near the trailing edge while the restoration of the suction, close to the leading edge, is only partially successful.

These same trends are also repeated at  $Re.=150,000$  as shown in Fig.(5.11), Fig.(5.12) and Fig.(5.13). In all these cases, there appears to be no discernible difference in the bubble location and size. Further studies of the boundary layer would need to be made to note any difference due to the increased free stream turbulence outside of the hysteresis loop.

It must also be noted that a further increase in free stream turbulence from 0.2% to 0.3% does not cause much change in the flow. This parallels the observations of Wells (32). Thus it was observed (34) that there exists a certain threshold disturbance condition which will cause this change although changes above this critical disturbance intensity does not appear to bring about any further alteration in global behavior.

The implications of this data are far-reaching. It is now apparent that the conditions of the test section and the quality of the flow can considerably mask the true performance of the wing. As mentioned, depending on the test conditions, the whole of the hysteresis phenomena may be eliminated and go unobserved, resulting in large errors in estimating airfoil performance in flight. It is imperative therefore, that a complete range of disturbance levels be used, starting with very 'clean' flow remembering that the turbulence intensity alone is inadequate to judge the 'cleanliness' of the flow. Unfortunately, on account of the very complicated flow-field involving the separation bubble, a correlation of those frequencies of the turbulence spectrum and the boundary layer parameters of the upper surface flow have yet to be made.

## 5.2 : EFFECT OF INCREASED ACOUSTIC DISTURBANCE.

Gaster (15) was one of the first investigators to study the effect of acoustic disturbances on the separation bubble. He found that oscillations in the shear layer could be induced by external acoustic disturbances. These oscillations were observed to be traveling waves, moving at about half the velocity of the external flow. The disturbance amplitude was found to grow exponentially with distance from separation with a maximum value along the center of the shear layer.

In this respect, they behaved much like small scale turbulence.

Collins (35) has investigated the effect of sound upon separated flow over wings. Using a NACA 2412 airfoil model of 1 foot chord, he was able to use sound to reattach flow over the wing upper surface at incidences of 20.25 and 23.9 degrees. This wing, under natural conditions, had a stall angle of 12 degrees (Fig.(5.14)). Various frequencies were used, and the sound pressure levels required for each were determined. This study, however, failed to take into account any off-tone frequencies and any higher harmonics that could be present in the test section environment during operation. Although certain frequencies requiring minimal acoustic energy to achieve stall suppression were identified, no correlation was made of these frequencies with flow qualities.

Ahuja and Burrin (36) have shown that flow separation over wings can be controlled both in pre- and post-stall regions by sound energy. Here, a system of four electro-acoustic drivers was used to provide the excitation at the distinct frequencies. Here again, a threshold level of acoustic excitation was observed below which the effect of acoustic excitation is negligible (Fig.(5.15)). All these cases were run on a GA(W)-1 airfoil of 10 inch chord with a leading edge trip in place. Certain frequencies were identified that provided the greatest increase in lift for fixed acoustic driver power levels (Fig.(5.16)). In order to

achieve any changes in flow behavior prior to stall, very large values of acoustic driver power levels were required leading to a test section reading of over 150dB SPL.

Both the above studies used airfoils where the occurrence of the separation bubble was precluded. No correlation of the optimum frequency and the flow conditions were made. Although the study of Schubauer and Skramstad (31) did observe a correlation between the 'strong' frequencies and the Branch II of the neutral stability curve, their experiment was conducted on a flat plate.

The procedures used to conduct the acoustic effect tests were mentioned in chapter 3. The loudspeaker was mounted directly over the wing, flush with the tunnel ceiling, an arrangement also used by Gaster (15) and Schubauer-Skramstad (31). Initially, the speaker was tested for its frequency response which was found to be not constant for the desired range of frequencies. Fig.(5.17) shows a plot of the total SPL measured at the wing 1/4 chord point for a range of frequencies and for a fixed amplifier power level of 1.0 W. The SPL readings were found to be higher at the lower frequencies. Furthermore, the presence of off-tone frequencies due to tunnel wall reflections and higher harmonics due to the speaker characteristics were suspected. Therefore, it was necessary to measure the acoustic spectrum at the wing under testing conditions for given values of amplifier power level

and dialled frequencies. This was done with a microphone buried in the wing and is described in chapter 3.

A commercially available speaker was used to generate the disturbances in the test section. These speakers possess a quality that bears note. For a chosen single frequency input, the speaker output contains not only this frequency but also fairly significant levels of the odd harmonics of this frequency (3x, 5x,...). The levels of the even harmonics (2x, 4x,...) are lower. In many cases, these harmonics may occur at frequencies that are too high to directly affect the flow.

Fig(5.18) shows a typical stall hysteresis loop with and without the presence of the acoustic disturbances. Here, a frequency of 5600 Hz. was dialed at the signal generator and the speaker power level was maintained at 0.5 W. Fig.(5.20) shows the spectrum of the acoustic disturbance for only the dominant frequencies, i.e., those frequencies with signals of SPL over 60 dB. In all cases, some disturbance corresponding to 60 Hz. was picked out although the frequencies of 15 Hz. (the frequency of the motor-generator set housed in a separate room) and the harmonics of the propeller frequency were not significant. In all cases, the spectrum of the dominant acoustic frequencies did not change significantly for tunnel-on and tunnel-off conditions. Fig.(5.19) shows the pressure distribution for the three points A,B,C also shown in Fig.(5.18).

It is evident once again, that the effect of increased acoustic disturbance is much like the effect of increased free stream turbulence. There is a considerable reduction in the size of the hysteresis loop accompanying the increased acoustic disturbance. This is again seen to be (Fig.(5.19)) mainly due to the ability of the disturbance to achieve earlier reattachment when reducing the angle of attack after stall. It is therefore possible to use the acoustic signal to change the flow from situation B, corresponding to separated flow on the lower part of the hysteresis loop, to point C where the restoration of the flow is complete. This is seen by comparing case C and case A.

A point to note in this behavior is that the sound signal need only be used as an 'on-off' switch in the sense that once the flow has been changed from B to C using sound, the speaker could be turned off and the flow stays restored on the upper portion of the hysteresis loop. Indeed, some researchers, working with tunnels having already high levels of disturbance, have reported such a switch from situation B to situation C merely by striking the wind tunnel walls or due to the switching on of an airconditioner unit in the background.

Examining the dominant frequencies in the acoustic spectrum for this case, Fig.(5.20) shows a behavior typical of most commercial speakers. Fig.(5.21) shows the same behavior for the wing at  $Re.=150,000$ . Here, a frequency of 580 Hz. at an amplifier power level of 0.5 W was used. Again, the

closure of the hysteresis loop takes place earlier, reducing the angular extent of hysteresis by about 2 degrees. Fig.(5.22) and Fig.(5.23) depict the pressure distribution and the spectrum of the dominant frequencies respectively.

The amplifier power levels should be chosen with care. For increased sound intensities (say over 1.0 W), a whole range of frequencies were found to be capable of effecting the switch from the lower portion of the loop to the upper. A gradual reduction of the intensity would reduce this range of effective frequencies. On the other hand, very low levels of the sound intensity were found to be incapable of achieving this change for the entire range of frequencies in use.

Two interesting features of the effect of acoustic disturbances need to be explained. For low Reynolds number ( $Re$  less than 70,000), where the airfoil was seen to experience thin airfoil stall under natural conditions, it was possible to alter the wing stalling behavior and cause leading edge stall (Fig.(5.24)). It appears that the increased disturbance induces the formation of the 'short' bubble, this coinciding with an increase in the lift curve slope (at about 6 degrees). The wing performance is vastly improved with the value of  $C_{Lmax}$  increasing from about 0.8 to about 1.35. The stall, when it occurs, is abrupt, as is characteristic of leading edge stall and as long as the disturbance remains, a hysteresis loop can be observed. Prior to the formation of the bubble, the two cases have similar performance.

Fig.(5.25) depicts the dominant frequency spectrum for this case.

Certain frequencies, which at initially chosen power levels, were incapable of achieving flow reattachment from the lower part of the hysteresis loop, were found to be capable of creating some improvement in lift. This improvement is dependent upon the existence of the disturbance and disappears when the signal is turned off. Fig.(5.26) shows two such frequencies capable of achieving only a 'partial effect' (5200 Hz. and 5500 Hz.) at an angle of attack of 15 degrees. The same plot also shows one frequency (4830 Hz.) that is able to achieve complete restoration of the flow. These plots indicate that those frequencies which achieved the partial effect lead to slightly improved lift because of delayed separation resulting in an increase in the leading edge suction. However, they are still unable to effect restoration of the bubble mechanism.

The above phenomena is very much a function of the location within the natural hysteresis loop. It appears that the 'readiness' of the flow to reattach increases with proximity to the point of closure of the natural hysteresis loop. In Fig.(5.18), the closure of the natural hysteresis loop occurs at about 10 degrees for  $Re.=200,000$ . For the range of angles between 10 degrees and 12 degrees, a number of frequencies were detected capable of achieving reattachment. Further into the hysteresis loop (at 14 degrees), some of

these frequencies could only achieve a partial effect while a few could cause the flow to change from the lower to the upper portions of the hysteresis loop.

It, therefore, appears that, apart from flow conditions and the frequency of the acoustic signal, the two factors, the 'readiness of the flow to reattach and the strength of the signal, are also crucial in determining the extent of the effect due to acoustic disturbances.

Although the effect of these two disturbances, acoustic and turbulence, were studied independently for reasons of better identification, it is to be expected that they will act together in any condition. Every wind tunnel, for each operating condition, will possess its own characteristic acoustic and turbulence 'signatures'. However, to understand the manner in which they act together requires further study. It is possible that in some situations, these two effects may be additive while in others, the larger disturbance may dominate.

Past studies have shed little light on the manner of this interaction. The results from van Ingen's formula for transition (2.5) showed good correlation for  $Tu$  greater than 0.1% but noticeably poorer correlation for  $Tu$  less than 0.1%. This was attributed to the increased effect of the acoustic disturbances that were unaccounted for  $Tu$  less than 0.1%. The results of Wells (32) also seem to confirm this trend. As reported, his results, in comparison to those of

Schubauer-Skramstad, showed much better agreement for Tu greater than 0.2%. For values of low free stream turbulence (Tu less than 0.1%), the difference between the two results was as much as 80% (Fig.(5.2)). The content and the distribution of the acoustic disturbances were different for the two cases and were reported to be the cause of the lack of agreement.

The matter of the limiting disturbance level also needs further study. This research reported one such level between  $Tu=0.02\%$  and  $Tu=0.2\%$ . Changes from  $Tu=0.2\%$  to  $Tu=0.3\%$  indicated no major alteration in the airfoil performance. This limiting disturbance level is very much dependent on the wind tunnel disturbance signature. A different wind tunnel with a higher proportion of acoustic content in the total disturbance could witness this change at a lower level of turbulence. Furthermore, a wind tunnel with lower overall levels of disturbance but with a significant content of disturbances close to the critical frequency of the flow, may still prove more sensitive to external disturbances. These critical frequencies themselves change with the model and the flow situation. It is clear that a great deal of further study is necessary in this area and extreme caution must be exercised in comparing airfoil performance in this sensitive low Reynolds number regime.

## CHAPTER 6. EFFECT OF CONTROL SURFACE DEFLECTIONS.

Another major area of interest of this study was the effect of control surface deflection on airfoil performance. A detailed description of the control surface model construction is presented in chapter 3.

Two wing models were used for these tests :

1. a wing of  $AR=4$  with a simple (plain) flap with flap-chord ratio,  $\lambda_f$ , of 0.3 and a flap-span ratio of 0.665.
2. a wing of  $AR=9$  with outboard ailerons (made of simple flap construction) with  $\lambda_f=0.3$  and control surface-span ratio of 0.605.

Fig.(3.11) shows the arrangement of these wings.

Plain flaps are among the easiest to construct and most consistent to use. The hinge point is easily fixed and flap deflections can be easily measured without ambiguity. For these reasons, there is a great bulk of available data for plain flaps. On the other hand, plain flaps are not the most efficient form of flaps. Due to model geometry and construction, the flow can easily separate from the suction side at the location of the flap. This problem is reduced in the case of the slotted flap and eliminated in the case of the

split flap. Large downward control surface deflections can also affect the upper surface flow causing larger suction and more lift - this is particularly true for split flaps. Split-flaps also have a more steady wake due to fixed locations of flow separation compared to plain flaps. In balance, the plain flaps were chosen because of the greater available data base, greater consistency and ease of construction. Fig.(6.1) shows a schematic of these types of flaps.

In practice, plain flaps with flap-chord ratios of 0.15 to 0.3 are used with 0.2 being the most widely used ratio. Wenzinger (38) has conducted experiments on Clark-Y section models and observed that  $\lambda_f=0.2$  yields the best improvement in performance. Since the present airfoil has more aft camber than the Clark-Y and due to the small size of the model, it was decided to use a flap chord ratio of 0.3 for the tests. The control surface span-ratios were likewise chosen on the basis of practice and construction constraints. The pressure taps were built into the starboard control surface section as described in chapter 3.

Prior to running the tests, some calculations were performed using thin airfoil theory to obtain expected performance changes with flap deflection. Thin airfoil theory uses the method of singularities to compute the performance of the airfoil. The airfoil is assumed to be very thin, permitting approximation of the airfoil by the camber line given by

$Z^c(x)$ . A further approximation requires small values of the camber, this allowing the singularities to be distributed on the chord line. To study the properties of a flapped airfoil, the section is approximated by a bent flat plate (Fig.(6.2)). A detailed derivation of the results of the thin airfoil theory as applied to this bent plate is presented in Appendix III. The reader is also referred to the section in the book by Schlichting and Truckenbrodt (39) for more discussion on the subject.

The coefficients for flap effectiveness calculated with this theory are shown to be

$$\begin{aligned} \frac{\partial C_L}{\partial \eta_f} &= 2( \phi_f + \sin \phi_f ) & (6.1) \\ \frac{\partial C_{Mo}}{\partial \eta_f} &= \frac{-1}{2} \sin \phi_f ( 1 + \cos \phi_f ) \\ \frac{\partial \alpha_o}{\partial \eta_f} &= - \frac{1}{\pi} ( \phi_f + \sin \phi_f ) \end{aligned}$$

$$\text{where} \quad \phi_f = \cos^{-1} ( 2X_f - 1 ) \quad (6.2)$$

where  $X_f$  is the dimensionless location of the flap hinge measured from the leading edge. Comparison of these results with experimental data has shown lower values of effectiveness for the experimental results. While some of this difference is due to profile thickness, friction and some flow separation also contribute to the difference. Frequently, these calculated values are modified with a empirically cho-

sen correction factor K. Usually  $K=0.75$  and Fig.(6.3) and Fig.(6.4) show the flap effectiveness for  $K=1$  and  $K=0.75$ .

These plots show that for a given flap-chord ratio, the effect of flap deflection is a negative shift in the angle of zero lift. Conventionally, flap deflection downward (trailing edge down) is considered positive. An examination of the equations for the coefficients of lift and moment are given by

$$C_L = \left( 2\alpha + \frac{2}{\pi} \eta_f \phi_f + \frac{2}{\pi} \eta_f \sin \phi_f \right) \quad (6.3)$$

$$C_{Mo} = \frac{-\eta_f \sin \phi_f (1 + \cos \phi_f)}{2}$$

where  $\eta_f$  is the flap deflection. For a given model, implying a given flap-chord ratio, these expressions are linear in flap deflection angle. These trends can be seen in Fig.(6.5) which show data for a Clark-Y airfoil compiled by Wenzinger (38) for small flap deflection angles.

The equations presented above are valid for small angles of flap deflection.

The procedure used by Hay and Eggington (40), also presented in Appendix III, is also based on thin airfoil theory but is applicable for large flap deflections. These predict slightly lower values for flap effectiveness. Fig.(6.6),

Fig.(6.7) and Fig.(6.8) show the results predicted by this theory.

Initially many experiments were conducted to refine the procedures and to ensure repeatability and accuracy of the results.

One of the main sources of inconsistency between published data for flap performance is the size of the hinge gap, the gap between the main airfoil and the flap section. The flow in this area is very complicated and can lead to leakages and loss in performance. Fig(6.9) shows a comparison of two sets of data for the same  $AR=4$  wing at  $Re.=200,000$ . In one case, the hinge gap was sealed with thin tape and care was taken to see that the tape did not cause any perceivable disturbance to the flow. In the other case, the gap was left open. For this model the close tolerances and the design used prevented any significant changes due to the hinge gap. This is also seen from the drag data (Fig.(6.10)). However, in accordance with past NACA practice to report flap data with a sealed hinge-gap, all subsequent data presented here are also for the case of the hinge-gap sealed.

Comparisons were also made to observe differences between a plain wing and one with flaps, the flaps being fixed at zero flap deflection and the hinge gap sealed. This was done to ensure that no changes in performance were observed due to the flap and the tape-seals. Fig(6.11), Fig.(6.12) and

Fig.(6.13) show no major changes in the force measurements between the two cases. The very similar curvature of the lift curve near maximum lift and the agreement in the stalling angle indicate no changes to the upper surface flow on account of the flaps and the seals.

The effect of flap deflection on lift behavior is shown in Fig.(6.14). This case represents the wing of AR=4 and  $Re.=200,000$ , where the wing would undergo combined leading edge and trailing edge stall. The lift curve slope remains unaltered with flap deflection ; Fig.(6.7) predicts a drop of less than 3% in lift curve slope for a thin airfoil going from a flap deflection of 0 degrees to 40 degrees. The stalling patterns are also not greatly affected though for large flap deflections, the wing stalls a little earlier. This has also been observed on the Clark-Y section by Wenzinger Fig.(6.5). It is also possible to see the trends in the behavior of the zero lift angle. For larger flap deflections (greater than 30 degrees), flap effectiveness falls off very rapidly. From  $\delta_f.=0$  degrees to  $\delta_f=28$  degrees, the value of  $C_{Lmax}$  increases from 1.48 to 1.64 while the increase from  $\delta_f=28$  degrees to  $\delta_f=40$  degrees causes a change from 1.64 to 1.68.

Post stall values of the lift are very similar for all the cases indicating relatively smaller contributions due to the lower surface pressure distributions. As mentioned in chapter 3, pressure data for the wing with control surfaces

could only be obtained on the main airfoil, the control surfaces being too small to accommodate the taps and the associated tubing. Fig.(6.15) shows the post-stall pressure distributions for  $\delta_f=18$  degrees and  $\delta_f=30$  degrees and this explains the very little variation in post stall lift for the two cases.

The drag data (Fig.(6.16)) show expected trends with overall increases in drag due to flap deflection. The effect of flap deflection is to cause a shift to the left of the whole drag curve. This is consistent with the behavior of the lift curves and the effective negative shift in the zero lift angle. The size of the drag hysteresis loops are similar with no significant change in drag increase after stall for various flap deflections.

Not much change is visible in the stalling characteristics of the wing due to flap deflections. Fig(6.17) shows the pressure distribution histories at stall with flap deflections of 0 degrees and 18 degrees and the forward movement of the location of turbulent separation can be seen.

The effect of negative flap deflection is seen to be more prominent than the case of positive flap deflection (Fig.(6.18)). The effect now is to shift the lift curve to the right and now the stall hysteresis loop does undergo some change. The greater sensitivity of the flow can be better understood by examining Fig.(6.19). The effect of positive flap deflection is small on the upper surface pressure dis-

tribution although a greater lower surface pressure coefficient is obtained. With negative flap deflections of about the same magnitude, the reduction in upper surface suction is substantial. There is also an accompanying reduction in the lower surface pressure values resulting in a large decrease in overall lift.

This same effect is seen even more clearly for larger flap deflections (Fig.(6.20)). The force data for this latter case is shown in Fig.(6.21) and Fig.(6.22). Examining the drag data, the minimum drag values for  $\delta_f=28$  degrees and  $\delta_f=-30$  degrees are of the same order although, as is to be expected, they occur for different ranges of angles of attack. Fig.(6.23) depicts the pitching moment data which shows more negative nose down) pitching moments for positive flap deflections mainly due to greater 'aft-loading' of the lower surface pressure distributions. For negative flap deflections, the absence of this loading combined with the much lower leading edge upper surface suction causes a more positive pitching moment. Fig.(6.20) also shows clearly that flap deflection does not cause much change in size and location of the separation bubble.

At lower Reynolds numbers, the same trends are again observed. Fig.(6.24) shows the effect of positive flap deflection at  $Re.=100,000$  and Fig.(6.25) compares positive and negative flap deflections. This latter case reveals one interesting feature. For  $\delta_f=-30$  degrees, the airfoil does not

appear to have any drop in lift at stall. In this respect, the airfoil appears to experience thin airfoil stall. The stall in this case is difficult to classify. Due to large negative flap deflections, the pressure distribution over the upper surface of the airfoil is considerably altered with much lower values of suction (Fig.(6.26)). Subsequently, when stall occurs, the change in the pressure distribution due to flow separation close to the leading edge is now not very large. The lower surface pressure distributions are virtually unchanged through stall. Fig.(6.27) and Fig.(6.28) compare the effect of Reynolds number for the AR=4 wing with a flap deflection of 33 degrees. The overall behavior remains the same as the case with zero flap deflection except now for higher values of lift. For  $Re.=70,000$ , the wing experiences thin airfoil stall, while at  $Re.=300,000$ , trailing edge stall is observed. In between, at  $Re.=100,000$ , the curves indicate leading edge stall while at  $Re.=200,000$ , they indicate combined leading edge and trailing edge stall. Fig.(6.29) shows the same effect for the case of a flap deflection of 15 degrees.

This is a rather important result since it confirms that the stalling behavior, and therefore the behavior of the separation bubble is not significantly changed due to positive flap deflections. This was already seen in the case of upper surface pressure distributions of Fig.(6.19) and Fig.(6.20). This result, at first reading, would appear in-

consistent with known behavior of separation bubbles. Classical theory tells us that increased circulation around the airfoil accompanies the flap deflection causing enhanced lift. This causes increased localized velocities over the airfoil upper surface which should result in a shorter bubble length. This behavior is very much a function of the airfoil contour and for the present airfoil, this effect is very small.

All force data presented hitherto, in this section, relate to the AR=4 wing with flaps. Turning now to the AR=9 wing with two symmetrically located control surfaces as shown in Fig.(3.11), force data were obtained for various control surface configurations. Although primarily intended for use as ailerons, data was also obtained for the case of symmetric control surface deflections. Fig.(6.30) shows the effect of symmetric control surface deflections for  $Re.=200,000$  for lift data while Fig.(6.31) shows the same effect for drag data.

It must be emphasized that the two wings are of very different construction with a single flap of flap-span ratio 0.665 for the AR=4 wing as opposed to two control surfaces of a total control surface-span ratio of 0.605 for the AR=9 wing. No direct comparisons between these two cases are therefore possible. A larger control surface span ratio would naturally mean a larger increment in lift. Typically flap-span ratios are of the order of 0.6 for which value, the

increment in lift is found to be about 0.7 times the value predicted for two-dimensional data such as Fig.(6.6).

The effect of Reynolds number on symmetric flap deflections is seen in Fig.(6.33). The expected stall patterns and hysteresis loops for the different Reynolds number regimes are still observed although there is now some increase in the slope of the lift curve for negative incidences.

Fig(6.34), Fig.(6.35) and Fig.(6.36) depict typical data for the FX-63-137- ESM airfoil along with data for NACA 23012 and Clark-Y sections. Table (6.1) shows the parameters of the wings used in these figures. The data for the NACA 23012 and the Clark-Y sections were obtained from the results of Wenzinger (38).

In view of their application as ailerons, the outboard control surface of the AR=9 wing are more likely to be deployed in an asymmetric configuration. For this reason, force and moment data were obtained for asymmetric control surface deflections of 16 and 30 degrees. In each case, a roll to port ( $\delta_{fport}=-15$ degrees,  $\delta_{fstarboard}=+15$  degrees) and a roll to starboard (reverse of the former) were both used to ensure consistency of the data. In practice, this test turns out to be very critical and requires very close manufacturing tolerances and symmetry for the wing. Minor surface irregularities are sufficient to cause differential behavior on the outboard spans. In view of the large span of this wing, these small differential forces can cause large

asymmetric moments. In spite of these difficulties, Fig.(6.37) shows fairly consistent data for the rolling moment coefficient for 30 degree control surface deflections for  $Re.=100,000$ . Here, the two cases of roll to port and roll to starboard are compared with the trim state (zero control surface deflections). The lift data for this asymmetric control surface deflection (Fig.(6.38)) shows a net decrease in lift compared to zero flap deflection. As was already noted, the magnitude of the lift decrement for negative flap deflections is larger than the magnitude of the lift increment for positive flap deflections of the same value. The same effects are also seen for 15 degree roll maneuvers (Fig.(6.39) and Fig.(6.40)).

Fig(6.41) shows the dependence of the rolling moment on asymmetric control surface deflections and this is seen to be almost linear. The starboard wing tip down is considered positive roll and accompanying this roll is a yaw moment arising out of the differential drag forces and this is shown in Fig.(6.42). As can be seen from these two figures, the roll to starboard is accompanied by a yaw toward port. This yaw is termed an 'adverse yaw' since it is directed away from the from the direction of the roll maneuver. The largest roll moments are obtained for wing incidence in the range of 5 to 8 degrees (Fig.(6.39)), this corressponding to the range of angles of attack where the lift differential between pos-

itive and negative flap/control surface deflections is largest (Fig.(6.18)).

It is seen therefore, that positive flap/control surface deflections do not significantly alter the flow over this airfoil. The pressure distributions have indicated virtually unchanged bubble length and bubble location. This was also confirmed with the flow visualization pictures. The force data have also indicated the typical stall patterns of the plain airfoil, that are dominated by bubble behavior, are carried over without significant changes for cases of positive flap deflections. Changes in the pressure distribution on the airfoil lower surface occur mainly aft of the flap hinge itself and these could not be measured on account of size requirements. The fore part of the airfoil registers only small changes.

The case of negative flap deflection is more complicated. In some cases, these deflections can cause total breakdown of the bubble mechanism. In these cases, the flat pressure distributions on the upper surface could be observed. This was accompanied by considerable change in the stall patterns.

For cases of asymmetric flap deflections, it was seen from the data that performance resembles that of any typical airfoil indicating a less direct role of the separation bubble. The main effect can only show up through the differential lift values. Once the behavior of the airfoil for positive and negative flap deflections is understood, the

estimation of the effect of asymmetric deflections follows fairly easily.

The study undertaken thus far did not call for tests to determine disturbance environment effects together with flap and control surface deflections. Earlier tests have indicated a greater influence of free stream turbulence on the performance of plain flaps compared to split flaps. This is mainly attributed to greater resistance to separation of a more turbulent free stream at the location of the flap. The split flap, having a smooth undeflected upper surface, avoids this problem. A similar effect due to acoustic disturbances or surface roughness can also be expected.

## CHAPTER 7. CONCLUSIONS AND RECOMMENDATIONS.

This research program was primarily concerned with studying the effects of increased disturbances and control surface deflection on airfoil performance in the low Reynolds number regime. This was done using three different wing models of the FX-63-137-ESM section in the range of  $Re.=60,000$  to  $Re.=300,000$ . Along the way many questions relating to the flow-field and the validity of some experimental techniques had to be answered. Many of the procedures developed, succeeded in providing sufficiently accurate and repeatable data for this regime. While some questions regarding the flow-field could be answered satisfactorily, there are some questions that still need further study.

It was shown in an earlier study (27), that the force data could be obtained with a high degree of confidence down to Reynolds numbers of around 100,000. At  $Re.=70,000$ , while the lift data was still of sufficient accuracy, the drag data needed backing up with alternate methods. The question of model-sizing was successfully resolved on account of the large size of the wind-tunnel test-section. Free development of the wing-tip vortices without tunnel-wall interference were obtained and wings of AR up to 10 could be tested without any significant error in the results.

The presence of the pressure taps were found to cause no discernible change in the flow over the wing. This was achieved by careful smoothening of the surface and polishing the wing before each run. Further, the arrangement of the taps along the diagonal helped reduce any interference between the taps and consequent contamination of the data. This was confirmed with many flow visualization studies. The accuracy of the pressure data was found to be very good, this was determined by comparing the integrated pressure loads with the strain-gauge data. Since the hysteresis loop remained unaltered, it further confirmed the lack of any significant disruption to the flow on account of the pressure taps.

The three different stall patterns were observed in the range of  $Re.= 60,000$  to  $Re.= 300,000$ . The mechanisms of each of these, thin airfoil stall, leading edge stall and trailing edge stall, were identified using pressure distribution data, force data and flow visualization studies. The stall hysteresis phenomena was also studied in detail using the above three techniques. The upper portion of the hysteresis loop corresponds to the occurrence of the separation bubble on the airfoil upper surface with considerable contribution to lift due to the upper surface suction. On the lower portion of the hysteresis loop, the flow over the upper surface was found to be separated for the most part.

Two wings of AR=4 and AR=9 using the same section (equipped with a plain flap and outboard control surfaces.) were tested. The flap/control surface chord ratio was 0.3. In accordance with NACA practice, all reported results are for the case with a sealed hinge-gap. However, for the present model, the case of gap-open and gap-closed yielded very similar results.

The effect of positive control surface deflection in this regime is very similar to the case at higher Reynolds number. There is an increase in  $C_L$  for up to stall for the range of 0 to 40 degrees. This is accompanied by a negative shift in the zero-lift angle of attack.

Stall patterns observed for cases of zero flap deflection are also carried over to the case of positive flap deflection for the range of flap deflections from 0 to 40 degrees. This would indicate behavior of the separation bubble that is unchanged compared to the case of zero flap deflection. This was also confirmed by the pressure distribution plots. Upstream of the flap, the pressure distributions were very similar for the two cases. In cases where some increased suction on the upper surface was present, it appeared as though the whole pressure distribution curve was shifted causing an almost identical pressure gradient distribution

along the chord. The bubble chordwise extent and location were practically unchanged. This also explains the very similar hysteresis loops seen for the two cases of zero and positive flap deflections. There is an increase in drag corresponding to the lift increase although the overall L/D ratio does show a slight decrease. Very little change can be observed in the bubble length and location due to flap deflection. Indeed, the airfoil surface, upstream of the flap hinge, sees only a small increase in upper surface suction and lower surface pressure coefficient with flap deflection. The effect of negative flap deflection is more pronounced with significant losses in lift. This is also seen as a sharp reduction in the upper surface suction. In some cases, the separation bubble can be completely eliminated causing considerable change in the stalling pattern. This change in stalling pattern seemed to be similar to the effect of a There is an increase in drag corresponding to the lift increase although Thus negative flap deflections could, in cases, cause a change from trailing edge stall to leading edge stall and from leading edge stall to thin airfoil stall.

Agreement with the results of thin airfoil theory was found to be rather poor. This is to be expected in view of the fairly large camber of the airfoil section. used. The presence of the separation bubble further complicates the picture, considerably affecting airfoil performance. This lack of agreement is not due to the low Reynolds number re-

gime of the present study alone. Comparison of the results of thin airfoil theory with the experimental results of other airfoil models with camber and for higher Reynolds numbers also show similar differences.

Asymmetric deflection of the control surface leads to expected performance in roll. For given deflections, these rolling moments decrease for incidences over about 10 degrees. These asymmetric deflections are also accompanied by an overall decrease in lift. The adverse yaw moments are not very large for the range of control surface deflections used. The dependence of the roll moment as well as yaw moment with control surface deflections was almost linear for greater than 10 degrees and upto 40 degrees.

The results presented for the effect of flap and control surface deflection all relate to the case of baseline levels of disturbance in the wind tunnel ( $Tu$  about 0.02% and no externally introduced acoustics). However, since it is evident that the separation bubble behavior remains basically unchanged for zero and positive flap deflections and dominates airfoil performance, any increased levels of disturbance in the wind tunnel are likely to have a similar role for the case of flap/control surface deflection as it does for the plain wing.

As might be expected, both externally introduced acoustic disturbances as well as increased free-stream turbulence have very similar effects on the airfoil performance.

Three different levels of free-stream turbulence intensity were used for the tests starting with the base-line level of 0.02% upto 0.3%. A bulk of the data was obtained for  $Tu=0.02\%$  and  $Tu=0.2\%$ . Going from 0.02% to 0.2%, there was a significant reduction in the size of the hysteresis loop. The increased free-stream turbulence is seen capable of achieving reattachment and restoration of the bubble much earlier compared to the base-line condition.

The primary effect of the increased turbulence seems to cause attached flow in the aft portion of the upper surface. The increase in the upper surface suction seems to be a second order effect. The upper portion of the hysteresis loop does not seem to be affected. The effect of increased turbulence is greater for conditions of low Reynolds number ( say  $Re.=100,000$  ) and proximity to the location of reattachment under natural conditions. A complete elimination of the hysteresis loop for some conditions appears possible due to the effect of free-stream turbulence. Increasing the turbulence level from 0.2% to 0.3% failed to show any major changes indicating a 'threshold value' of disturbance necessary. It must be stressed that the turbulence intensity alone is inadequate to characterize the disturbance environment. The turbulence spectrum must be used in all these

cases to denote the manner of the disturbance. However, a lack of the immense database required for such correlation with boundary layer qualities, prevent any further conclusions from being drawn at this stage.

Much of what was said with regard to turbulence also applies to the effect of externally introduced acoustic disturbances. The major effect again is the considerable reduction in the size of the hysteresis loop. The flow situation could be triggered from the lower portion of the loop to the upper portion by these acoustic disturbances, with certain preferential frequencies working better than others. The ability of the disturbance to cause this switch depended upon the frequency and intensity of the disturbance, the Reynolds number of the flow, and proximity to the point of closure of the natural hysteresis loop. The acoustic disturbance could be used as an 'on-off' switch and once the restoration of the flow was achieved, the disturbance could be turned off while the flow remained restored. Certain frequencies at chosen power levels could only achieve a partial effect - a marginal improvement in performance due to some increased upper-surface suction - but in these cases, the effect was sustained only by the presence of the disturbance. Here again, the acoustic spectrum should be obtained at the wing in order to account for the presence of reflected frequencies and speaker output.

These results have important consequences. In some tunnels, due to a combination of these disturbances, flow phenomena such as stall-hysteresis may be completely masked, leading to substantial errors in the estimated airfoil performance. It is therefore very important that these wings be completely studied for a range of disturbance conditions from very 'clean' flow. This is impossible in some tunnels on account of the baseline disturbance level - both turbulence and acoustic.

These experiments were but a single step along the way to a complete understanding of the effect of disturbances. The key to this mechanism appears to be the changes in the boundary layer behavior. However, in view of the large number of variables and an inadequate database, satisfactory formulations are still lacking. Since free-stream turbulence, acoustic disturbances and the model surface condition can all contribute to this, wind tunnel tests must be conducted with a cataloging of all of these parameters. Tests with independent variation of these parameters must be performed to study the individual influences and this is again impossible in some tunnels due to dependence of both acoustic and turbulence content of the disturbances on the free-stream velocity.

It is evident that a great deal of research remains to be done in this area in order to fully comprehend the flow-field and its effect on airfoil performance. In view of the

large number of factors, influencing the flow, it is imperative that these experiments be conducted in 'controlled' environments reducing the number of unknown variables. To date, a fair number of studies have been conducted in many wind-tunnels, where a complete cataloging of the flow conditions is either available or possible. This database is by no means adequate in order to understand the effect of these factors. It is therefore necessary to expand on this already existent database and complete the range of experiments for different 'controlled' conditions such as free-stream turbulence and acoustic disturbances. Interpreting the results of new testing procedures should be done with great care since they could give rise to more confusion due to the introduction of new and 'uncontrolled' factors.

With regard to better understanding of global airfoil performance, many recommendations may be made :

1. A larger chord model may be used to obtain better resolution of the pressure distribution enabling more accurate determination of the location and size of the separation bubble. Pressure distribution on the control surface may also be obtained this way.
2. Tests of the same model in different wind tunnels should be conducted to eliminate differences due to model sur-

face and manufacturing tolerances from the list of variables.

3. Further studies of the airfoil performance with a complete elimination of the separation bubble by suitable tripping of the boundary layer are necessary.
4. Further studies should also be made of the effect of the disturbance environment aimed at eliminating or minimizing the hysteresis loop. This could lead to considerably enhanced performance for the vehicle, permitting safer operation close to  $C_{Lmax}$
5. The use of a single frequency acoustic driver rather than a speaker would permit elimination of the harmonics. The effects of external versus internal excitations should also yield interesting results.
6. Conditions under which the free stream turbulence and the acoustic disturbances act cumulatively and conditions when the dominant disturbance acts independently must be studied in greater detail.

Recommendations may also be made for better understanding of the boundary layer flow.

1. Simulation of the separation bubble is possible on a flat plate on an expanded scale by the imposition of a suitable pressure gradient distribution. The expanded scale would permit better study of the structure of the boundary layer
2. Correlations between the frequencies present in the disturbance environment and the more unstable frequencies in the shear layer are necessary to identify the most unstable disturbances.
3. A more detailed examination of the surface conditions especially the 'receptivity' of the surface to the disturbance is necessary.
4. The features of the flow field in and around the control surface hinge-gap must also be made.

APPENDIX I. COORDINATES OF THE WORTMANN AIRFOIL.

Point #	x/c	y/c upper	y/c lower
1	1	0	0
2	.9989	.0007	.0004
3	.9957	.0025	.0017
4	.9904	.0050	.0037
5	.9830	.0082	.0063
6	.9735	.0119	.0092
7	.9619	.0160	.0122
8	.9484	.0204	.0151
9	.9330	.0252	.0179
10	.9157	.0302	.0205
11	.8967	.0355	.0228
12	.8759	.0411	.0248
13	.8535	.0471	.0263
14	.8297	.0532	.0273
15	.8044	.0596	.0277
16	.7778	.0661	.0274
17	.7500	.0727	.0267
18	.7211	.0793	.0253
19	.6913	.0859	.0234
20	.6607	.0921	.0210
21	.6294	.0980	.0181
22	.5975	.1034	.0148
23	.5653	.1082	.0111
24	.5327	.1123	.0072
25	.5000	.1157	.0031
26	.4673	.1184	-.0010
27	.4347	.1203	-.0049
28	.4024	.1214	-.0084
29	.3706	.1218	-.0117
30	.3393	.1214	-.0145
31	.3087	.1201	-.0169
32	.2787	.1180	-.0189
33	.2500	.1151	-.0204
34	.2222	.1113	-.0215
35	.1956	.1069	-.0223
36	.1703	.1018	-.0227
37	.1464	.0961	-.0227
38	.1241	.0898	-.0225
39	.1033	.0829	-.0219
40	.0843	.0757	-.0211

Point #	x/c	y/c upper	y/c lower
41	.0670	.0681	-.0201
42	.0516	.0603	-.0188
43	.0381	.0522	-.0172
44	.0265	.0440	-.0152
45	.0170	.0357	-.0128
46	.0096	.0270	-.0097
47	.0043	.0157	-.0057
48	.0011	.0090	-.0023
50	0	0	0

## APPENDIX II. COORDINATES OF THE PRESSURE TAPS.

### A2.1 : PLAIN WING.

Tap #	x/c	y/c	Tap #	x/c	y/c
1.	0.83	.053	21.	0.02	-.014
2.	0.79	.063	22.	0.06	-.019
3.	0.74	.075	23.	0.10	-.021
4.	0.70	.084	24.	0.15	-.023
5.	0.66	.092	25.	0.18	-.023
6.	0.61	.101	26.	0.22	-.022
7.	0.56	.109	27.	0.30	-.017
8.	0.52	.114	28.	0.35	-.014
9.	0.48	.117	29.	0.39	-.010
10.	0.41	.121	30.	0.43	-.005
11.	0.37	.122	31.	0.48	.001
12.	0.34	.121	32.	0.53	.007
13.	0.30	.119	33.	0.56	.010
14.	0.28	.118	34.	0.62	.017
15.	0.20	.108	35.	0.66	.021
16.	0.16	.099	36.	0.69	.023
17.	0.13	.091	37.	0.72	.025
18.	0.09	.078	38.	0.77	.027
19.	0.05	.059	39.	0.82	.027
20.	0.003	.013			

A2.2 : WING WITH FLAP SECTION.

Tap #	x/c	y/c
1.	0.609	0.101
2.	0.590	0.104
3.	0.539	0.111
4.	0.483	0.117
5.	0.384	0.122
6.	0.338	0.121
7.	0.230	0.112
8.	0.197	0.107
9.	0.165	0.100
10.	0.139	0.094
11.	0.092	0.078
12.	0.040	0.054
13.	0.000	0.003
14.	0.060	-0.019
15.	0.110	-0.022
16.	0.152	-0.023
17.	0.216	-0.022
18.	0.253	-0.020
19.	0.426	-0.006
20.	0.570	0.012

### APPENDIX III THIN AIRFOIL THEORY - BENT FLAT PLATE.

In this section, the thin airfoil theory equations as applied to a bent plate will be derived. A more detailed treatment of the subject is available in (39). Thin airfoil theory is applicable to thin profiles with small camber.

With the assumptions of this theory, the singularities can be distributed on the chord line (Fig.(A3.1)). The u and w velocity components can be calculated using Biot-Savart's law as :

$$u(x,z) = \frac{1}{2\pi} \int_0^c k(x') \frac{z \, dx'}{(x-x')^2 + z^2} \quad (A3.1)$$

$$w(x,z) = \frac{1}{2\pi} \int_0^c k(x') \frac{(x-x') \, dx'}{(x-x')^2 + z^2} \quad (A3.2)$$

where  $k(x)$  denotes the vortex strength per unit length.  $\Gamma(x)$ , the vortex strength is

$$d\Gamma(x) = k(x) \, dx \quad (A3.3)$$

$Z^C(x)$  denotes the camber line and the dimensionless quantities are derived as

$$\begin{aligned} X &= \frac{x}{c} \\ Z^c &= \frac{z^c}{c} \end{aligned} \quad (A3.4)$$

where  $c$  is the chord length.

The kinematic flow condition requires zero normal velocity on the camber line. In view of the approximations in use, this condition can be satisfied at the chord line for  $Z=0$

$$U_\infty \left( \alpha - \frac{dZ^c(X)}{dX} \right) + w(X) = 0 \quad (A3.5)$$

The  $u$  and  $w$  velocity components on the profile chord can be obtained from (A3.1) and (A3.2) through the limit operation  $z=0$

$$\begin{aligned} u(X) &= \pm (1/2) k(X) \\ w(X) &= -\frac{1}{2\pi} \int_0^1 k(X') \frac{dX'}{(X-X')} \end{aligned} \quad (A3.6)$$

The velocity distribution on the profile surface is thus given by :

$$U(X) = U_\infty + u(X) = U_\infty \pm (1/2) k(X) \quad (A3.7)$$

for small angles of attack.

Using Bernoulli's equation to obtain the pressure difference between the upper and the lower surface,

$$P_l - P_u = \rho U_\infty \Delta u = \rho U_\infty k \quad (\text{A3.8})$$

$$\Delta C_p (X) = \frac{P_l - P_u}{q_\infty} = 2 \frac{k(X)}{U_\infty} \quad (\text{A3.9})$$

where  $C_p$  is the coefficient of pressure and  $q$ , the free-stream dynamic pressure. The lift coefficient is then obtained as

$$\begin{aligned} C_L &= \int_0^1 \Delta C_p (X) dX \\ &= \frac{2}{U_\infty} \int_0^1 k(X) dX \end{aligned} \quad (\text{A3.10})$$

and the pitching moment about the leading-edge (tail down is positive).

$$C_{M_{LE}} = - \int_0^1 \Delta C_p (X) X dX \quad (\text{A3.11})$$

$$C_M = - (2/U_\infty) \int_0^1 k(X) X dX \quad (\text{A3.12})$$

The theory of Glauert is used to calculate the circulation distribution for arbitrary camber distributions. A Fourier series expansion for the circulation distribution is used as

$$k(\phi) = 2 U_{\infty} \left( A_0 \tan(\phi/2) + \sum_{n=1}^N A_n \sin(n\phi) \right) \quad (\text{A3.13})$$

where the coordinate transformation given by

$$X = 0.5 (1 + \cos(\phi)) \quad (\text{A3.14})$$

is used. From (A3.6),

$$w(X) = - \frac{0.5}{\pi} \int_0^1 k(X') \frac{dX'}{X-X'} \quad (\text{A3.15})$$

$$w(\phi) = - \frac{0.5}{\pi} \int_0^{\phi} k(\phi') \frac{d\phi'}{0.5(\cos\phi - \cos\phi')}$$

Substituting for  $k(\phi')$  from (A3.12),

$$\frac{w(\phi)}{U_{\infty}} = - \left( A_0 + \sum_{n=1}^N A_n \cos(n\phi) \right) \quad (\text{A3.16})$$

where the Fourier coefficients are evaluated from Fourier analysis as

$$A_0 = \alpha - (1/\pi) \int_0^{\pi} (dZ^C(X)/dX) d\phi$$

$$A_n = - (2/\pi) \int_0^{\pi} (dZ^C(X)/dX) \cos(n\phi) d\phi \quad (\text{A3.17})$$

Further substituting for the circulation distribution from (A3.12), one obtains

$$C_L = \pi (2 A_0 + A_1) \quad (A3.18A)$$

$$C_{M_{LE}} = -0.25 \pi (2 A_0 + 2 A_1 + A_2)$$

using (A3.10) and (A3.11). From the definition of the centre of pressure, one can also show

$$C_{M_{0.25c}} = -0.25 \pi (A_1 + A_2) \quad (A3.18B)$$

For the case of the bent flat plate, (Fig.(6.2)), the camber line for a flap deflection of  $\eta_f$  degrees and a flap chord ratio of  $\lambda_f$  is given by :

$$z^c(x) = \lambda_f \cdot \eta_f \cdot x \quad 0 \leq x \leq x_f \quad (A3.19)$$

$$z^c(x) = (1 - \lambda_f) \cdot (1 - x) \cdot \eta_f \quad x_f \leq x \leq 1$$

The Fourier coefficients are then found to be

$$\begin{aligned}
A_0 &= \alpha + (\eta_f \phi_f) / \pi \\
A_1 &= (2/\pi) \eta_f \sin \phi_f \\
A_2 &= (\eta_f / \pi) \sin (2 \phi_f)
\end{aligned}
\tag{A3.20}$$

The lift and moment coefficients are then calculated from (A3.17) and (A3.18)

$$\begin{aligned}
C_L &= \pi ( 2\alpha + (2 \eta_f \phi_f / \pi) + 2 \eta_f \sin \phi_f / \pi ) \\
C_{M_{0.25c}} &= - 0.5 \eta_f \sin \phi_f ( 1 + \cos \phi_f )
\end{aligned}
\tag{A3.21}$$

The effect of flap deflections are then obtained as

$$\begin{aligned}
\frac{\partial C_L}{\partial \eta_f} &= 2 ( \phi_f + \sin \phi_f ) \\
\frac{\partial \alpha_0}{\partial \eta_f} &= -(1/\pi) ( \phi_f + \sin \phi_f ) \\
\frac{\partial C_{M_0}}{\partial \eta_f} &= - 0.5 \sin \phi_f ( 1 + \cos \phi_f )
\end{aligned}
\tag{A3.22}$$

Thus, the flap effectiveness is purely a function of the flap hinge (i.e. the flap chord ratio) according to this theory

Fig(6.3) and Fig.(6.4) show the variation of these parameters.

The theory presented thus far is valid only for small flap deflections. For large flap deflections, Hay and Eggington (40) have developed a procedure using conformal transformations for estimating the lift increment based on a method used by Lighthill.

The complex potential for the flow around a unit circle in the  $\zeta$  plane is

$$F(\zeta) = \exp(-i\alpha) + (1/\zeta) \exp(i\alpha) + iK \log \zeta \quad (A3.23)$$

where the flow has unit velocity at an angle of attack of  $\alpha$  to the real axis at infinity. The complex velocity is

$$W(\zeta) = \frac{dF(\zeta)}{d\zeta} = \exp(-i\alpha) - (1/\zeta^2) \exp(i\alpha) + iK/\zeta \quad (A3.24)$$

To achieve rear stagnation point at  $\zeta = 1$  (Kutta condition),

$$K = 2 \sin\alpha \quad (A3.25)$$

giving

$$W(\zeta) = 4i \exp(-i\theta) \cos((\theta/2) - \alpha) \sin(\theta/2) \quad (\text{A3.26})$$

In the physical  $z$ -plane, the velocity is given by

$$W_z = \left| \frac{dW(z)}{dz} \right| = \left| \frac{dW}{d\zeta} \right| \left| \frac{d\zeta}{dz} \right| \quad (\text{A3.27})$$

On the airfoil surface,

$$dz = ds \exp(i\chi) \quad (\text{A3.28})$$

On the circle

$$\begin{aligned} \zeta &= \exp(i\theta) \\ d\zeta &= i \exp(i\theta) d\theta \end{aligned} \quad (\text{A3.29})$$

$$W_{\alpha=0} = 4 \cos(\theta/2) \sin(\theta/2) \left| \frac{d\theta}{ds} \right| \quad (\text{A3.30})$$

$$W = W_{\alpha=0} \frac{\cos((\theta/2) - \alpha)}{\cos(\theta/2)}$$

On the airfoil, at zero lift,

$$\frac{dF_{\alpha=0}}{dz} = W_{\alpha=0} \exp(i\chi) \quad (\text{A3.31})$$

$$\log \left| \frac{dF_{\alpha=0}}{dz} \right| = \log W_{\alpha=0} - i\chi$$

where  $\log W$  and  $-i\chi$  are complex conjugate functions. Any pair of complex conjugate functions,  $\phi(\theta)$  and  $\xi(\theta)$  are related by

$$\phi(\theta) + i\chi(\theta) = - (1/2\pi) \int_0^{2\pi} (\phi(t) + i\chi(t)) \cot((\theta-t)/2) dt \quad (\text{A3.32})$$

Therefore,

$$\begin{aligned} \log W_0(\theta) &= - (1/2\pi) \int_0^{2\pi} \chi(t) \cot((\theta-t)/2) dt \quad (\text{A3.33}) \\ \chi(\theta) &= (1/2\pi) \int_0^{2\pi} \log W_0(t) \cot((\theta-t)/2) dt \end{aligned}$$

For a thin airfoil with a flap as shown in Fig.(A3.2) where

$\theta=\beta$  is the hinge location on the upper surface,

$\theta=2\pi-(\beta-\gamma)$  is the hinge location on the lower surface

Applying (A3.33), one obtains

$$\begin{aligned}
\int_0^{2\pi} x \, d\theta &= -\pi (\omega - \pi) - (\delta \beta - \gamma) + 2\pi \alpha_0 = 0 \\
\int_0^{2\pi} x \sin \theta \, d\theta &= \pi (\cos \omega + 1) + \delta (\cos \beta - \cos (\beta - \gamma)) = 0 \\
\int_0^{2\pi} x \cos \theta \, d\theta &= \pi \sin \omega + \delta (\sin \beta + \sin (\beta - \gamma)) = 0
\end{aligned}
\tag{A3.34}$$

whereupon, substituting

$$\sigma = \frac{\sin \beta}{\pi/\delta + \cos \beta} \tag{A3.35}$$

$$\sin \omega = \frac{-2}{\sigma + 1/\sigma} \tag{A3.36}$$

$$\sin (\beta + \gamma) = \frac{2 (\pi/\delta)}{\sigma + 1/\sigma} - \sin \beta$$

$$\alpha_0 = \frac{\omega - \pi}{2} + (\delta / 2\pi) (\delta \beta - \gamma)$$

Using the expression for  $C_L$  (40)

$$C_L = \frac{8 \pi}{\text{chord}} \sin (\alpha - \alpha_0) \tag{A3.37}$$

gives the lift increment as

$$C_L = (8\pi/C_1) \sin(\alpha - \alpha_0) - (8\pi/C) \sin\alpha \quad (A3.38)$$

where

$C_1$  = chord of the airfoil with flap,

$C$  = chord of the airfoil with no flap deflection,

$\alpha_0$  = zero lift angle for the airfoil with deflected flap

Fig.(6.6) and Fig.(6.7) show this behavior.

## LIST OF REFERENCES.

1. Lissaman, P.B.S. : Low Reynolds number Airfoils. Annual Review of Fluid Mechanics. Vol.15 pp 223-239. 1983.
2. Miley, S.J. : An Analysis of the Design of Airfoil Sections for Low Reynolds number. Ph.D. Thesis. Mississippi State Univ. Jan. 1972.
3. Eppler, R., Somers, D.M. : A Computer Program for the Design and Analysis of Low Speed Airfoils. NASA TM 80210 1980.
4. Wortmann, F.X. : A Critical Review of the Physical Aspects of Airfoil Design at low Mach Numbers. NASA CR 2315. Nov. 1973.
5. Millikan, C.B., Klein, A.L. : The Effect of Turbulence. Aircraft Engineering Vol.5 No.8 Aug. 1933. pp 169-174.
6. Jones, B.M. : An Experimental Study of the Stalling of Wings. British A.R.C. R&M No. 1588. 1933.

7. von Doenhoff, A.E. : A preliminary Investigation of Boundary Layer Transition along a Flat Plate with Adverse Pressure Gradient. NACA TN 639. 1938.
8. White, F.M. : Viscous Fluid Flow. McGraw Hill. 1974
9. Briley, R.W. : A Numerical Study of Laminar Separation Bubbles using the Navier Stokes Equations. Journal of Fluid Mech. Vol.47 Part 4 pp 713-736.
10. Gault, D.E.: An Experimental investigation of Regions of Separated Laminar Flow. NACA TN 3505. 1955.
11. Tani, I. : Boundary Layer Transition. Annual Review of Fluid Mech. Vol.1 1969. pp 169-196.
12. Gaster, M. : The Role of Spatially Growing Waves in the Theory of Hydrodynamic Stability. Progress in Aerospace Sciences Vol.6 1965. pp 251-270.
13. Herbert, T., Bertolotti, F.P. : Effect of Pressure Gradient on the Growth of Subharmonic disturbances in Boundary Layers. Proc. of the Conference on low Reynolds Number Airfoil Aerodynamics, Univ. of Notre-Dame, Jun. 1985.

14. van Ingen, J.L., Boermanns, L.M.M. : Research on Laminar Separation Bubbles at Delft Univ. of Tech. in relation to Low Reynolds number Airfoil Aerodynamics Proc. of the Conference on low Reynolds Number Airfoil Aerodynamics, Univ. of Notre-Dame, Jun. 1985.

15. Gaster, M. : The Structure and Behavior of Laminar Separation Bubbles. Separated Flows. Part 2. AGARD CP 4. pp 819-836.

16. Young, A.D., Horton, H.P. : Some Results of Investigations of Separation Bubbles. Separated Flows. Part 2. AGARD CP 4. pp785-816.

17. Wallis, R.A. : Aero Note 141. ARL Melbourne. 1954.

18. Tani, I. : Low Speed Flows involving Bubble Separations. Progress in Aerospace Sciences. Vol.5 1964. pp 70-103.

19. Gleyzes, C., Coustieux, J., Bonnet, J.L. : Theoretical and Experimental Study of Low Reynolds number Transitional Separation Bubbles. Proc. of the Conference on Low Reynolds number Airfoil Aerodynamics, Univ. of Notre-Dame. Jun. 1985.

20. Crimi, P., Reeves, B.L. : Analysis of Leading Edge Separation Bubbles on Airfoils. AIAA Journal Vol.14, No.11. p1548.

21. Carter, J.E., Vatsa, V.N. : Analysis of Airfoil Leading Edge Separation Bubbles. NASA CR 165935. May 1982.

22. Briley, R.W., McDonald, H. : Numerical Prediction of Incompressible Separation Bubbles. Journal of Fluid Mech. Vol.69, Part 4. 1975. pp 631-656.

23. McCullough, G.B., Gault, D.E. : Examples of three representative types of Airfoil Section Stall at Low Speed. NACA TN 2502. 1951.

24. Gault, D.E. : A Correlation of Low Speed Airfoil section Stalling Characteristics with Reynolds Number and Airfoil Geometry. NACA TN 3963. 1957.

25. Yeates, L.G., Saric, W.S. : Generation of Crossflow Vortices in a three- dimensional Flat Plate Flow. VPI Report E-84.35

26. Reynolds, G.A. : Experiments on the Stability of the Flat Plate Boundary Layer with Suction. VPI&SU Ph.D. Dissertation. Jan. 1982.

27. Abtahi, A.A. : Effect of Aspect Ratio on Wings at Low Reynolds Numbers. VPI&SU Ph.D. Dissertation. May 1985.
28. Programming Techniques for the HP 9836 Desktop Computer : H-P Desktop Computer Div., Fort Collins, Colorado. 1976.
29. 3052 Automatic Data Acquisition System Guide. : H-P Desktop Computer Div., Fort Collins, Colorado. 1976.
30. Schetz, J.A. : Foundations of Boundary Layer Theory for Momentum, Heat and Mass Transfer. Prentice Hall 1984.
31. Schubauer, G.B., Skramstad, H.K. : Laminar Boundary Layer Oscillations and Transition on a Flat Plate. NACA TR 909. 1948.
32. Wells, C.S. : Effect of Free Stream Turbulence on Boundary Layer Transition  
AIAA Journal Vol.5 No.1. 1967. pp 172-174.
33. Corke, T.C., Morokovin, M.V. : On Effects of three dimensional Roughness on Transition and Receptivity to Disturbances. Proc. of the Conference on Low Reynolds Number Airfoil Aerodynamics, Univ. of Notre-Dame, Jun. 1985.

34. Sun, Z., Sumantran, V., Marchman, J.F. : An Examination of Flow and Environmental Effects on Chordwise Pressure Distributions for a Finite Wortmann Wing at Low Reynolds Numbers. VPI Aero. Report 149. Jul. 1985.
35. Collins, F.G., Zelenevitz, J. : Influence of Sound upon Separated Flow over Wings. AIAA Journal Vol.13 No.3 1975. pp 408-410.
36. Ahuja, K.K., Burrin, R.H. : Control of Flow Separation by Sound. AFWAL-TR-84-3096. Feb. 1985.
37. Goldstein, S. : Modern Development in Fluid Dynamics. Vol.II Oxford. 1938.
38. Wenzinger, C.J. : Wind Tunnel Investigation of Ordinary and Split Flaps on Airfoils of different Profile. NACA TR 554. 1936.
39. Schlichting, H., Truckenbrodt, E. : Aerodynamics of the Airplane. McGraw Hill 1979.

40. Hay, J.A., Eggington, W.J. : An Exact Theory of a Thin Airfoil with Large Flap Deflection. Journal of R.Ae.S. Vol.60 Nov. 1954. pp753-757.
41. Hoerner, S.F. : Fluid Dynamic Lift. Hoerner Fluid Dynamics. 1975.
42. Carmicheal, B.H. : Low Reynolds Number Airfoil Survey. Vol.1. NASA CR 165803. Nov. 1981.
43. Mueller, T.J. : Low Reynolds Number Vehicles. AGARD-AG-288. Feb. 1985.
44. Schmitz, F.W. : Aerodynamics of Model Aircraft Wing Measurements. Part I. NTIS N70-70063. pp 1-63.
45. Batchelor, G.K. : An Introduction to Fluid Dynamics. Cambridge Univ. Press. 1979.
46. Curle, N., Skan, S.W. : Approximate Methods for predicting Separation Properties of Laminar Boundary Layers. Aero. Quarterly. Vol.8 Part 3. 1957.
47. van Ingen, J.L. : On the Calculation of Laminar Separation Bubbles in two dimensional Incompressible Flows. AGARD CP 168. 1975.

TABLE 3.1 : FREE-STREAM TURBULENCE LEVELS \*

$U_{\infty}$ (m/s)	$ u /U_{\infty}$ (%)
9.0	0.018
12.0	0.018
15.0	0.022
20.0	0.028
30.0	0.045

\* due to YEATES and SARIC

TABLE 3.2 : LIST OF HARDWIRED CHANNELS FOR DATA ACQUISITION IN  
THE VIRGINIA TECH STABILITY WIND-TUNNEL.

CHANNEL #	DATA
1	TUNNEL TEMPERATURE
2	TUNNEL STATIC PRESSURE
3	LIFT
4	DRAG
5	PITCHING MOMENT
6	SIDEFORCE
7	YAWING MOMENT
8	ROLLING MOMENT
9	TUNNEL DYNAMIC PRESSURE

Table 6.1 : DATA FOR THE WING MODELS USED IN THE COMPARISONS  
IN FIG.(6.34), FIG.(6.35) AND FIG.(6.36).

	FX-63-137-ESM	FX-63-137-ESM	CLARK-Y	NACA 23012
AR	4	9	6	6
CHORD (IN.)	5.0	5.0	10.0	10.0
FLAP-CHORD RATIO $\lambda_f$	0.3	0.3	0.3	0.2
FLAP-SPAN RATIO	0.665	0.605	1.0	1.0
TEST RE #	200,000	200,000	600,000	600,000

DATA FOR CLARK-Y AND NACA 23012 FROM REFERENCE (38).

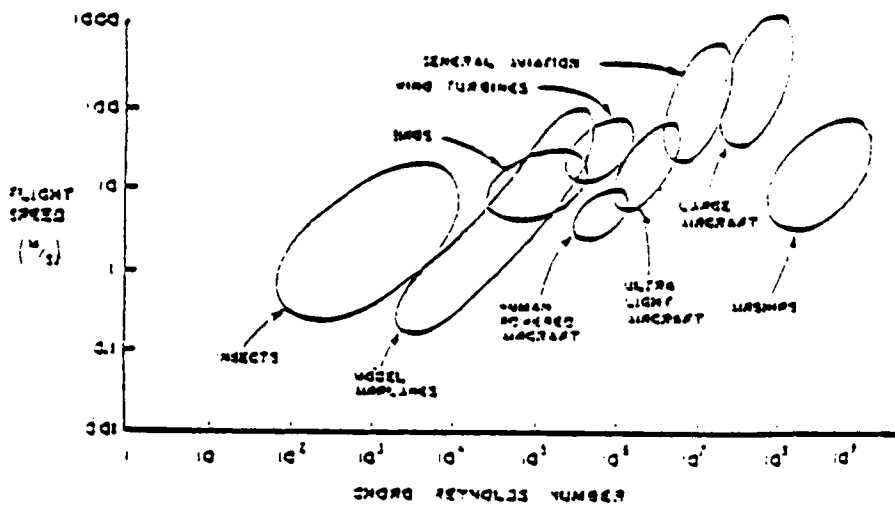


Fig. 1.1 : TYPICAL RANGES OF REYNOLDS NUMBER FOR VARIOUS APPLICATIONS.

FROM REFERENCE (1)

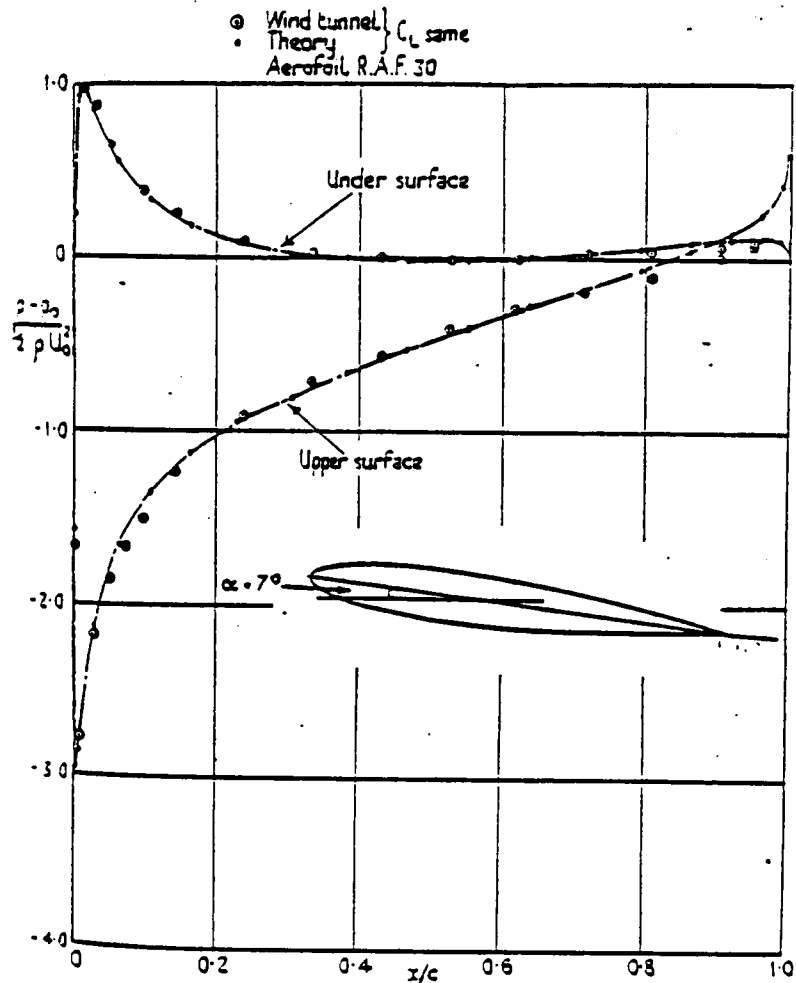


Fig. 179.

Fig.2.1 : TYPICAL AIRFOIL SURFACE PRESSURE DISTRIBUTION  
 FOR POSITIVE INCIDENCE.  
 FROM REFERENCE (8)

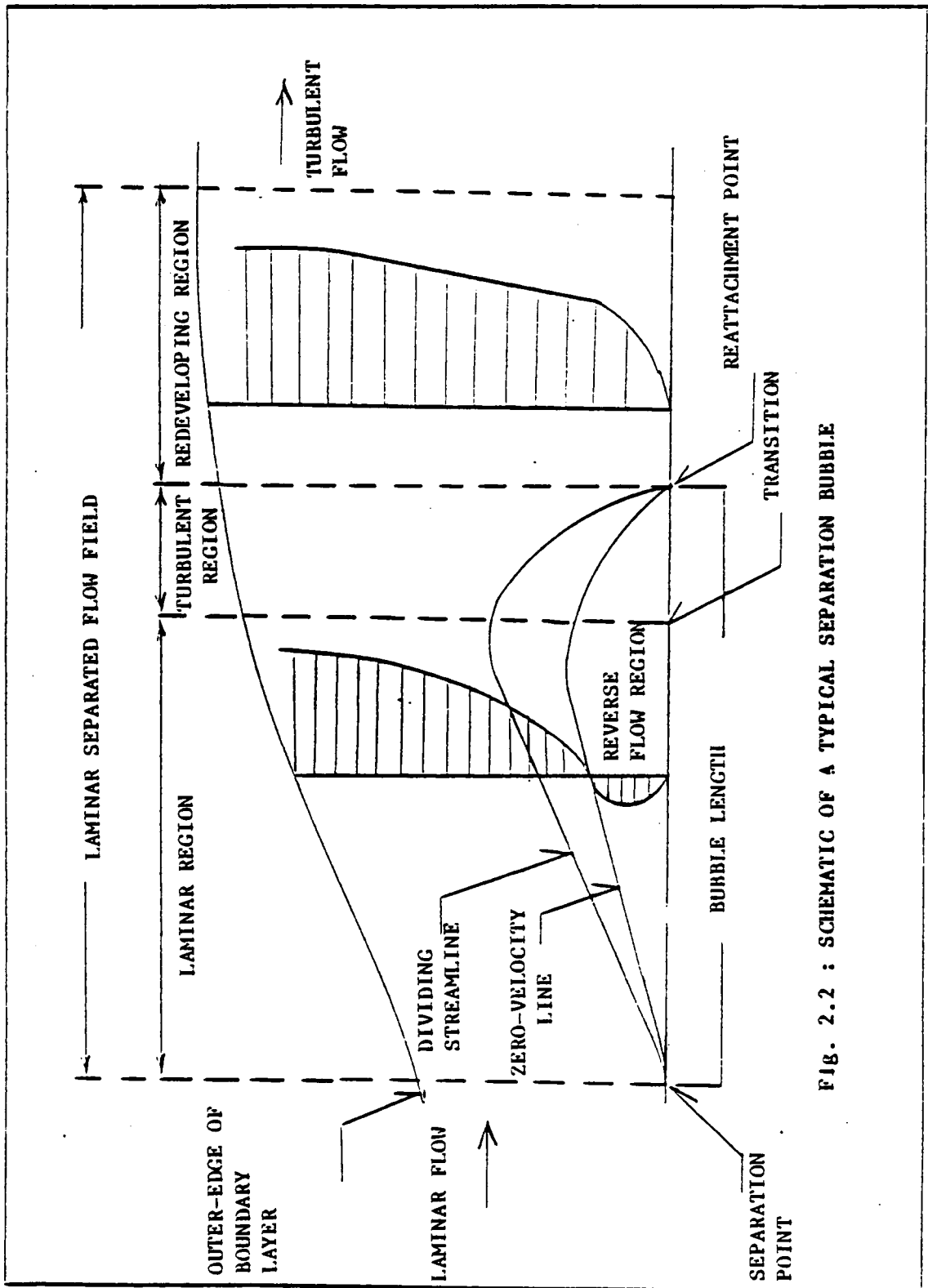


FIG. 2.2 : SCHEMATIC OF A TYPICAL SEPARATION BUBBLE

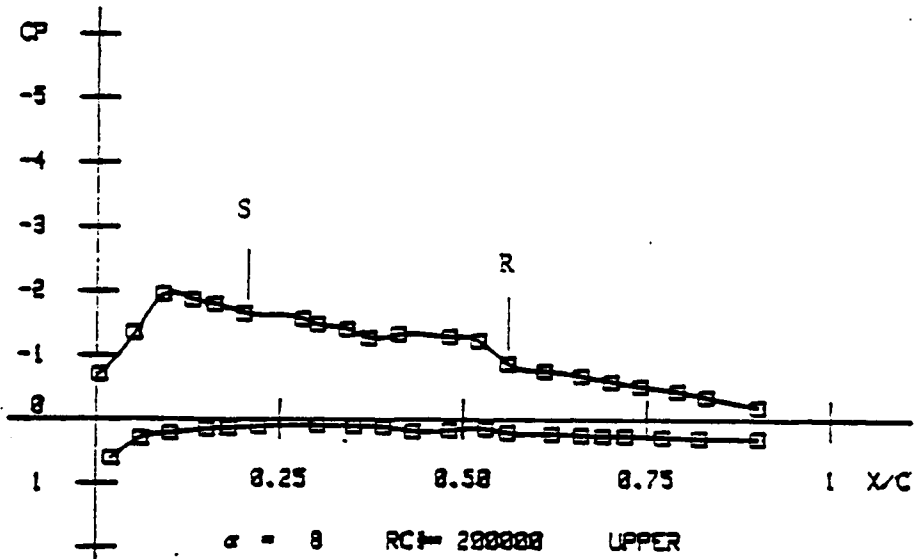


Fig.2.3 : TYPICAL AIRFOIL SURFACE PRESSURE DISTRIBUTION WITH THE SEPARATION BUBBLE.

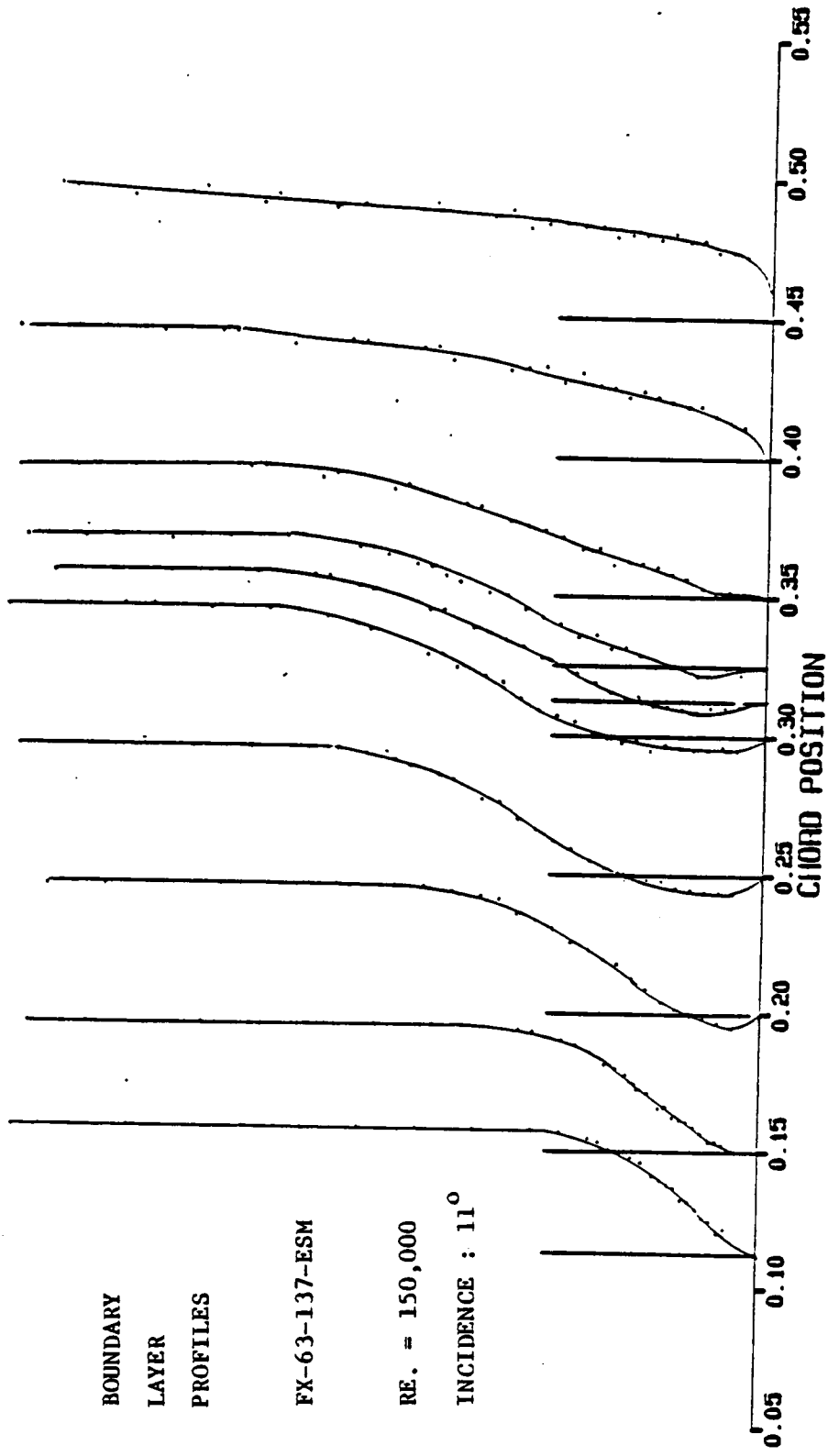


FIG. 2.4 : TYPICAL BOUNDARY LAYER PROFILES THROUGH THE SEPARATION BUBBLE. FROM REF. (26)

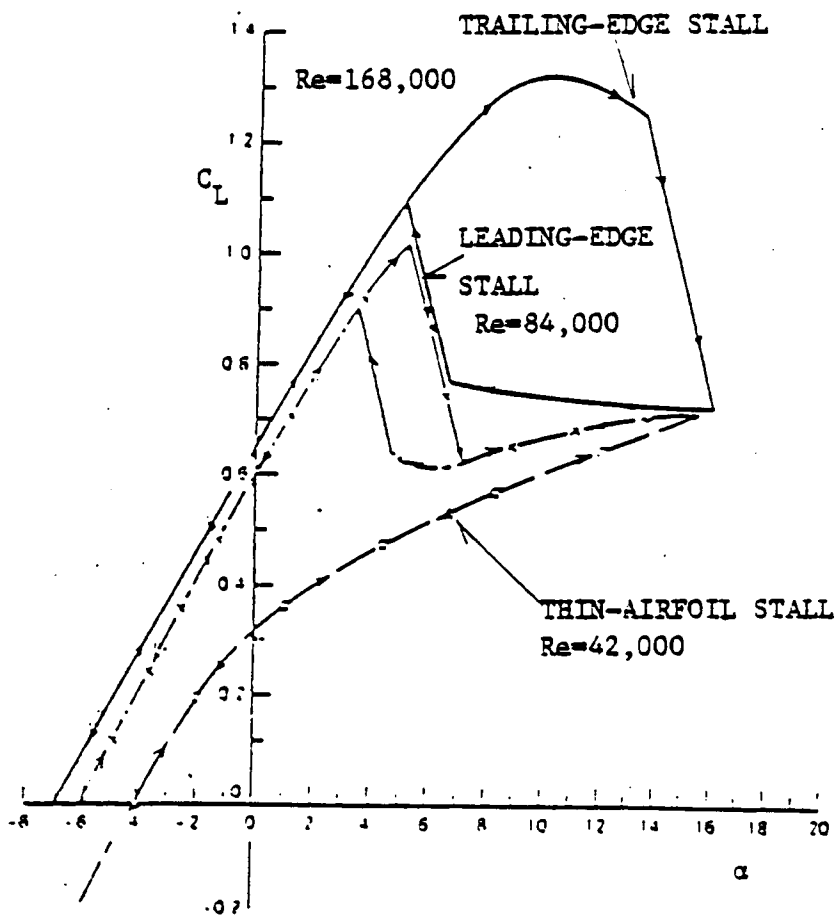


Fig.2.5 : TYPICAL STALL PATTERNS FOR AN N60 AIRFOIL  
FROM REFERENCE (44).

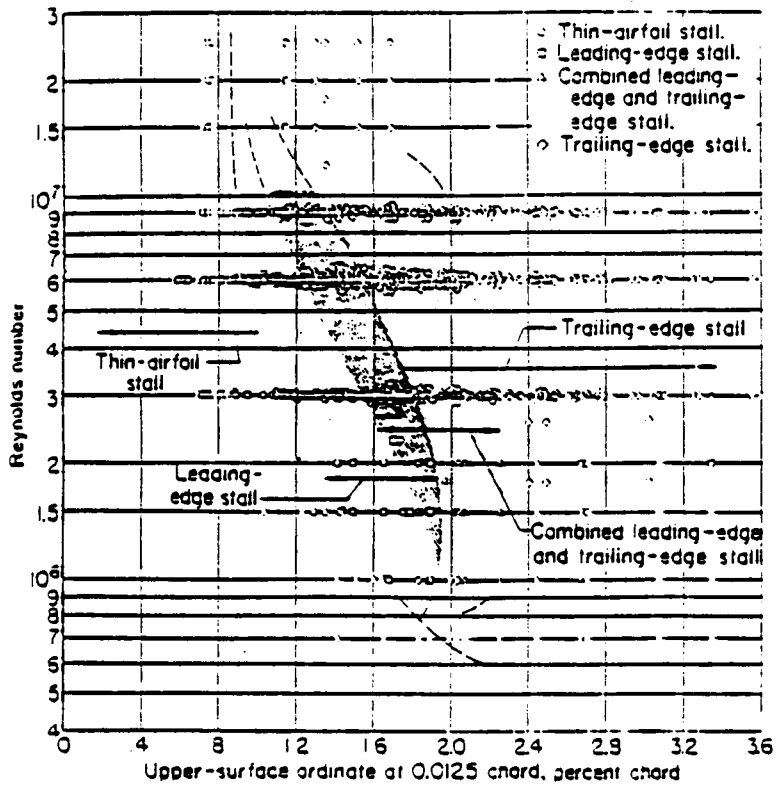


Fig.2.6 : CORRELATION OF REYNOLDS NUMBER AND STALL TYPE DUE TO GAULT (24)

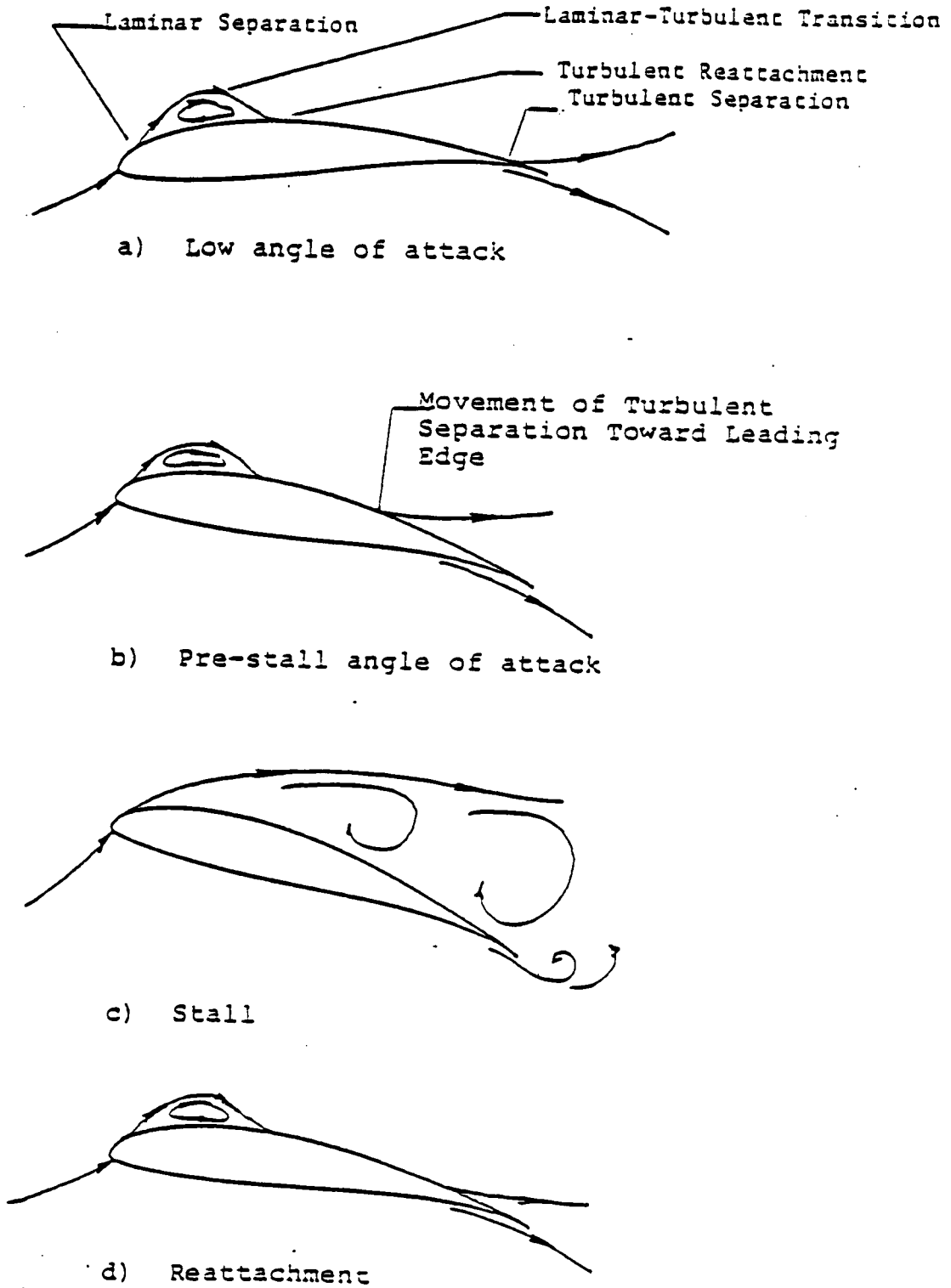


Fig.2.7 : TYPICAL HISTORY OF EVENTS DURING STALL.

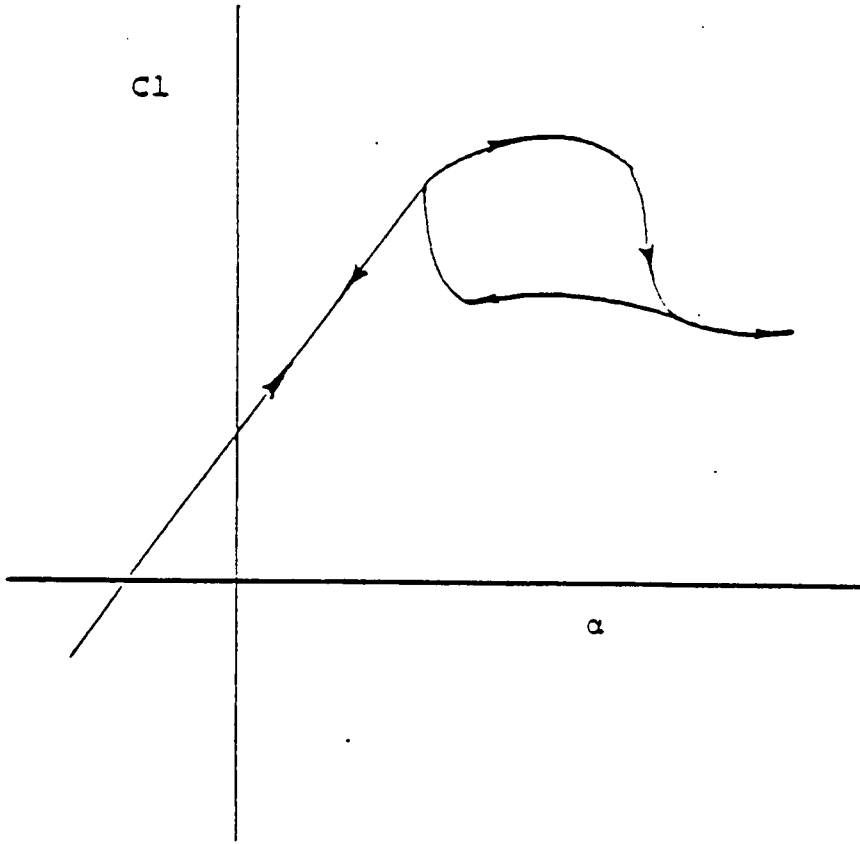


Fig.2.8 : A TYPICAL STALL HYSTERESIS LOOP

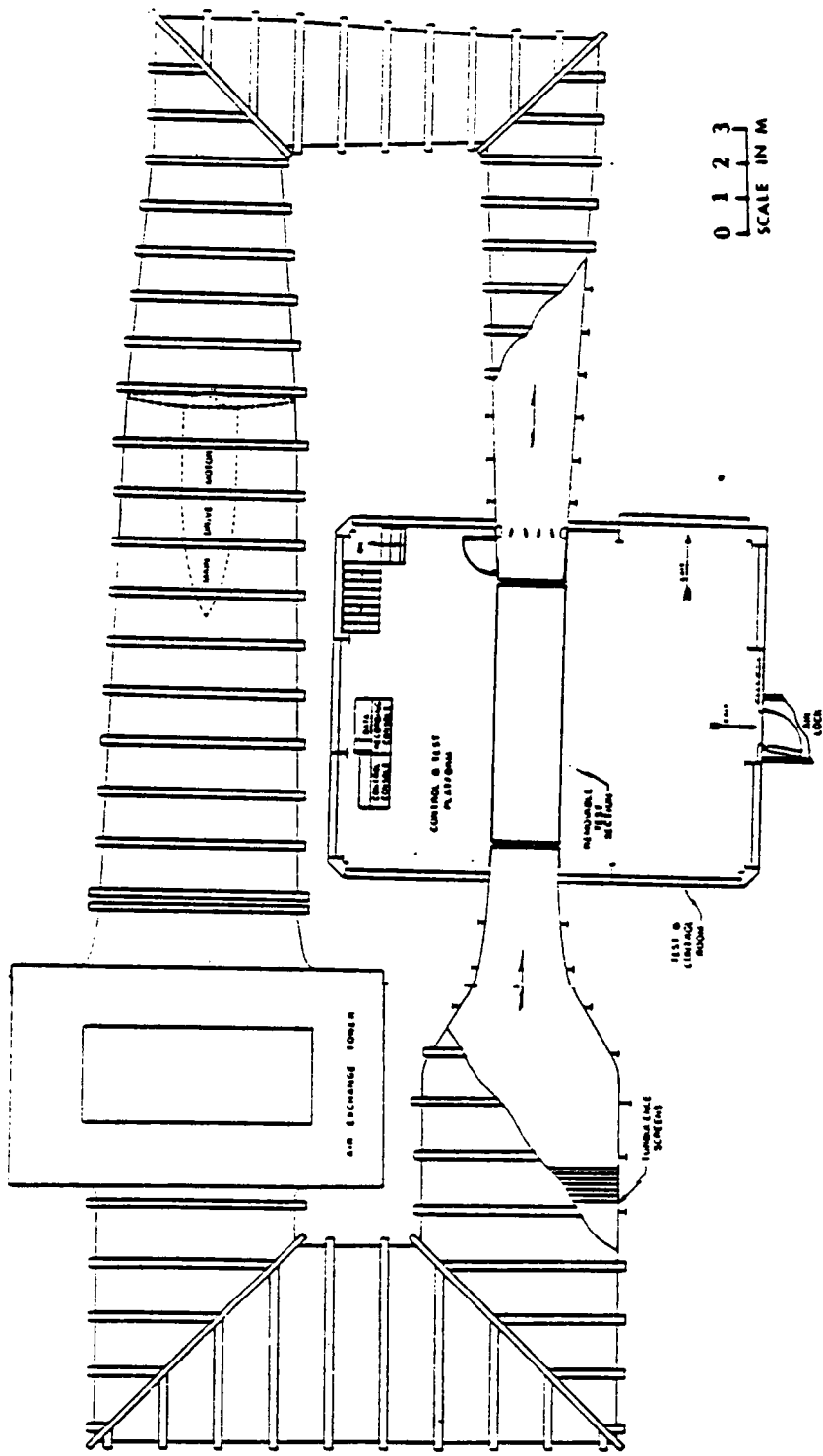


FIG. 3.1 : SCHEMATIC OF THE VIRGINIA TECH STABILITY WIND TUNNEL.

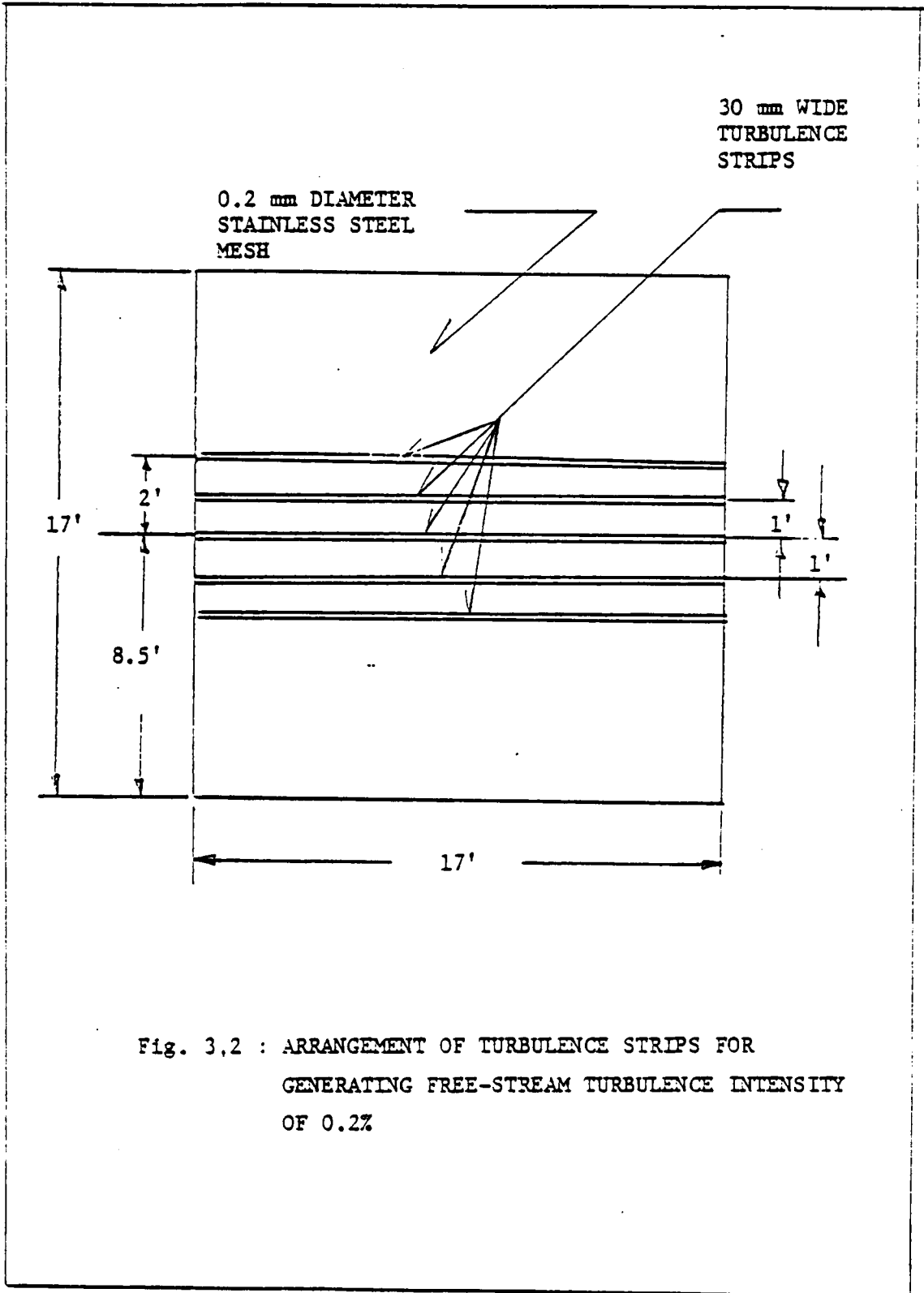
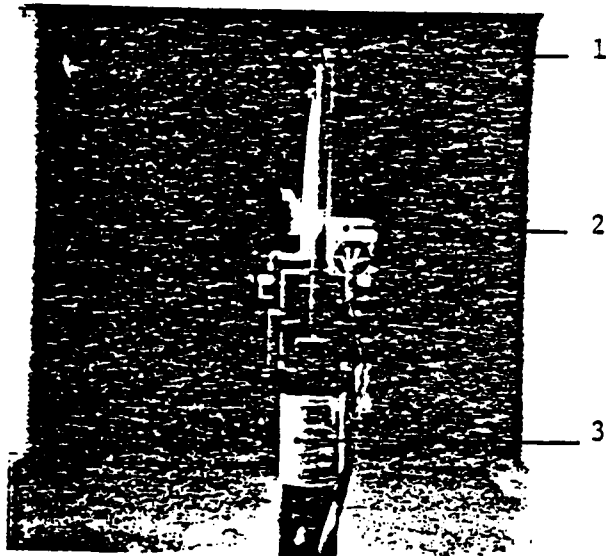


Fig. 3,2 : ARRANGEMENT OF TURBULENCE STRIPS FOR  
GENERATING FREE-STREAM TURBULENCE INTENSITY  
OF 0.2%



- 1 : HINGED PLATFORM FOR WING MOUNT.
- 2 : ELECTRONIC INCLINOMETER
- 3 : DRIVE MOTOR

Fig. 3.3 : ARRANGEMENT FOR REMOTE ACTUATION OF MODEL  
ANGLE OF ATTACK.

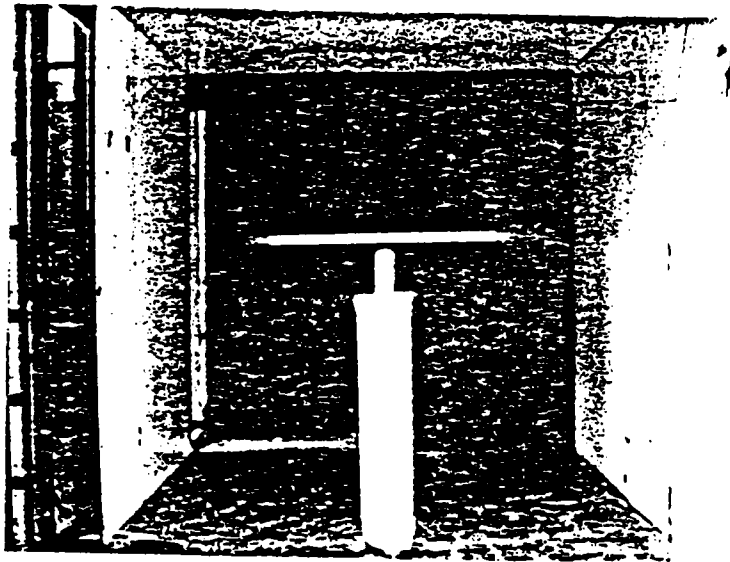


Fig. 3.4 : PICTURE OF THE SHROUDED STRUT AND WING (AR=4)  
IN THE TEST SECTION OF THE VIRGINIA TECH STABILITY  
WIND TUNNEL.

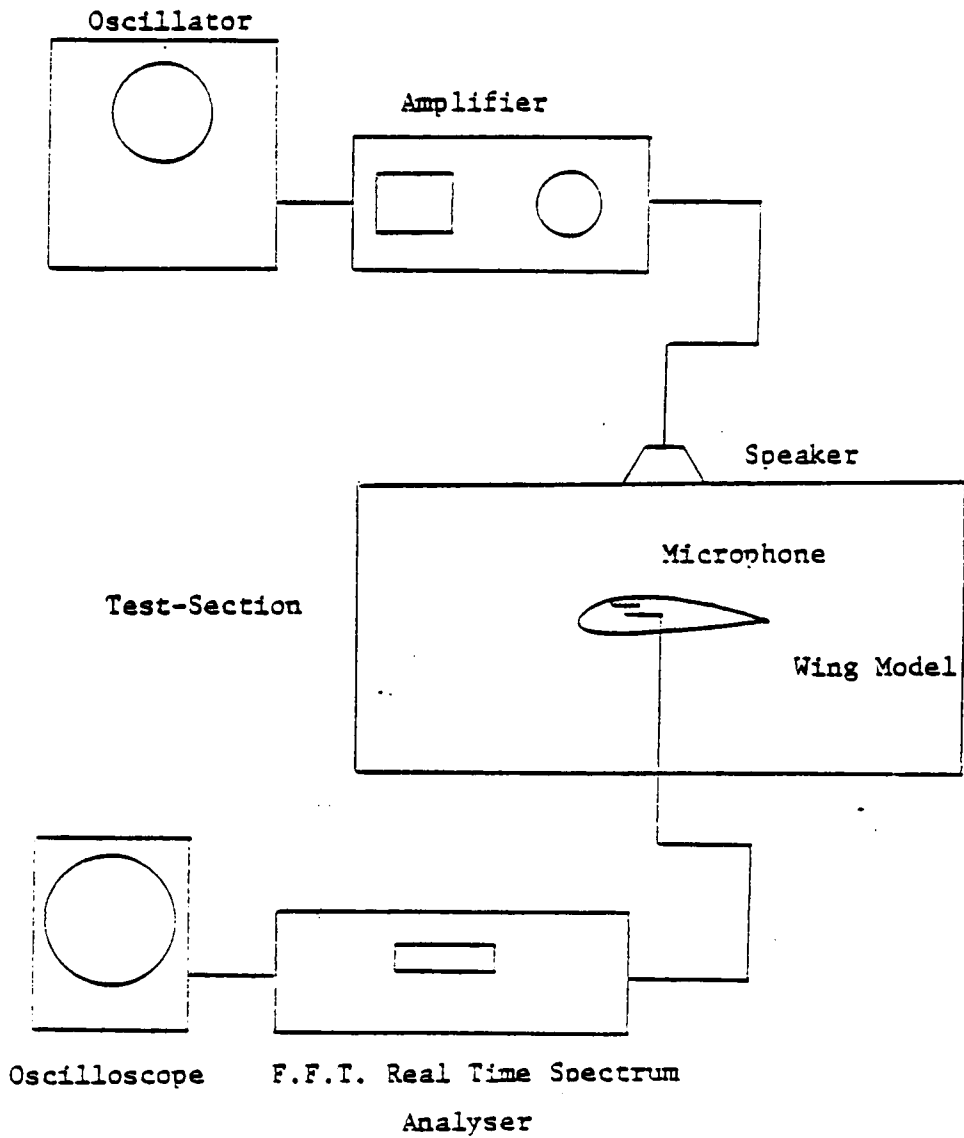


Fig. 3.5 : SET-UP FOR THE CREATION AND ANALYSIS OF THE ACOUSTIC DISTURBANCES.

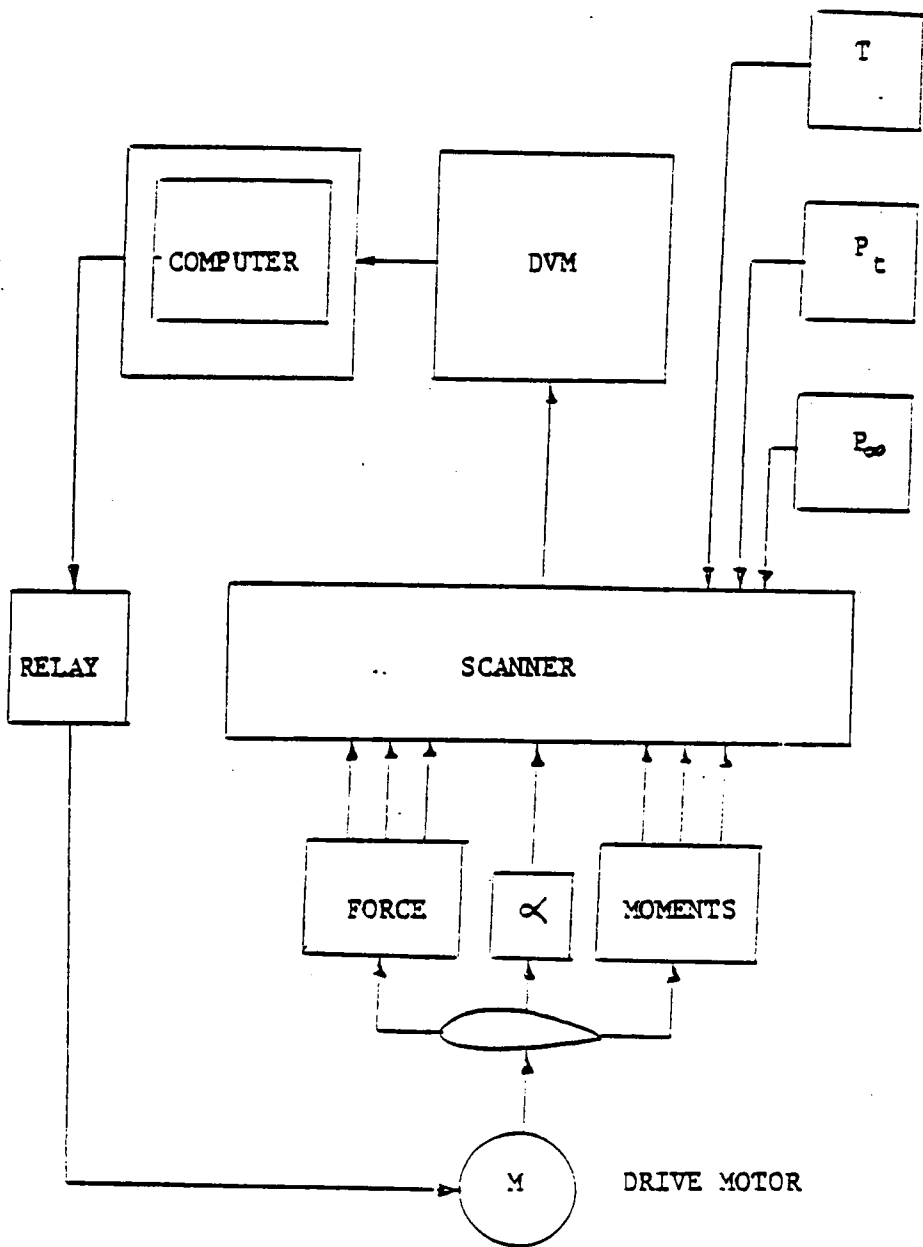


Fig. 3.6 : SET-UP FOR FORCE DATA ACQUISITION AND MODEL ACTUATION.

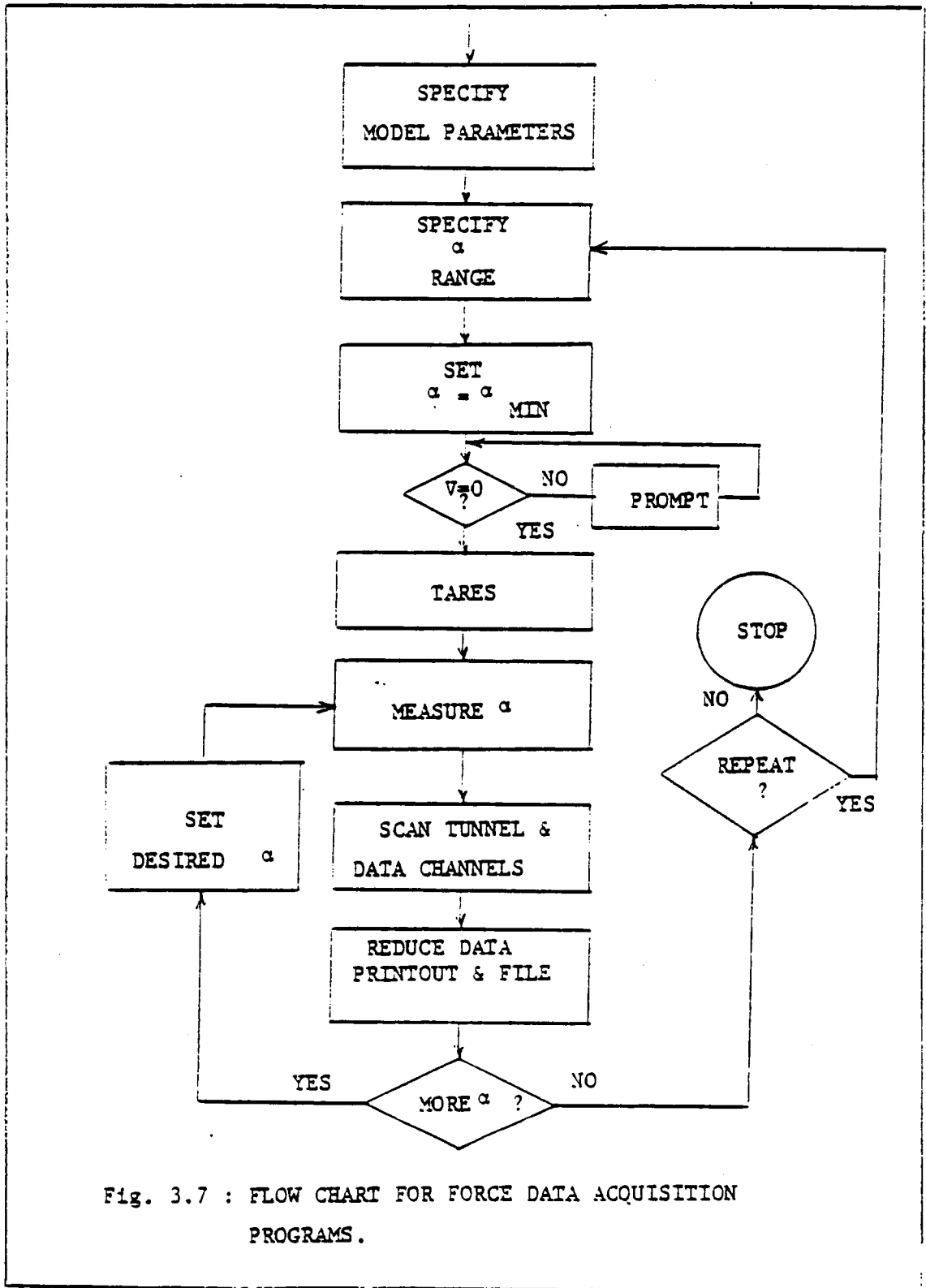


Fig. 3.7 : FLOW CHART FOR FORCE DATA ACQUISITION PROGRAMS.

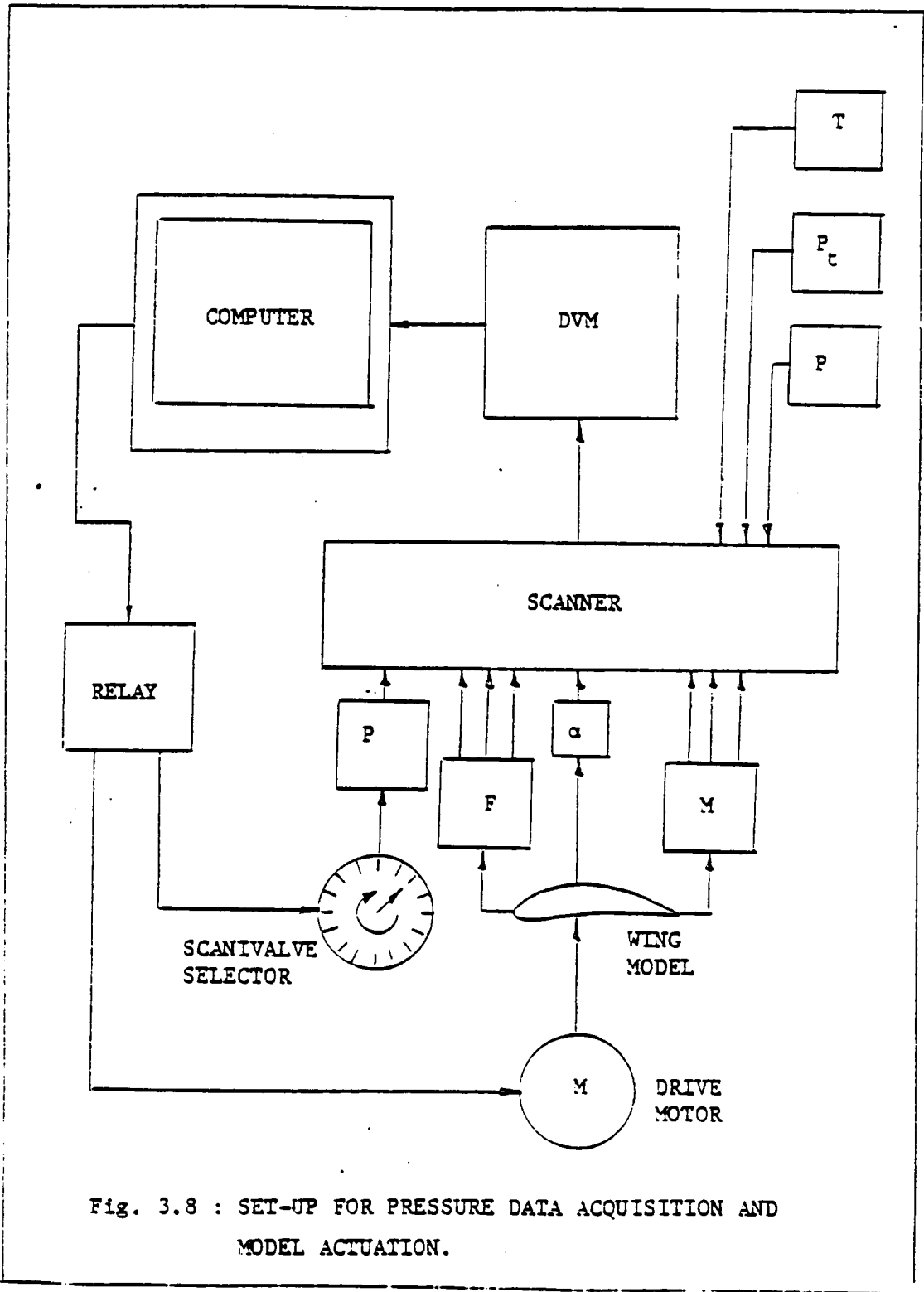


Fig. 3.8 : SET-UP FOR PRESSURE DATA ACQUISITION AND MODEL ACTUATION.

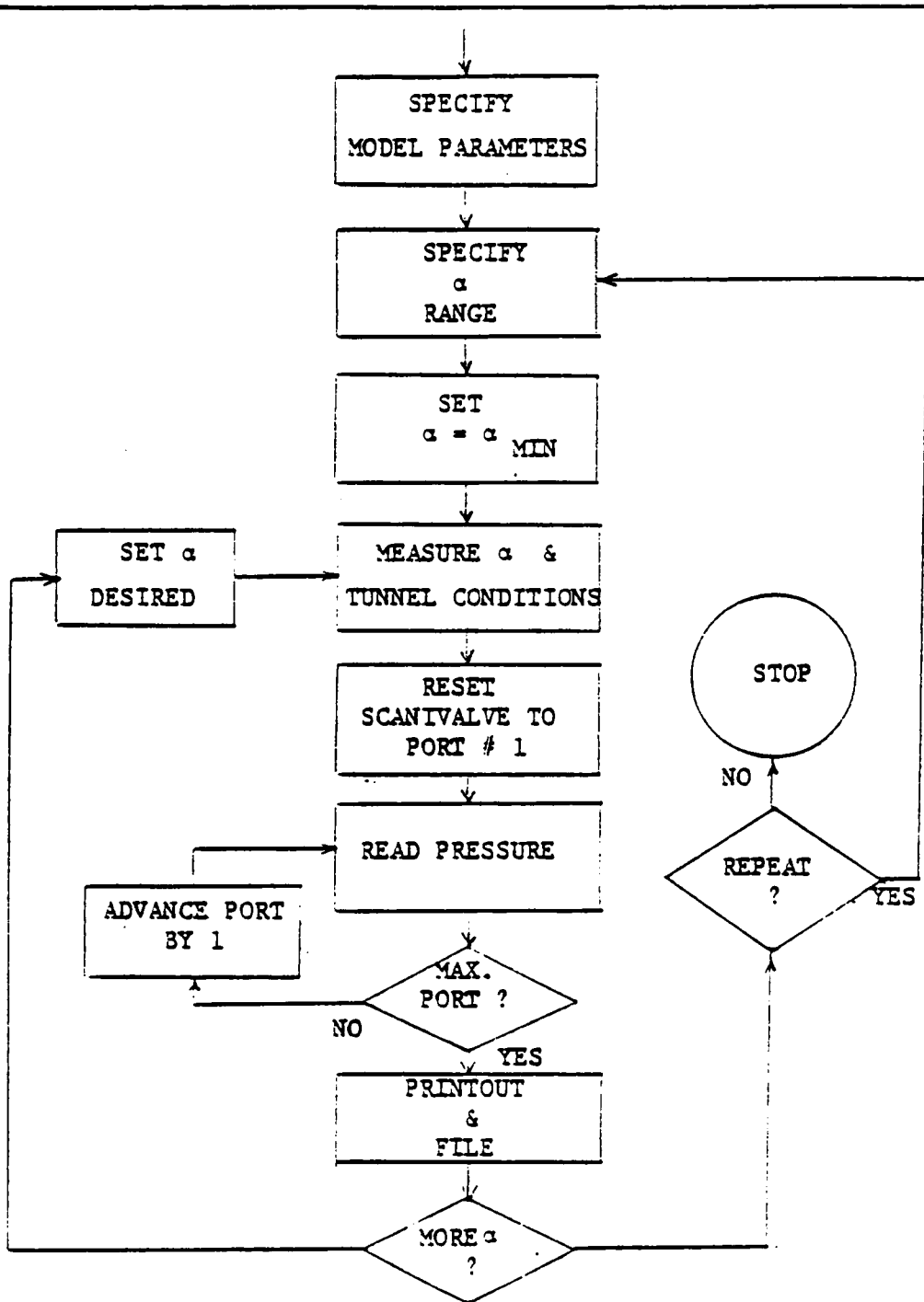


Fig. 3.9 : FLOW CHART FOR PRESSURE DATA ACQUISITION PROGRAMS.

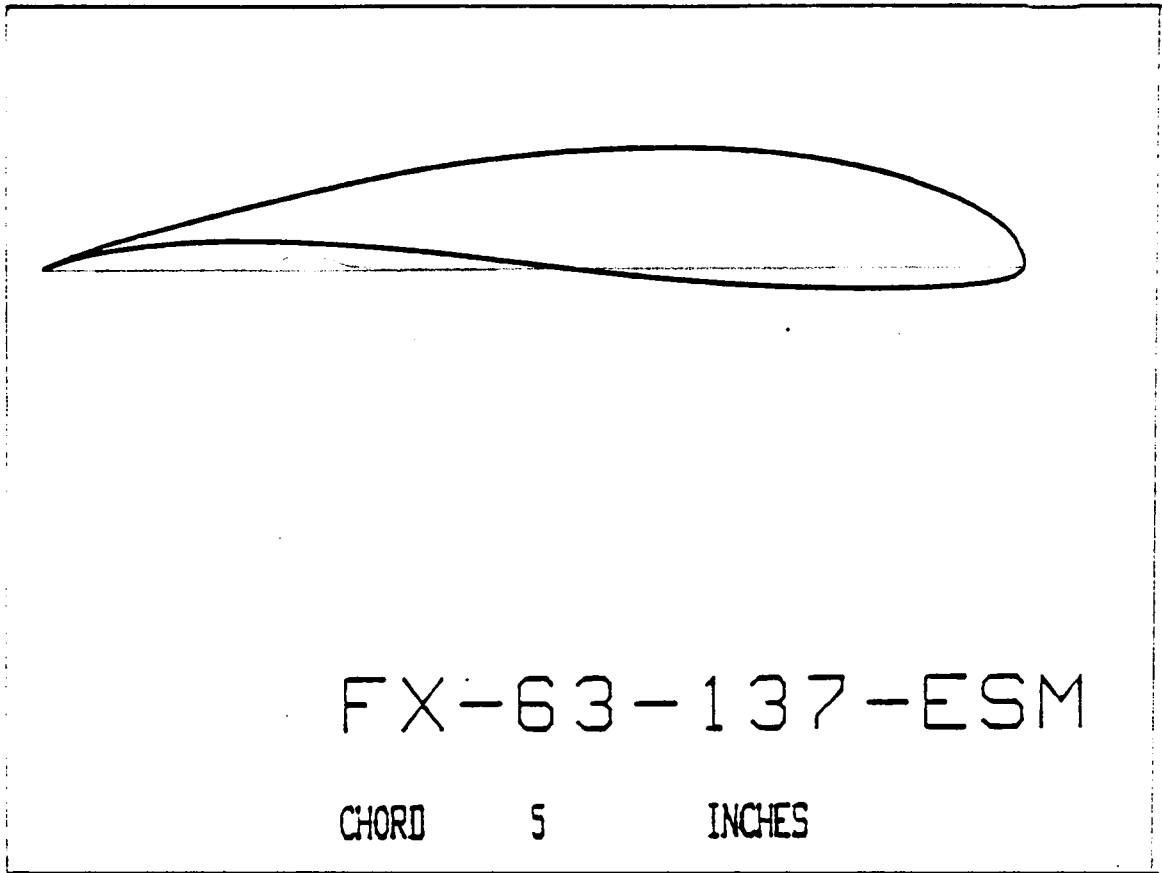
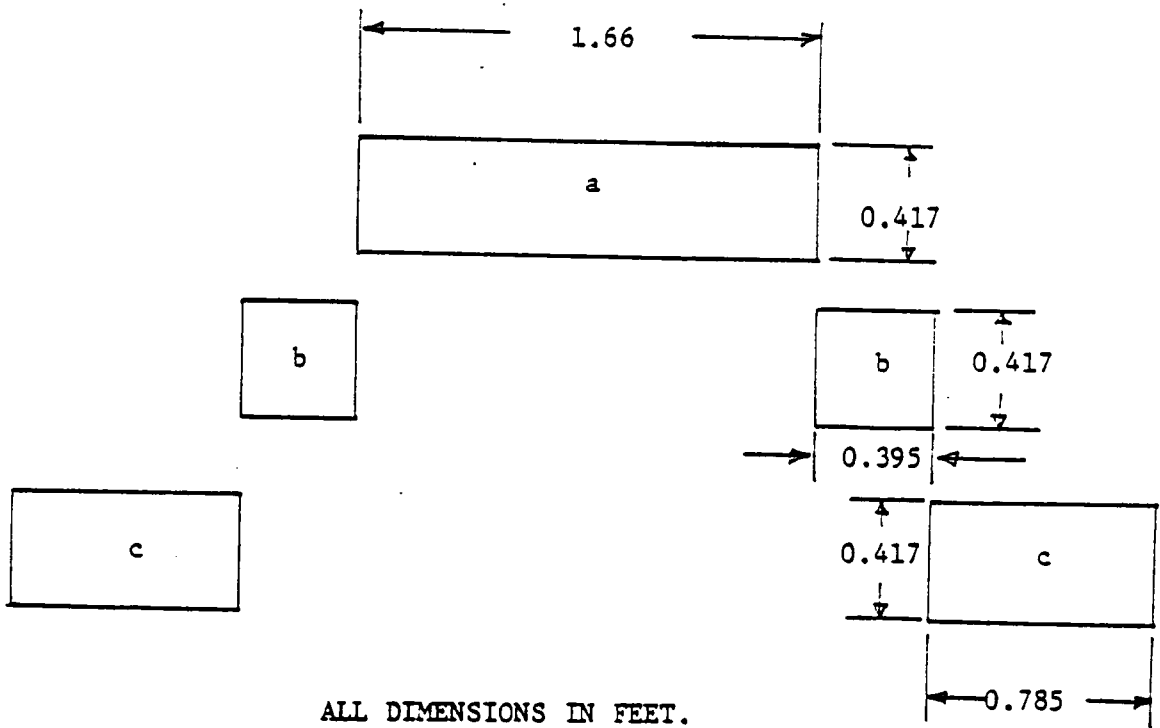
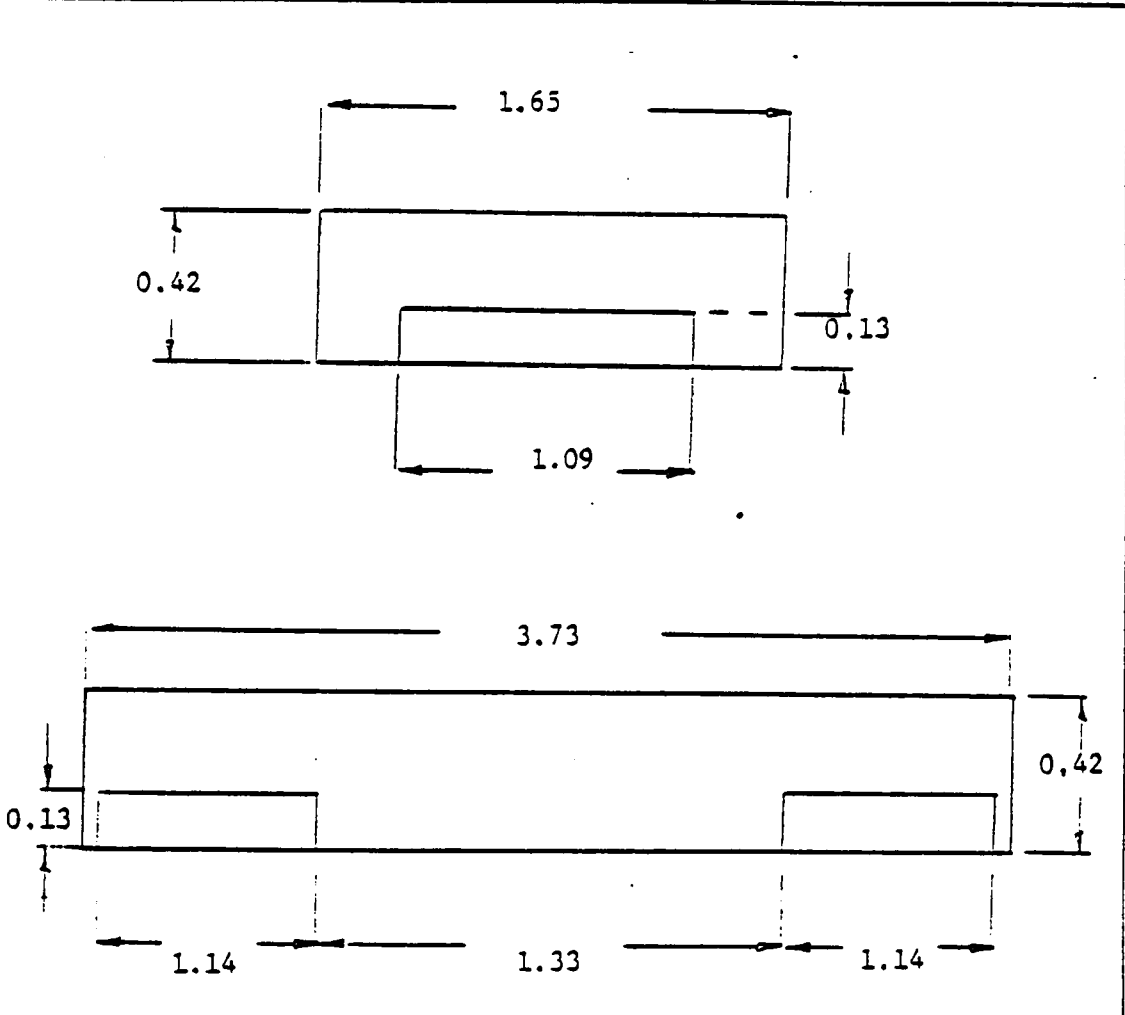


Fig. 3.10 : CONTOUR OF THE WORTMANN AIRFOIL SECTION



CONFIGURATION	SPAN	AR
a	1.66	3.98
b+a+b	2.45	5.88
c+a+c	3.23	7.85
c+b+a+b+c	4.02	9.65

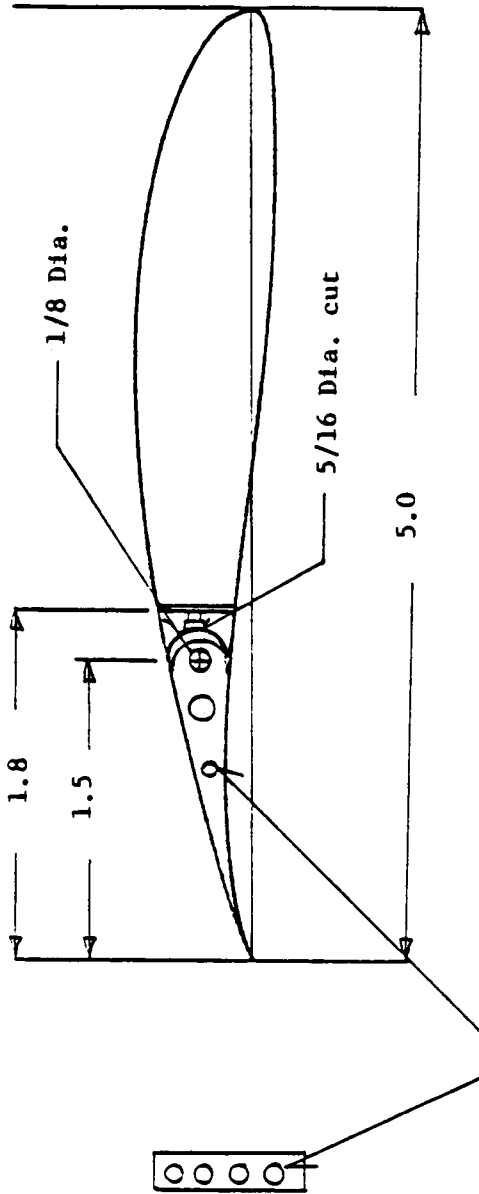
Fig. 3.11 : VARIOUS CONFIGURATIONS OF THE MODULAR PLAIN WING



ALL DIMENSIONS IN FEET.

AR	4	9
flap chord ratio	0.3	0.3
flap span ratio	0.665	0.605
chord (inches)	5.0	5.0

Fig. 3.12 : WING WITH FLAPS AND CONTROL SURFACES.



ALL DIMENSIONS IN INCHES

Fig. 3.13 : CONSTRUCTION OF FLAPS AND CONTROL SURFACES.

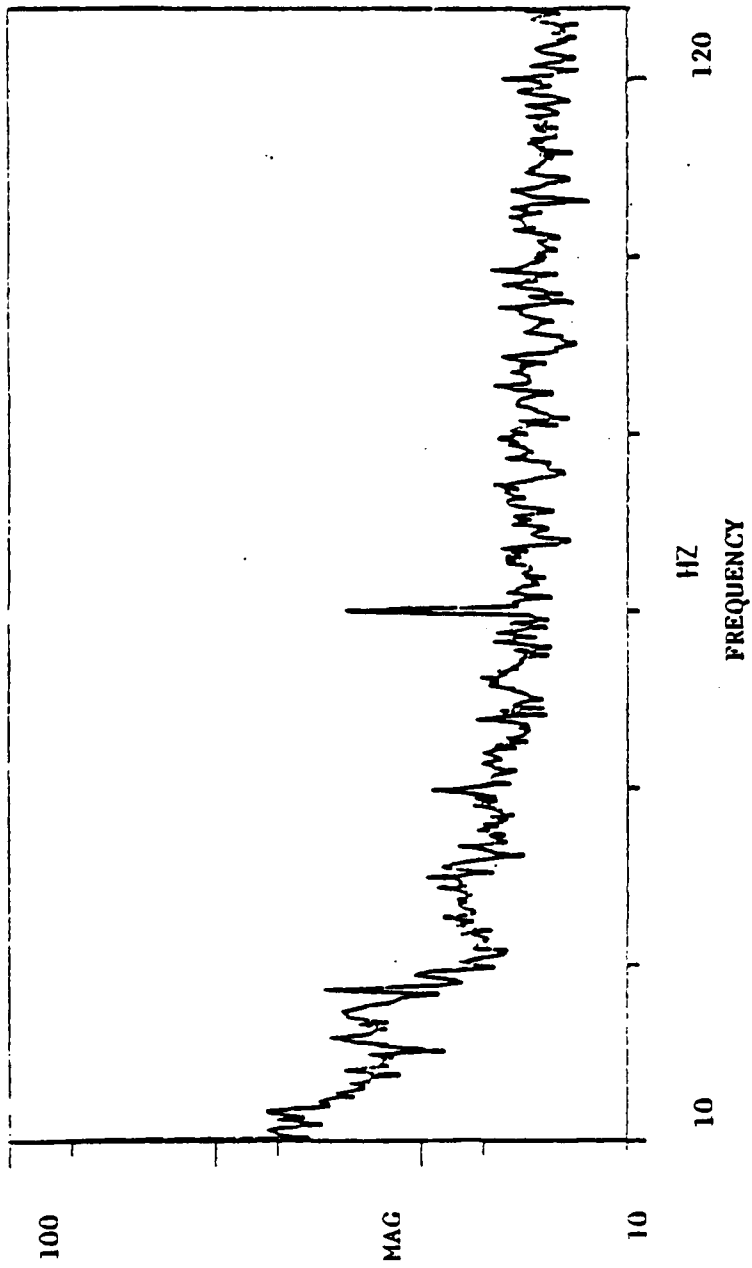


FIG. 3.14: TYPICAL TURBULENCE SPECTRUM AT  $U=15$  m/s WHERE  $u'/U = 0.018\%$   
FROM REF. (26).

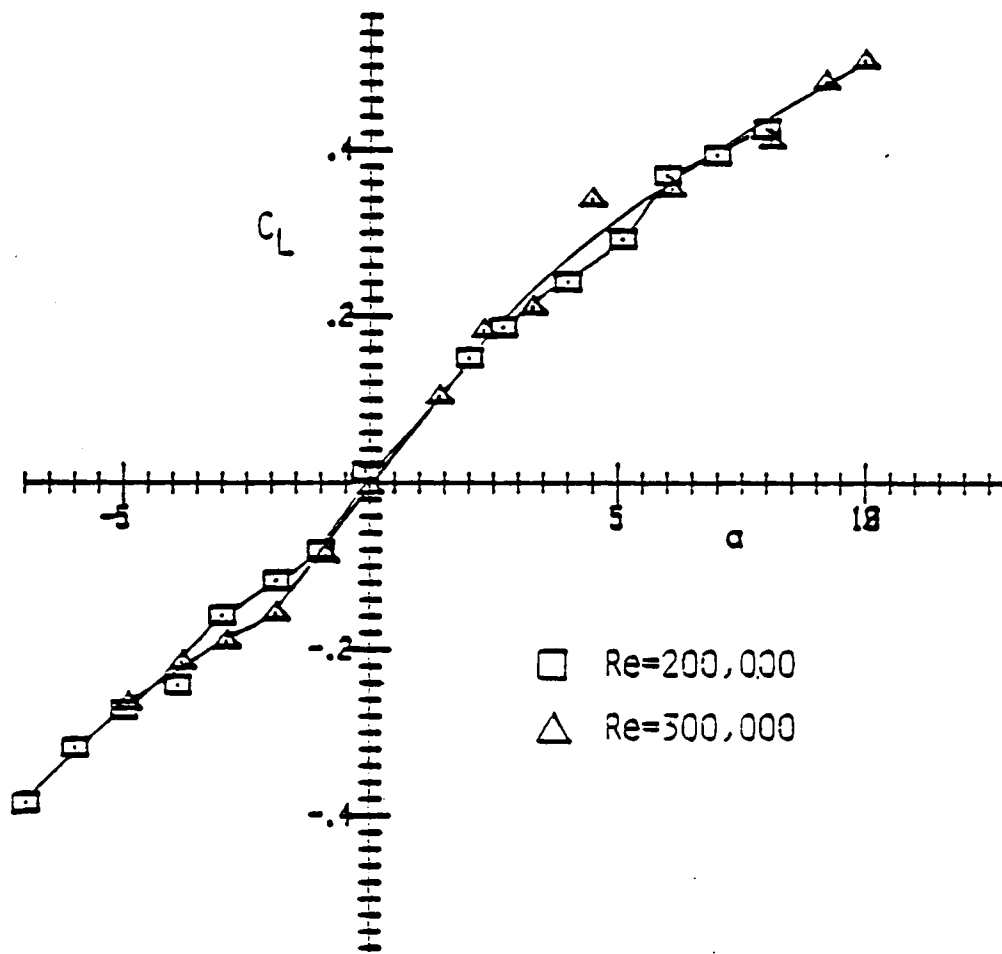
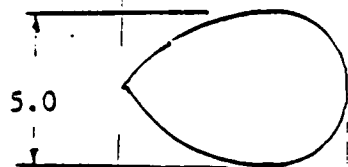
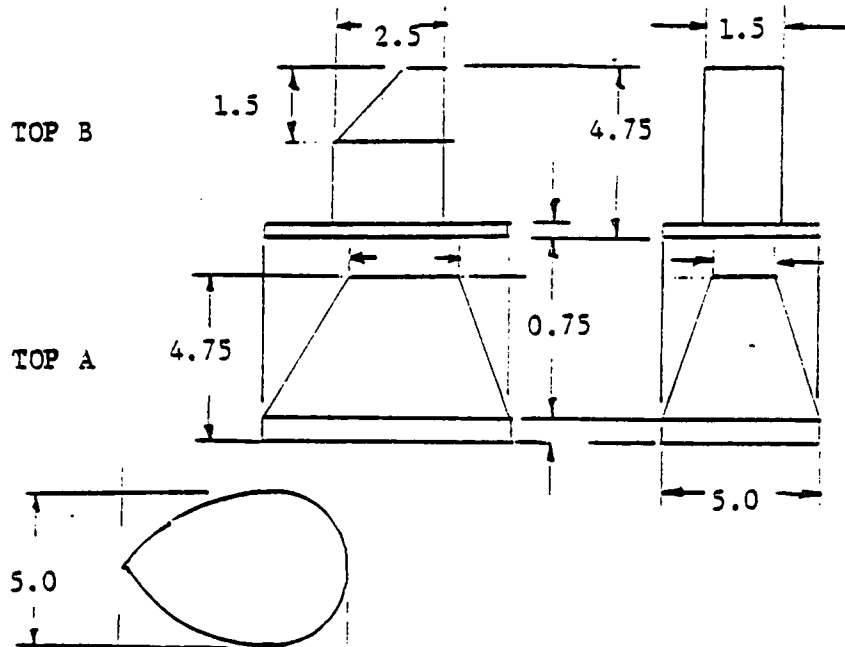


Fig. 4.1 : LIFT DATA FOR STRUT MOUNTED FLAT PLATE AR = 6.

SHROUD TOP B

SHROUD TOP A



ALL  
DIMENSIONS  
IN INCHES.

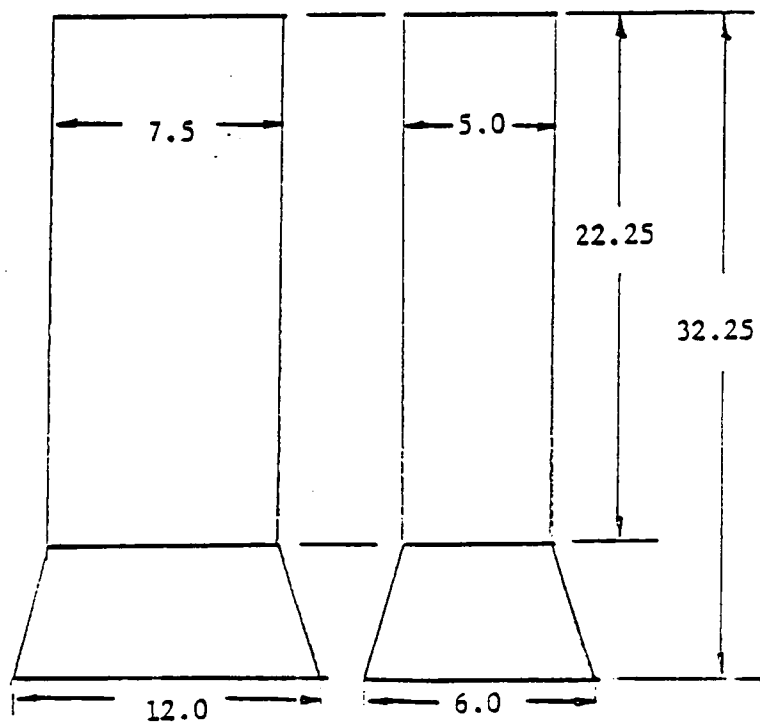
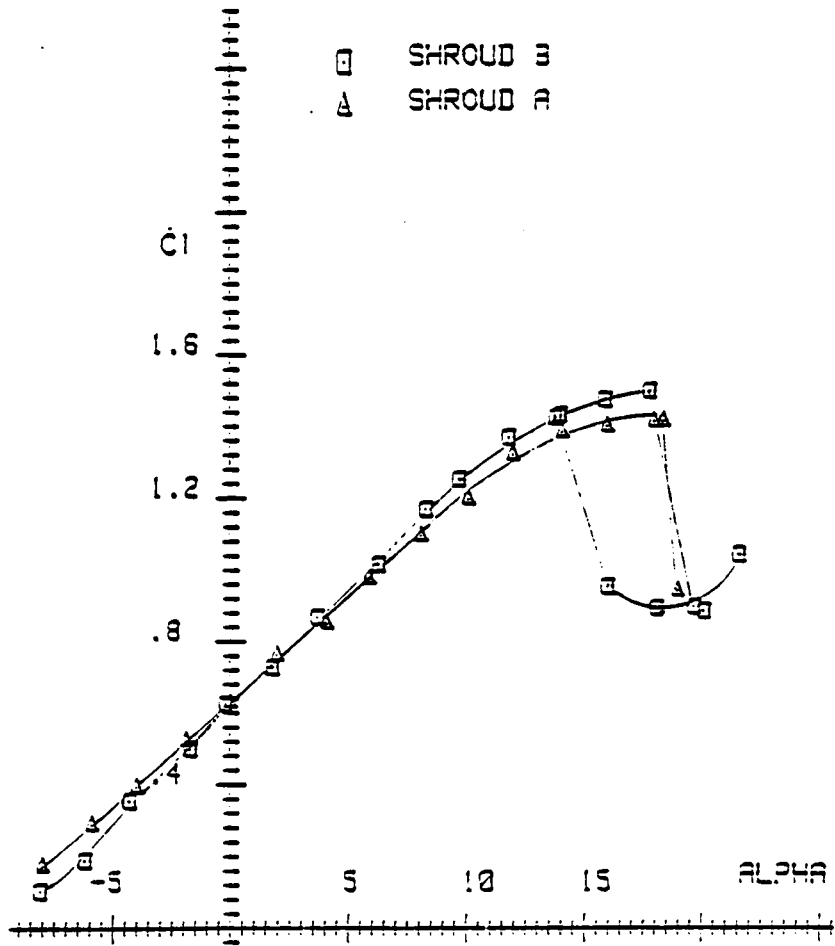


Fig. 4.2 : TWO CONFIGURATIONS OF THE SHROUD TOP.

FX-63-137-ESM



SHROUD TOP EFFECT RE=200K AR=4

Fig. 4.3 : LIFT DATA FOR THE TWO DEFFERENT SHROUD TOPS USED.  
AR = 4 RE. = 200,000

FX-63-137-ESM  
Re. = 200,000

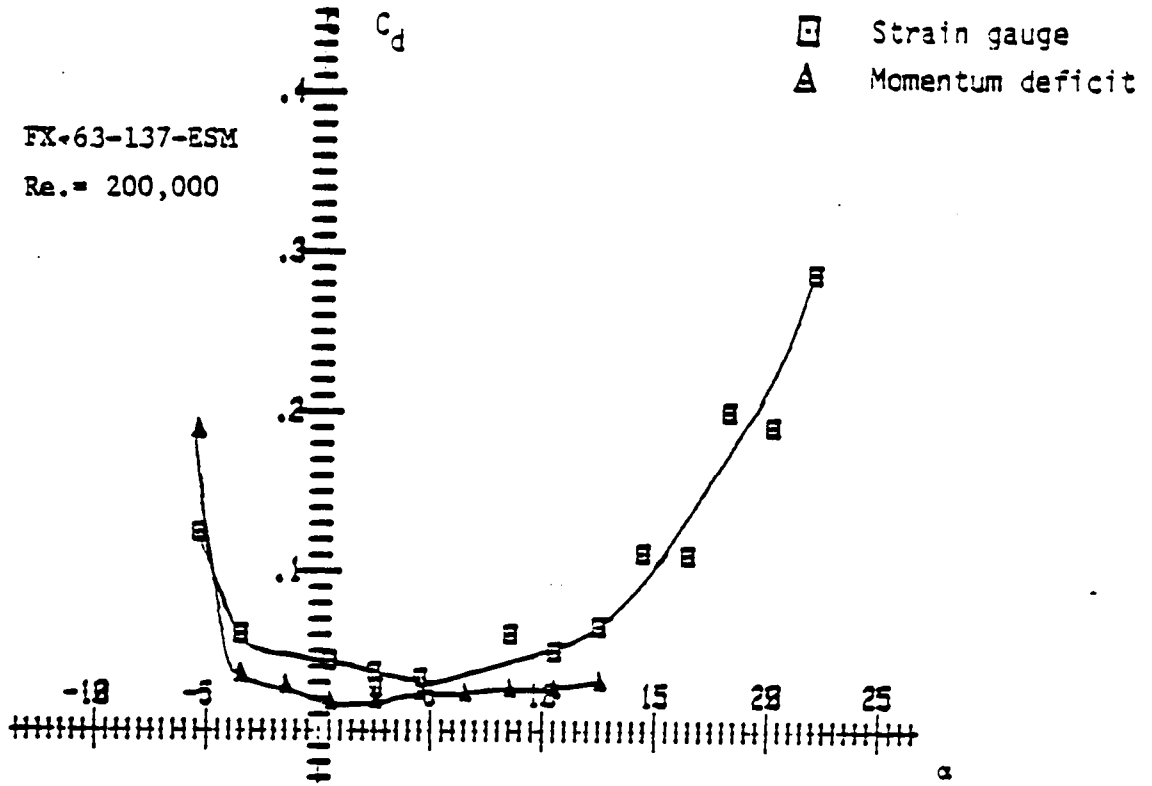
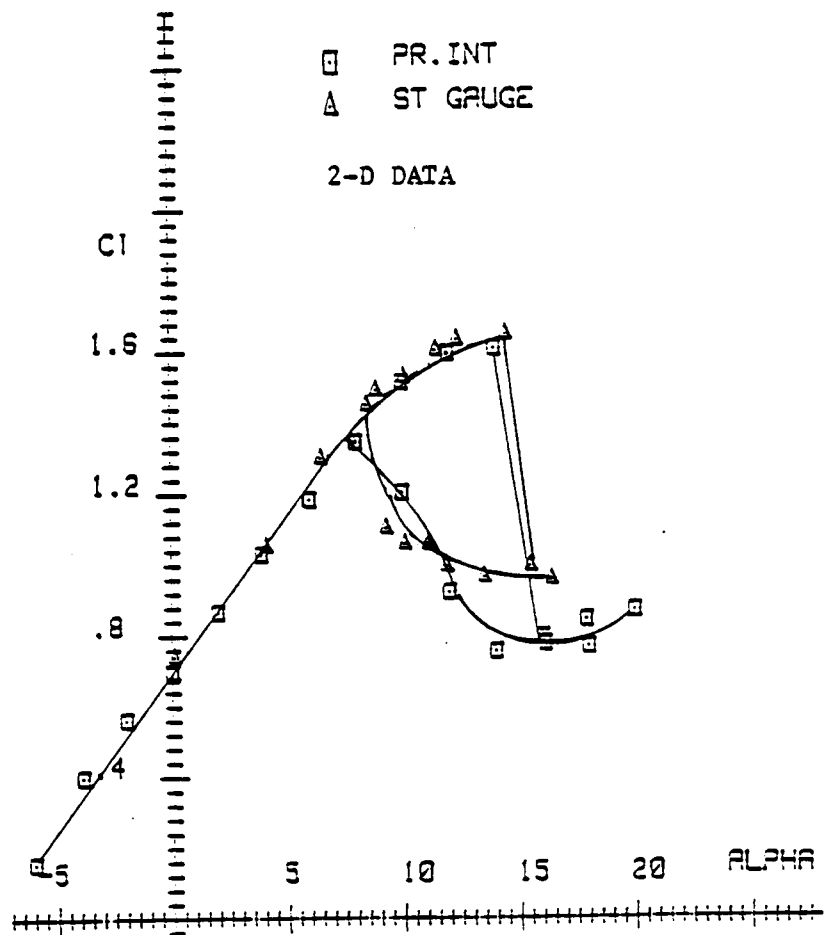


Fig. 4.4 : DRAG DATA OBTAINED FROM STRAIN GAUGE AND MOMENTUM DEFECIT METHODS.



INTEGRATED PRESSURE DATA RE=150K

Fig. 4.5 : COMPARISON OF LIFT DATA FROM PRESSURE INTEGRATION AND STRAIN GAUGE. RE. = 150,000

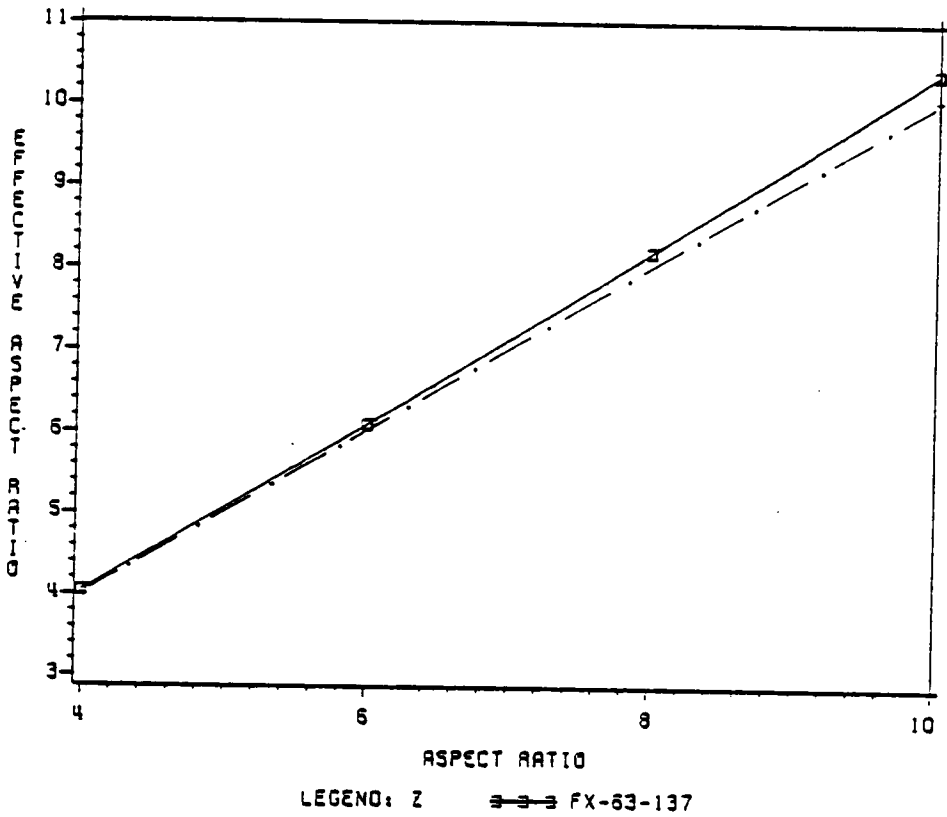


Fig. 4.6 : CALCULATED VALUES OF THE EFFECTIVE ASPECT RATIOS FOR THE VARIOUS WINGS TESTED. FROM REFERENCE (27).

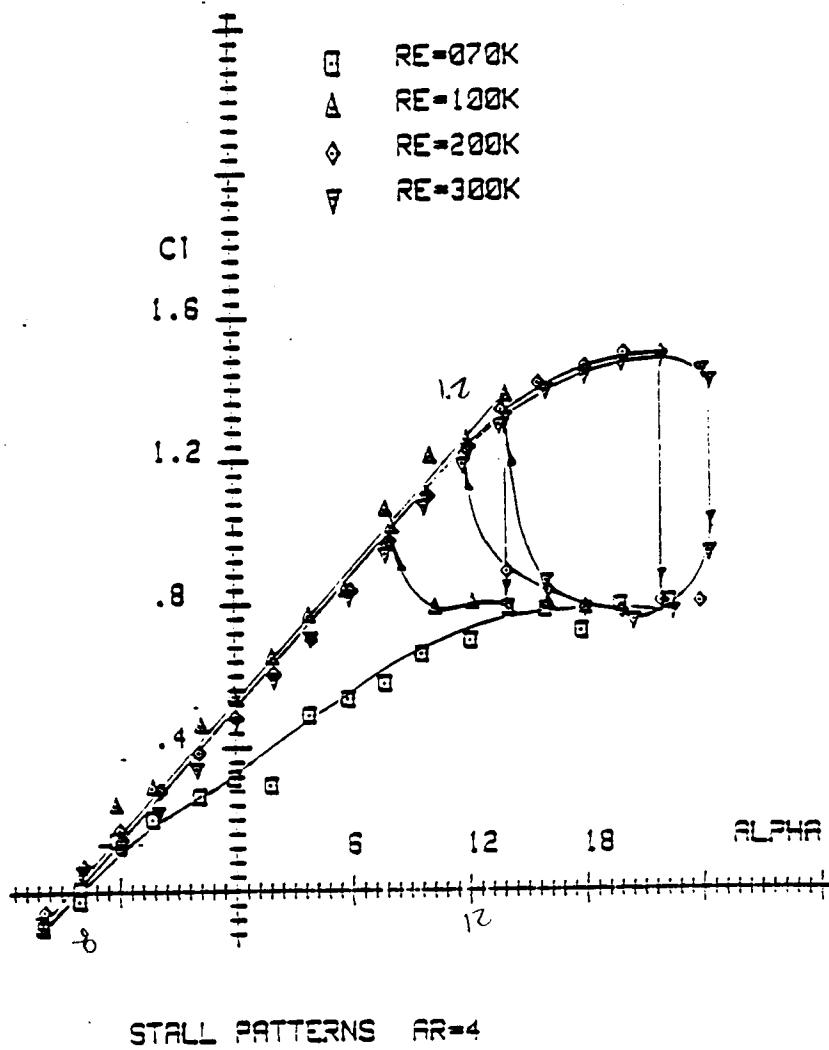


Fig. 4.7 : TYPICAL STALL PATTERNS FOR THE FX-63-137-ESM AIRFOIL WING MODEL OF AR=4.

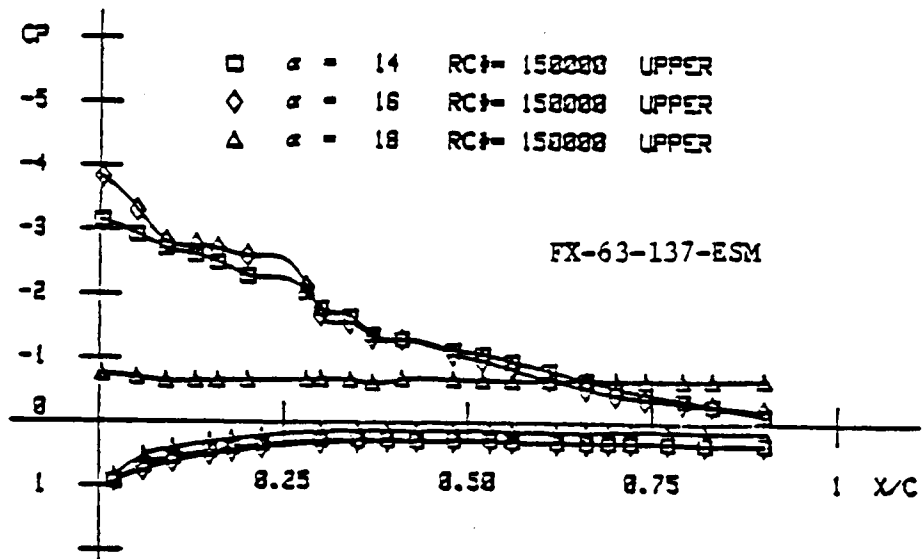


Fig. 4.8 : PRESSURE DISTRIBUTION HISTORY DURING STALL  
 Re. = 150,000.

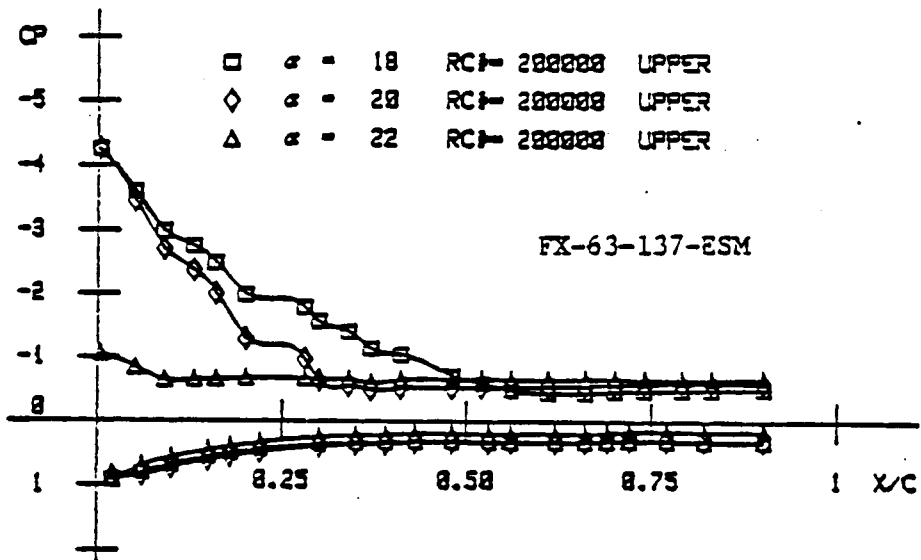


Fig. 4.9 : PRESSURE DISTRIBUTION HISTORY DURING STALL

$Re. = 200,000$

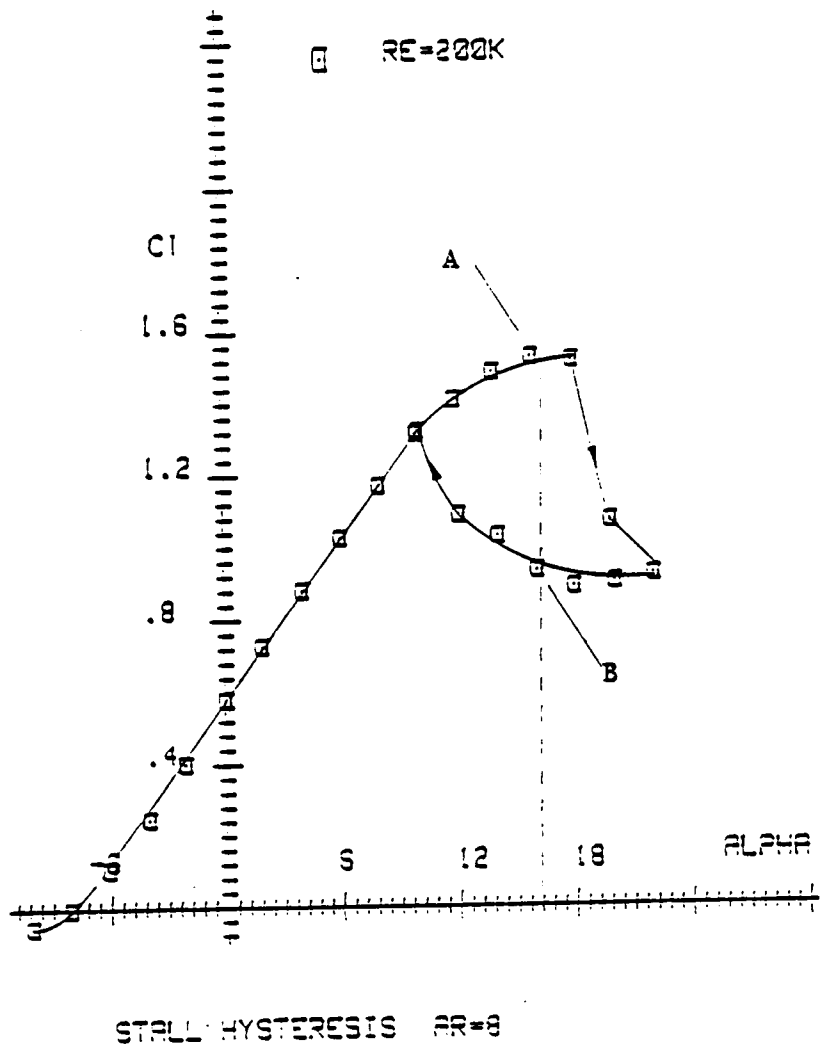


Fig. 4.10 : TYPICAL STALL HYSTERESIS LOOP FOR THE FX-63-137-ESM WING MODEL OF AR=8 AT RE.=200,000

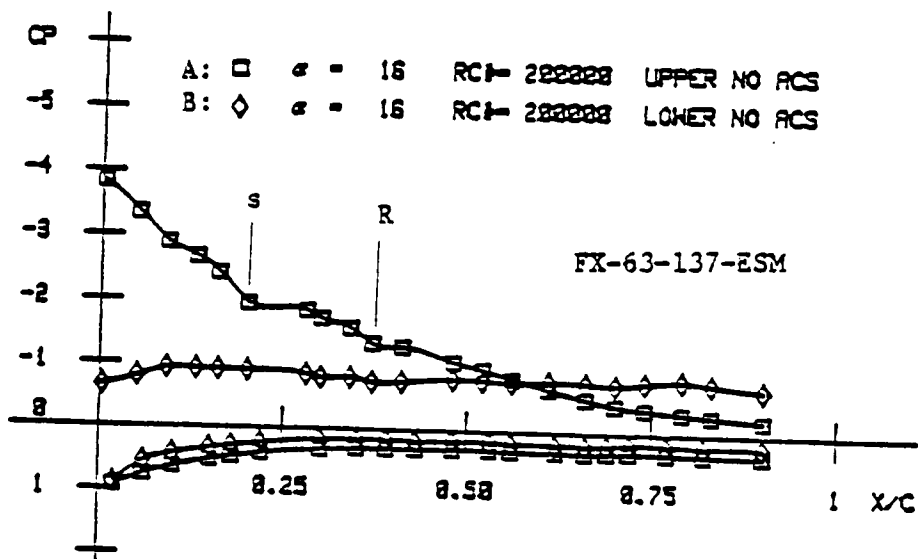


Fig. 4.11 : TYPICAL PRESSURE DISTRIBUTION ON THE UPPER AND LOWER PORTIONS OF THE HYSTERESIS LOOP.

Re. = 200,000

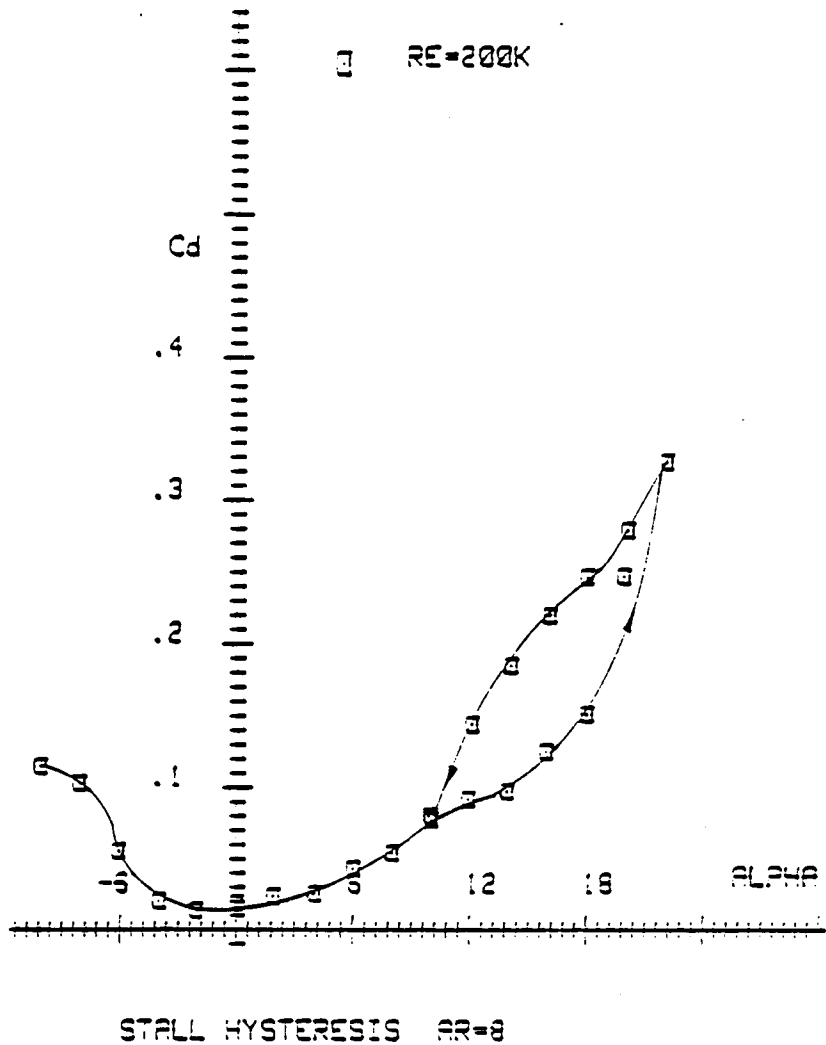


Fig. 4.12 : DRAG DATA FOR STALL HYSTERESIS FOR THE FX-63-137-ESM WING MODEL OF AR=8 AT RE.=200,000

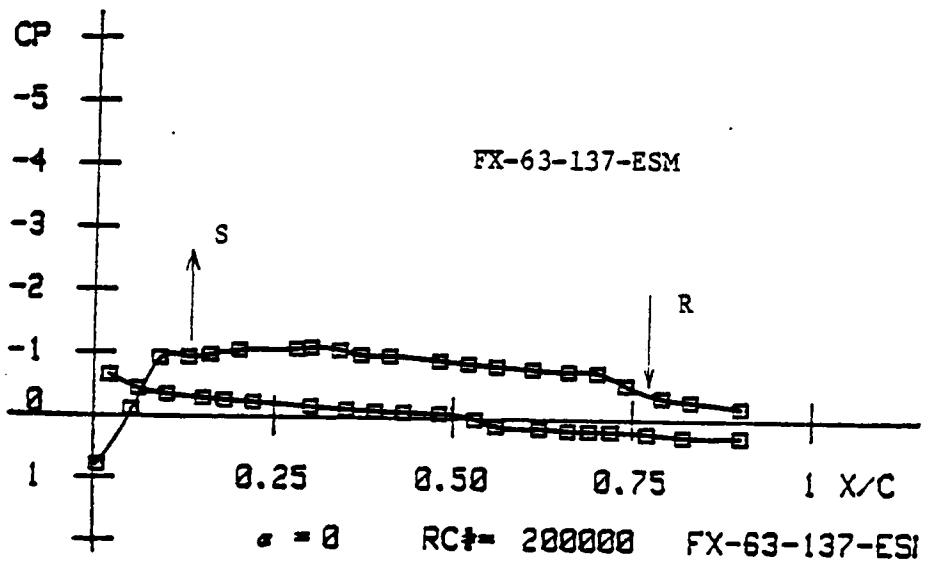
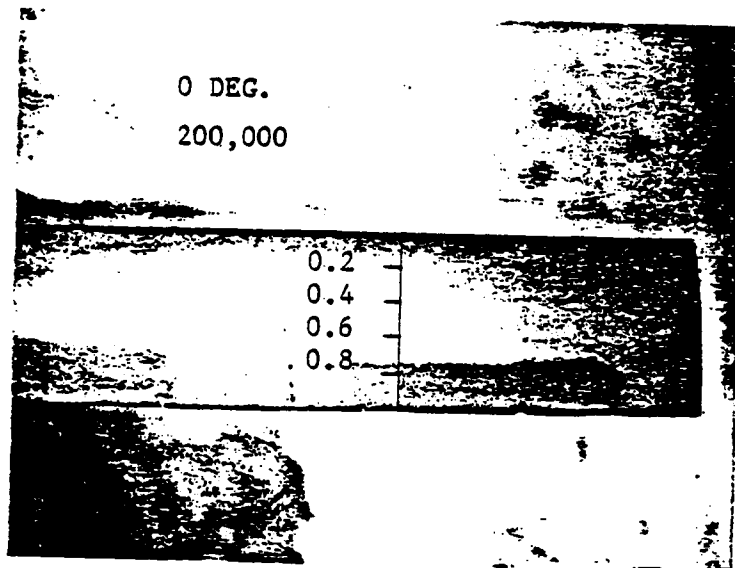


Fig. 4.13 : COMPARISON OF FLOW VISUALIZATION AND PRESSURE DISTRIBUTION PLOTS FOR  $RE=200,000$  ANGLE OF ATTACK = 0 DEG.

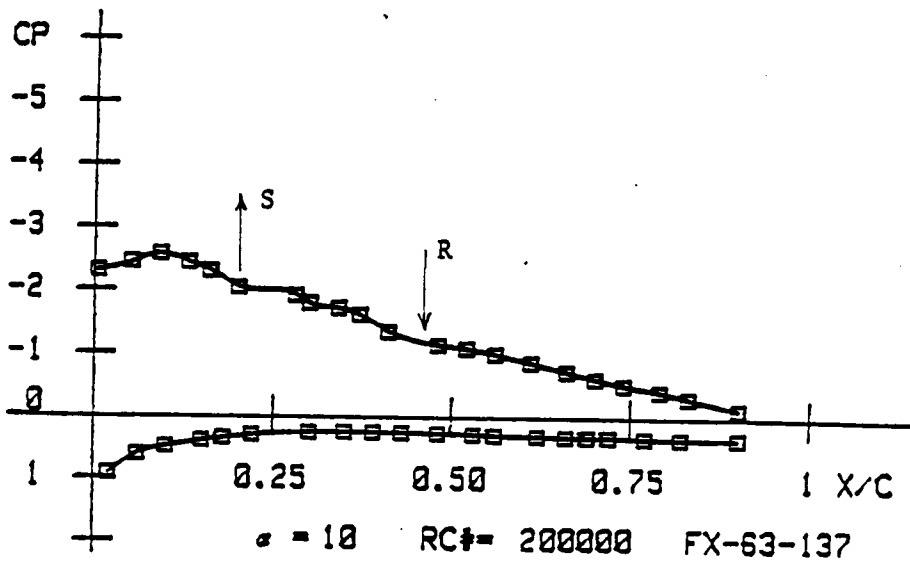
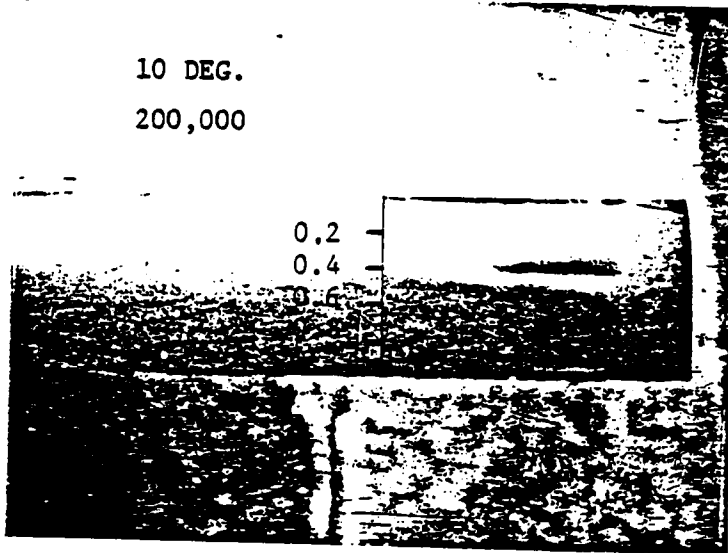


Fig. 4.14 : COMPARISON OF FLOW VISUALIZATION AND PRESSURE DISTRIBUTION PLOTS FOR  $Re = 200,000$ .  
ANGLE OF ATTACK = 10 DEG.

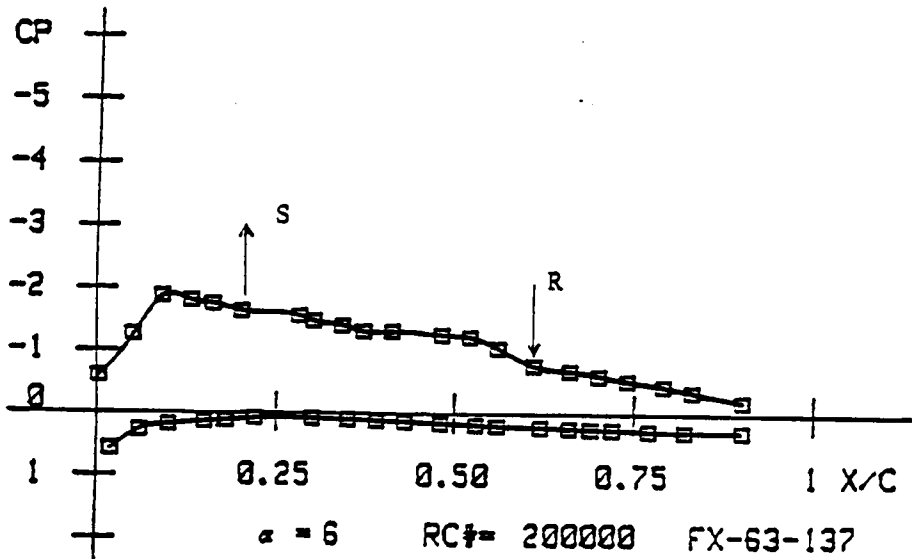
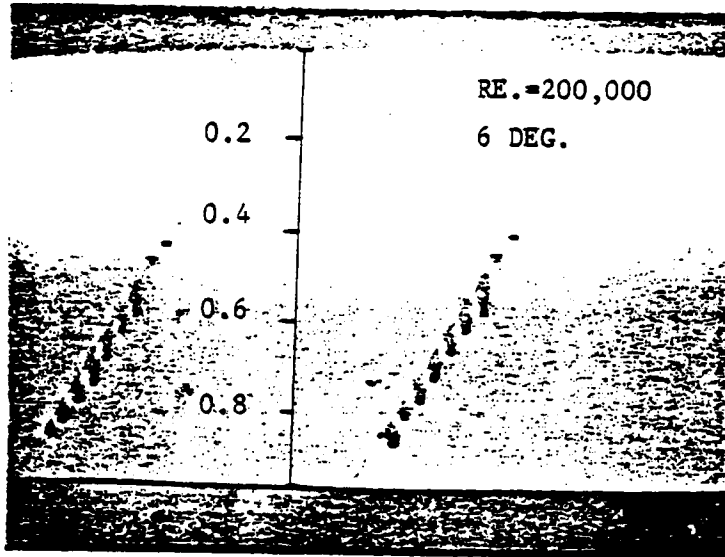


Fig. 4.15 : OIL DROP FLOW VISUALIZATION TECHNIQUE AT AN ANGLE OF ATTACK OF 6 DEGREES AND RE. = 200,000

FX-63-137-ESM

- $\lambda R=4$
- △  $\lambda R=6$
- ◇  $\lambda R=8$
- ▽  $\lambda R=10$

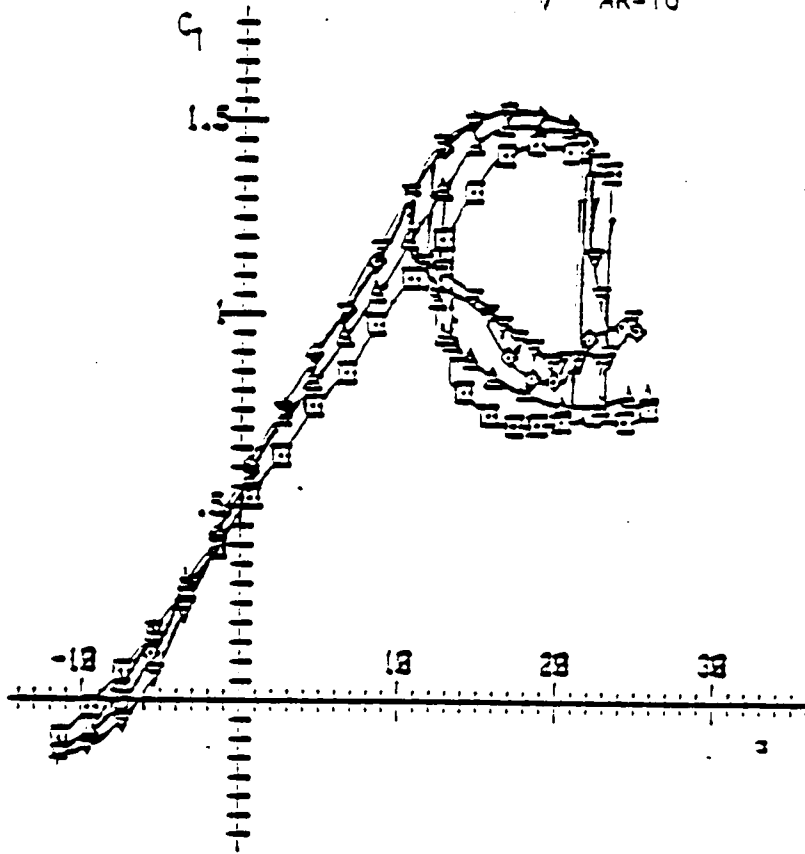


Fig. 4.16 : ASPECT RATIO EFFECTS FOR THE FX-63-137-ESM AIRFOIL AT RE. = 200,000

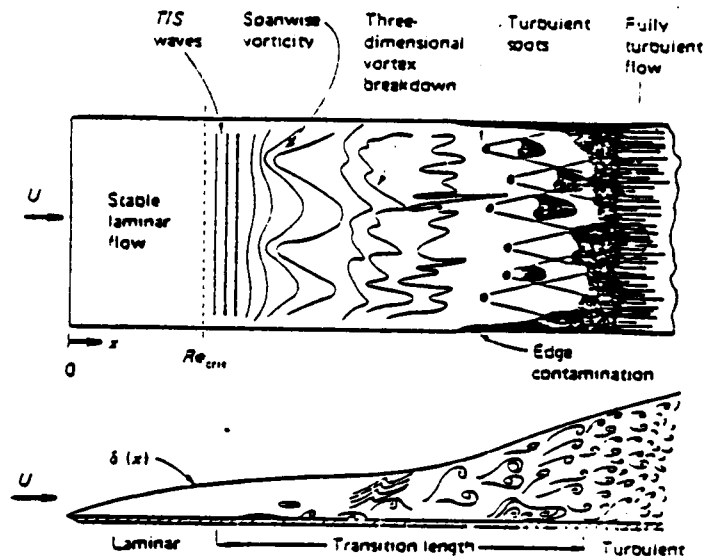


Fig. 5.1 : IDEALIZED SKETCH OF THE TRANSITION PROCESS ON A FLAT PLATE FROM REF. (8).

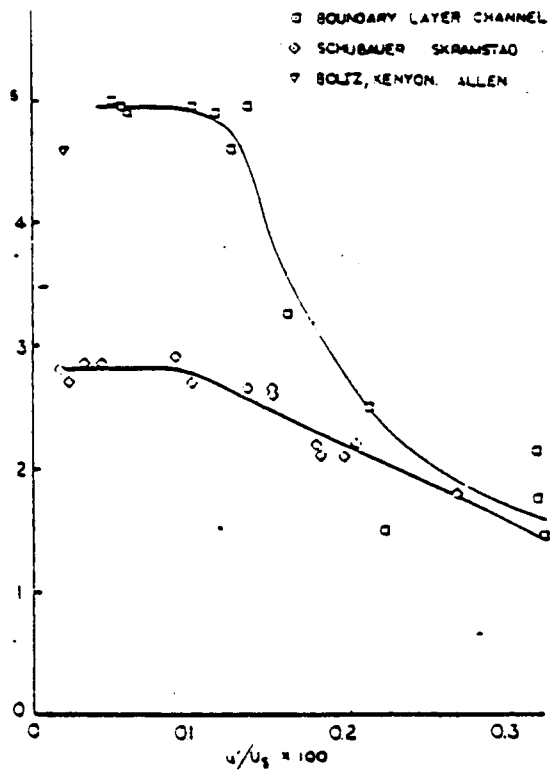
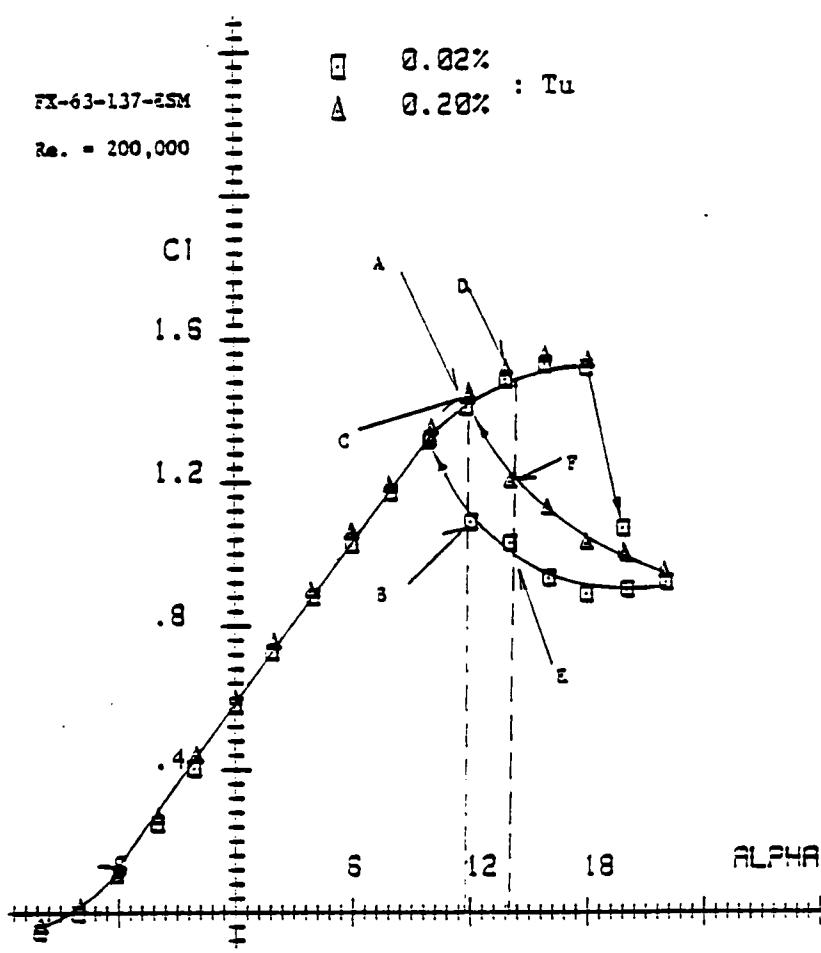


Fig. 5.2 : COMPARISON OF DATA FOR THE EFFECT OF FREE-STREAM TURBULENCE ON BOUNDARY LAYER TRANSITION ON A FLAT PLATE FROM REF. (32)



TURBULENCE EFFECT AR=8

Fig. 5.3 : EFFECT OF INCREASED FREE STREAM TURBULENCE FOR AR = 8 WING AT RE. = 200,000.

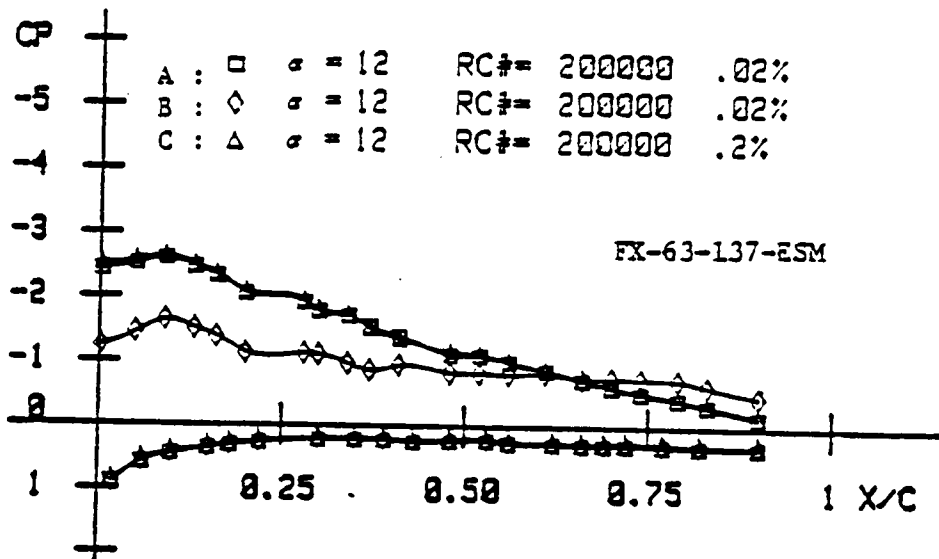


Fig. 5.4 : EFFECT OF INCREASED FREE-STREAM TURBULENCE AT  
 $\alpha = 12$  DEGREES AND  $Re. = 200,000$

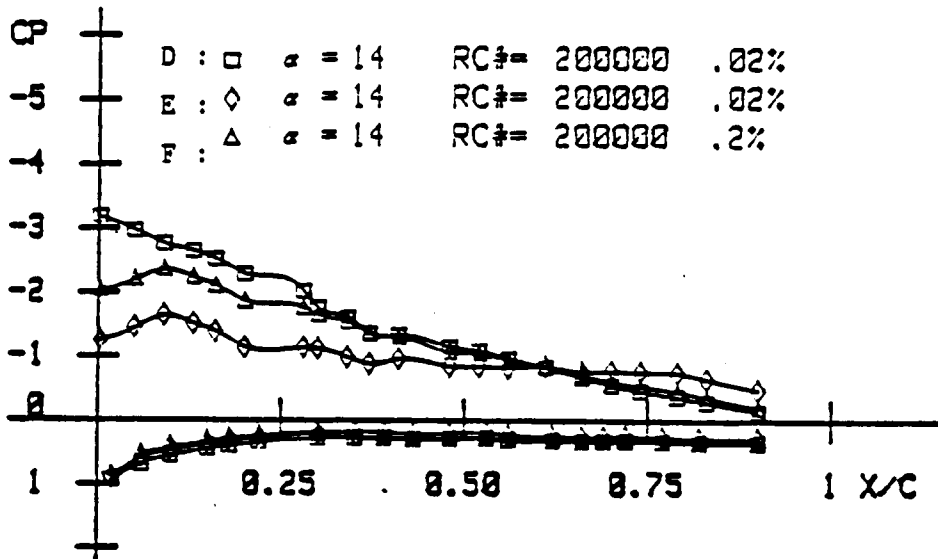


Fig. 5.5 : EFFECT OF INCREASED FREE-STREAM TURBULENCE  
 AT  $\alpha = 14$  DEGREES AND  $Re. = 200,000$

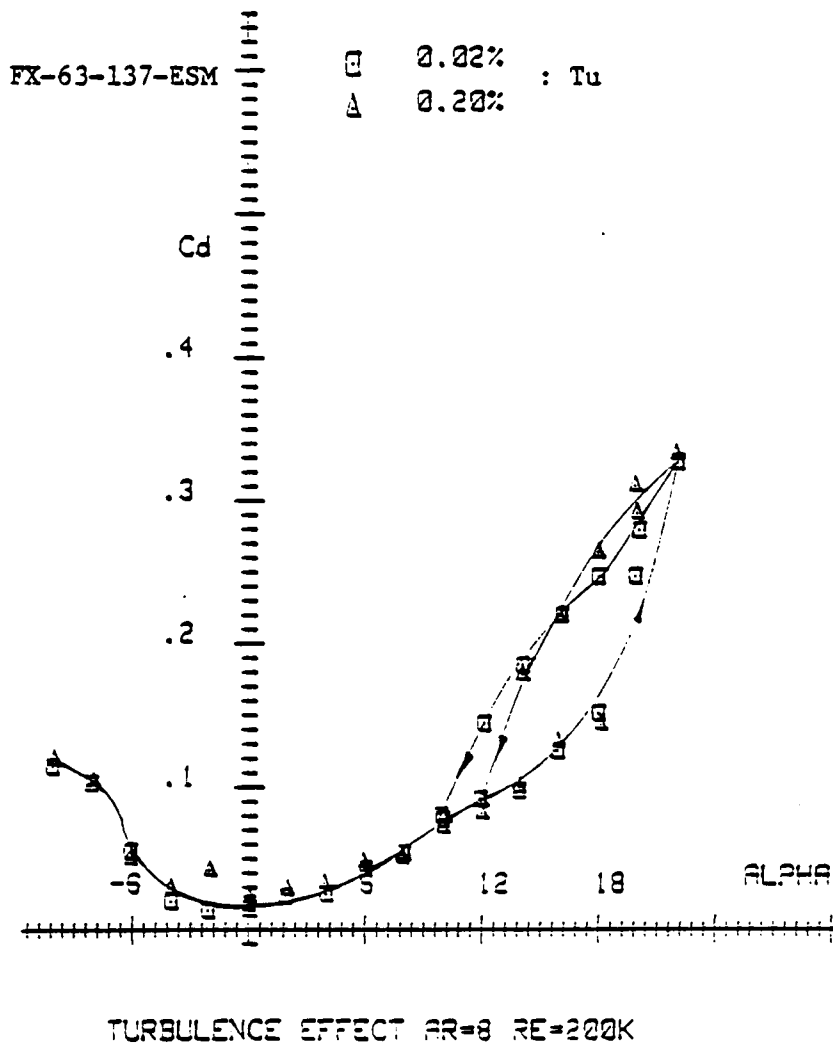
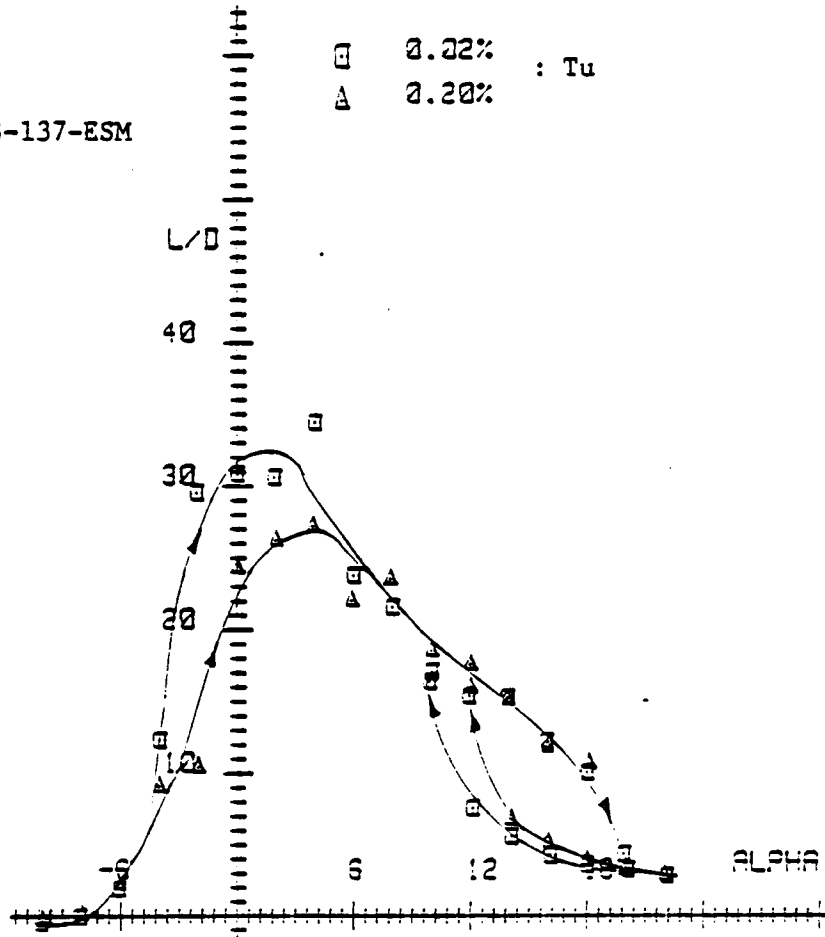


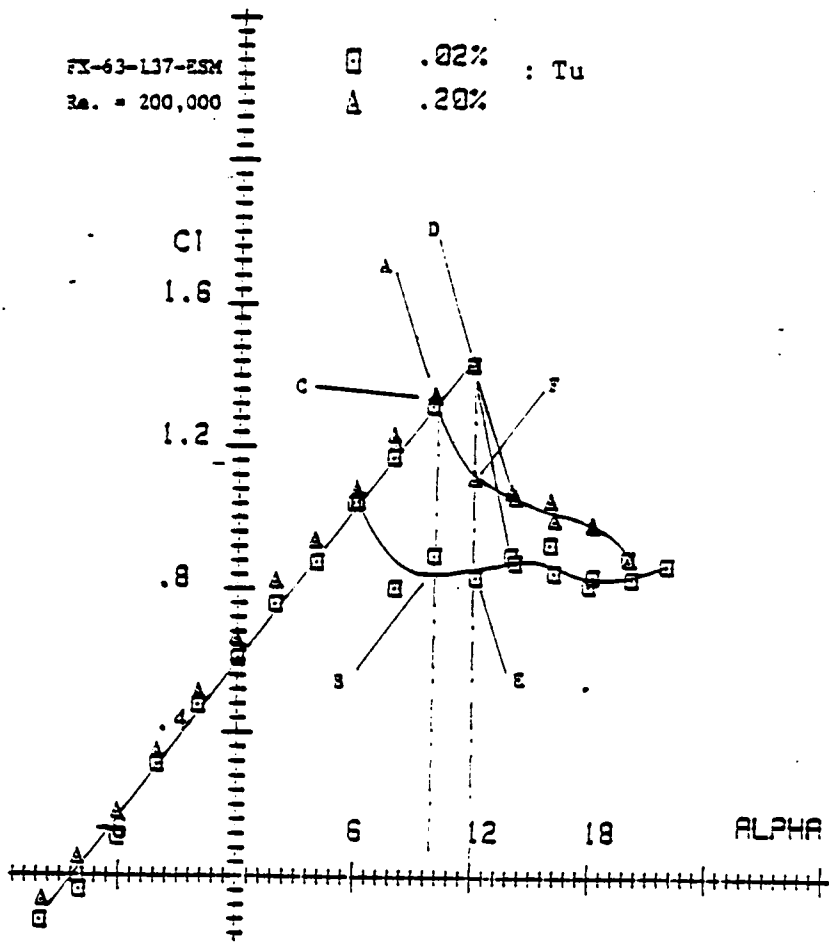
Fig. 5.6 : DRAG DATA SHOWING THE EFFECT OF INCREASED FREE  
 STREAM TURBULENCE FOR AR = 8 WING AT  
 RE. = 200,000

FX-63-137-ESM



TURBULENCE EFFECT AR=8 RE=200K

Fig. 5.7 : EFFECT OF INCREASED FREE STREAM TURBULENCE ON THE LIFT/DRAG RATIO FOR THE AR = 8 WING AT RE. = 200,000



TURBULENCE EFFECT AR=8

Fig. 5.8 : EFFECT OF INCREASED FREE STREAM TURBULENCE ON LIFT DATA FOR THE AR = 8 WING AT RE. = 100,000

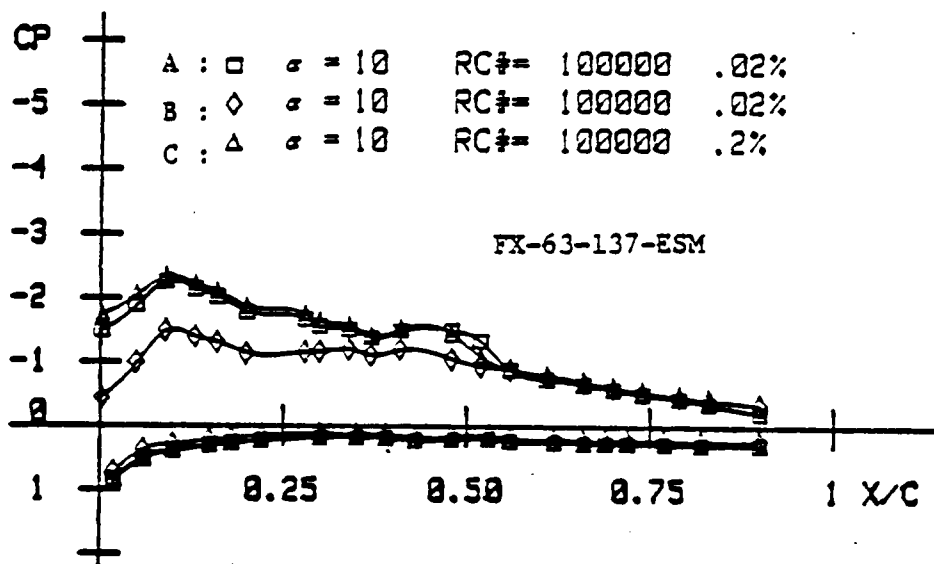


Fig. 5.9 ; EFFECT OF INCREASED FREE-STREAM TURBULENCE ON THE LOWER PORTION OF THE HYSTERESIS LOOP.  
 RE. = 100,000  $\alpha$  = 10 DEGREES.

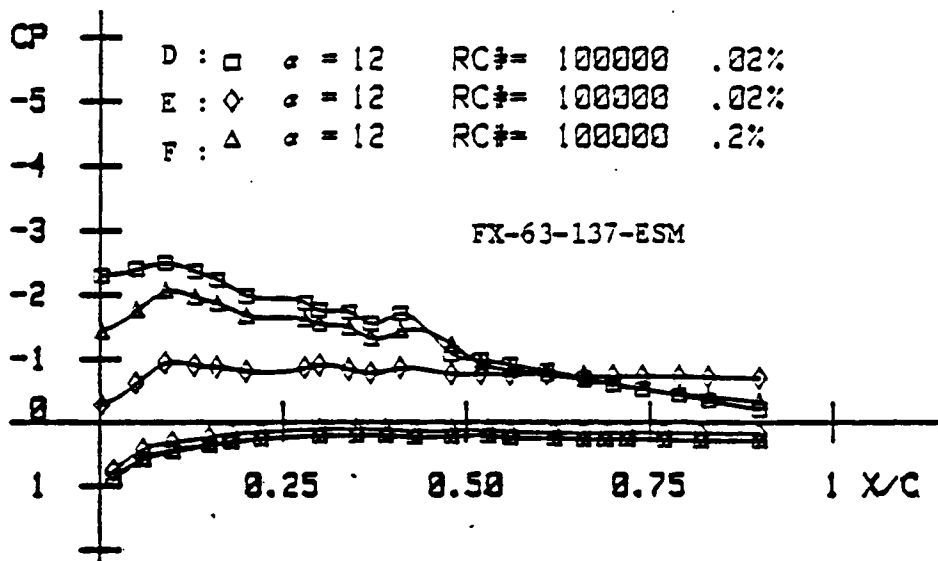
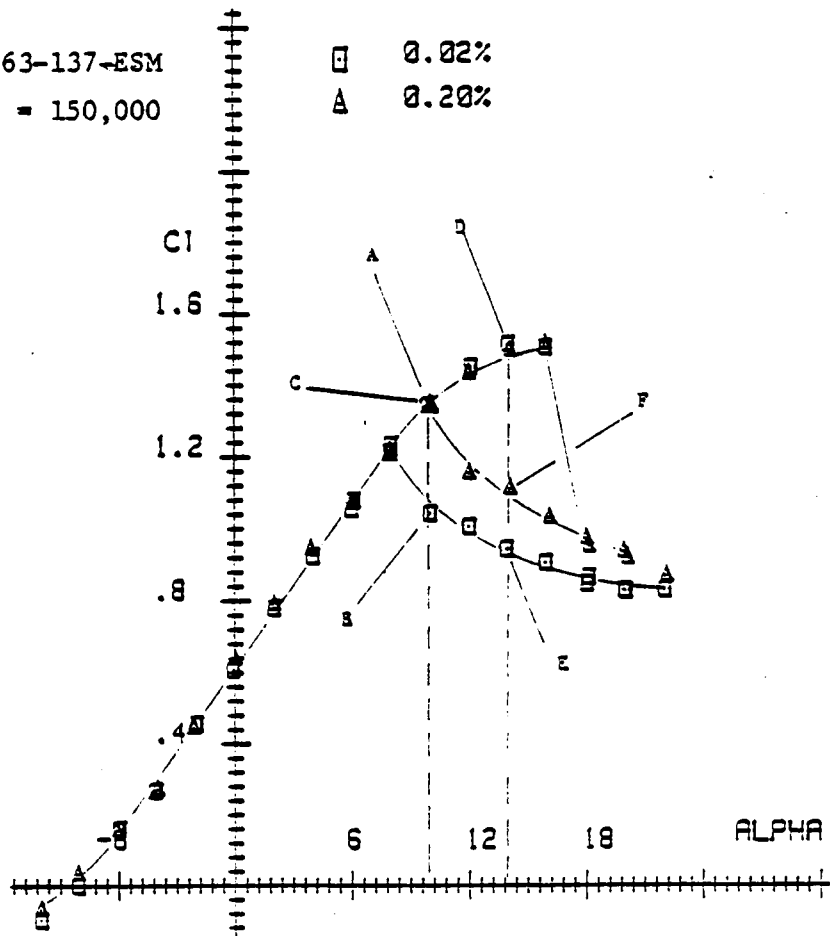


Fig. 5.10 : EFFECT OF INCREASED FREE-STREAM TURBULENCE ON THE LOWER PORTION OF THE HYSTERESIS LOOP.

RE. = 100,000  $\alpha = 12$  DEGREES

FX-63-137-ESM  
 RE. = 150,000

□ 0.02%  
 △ 0.20%



TURBULENCE EFFECT AR=8

Fig. 5.11 : EFFECT OF INCREASED FREE STREAM TURBULENCE ON LIFT  
 DATA FOR THE AR = 8 WING AT RE. = 150,000

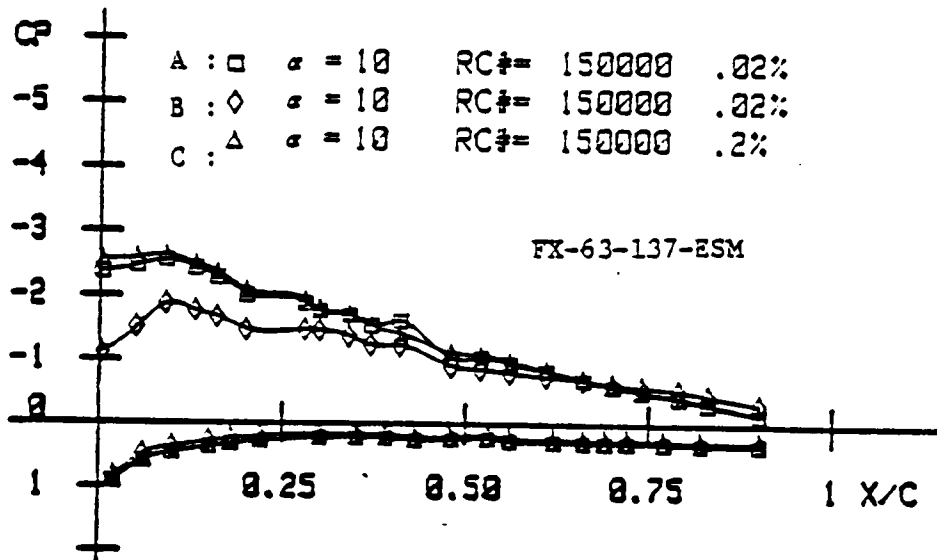


Fig. 5.12 : EFFECT OF INCREASED FREE-STREAM TURBULENCE ON THE  
 LOWER PORTION OF THE HYSTERESIS LOOP  
 $RE. = 150,000$   $\alpha = 10$  DEGREES

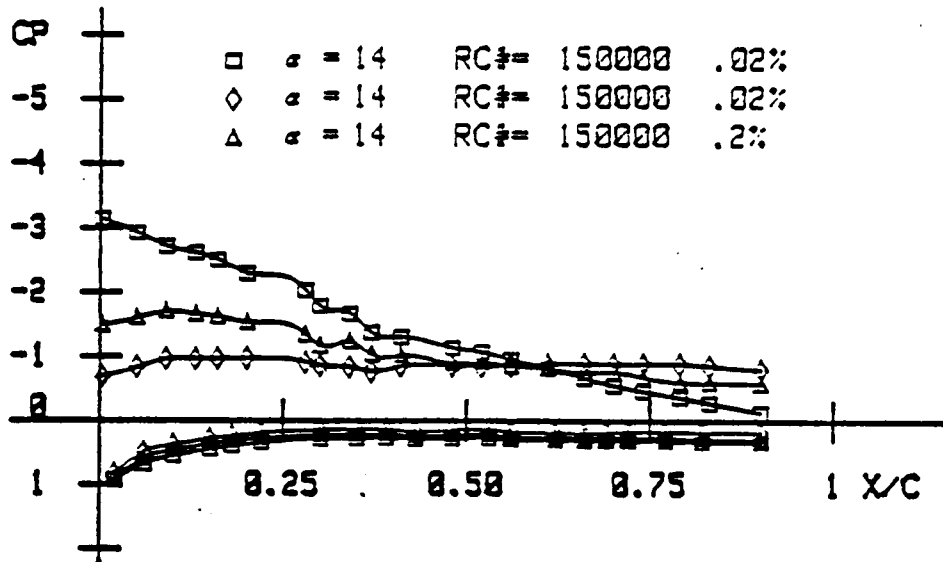


Fig. 5.13 : EFFECT OF INCREASED FREE-STREAM TURBULENCE ON THE LOWER PORTION OF THE HYSTERESIS LOOP.  
 RE. = 150,000       $\alpha$  = 14 DEGREES.

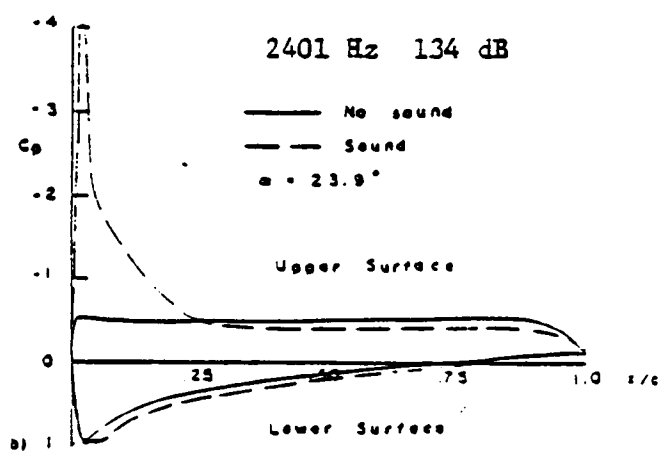
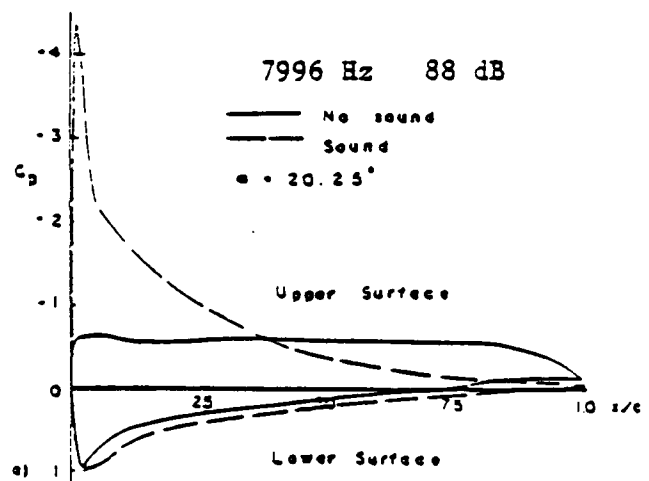


Fig. 5.14 : PRESSURE DISTRIBUTIONS AROUND THE NACA 2412 AIRFOIL SECTION WITH AND WITHOUT SOUND. FROM REF. (35).

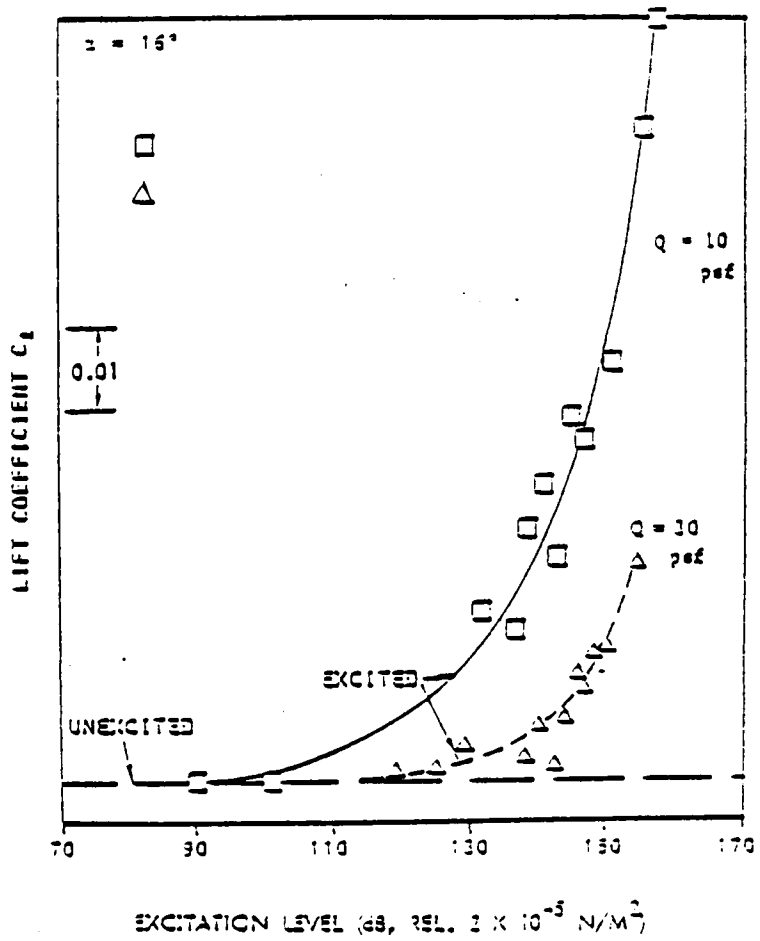


Fig. 5.15 : INCREMENT IN THE LIFT COEFFICIENT WITH THE EXCITATION LEVEL OF THE ACOUSTIC DISTURBANCE. FROM REFERENCE (36)

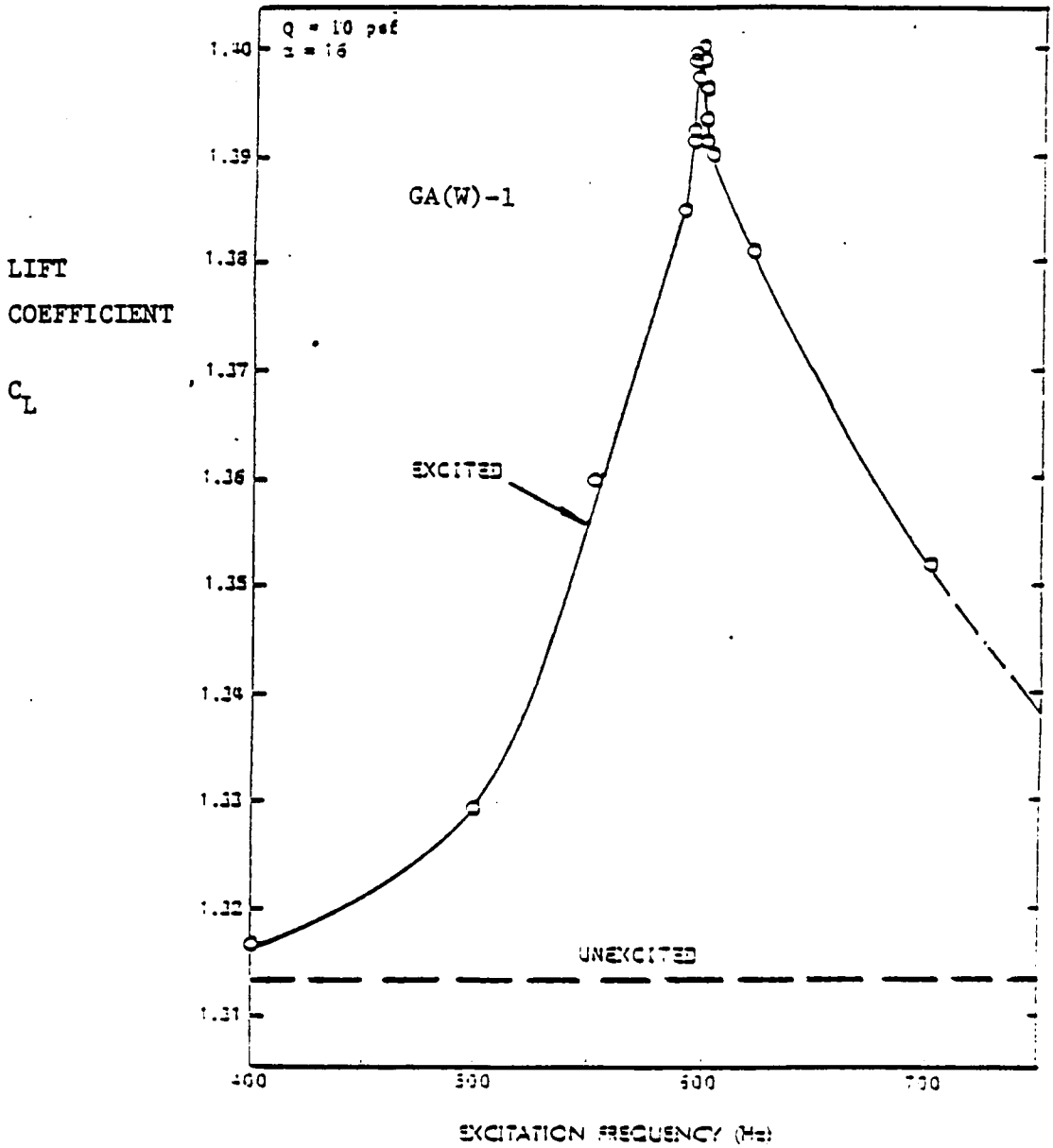


FIG. 5.16 : INCREMENT IN LIFT COEFFICIENT WITH EXCITATION  
 FREQUENCY AT CONSTANT DRIVER VOLTAGE.  
 FROM REFERENCE (36).

SPEAKER FREQUENCY RESPONSE PWR = 1.0 W

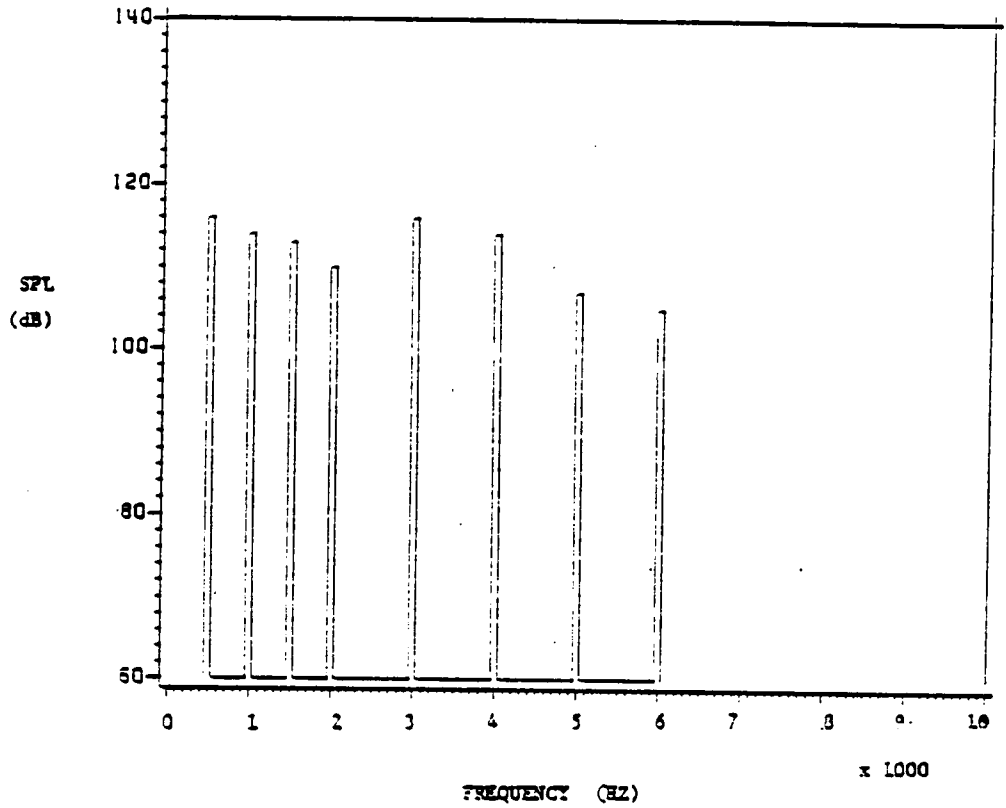


Fig. 5.17 : SPEAKER OUTPUT FOR A CONSTANT AMPLIFIER OUTPUT OF 1.0 W AT VARIOUS FREQUENCIES.

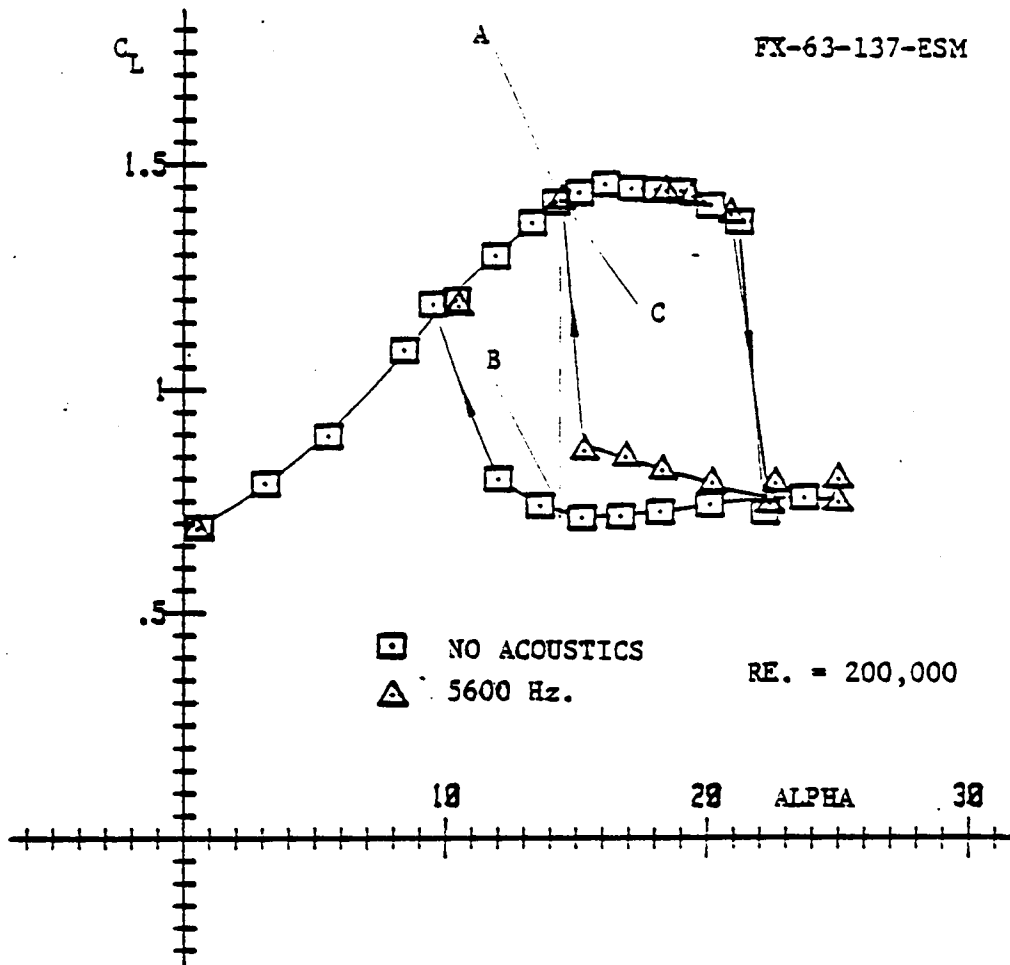


Fig. 5.18 : LIFT DATA FOR EFFECT OF ACOUSTIC DISTURBANCES

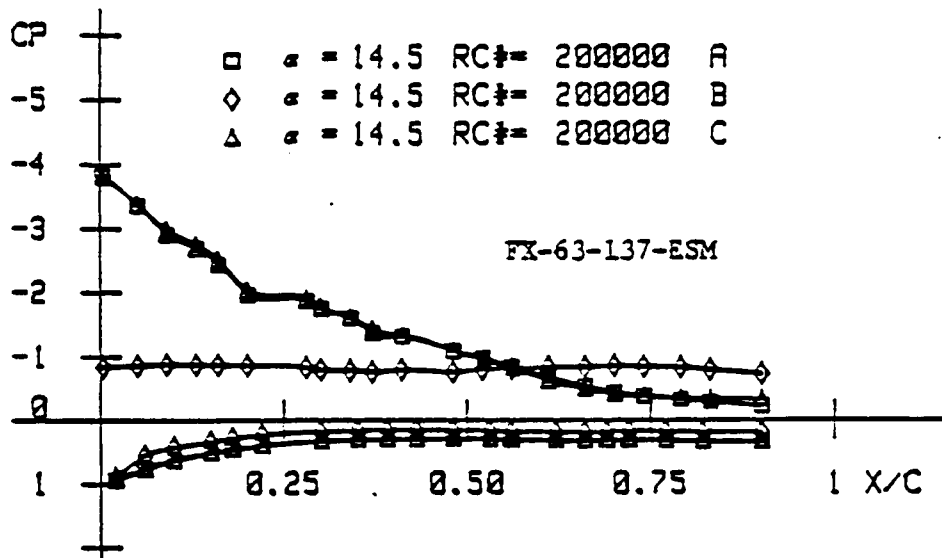


Fig. 5.19 : EFFECT OF ACOUSTIC DISTURBANCES ON THE PRESSURE DATA FOR  $RE. = 200,000$   
 FREQUENCY = 5600 Hz      POWER LEVEL = 0.5 W

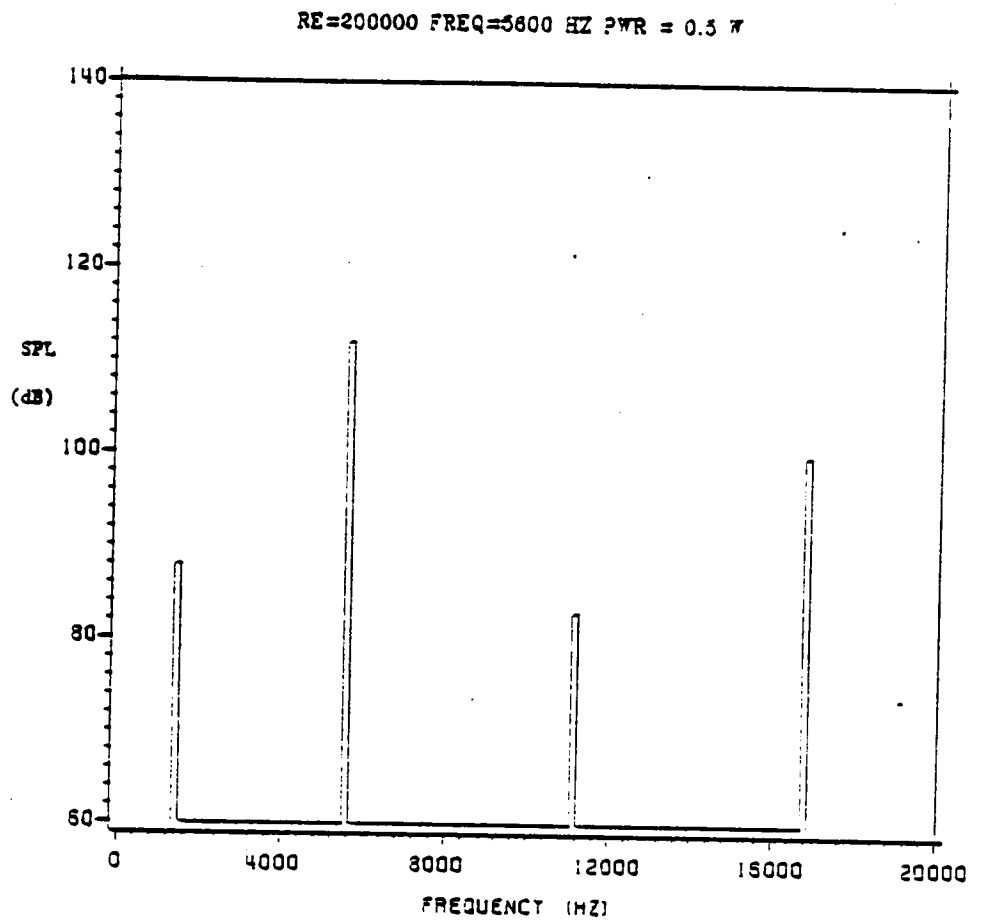


Fig. 5.20 : SPECTRUM OF THE DOMINANT FREQUENCIES FOR A DIALED FREQUENCY OF 5600 HZ AND AN AMPLIFIER OUTPUT OF 0.5 W.

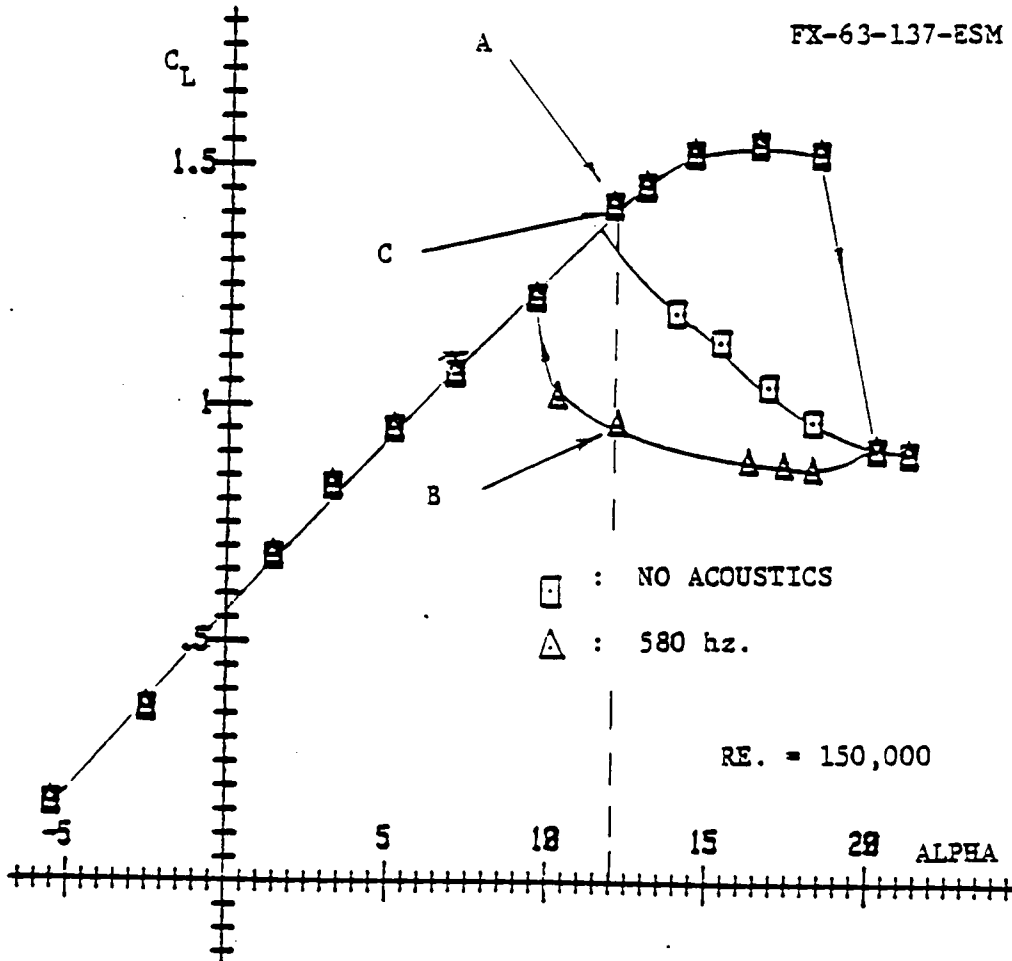


Fig. 5.21 : EFFECT OF ACOUSTIC DISTURBANCES ON THE LIFT DATA AT  
 RE. = 150,000.

FREQUENCY = 580 Hz.

POWER LEVEL = 0.5 W

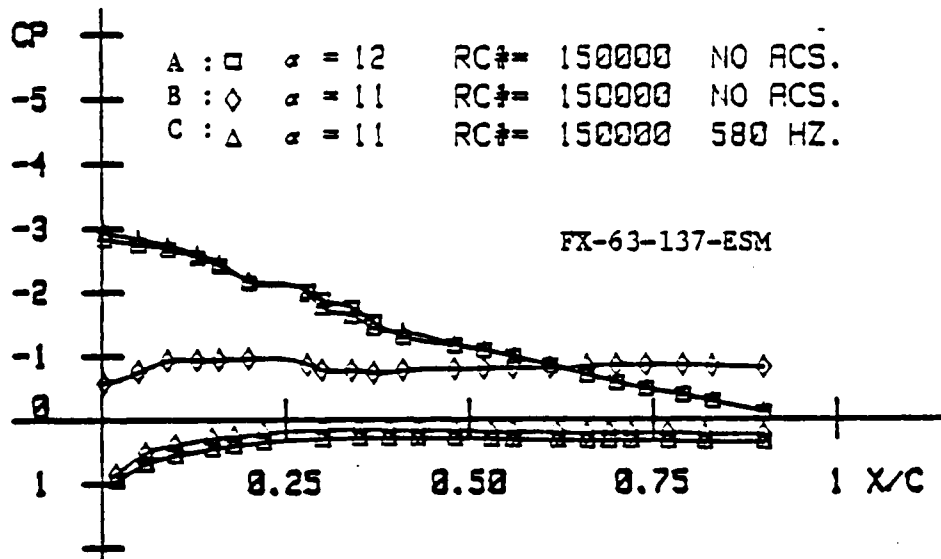


Fig. 5.22 : EFFECT OF ACOUSTIC DISTURBANCES ON THE PRESSURE DATA AT RE. = 150,000.  
 FREQUENCY = 580 Hz. POWER LEVEL = 0.5 W

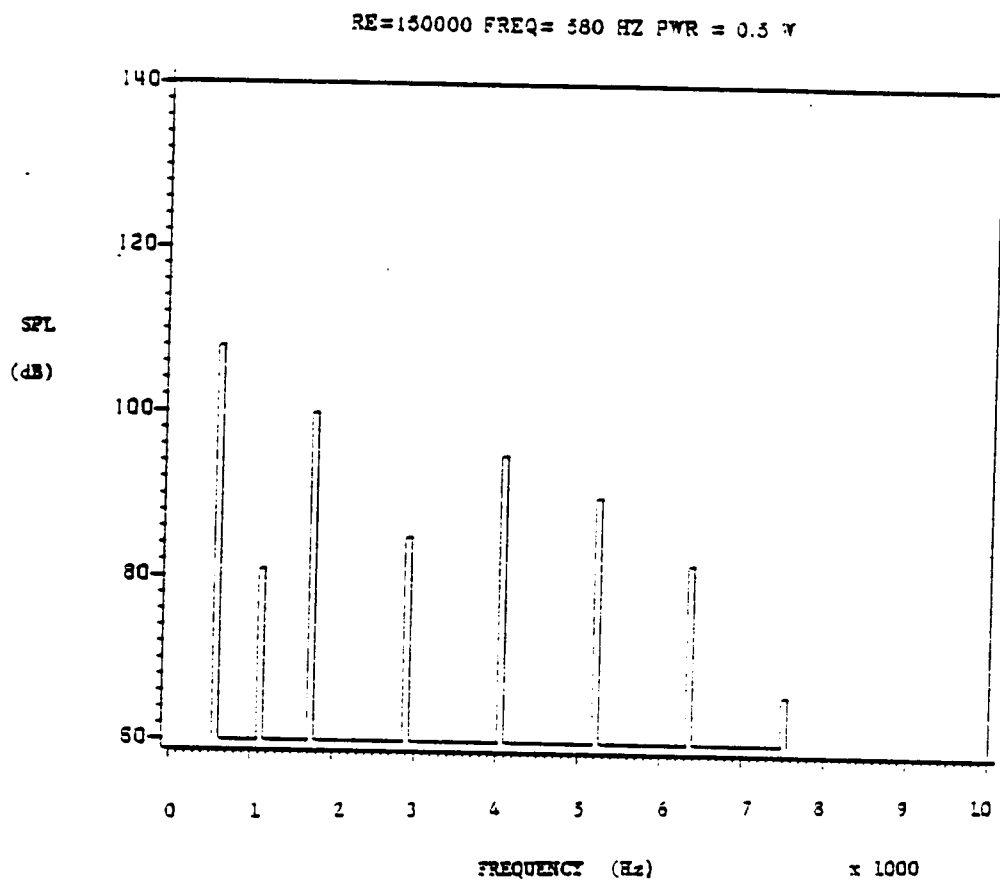


Fig. 5.23 : SPECTRUM OF THE DOMINANT FREQUENCIES FOR A DIALED FREQUENCY OF 580 HZ AND AN AMPLIFIER OUTPUT OF 0.5 W.

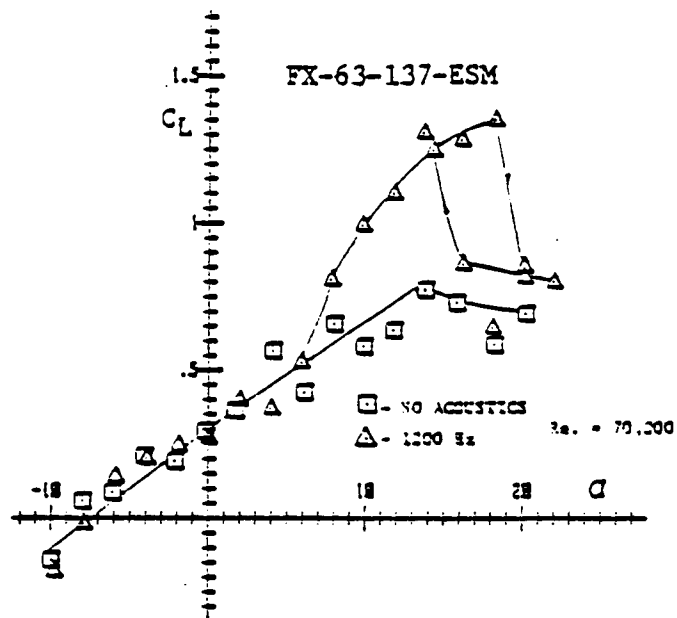


Fig. 5.24 : ALTERATION IN THE STALLING BEHAVIOR WITH ACOUSTIC DISTURBANCES AT  $Re. = 70,000$   
 FREQUENCY = 1200 Hz POWER LEVEL = 0.5W

RE-70000 FREQ=1200 HZ PWR = 0.5 W

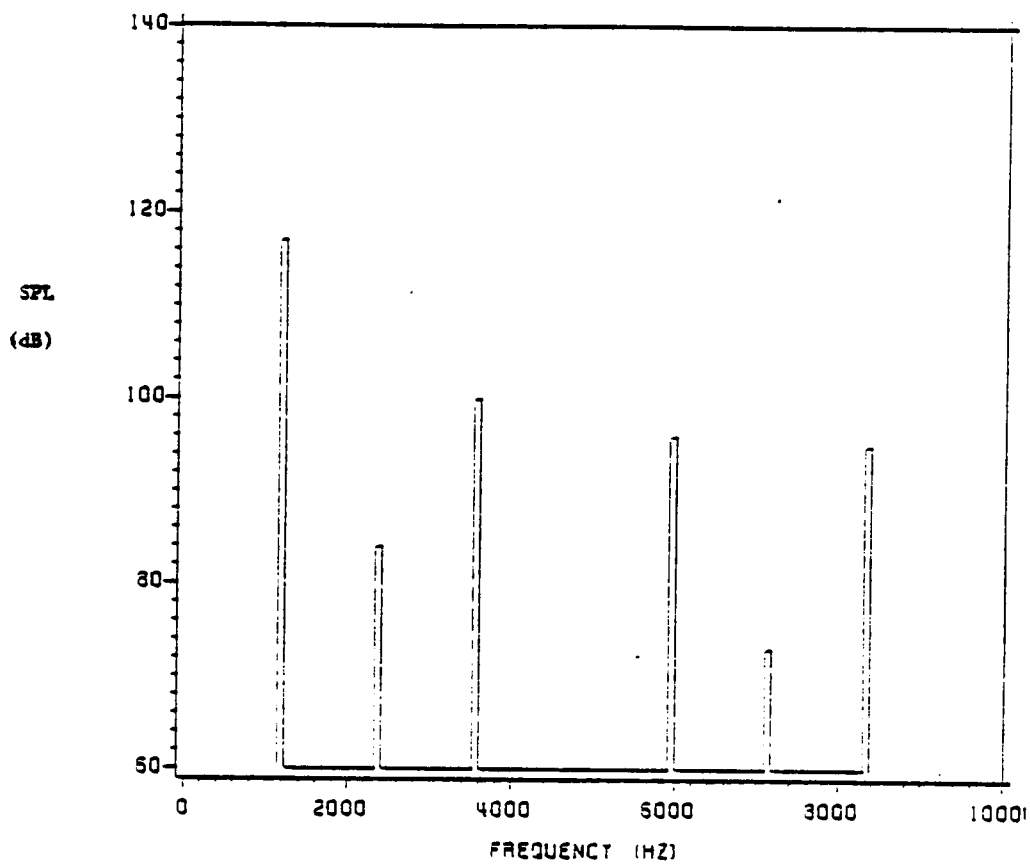


Fig. 5.25 : SPECTRUM OF THE DOMINANT FREQUENCIES FOR A DIALED FREQUENCY OF 1200 HZ AND AN AMPLIFIER OUTPUT OF 0.5 W.

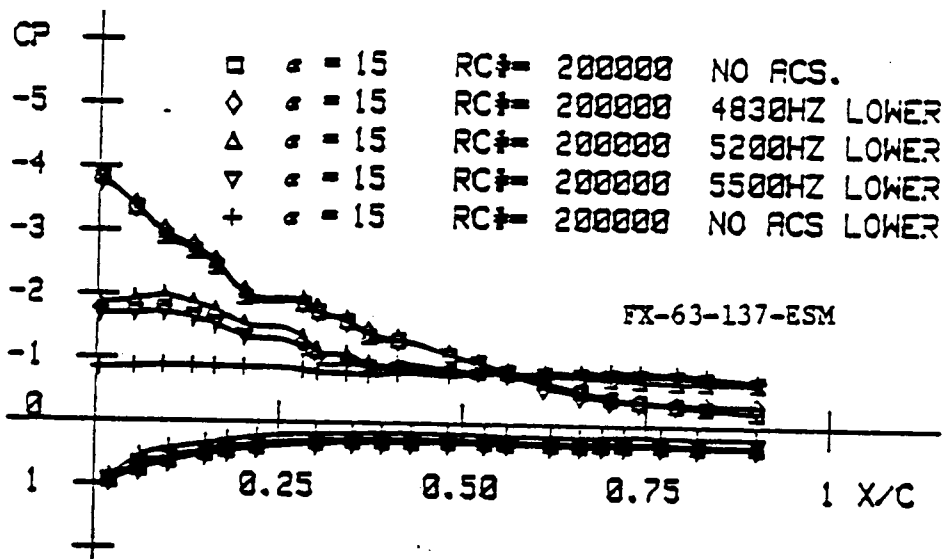
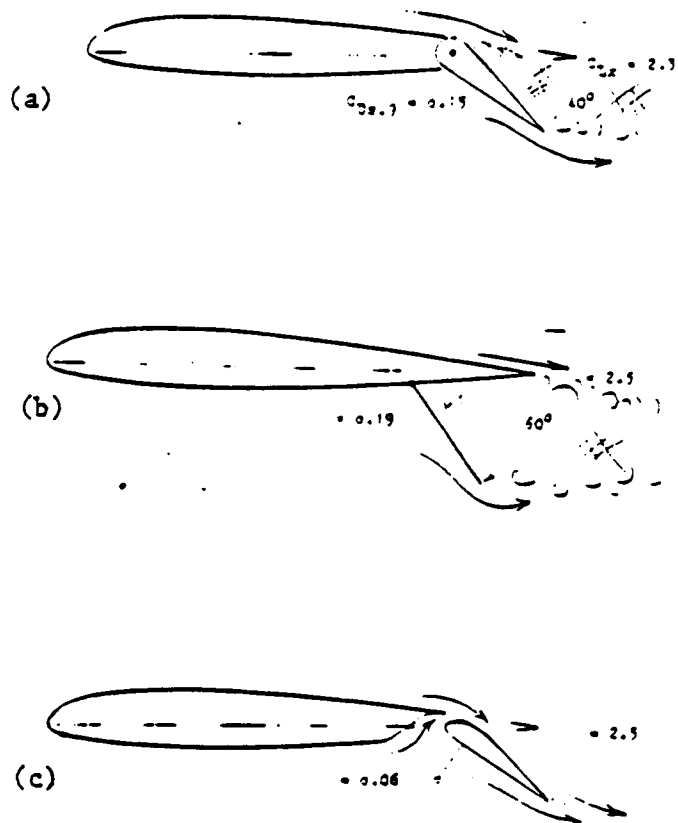


Fig. 5.26 : EFFECT OF ACOUSTIC FREQUENCIES WITH PARTIAL AND FULL EFFECT AT RE. = 200,000. AND CONSTANT POWER LEVEL OF 0.5 W



- (a) : PLAIN FLAP
- (b) : SPLIT FLAP
- (c) : SLOTTED FLAP

Fig. 6.1 : PRINCIPAL TYPES OF TRAILING -EDGE FLAPS  
FROM REF. (41)

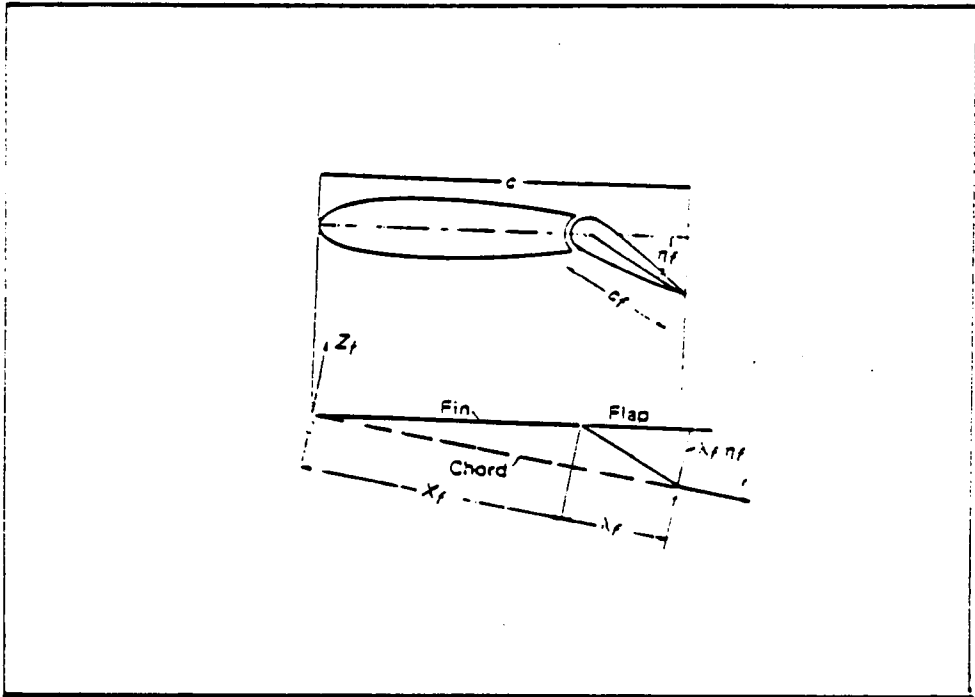


Fig. 6.2 : REPRESENTATION OF A PLAIN FLAP IN THIN-AIRFOIL THEORY.  
FROM REF. (39).

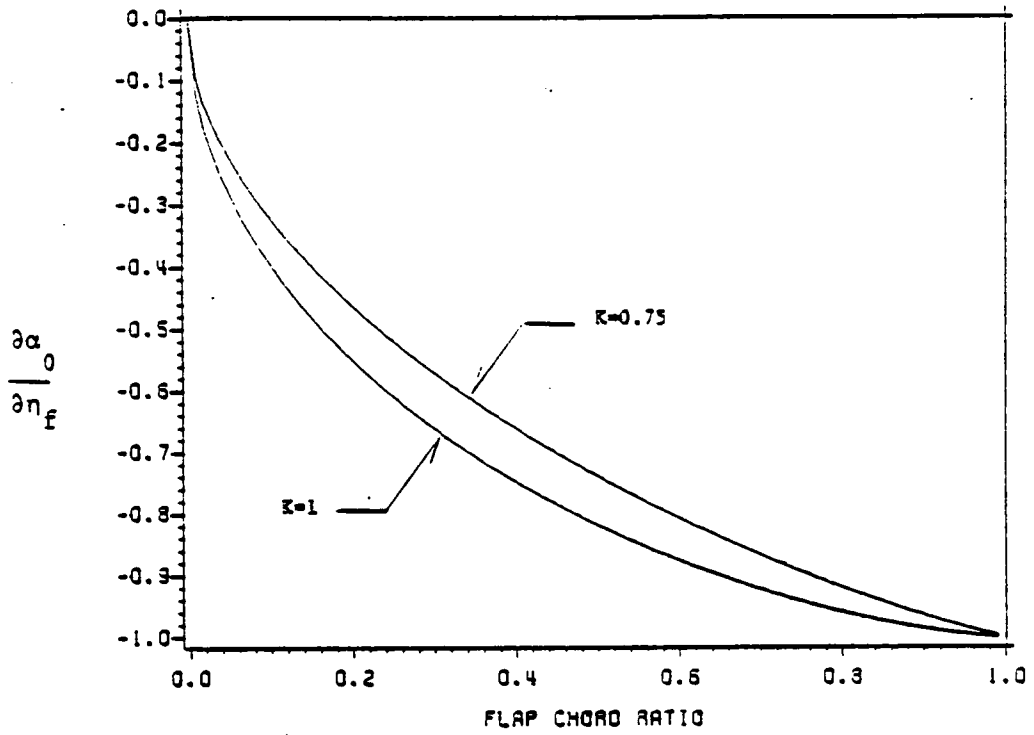


Fig. 6.3 : RATE OF CHANGE OF THE ZERO LIFT ANGLE OF ATTACK WITH FLAP DEFLECTION : RESULTS OF THIN AIRFOIL THEORY.

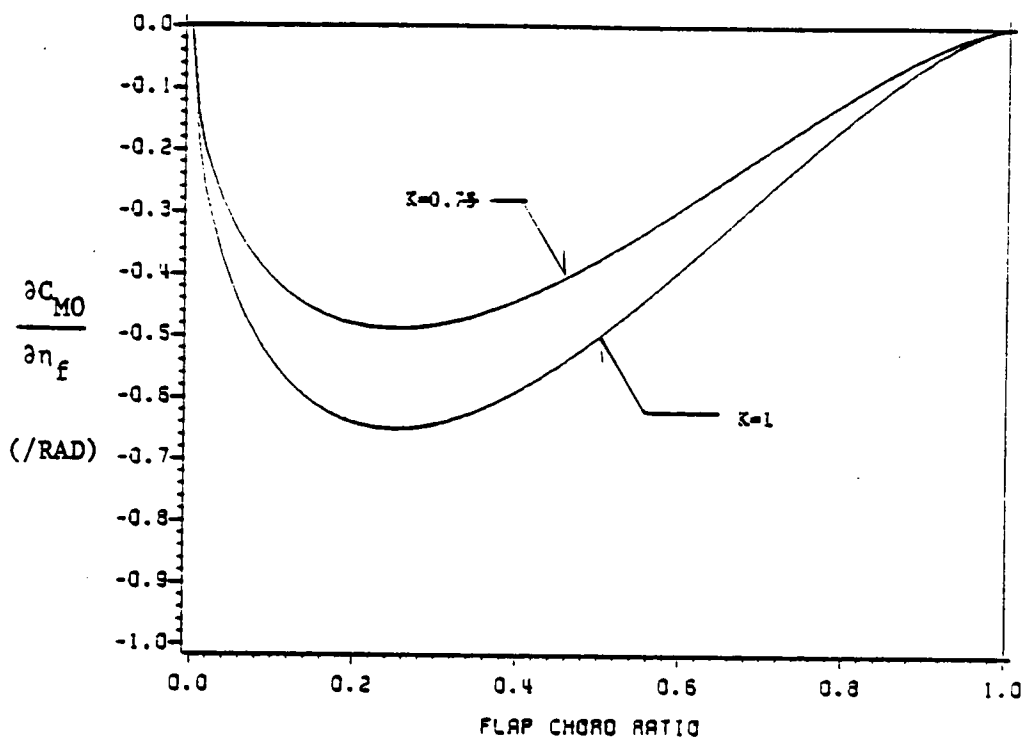


Fig. 6.4 : RATE OF CHANGE OF THE QUARTER CHORD PITCHING MOMENT WITH FLAP DEFLECTION : RESULTS OF THIN AIRFOIL THEORY.

HINGE-GAP  
SEALED

—	$\delta_f = 0^\circ$ Down	○
- - -	5°	△
· · ·	10°	□
- - -	15°	◇
- - -	30°	△
- - -	45°	△
- - -	50°	×
- - -	75°	▽
- - -	90°	▽

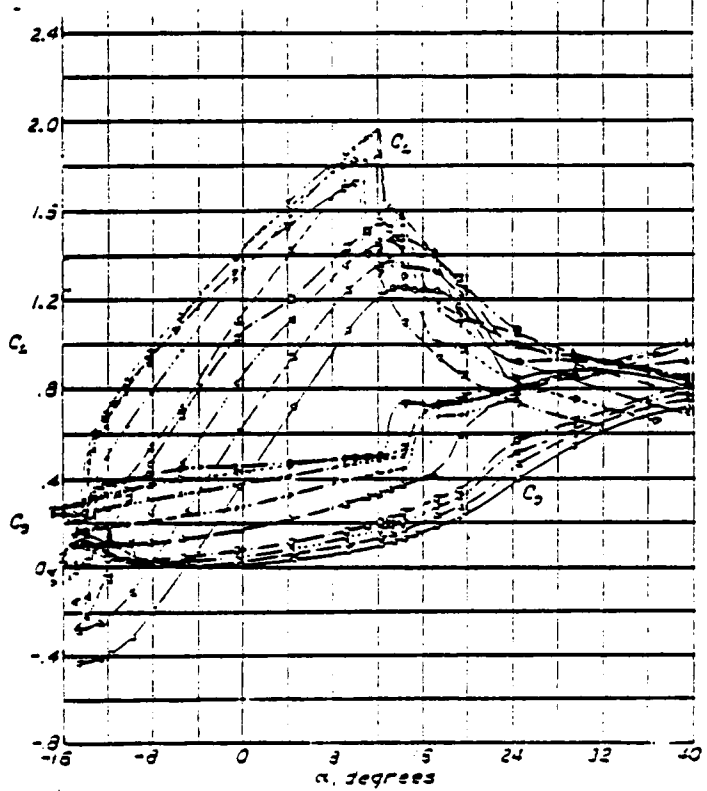
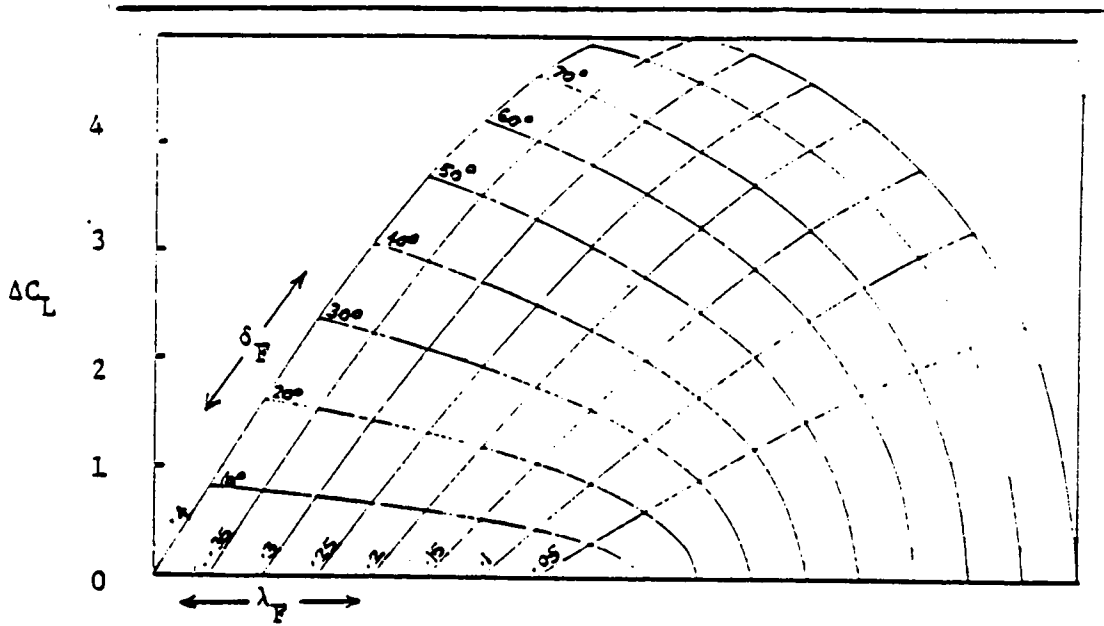
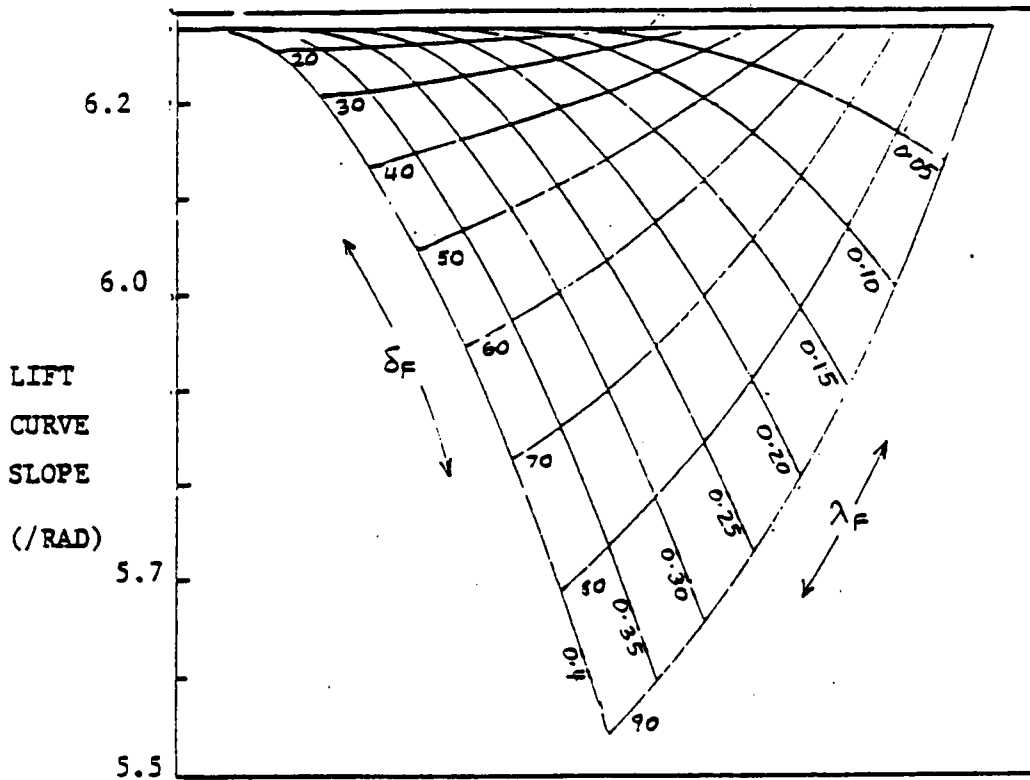


Fig. 6.5 : TYPICAL PERFORMANCE OF THE CLARK-Y AIRFOIL WITH A 0.3C FULL-SPAN FLAP AT  $Re = 600,000$  FROM REF. (38).



$\delta_F$  : FLAP DEFLECTION (deg.)       $\lambda_F$  : FLAP-CHORD RATIO

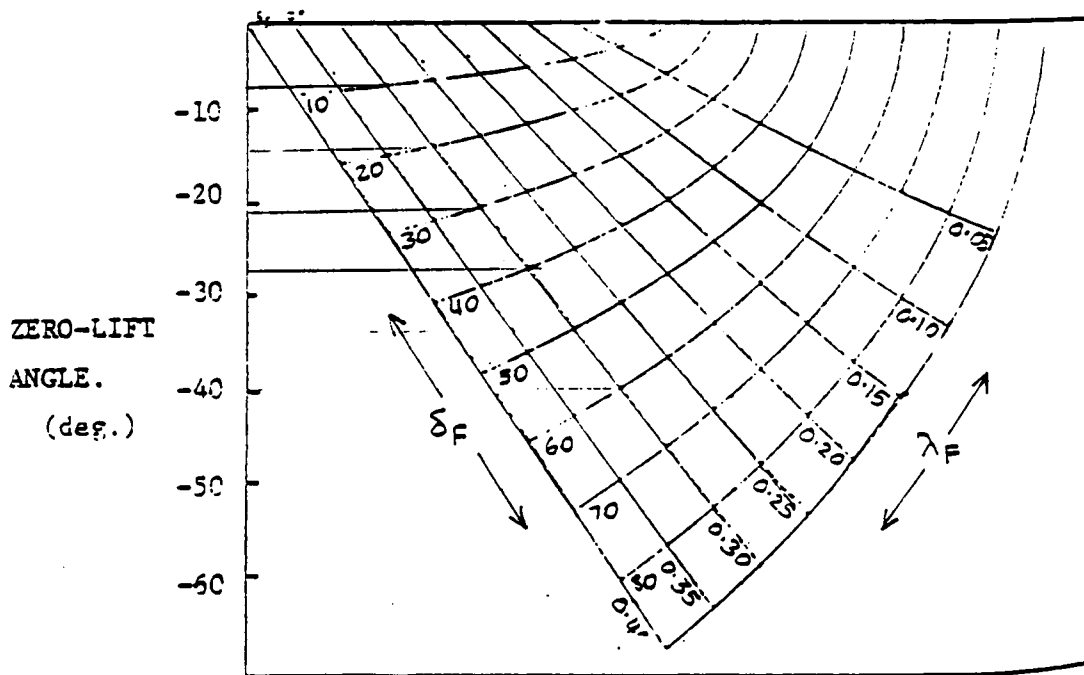
Fig. 6.6 : LIFT INCREMENT DUE TO FLAP DEFLECTIONS FOR VARIOUS FLAP-CHORD RATIOS FROM REF. (40).



$\delta_F$  : FLAP DEFLECTION (deg.)

$\lambda_F$  : FLAP-CHORD RATIO

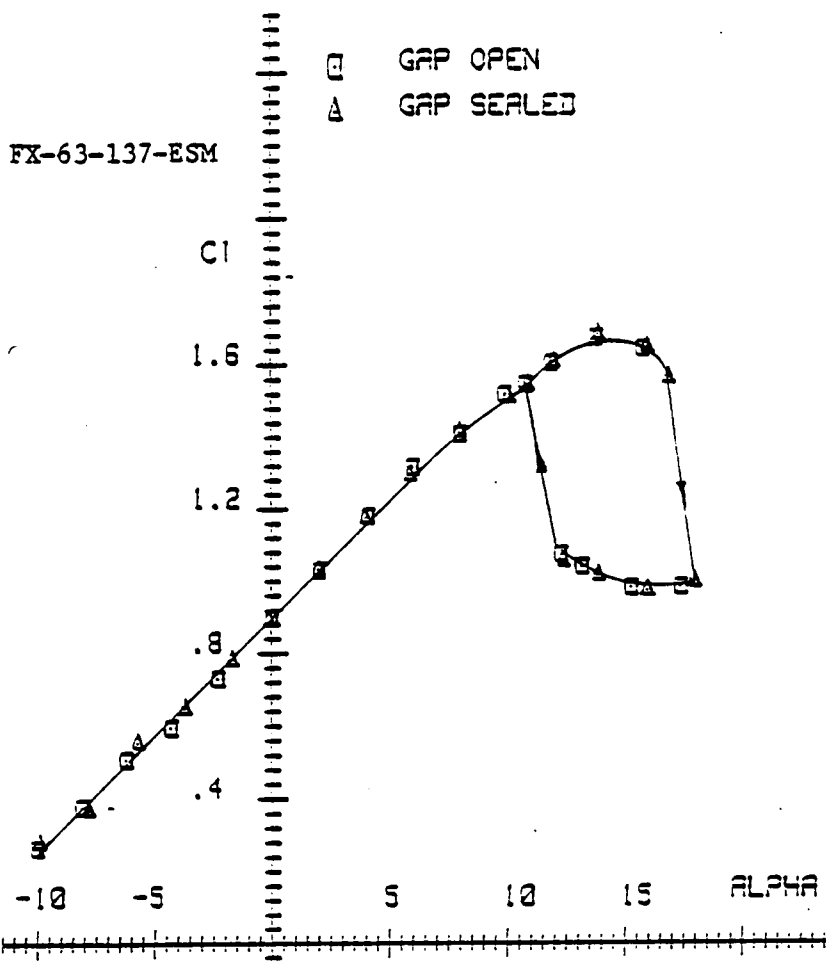
Fig. 6.7 : VARIATION IN LIFT CURVE SLOPE DUE TO FLAP DEFLECTION FOR VARIOUS FLAP-CHORD RATIOS FROM THE THEORY OF REF. (40).



$\delta_F$  : FLAP DEFLECTION (deg.)

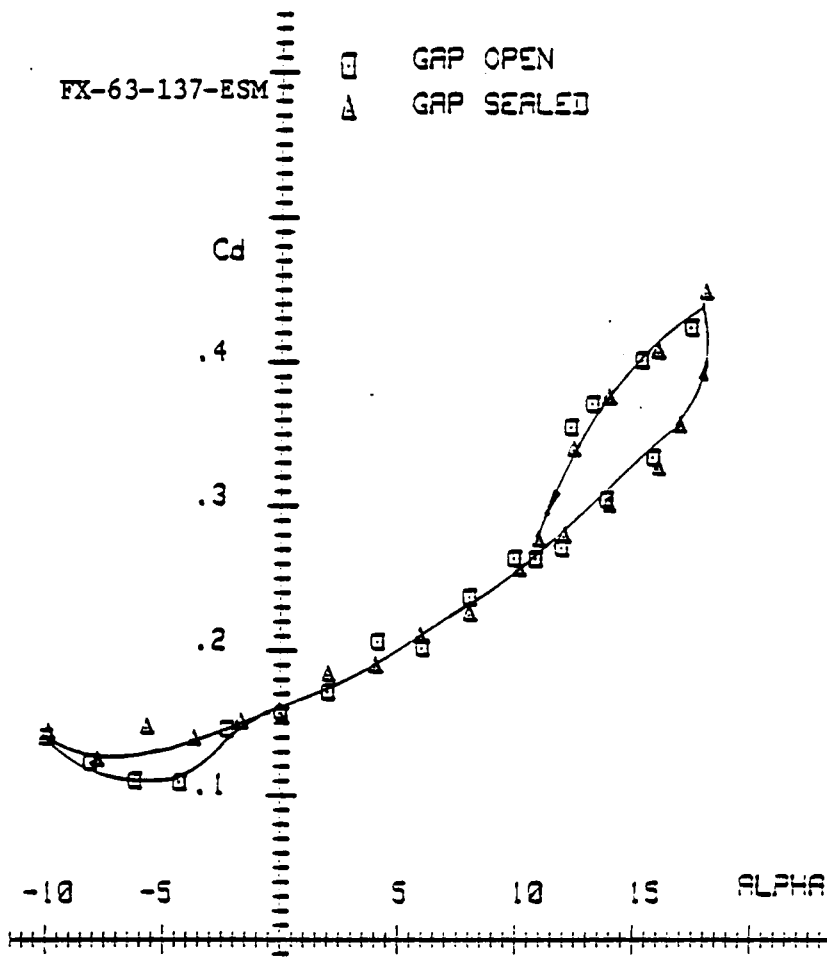
$\lambda_F$  : FLAP-CHORD RATIO

Fig. 6.8 : CHANGE IN ZERO-LIFT ANGLE DUE TO FLAP DEFLECTION FOR VARIOUS FLAP-CHORD RATIOS FROM THE THEORY OF REF. (40).



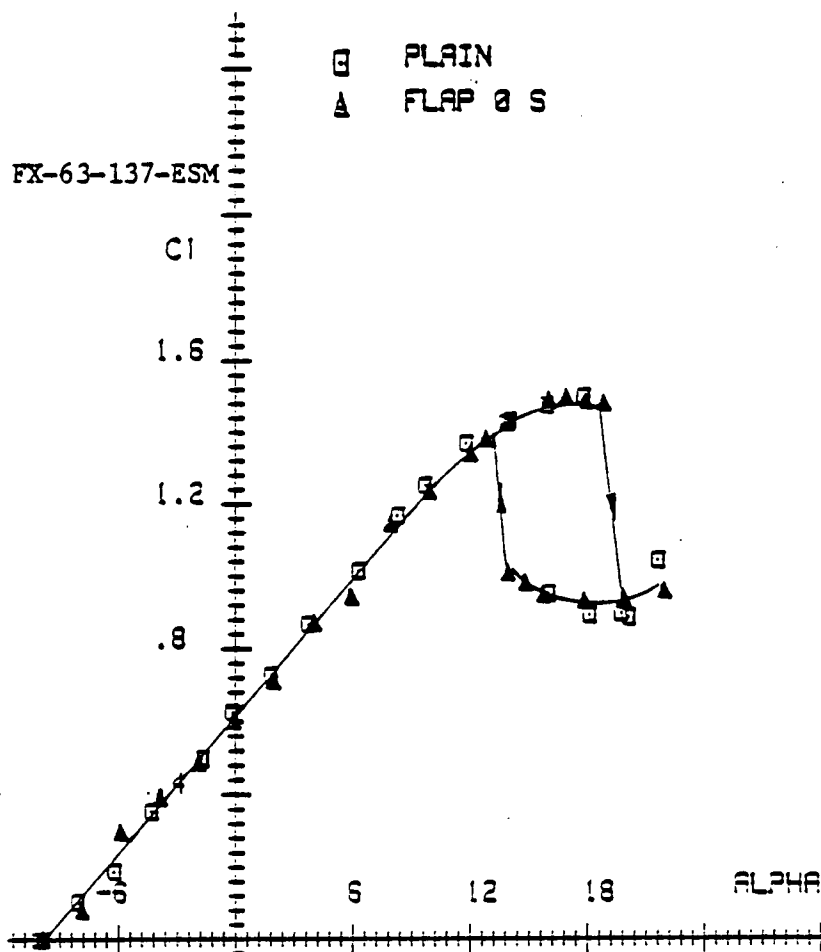
HINGE GAP EFFECT RE=200K AR=4

Fig. 6.9 : EFFECT OF THE HINGE GAP ON THE LIFT DATA FOR THE  
AR = 4 WING AT RE. = 200,000



HINGE GAP EFFECT RE=200K AR=4

Fig. 6.10 : EFFECT OF THE HINGE GAP ON THE DRAG DATA FOR THE  
AR = 4 WING AT RE. = 200,000

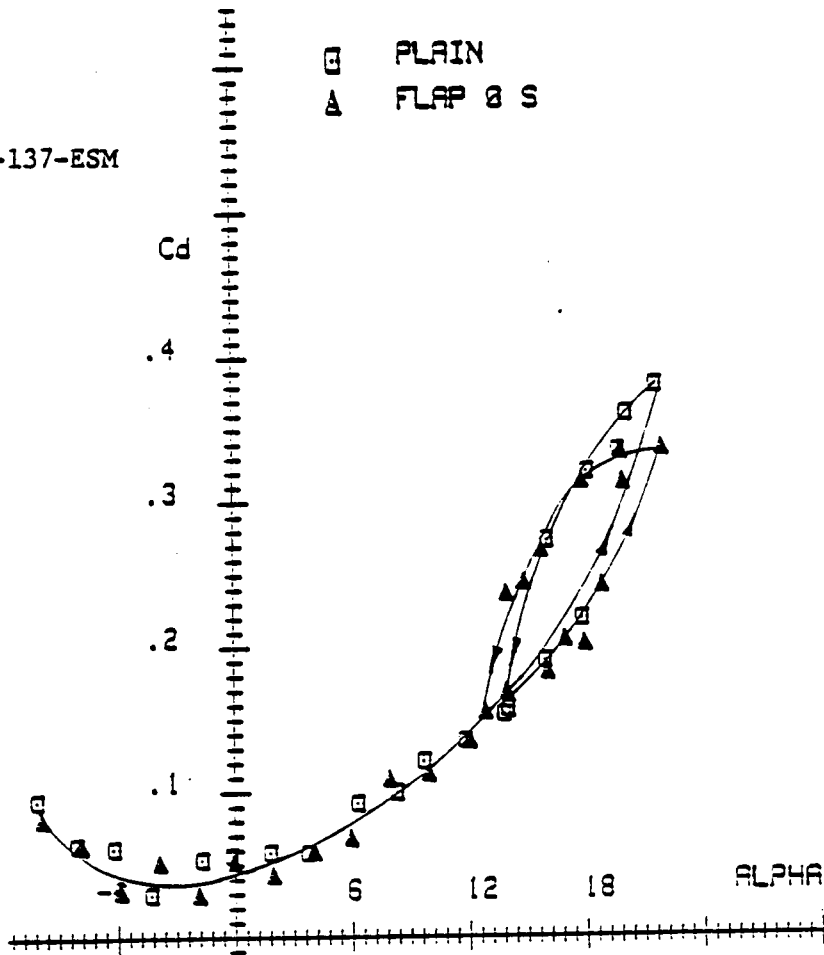


COMPARISON OF FLAP WING RE=200K AR=4

Fig. 6.11 : COMPARISON OF LIFT DATA FOR PLAIN-WING AND FLAP-WING WITH ZERO FLAP DEFLECTION.

AR = 4 RE. = 200,000

FX-63-137-ESM



COMPARISON OF FLAP WING  $RE=200K$   $AR=4$

Fig. 6.12 : COMPARISON OF DRAG DATA FOR PLAIN-WING AND FLAP-WING WITH ZERO FLAP DEFLECTION.

$AR = 4$        $RE. = 200,000$

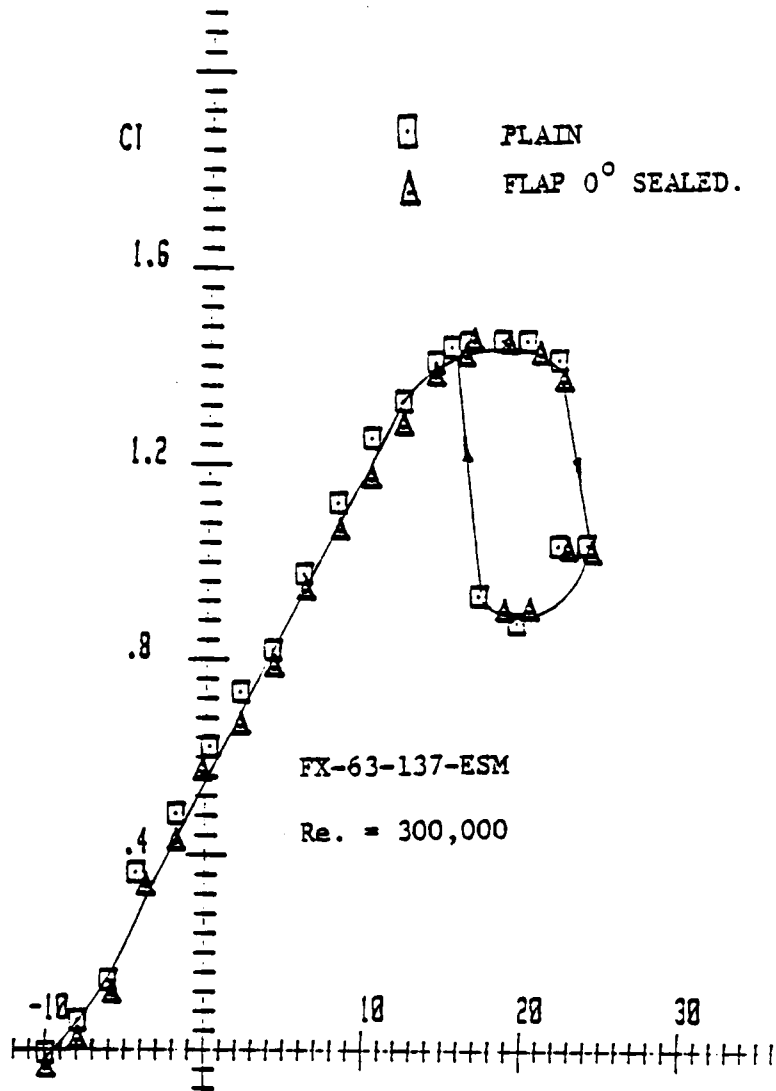
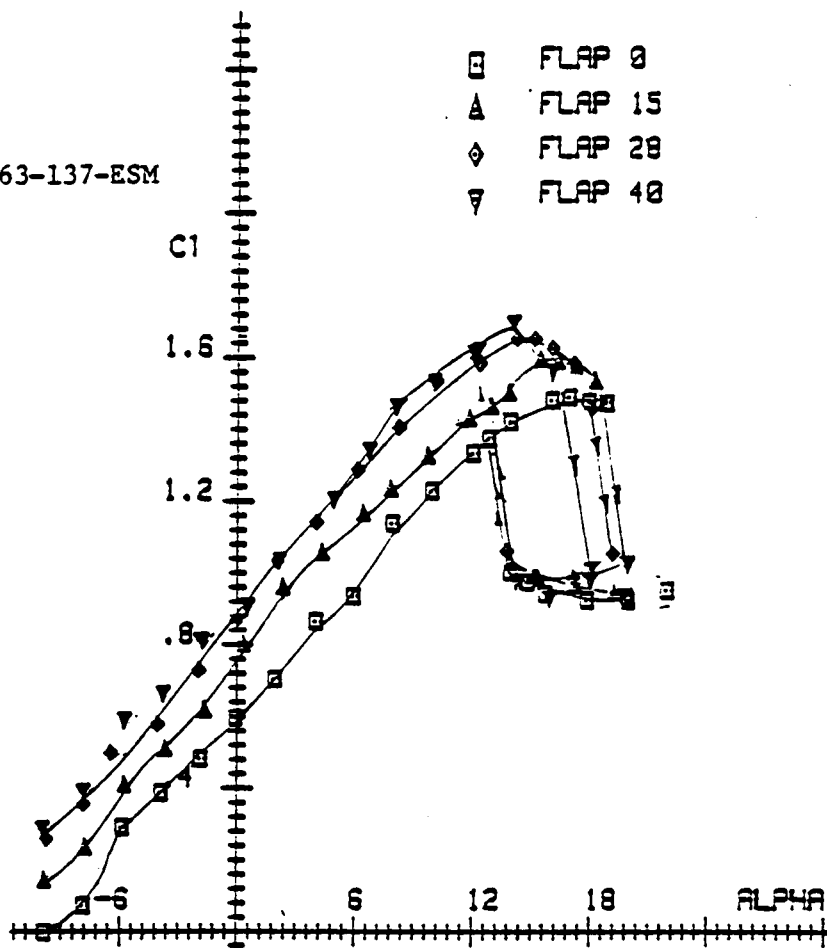


Fig. 6.13 : COMPARISON OF LIFT DATA FOR PLAIN WING AND  
 FLAP WING WITH ZERO FLAP DEFLECTION AT  
 RE. = 300,000

FX-63-137-ESM



CL VS. ALPHA AR=4 RE=200000

Fig. 6.14 : EFFECT OF FLAP DEFLECTION ON THE LIFT DATA FOR THE  
AR = 4 WING AT RE. = 200,000

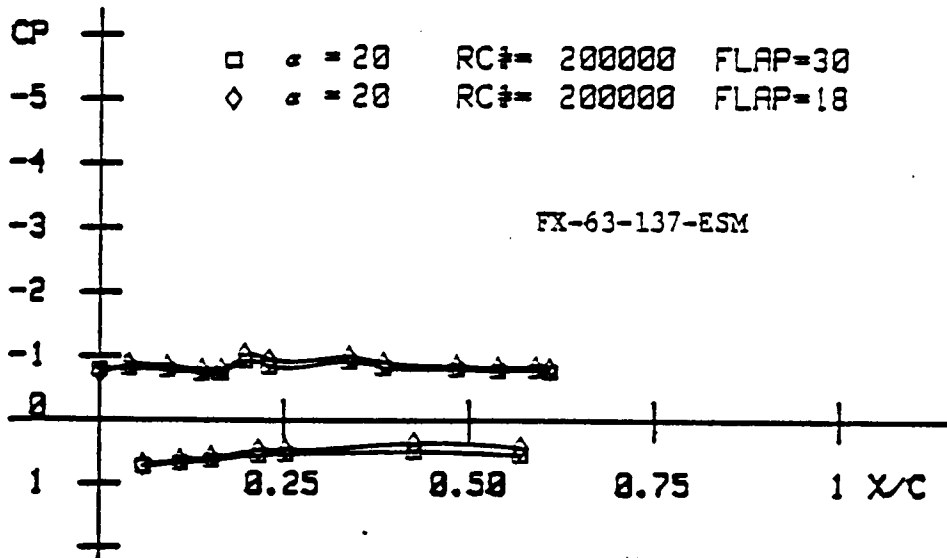
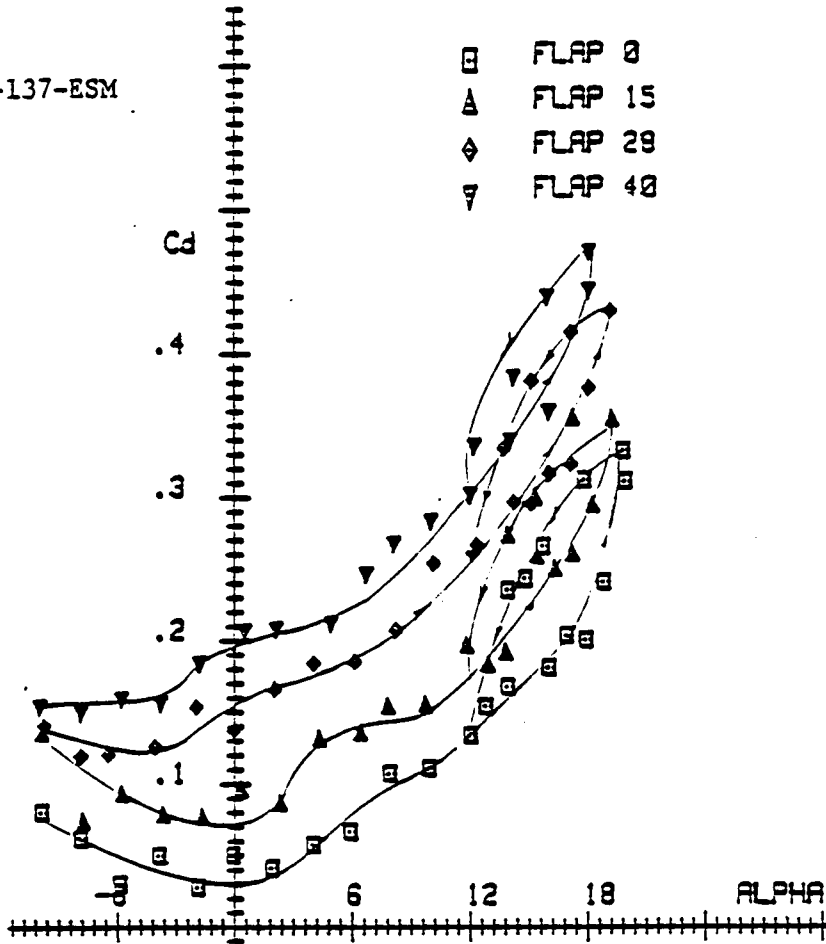


Fig. 6.15 : POST-STALL PRESSURE DISTRIBUTIONS FOR 18 DEG.  
AND 30 DEG. FLAP DEFLECTIONS AT  $RE. = 200,000$

FX-63-137-ESM



$C_D$  VS. ALPHA AR=4 RE=200000

Fig. 6.16 : EFFECT OF FLAP DEFLECTION ON THE DRAG DATA FOR THE AR = 4 WING AT RE. = 200,000

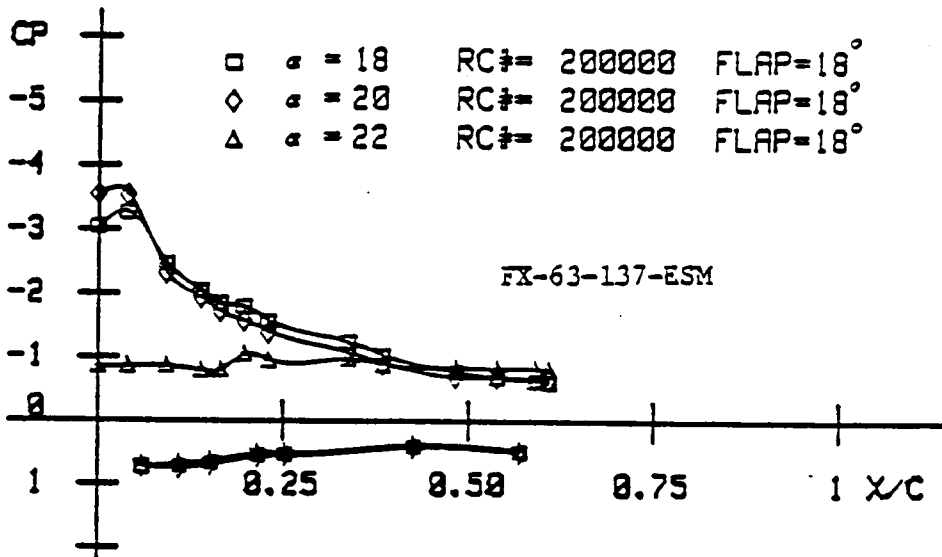
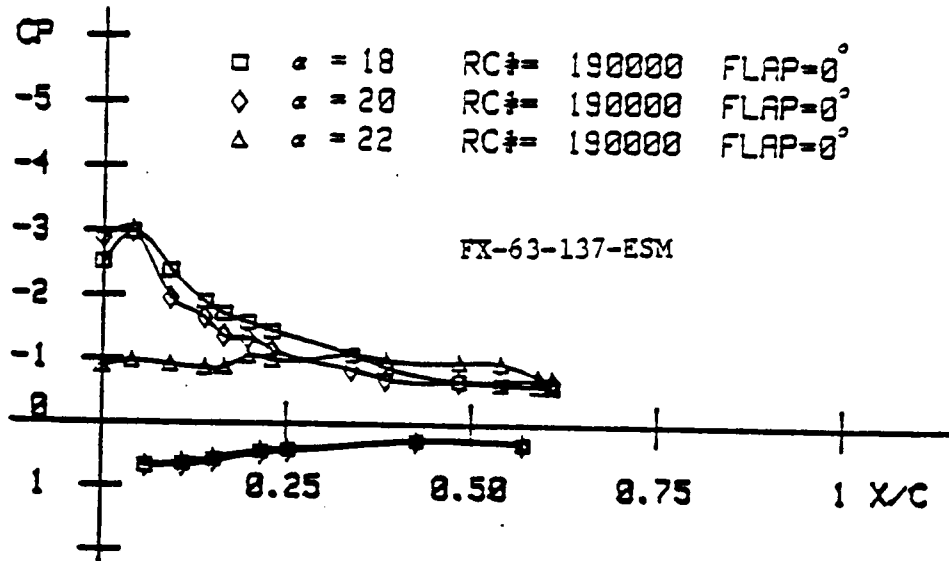
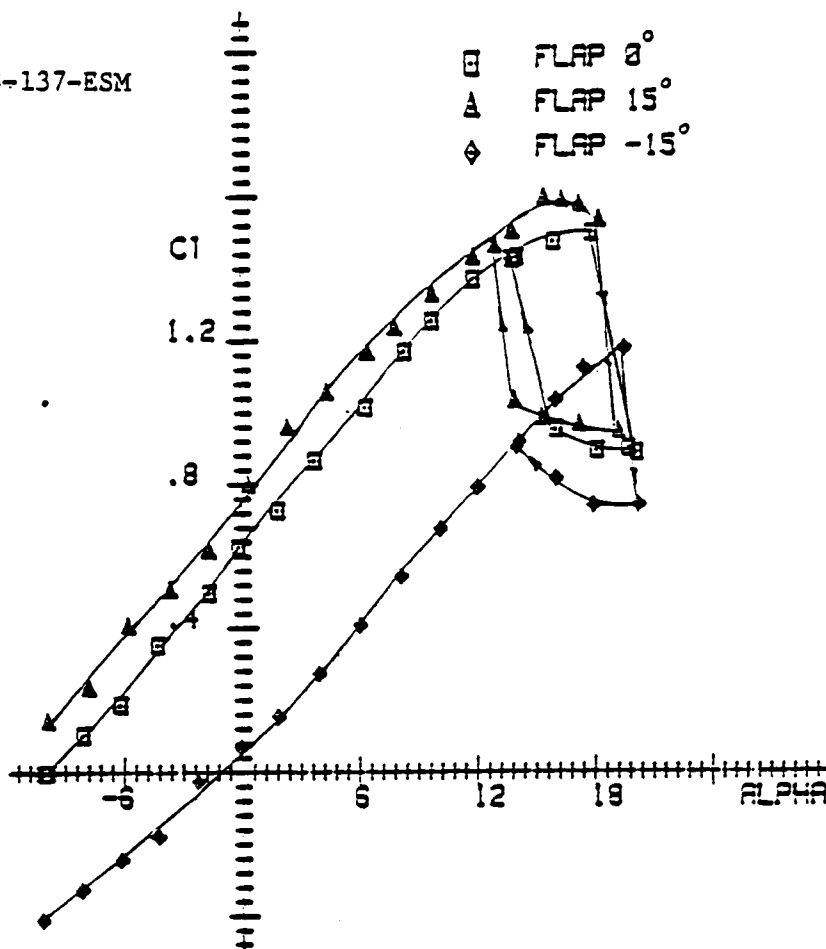


Fig. 6.17 : COMPARISON OF PRESSURE DISTRIBUTION HISTORIES AT STALL WITH AND WITHOUT FLAP DEFLECTIONS AT  $Re = 200,000$

FX-63-137-ESM



CL VS. ALPHA AR=4 RE=200000

Fig. 6.18 : EFFECT OF POSITIVE AND NEGATIVE FLAP DEFLECTIONS ON THE LIFT DATA FOR THE AR = 4 WING AT RE. = 200,000

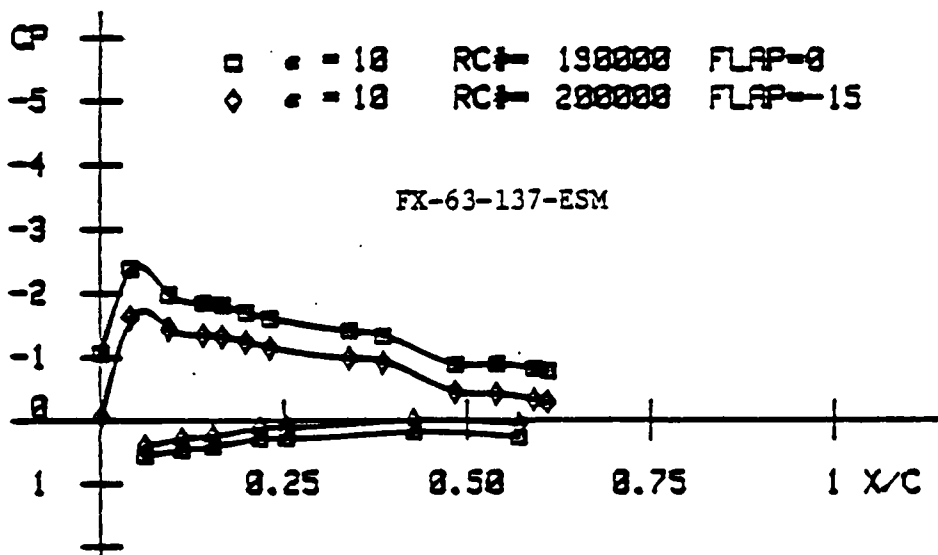
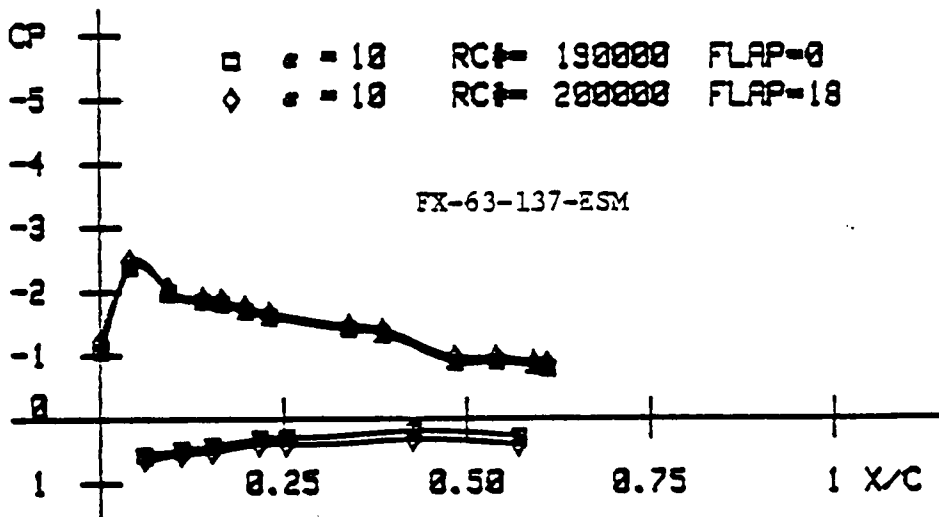


Fig. 6.19 : EFFECT OF POSITIVE AND NEGATIVE FLAP DEFLECTIONS ON PRESSURE DISTRIBUTIONS AT  $RE. = 200,000$

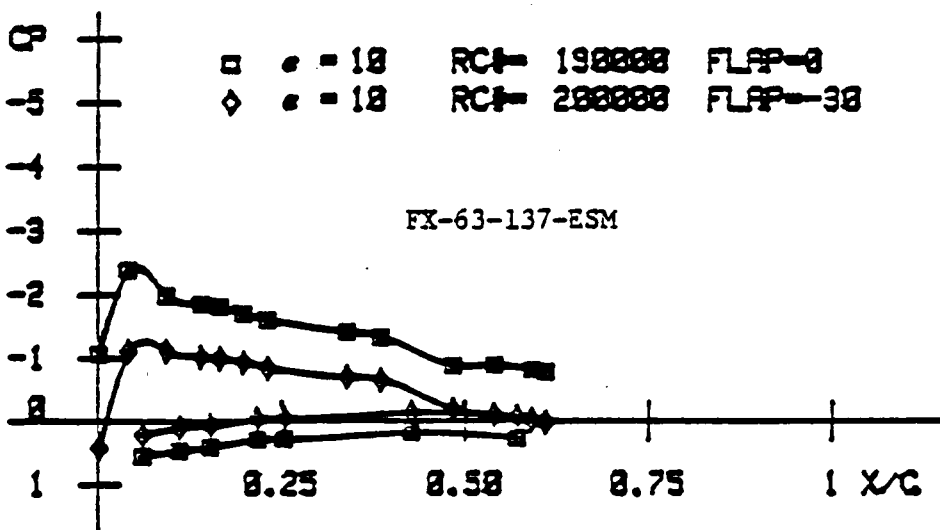
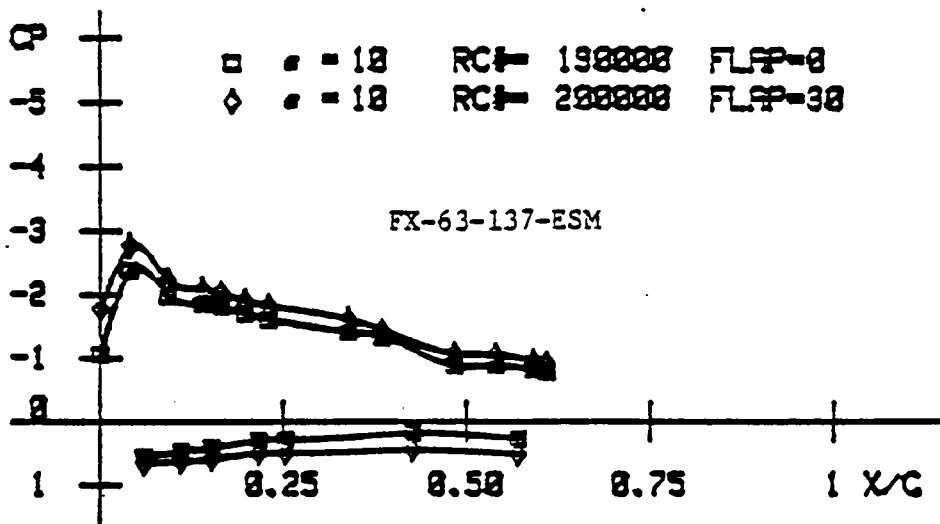


Fig. 6.20 : EFFECT OF POSITIVE AND NEGATIVE FLAP DEFLECTIONS ON PRESSURE DISTRIBUTIONS AT  $Re = 200,000$

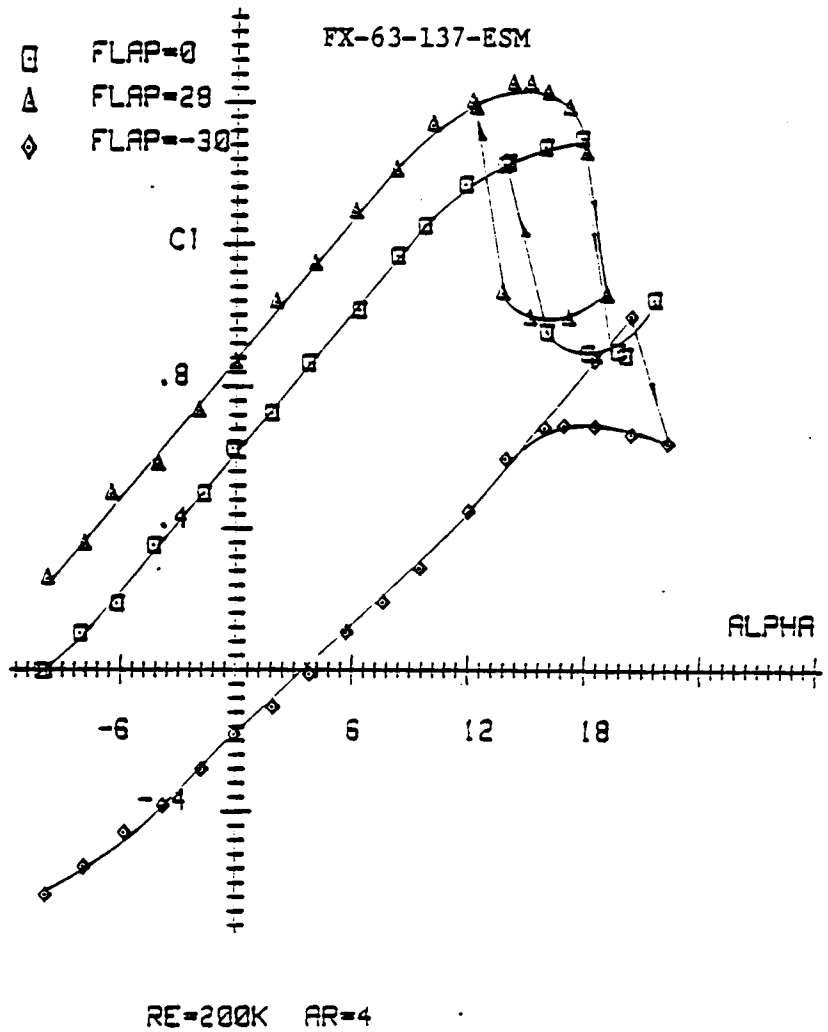
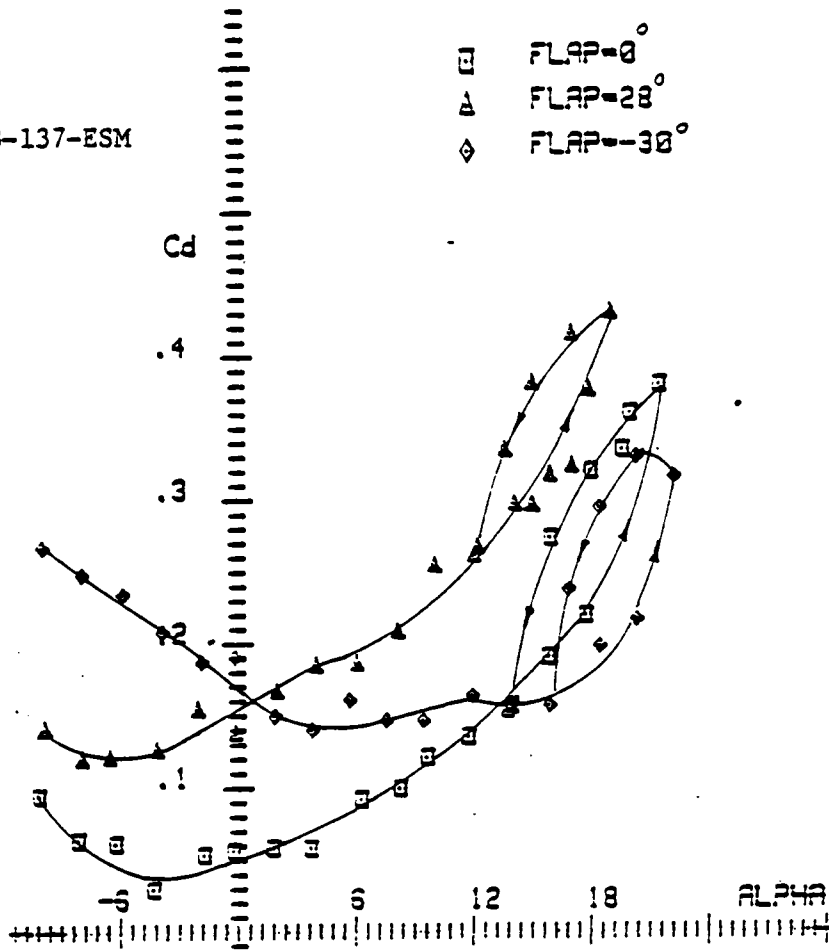


Fig. 6.21 : EFFECT OF POSITIVE AND NEGATIVE FLAP DEFLECTION ON THE AR = 4 WING AT RE. = 200,000

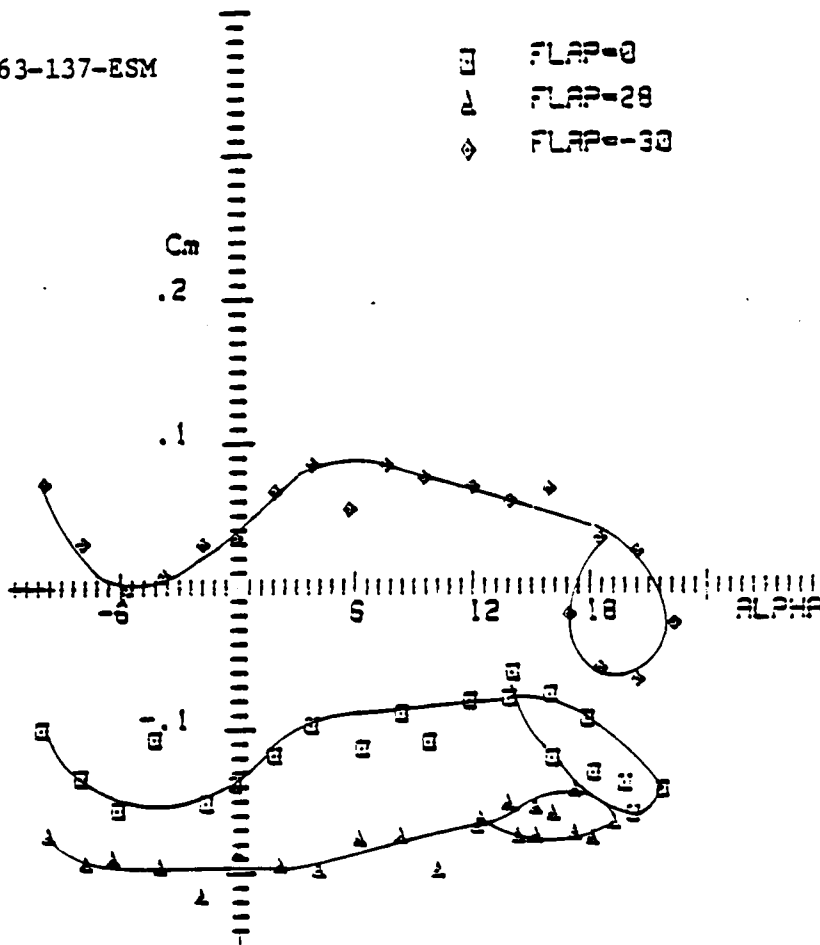
FX-63-137-ESM



CD VS. ALPHA AR=4 RE=200000

Fig. 6.22 : EFFECT OF POSITIVE AND NEGATIVE FLAP DEFLECTIONS ON THE DRAG DATA FOR THE AR=4 WING AT RE.=200,000

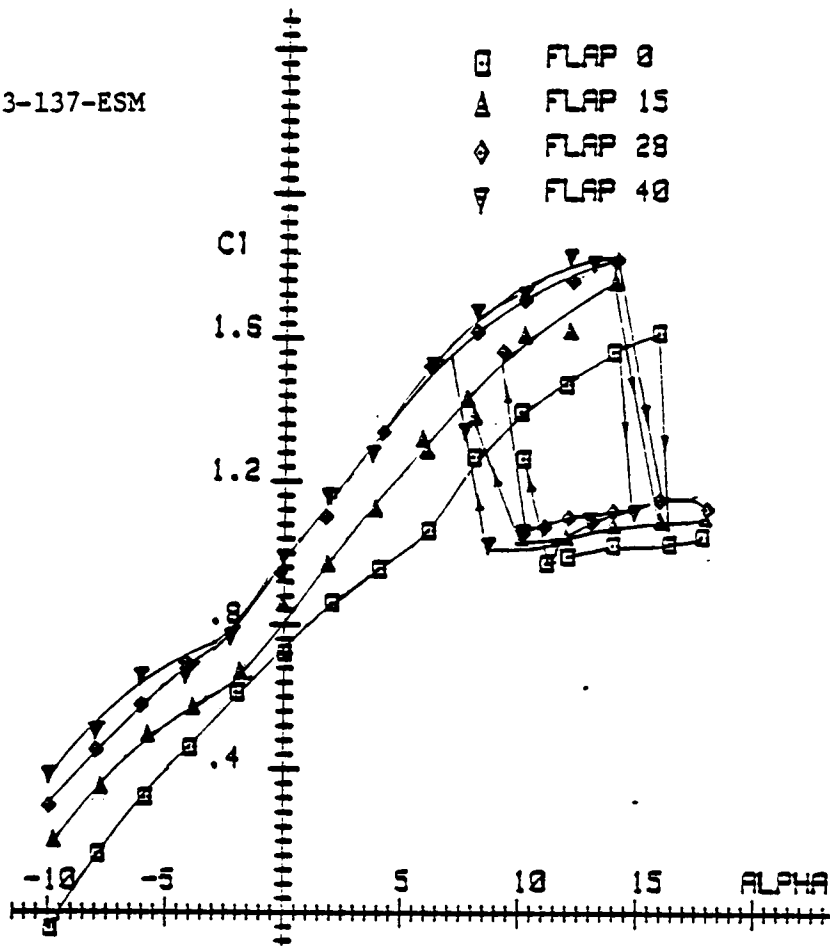
FX-63-137-ESM



CM VS. ALPHA AR=4 RE=200000

Fig. 6.23 : EFFECT OF POSITIVE AND NEGATIVE FLAP DEFLECTION ON PITCHING MOMENT DATA FOR THE AR = 4 WING AT RE. = 200,000

FX-63-137-ESM



CL VS. ALPHA AR=4 RE=100000

Fig. 6.24 : EFFECT OF FLAP DEFLECTION ON THE LIFT DATA FOR THE  
AR = 4 WING AT RE. = 100,000.

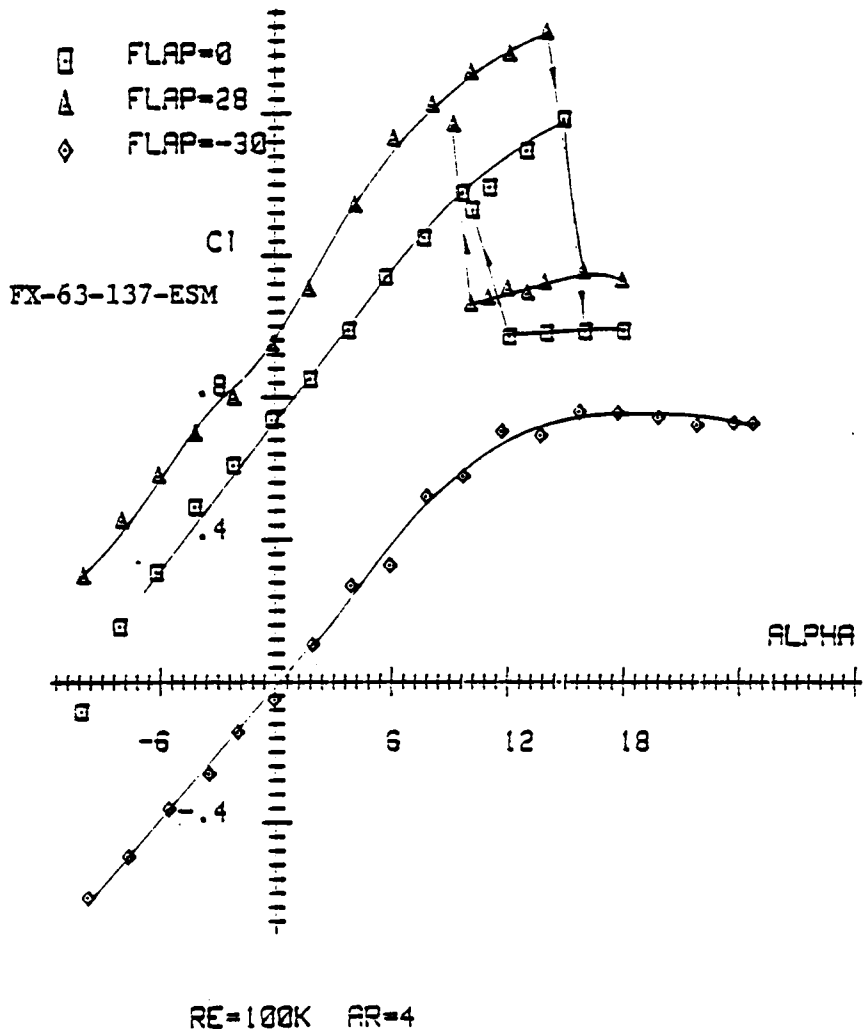


Fig. 6.25 : EFFECT OF POSITIVE AND NEGATIVE FLAP DEFLECTION ON THE AR = 4 WING AT RE. = 100,000.

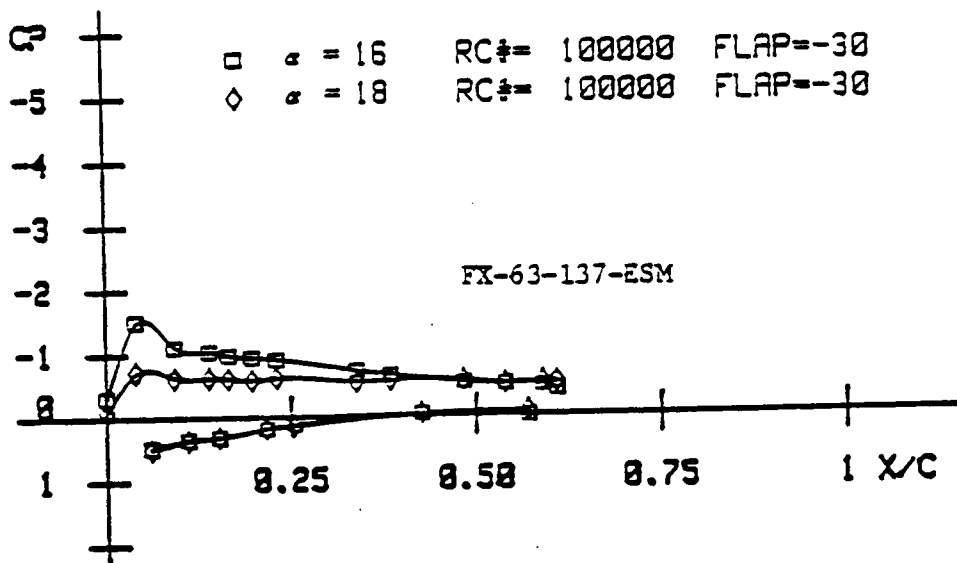
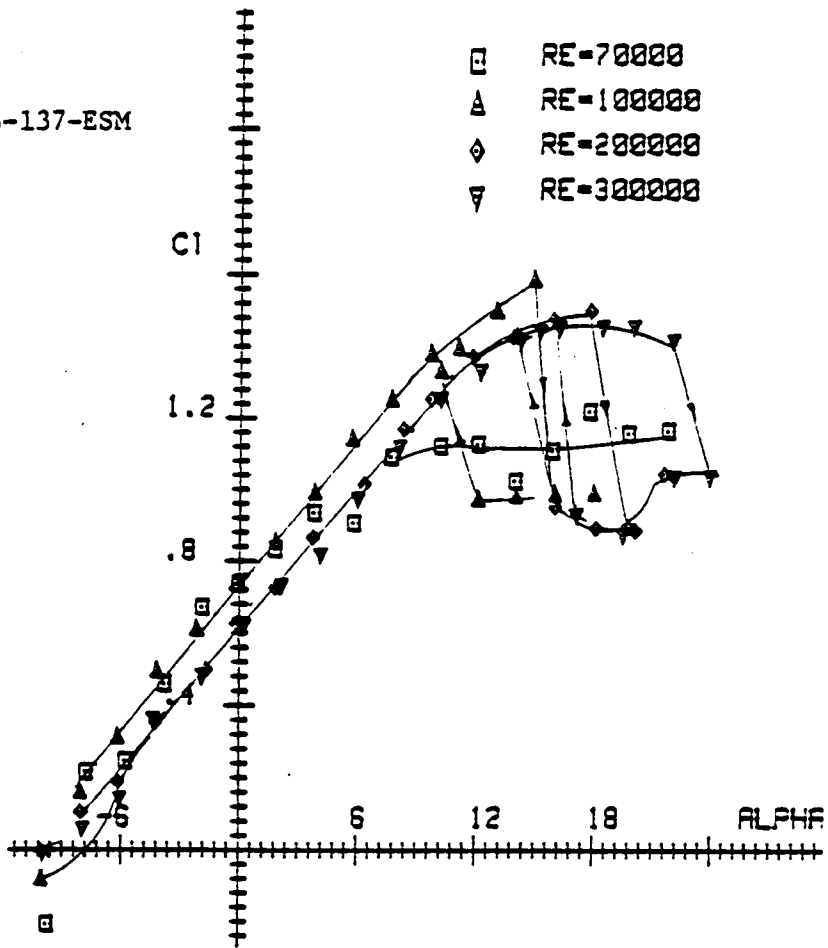


Fig. 6.26 : PRESSURE DISTRIBUTION AT STALL FOR THE CASE OF  
 $Re = 100,000$      $FLAP DEFLECTION = -30$  DEGREES

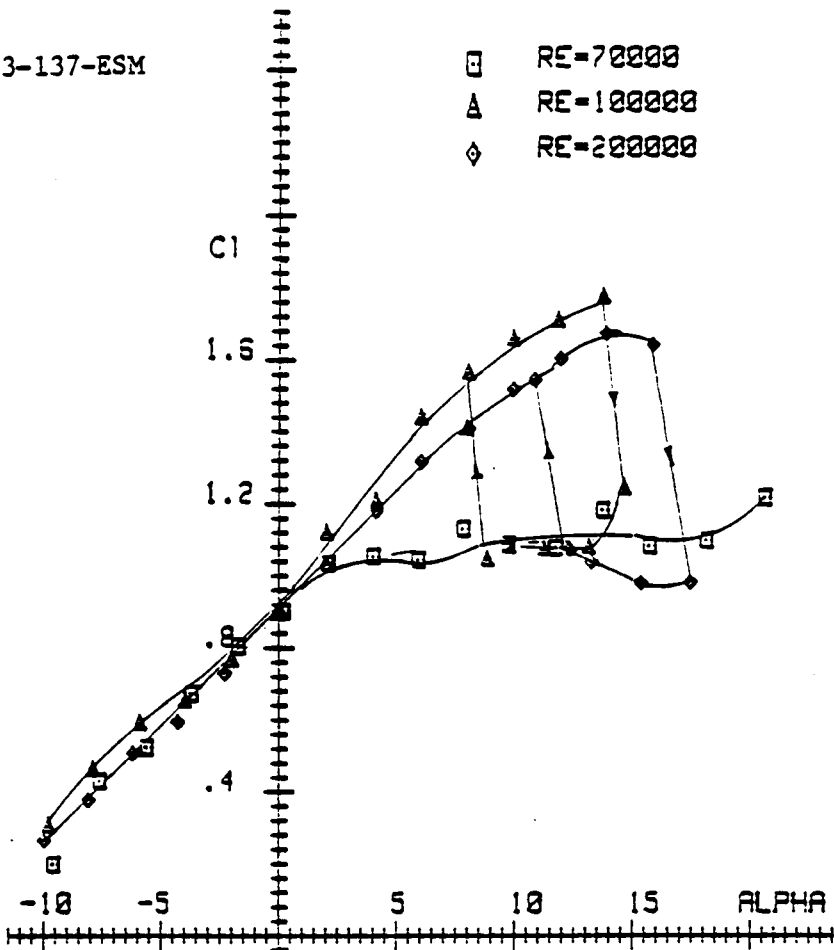
FX-63-137-ESM



CL VS. ALPHA AR=4 FLAP=0

Fig 6.27 : EFFECT OF REYNOLDS NUMBER ON THE LIFT DATA FOR THE AR = 4 WING WITH ZERO FLAP DEFLECTION.

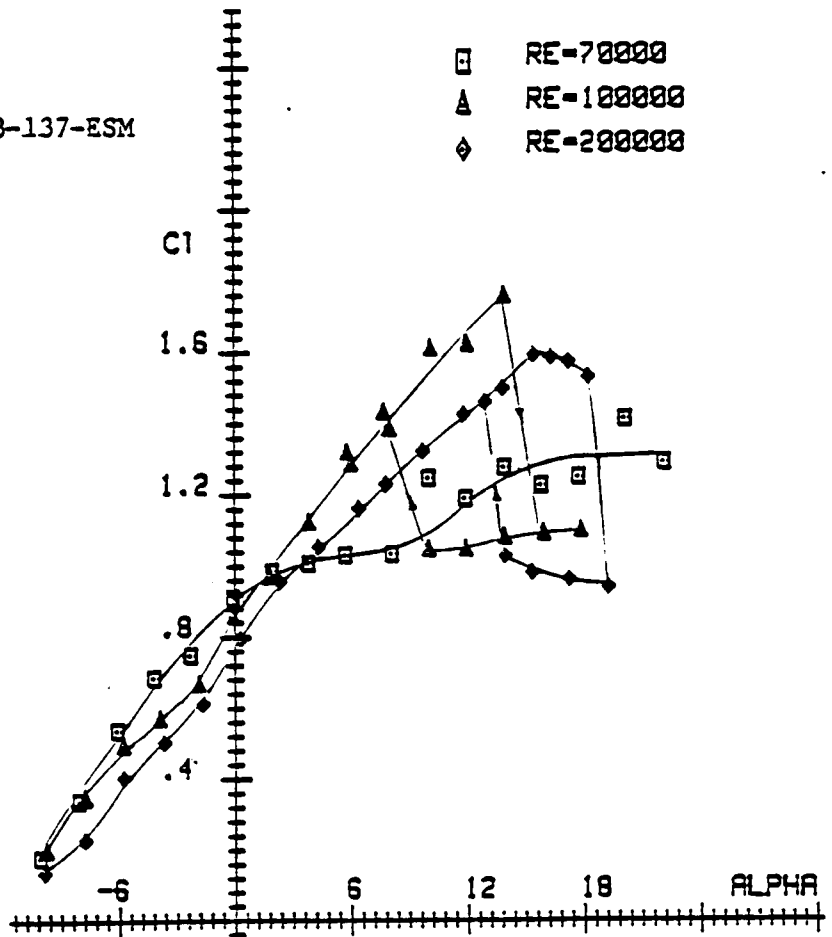
FX-63-137-ESM



CL VS. ALPHA AR=4 FLAP=33

Fig. 6.28 : EFFECT OF REYNOLDS NUMBER ON THE LIFT DATA FOR THE AR = 4 WING WITH ZERO FLAP DEFLECTION.

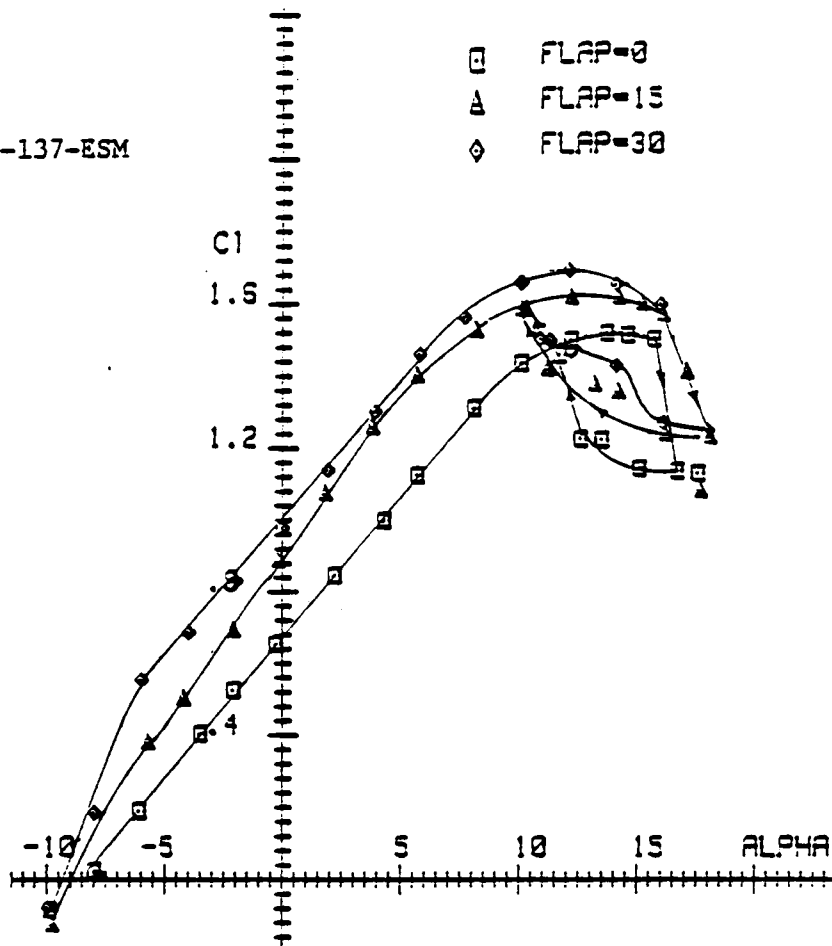
FX-63-137-ESM



CL VS. ALPHA AR=4 FLAP=15

Fig. 6.29 : EFFECT OF REYNOLDS NUMBER ON THE LIFT DATA FOR THE WING OF AR = 4 AND FLAP DEFLECTION OF 15 DEG.

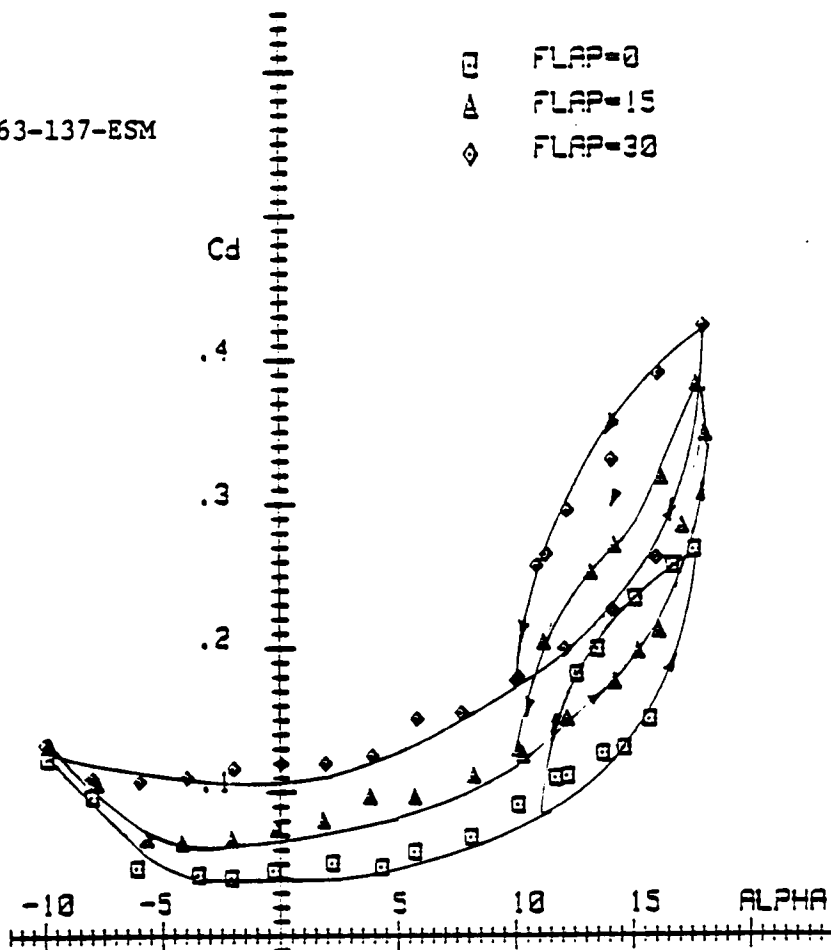
FX-63-137-ESM



CL VS. ALPHA AR=9 RE=200000

Fig. 6.30 : EFFECT OF SYMMETRIC CONTROL SURFACE DEFLECTION ON THE LIFT DATA FOR THE AR = 9 WING AT RE. = 200,000

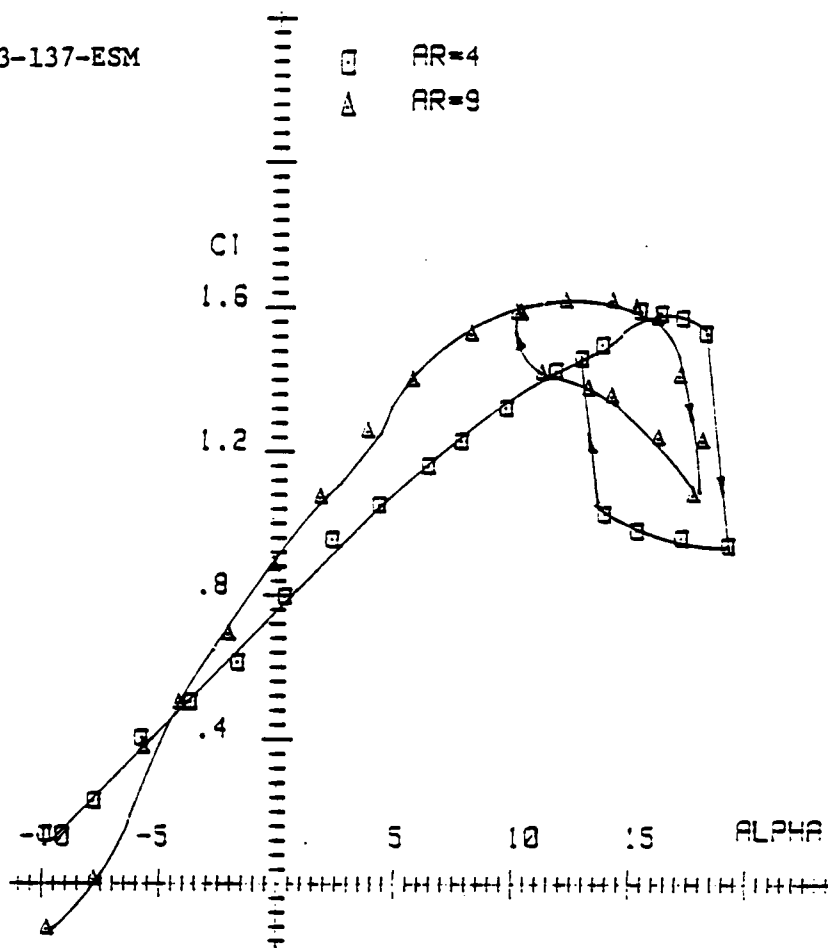
FX-63-137-ESM



CD VS. ALPHA AR=9 RE=200000

Fig. 6.31 : EFFECT OF SYMMETRIC CONTROL SURFACE DEFLECTION ON DRAG DATA FOR THE AR=9 WING AT RE. = 200,000

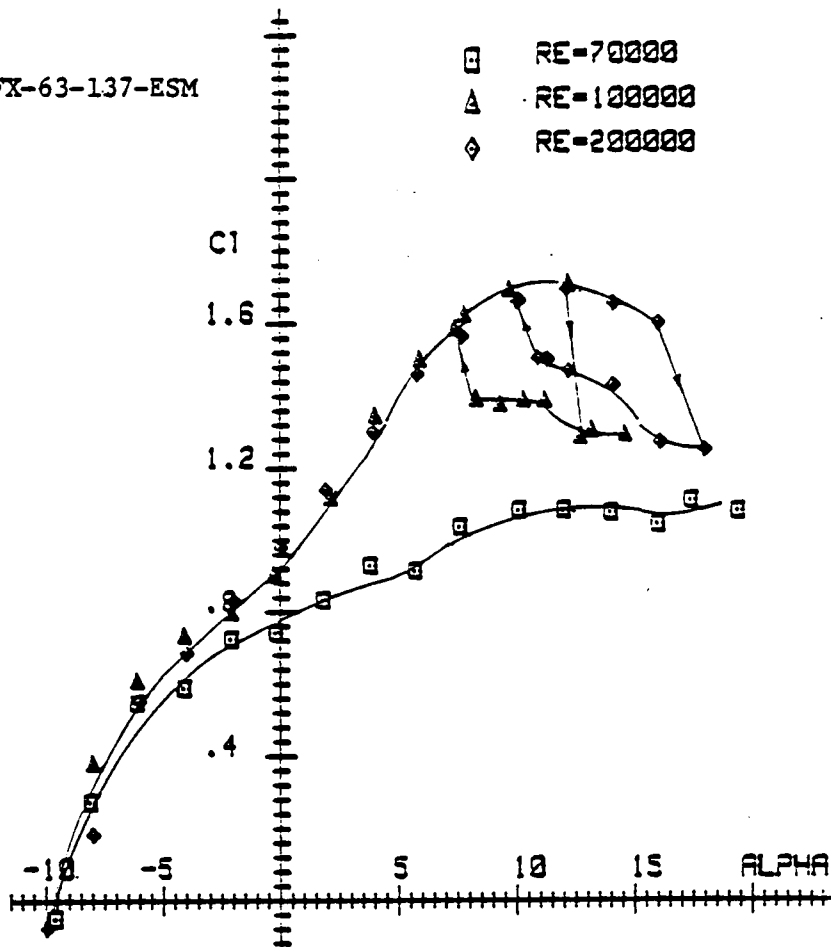
FX-63-137-ESM



RE = 200K FLAP DEFLECTION = 15 DEG.

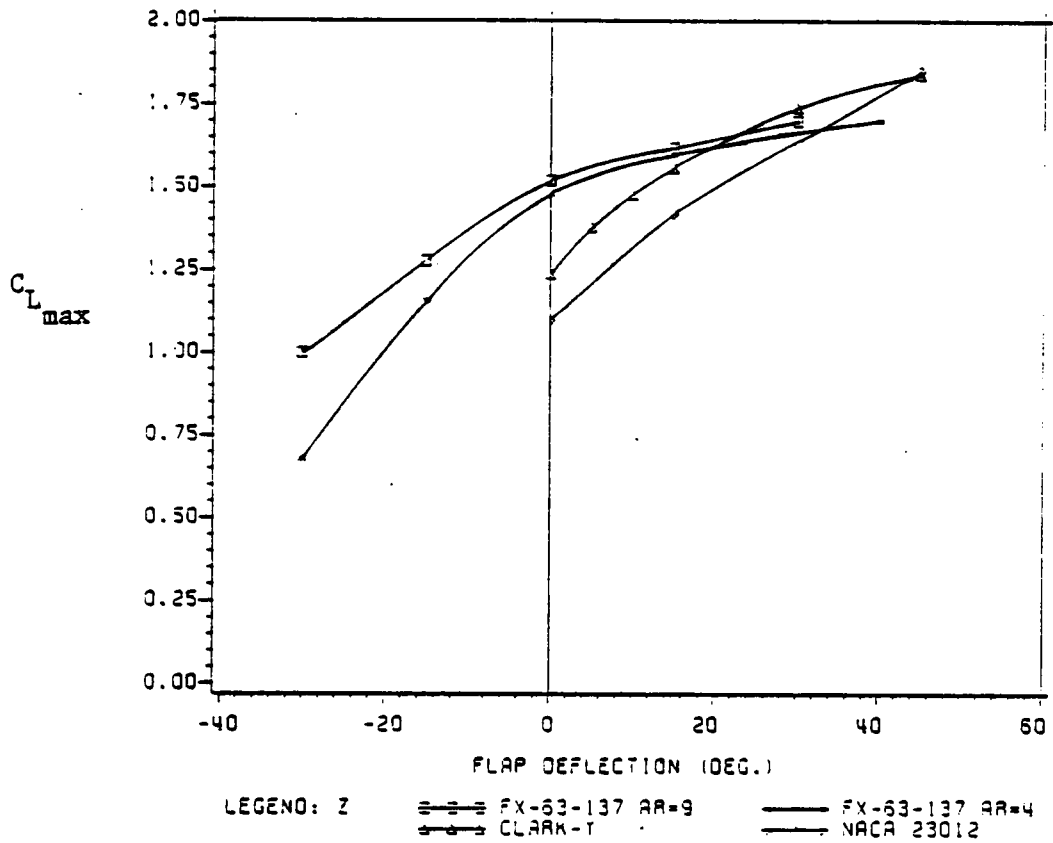
Fig. 6.32 : BEHAVIOR OF THE LIFT DATA FOR THE AR=4 AND THE AR=9 WINGS WITH FLAP/CONTROL SURFACE DEFLECTION OF 15 DEGREES AT RE. = 200,000.

FX-63-137-ESM



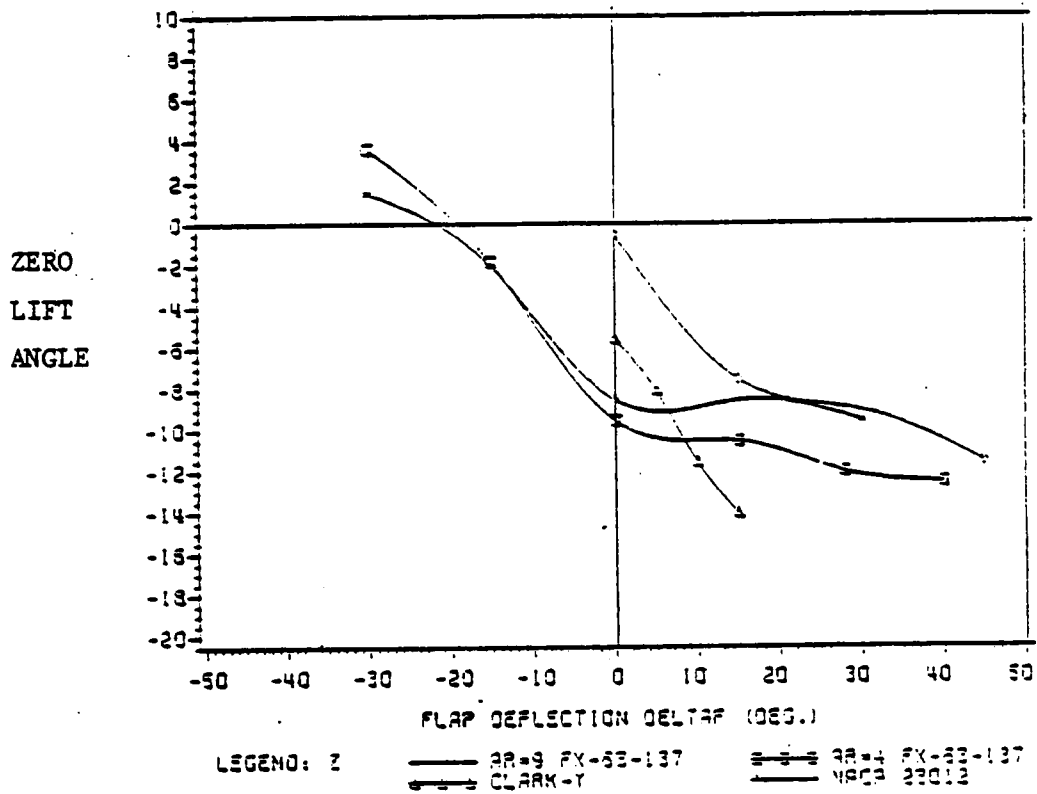
CL VS. ALPHA AR=9 FLAP=30

Fig. 6.33 : EFFECT OF REYNOLDS NUMBER ON THE LIFT DATA FOR THE WING OF AR=9 WITH SYMMETRIC CONTROL SURFACE DEFLECTION OF 30 DEGREES



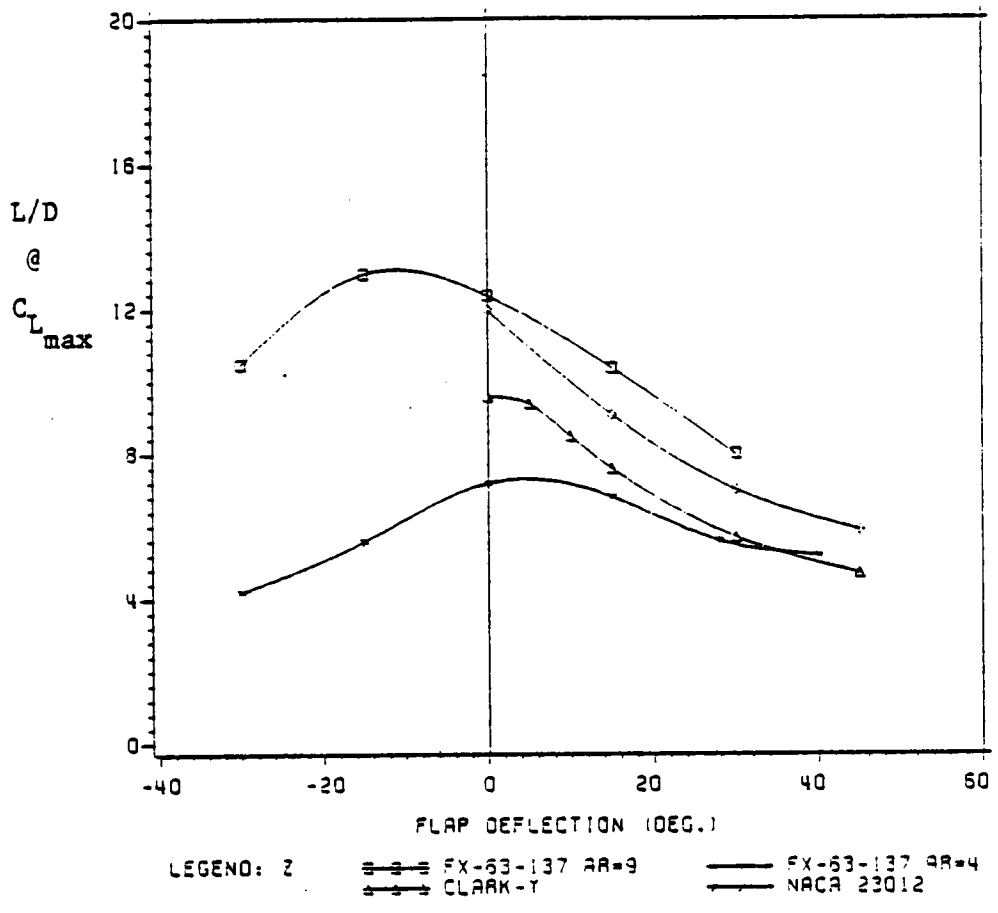
CONDITIONS PRESENTED IN TABLE 6.1

Fig. 6.34 : VARIATION OF MAXIMUM LIFT COEFFICIENT WITH FLAP DEFLECTION. COMPARISON OF FX-63-137-ESM DATA WITH CLARK-Y AND NACA 23012.



CONDITIONS PRESENTED IN TABLE 6.1

Fig. 6.35 : VARIATION OF THE ZERO LIFT ANGLE WITH FLAP DEFLECTION : COMPARISON OF FX-63-137-ESM DATA WITH CLARK-Y AND NACA 23012.



CONDITIONS PRESENTED IN TABLE 6.1

Fig 6.36 : VARIATION OF THE L/D RATIO AT  $C_{L_{max}}$  WITH FLAP DEFLECTION : COMPARISON OF FX-63-137-ESM DATA WITH CLARK-Y AND NACA 23012.

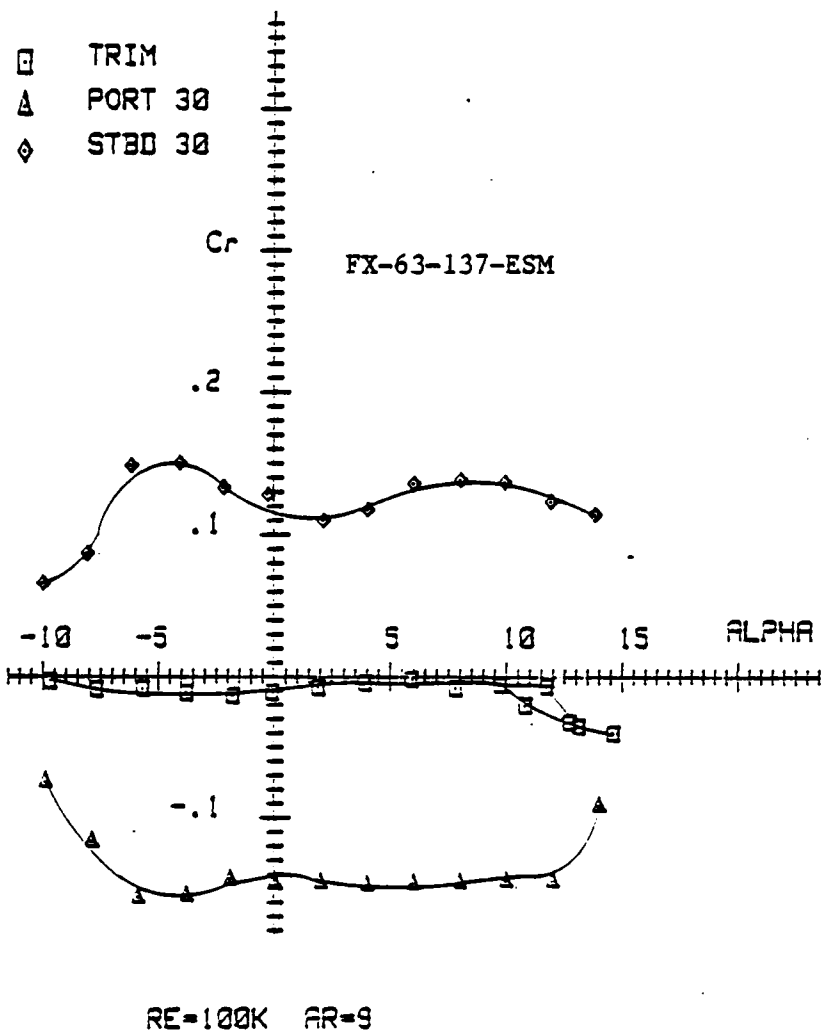


Fig. 6.37 : ROLLING MOMENT DATA FOR ASYMMETRIC CONTROL SURFACE DEFLECTIONS OF 30 DEGREES TO PORT AND STARBOARD COMPARED TO THE TRIM STATE. RE. = 100,000.

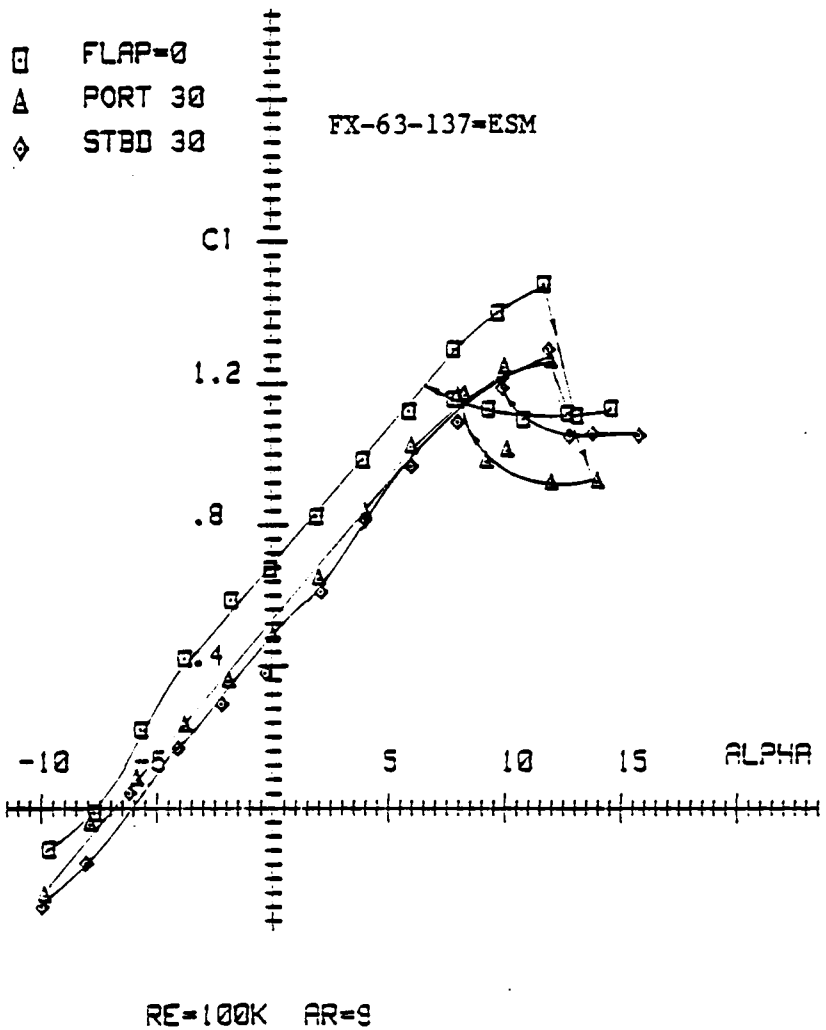


Fig. 6.38 : EFFECT OF ASYMMETRIC CONTROL SURFACE DEFLECTIONS OF  
 30 DEGREES TO PORT AND STARBOARD ON THE LIFT DATA.  
 AR = 9 RE. = 100,000.

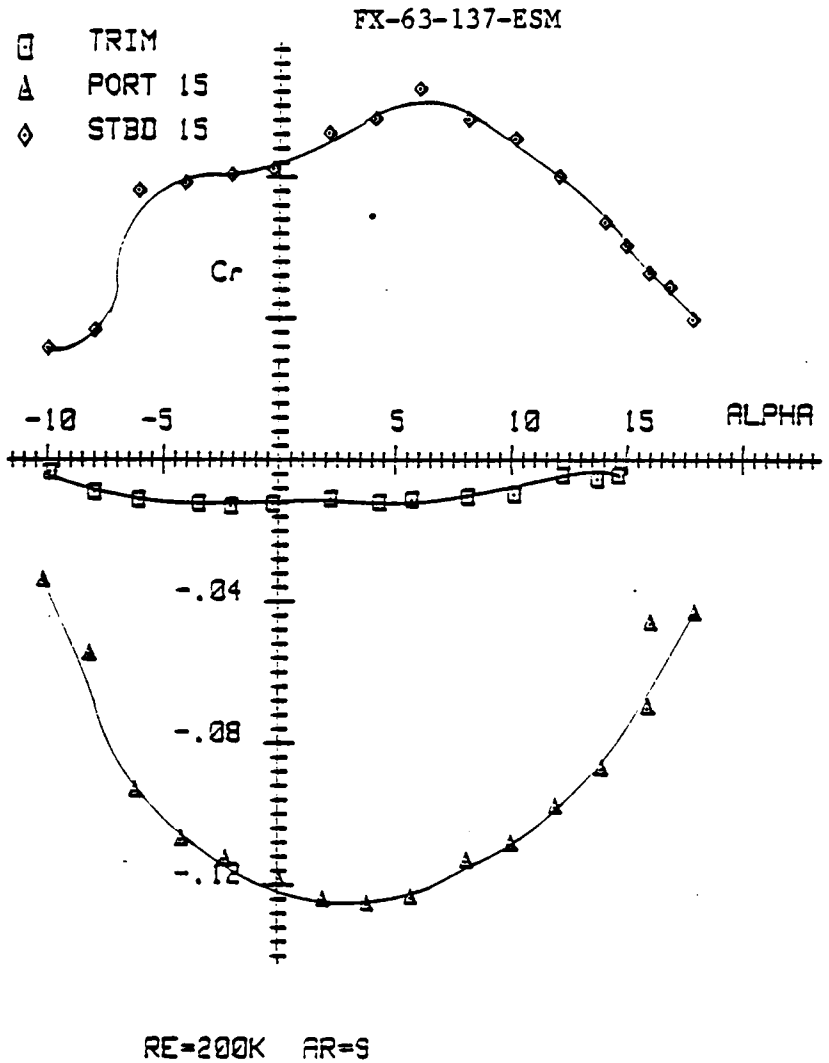
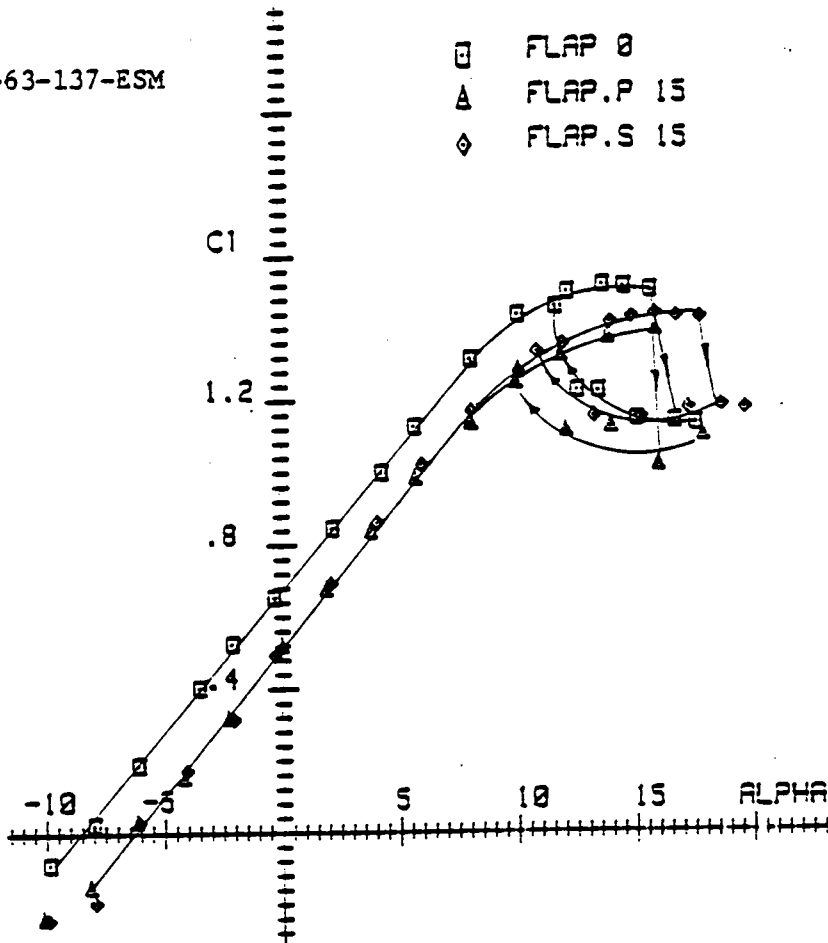


Fig. 6.39 : ROLLING MOMENT DATA FOR ASYMMETRIC CONTROL SURFACE DEFLECTIONS OF 15 DEGREES TO PORT AND STARBOARD FOR AR = 9 WING AT RE. = 200,000.

FX-63-137-ESM



CL VS. ALPHA AR=9 RE=200000

Fig. 6.40 : COMPARISON OF LIFT DATA FOR ASYMMETRIC CONTROL SURFACE DEFLECTION WITH THE TRIM STATE.

AR =9 RE. = 200,000.

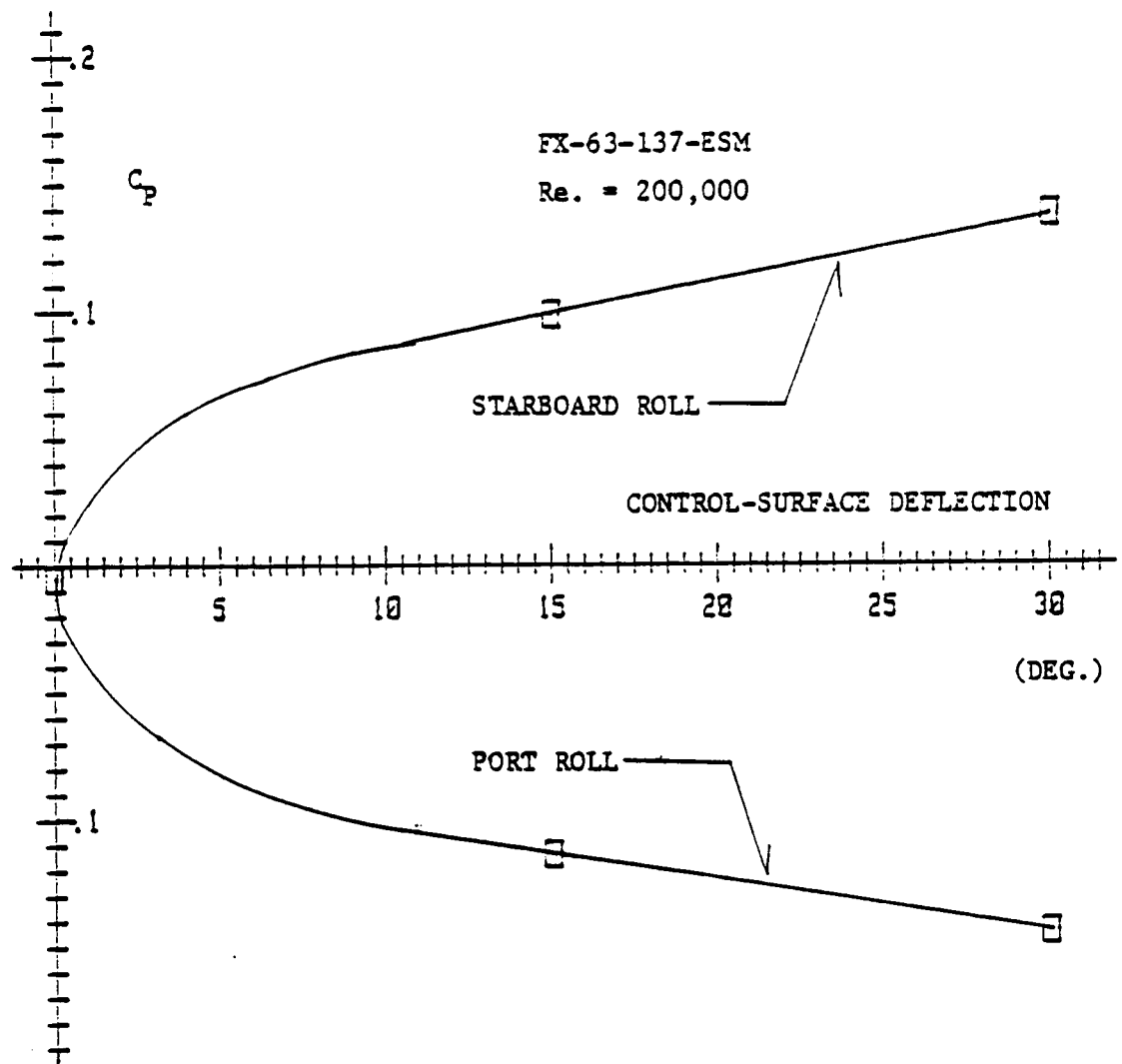


Fig. 6.41 : ROLLING MOMENT COEFFICIENT FOR ASYMMETRIC CONTROL-SURFACE DEFLECTIONS AT AN ANGLE OF ATTACK OF 10 DEGREES AND RE. = 200,000

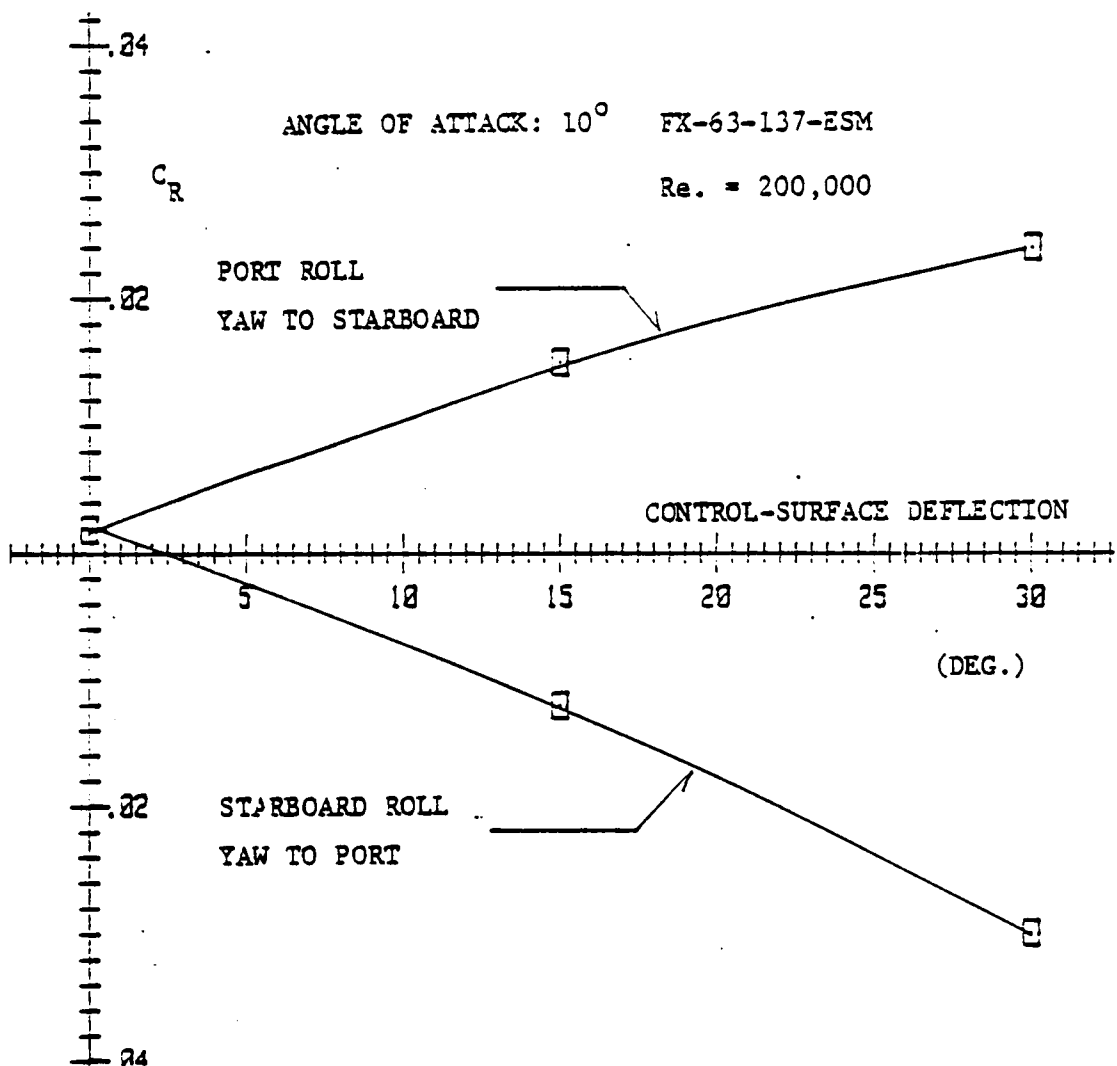


Fig. 6.42 : ADVERSE YAW MOMENT DUE TO ASYMMETRIC CONTROL-SURFACE DEFLECTION AT AN ANGLE OF ATTACK OF 10 DEGREES AND RE. = 200,000

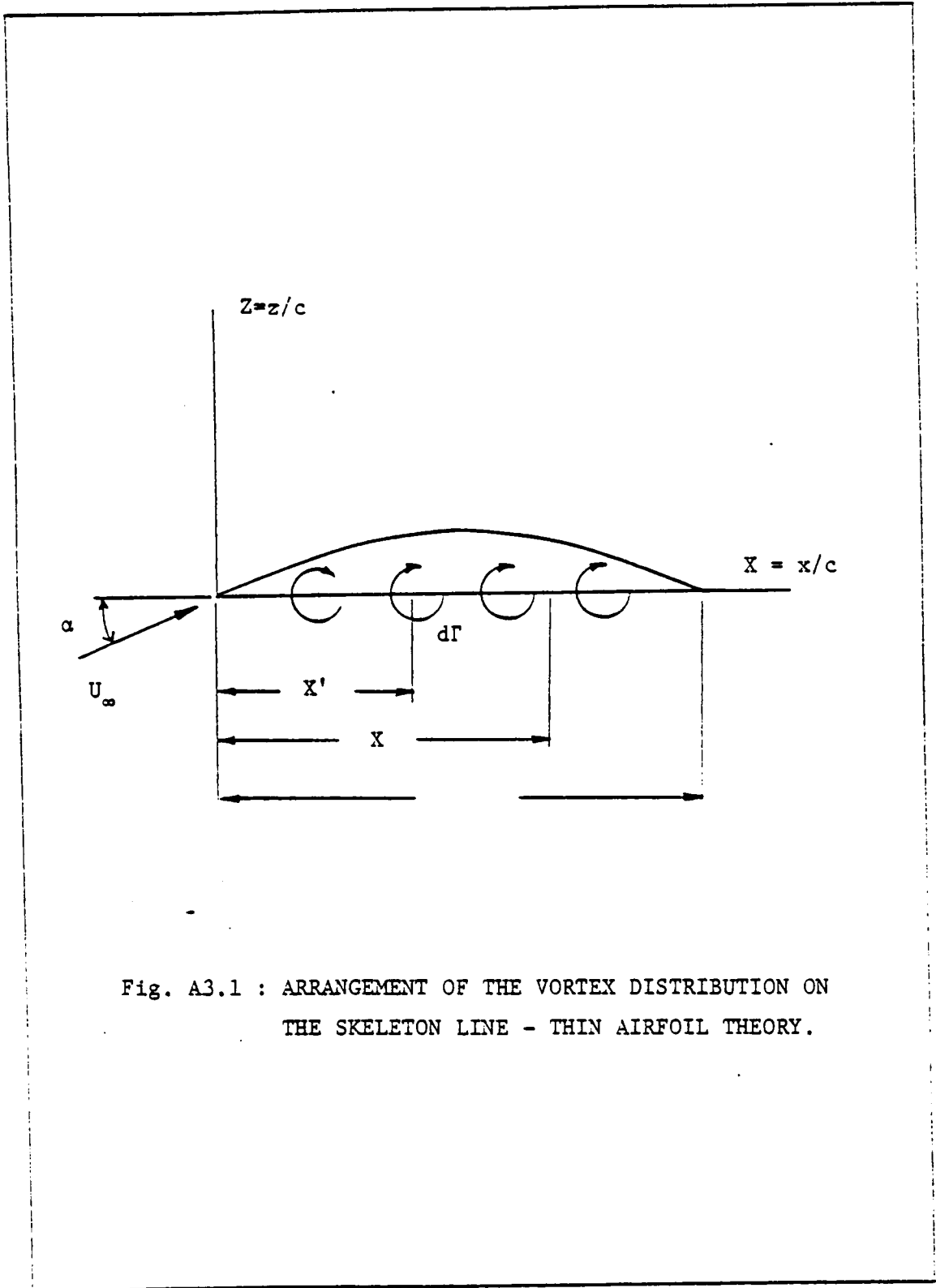


Fig. A3.1 : ARRANGEMENT OF THE VORTEX DISTRIBUTION ON THE SKELETON LINE - THIN AIRFOIL THEORY.

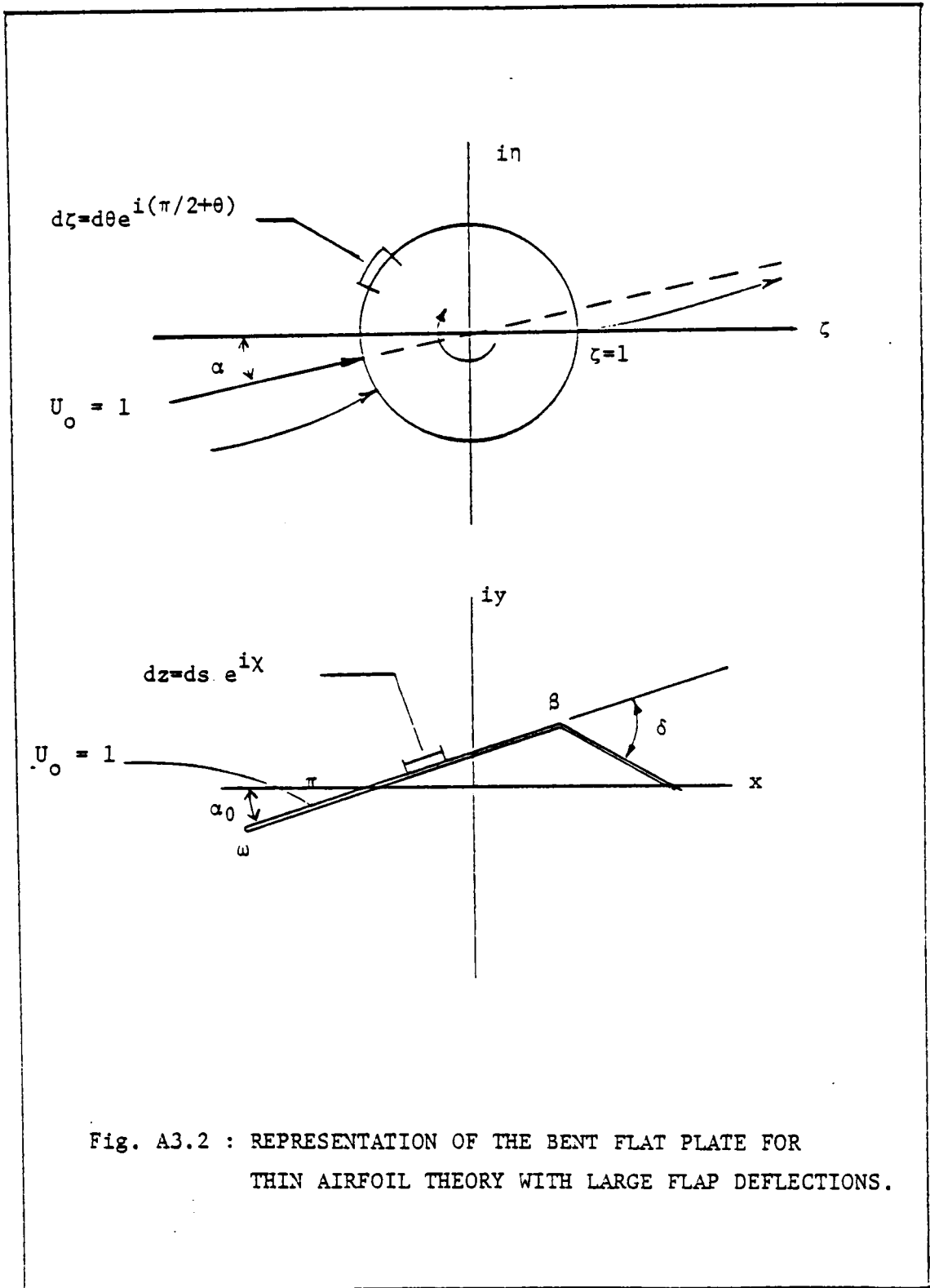


Fig. A3.2 : REPRESENTATION OF THE BENT FLAT PLATE FOR THIN AIRFOIL THEORY WITH LARGE FLAP DEFLECTIONS.

**The vita has been removed from  
the scanned document**